Nanoparticular Iron Complex Drugs for Parenteral Administration - Physicochemical Characterization, Biological Distribution and Pharmacological Safety

Dissertation
zur Erlangung des Grades

"Doktor der Naturwissenschaften" (Dr. rer. nat.)

im Promotionsfach
Pharmazie

am Fachbereich Chemie, Pharmazie und Geowissenschaften der Johannes Gutenberg-Universität in Mainz

Sören Fütterer
geb. in Heilbad Heiligenstadt

Mainz, 2014

Tag der mündlichen Prüfung: 31.07.2014

D77 (Dissertation Universität Mainz)

“Erfolg ist nicht endgültig, Mißerfolg ist nicht fatal; was zählt ist der Mut weiterzumachen.”

Winston Churchill

Table of contents

Table of contents

Abbreviations

ACD	Anemia of chronic diseases
ADEs	Adverse drug events
ADF	Annular dark field
AGP	Advanced glycation end products
AOPP	Advanced oxidation protein products
API	Active pharmaceutical ingredient
apo-Tf	Apotransferrin (iron free transferrin)
AUC	Area under plasma-concentration-time curve
BDI	Bleomycin detectable iron
BF	Bright field
Caco-2	Heterogeneous human epithelial colorectal adenocarcinoma cell line
CAM	Chorioallantoic membrane
CCD	Charge coupled device
CKD	Chronic kidney diseases
Cmax	Maximum concentration in plasma
CV	Cardiovascular
CVD	Cardiovascular disease
Cybrd1	see DCYTB
DCI	Directly chelatable iron
DCT-1	Divalent cation transporter (=DMT-1 / SLC11A2)
DCYTB	Membrane associated ferrireductase (=Cybrd1)
DF	Dark field
DLS	Dynamic light scattering
DMT-1	Divalent metal transporter 1
ED	Electron diffraction
EDTA	Ethylenediaminetetraacetic acid
EDX	Energy disperse X-ray spectroscopy
EMA	European Medicines Agency
EPO	Erythropoietin
ER	Endoplasmatic reticulum
Fe	Iron
Fe_3O_4	Magnetite
FeCM	Ferric carboxymaltose (Ferinject®)
FeG	Sodium ferric gluconate sucrose
FeHES	Iron hydroxyethyl starch (Feramyl®)
FeIM	Iron isomaltoside 1000 (Monofer®)
Fe-NbCD	Iron containing non-biological complex drugs
FeNP	Iron nanoparticle
FeOOH	Iron oxy hydroxide
α-Fe_2O_3	Hematite

α-FeOOH	Goethite
ß-FeOOH	Akaganéite
γ-Fe_2O_3	Maghemite
γ-FeOOH	Lepidocrocite
FePSC	Ferric ironpolymaltose sorbitol carboxymethylether
Fe-S	Iron sulfur
FeSuc	Iron sucrose (Venofer®)
FLVRC1	Feline leukemia virus, subgroup c surface receptor
Fpn	Ferroportin
Ftn	Ferritin
Fz	FerroZine®
HAADF	High angle annular dark field
Hb	Hemoglobin
HCP-1	Heme carrier protein 1 (=PCFT/SLC46A1)
HD	Hemodialysis
HepG2	Human hepatocellular carcinoma cell line
HF	Heart failure
HFE	Human hemochromatosis protein
HFeD	High molecular weight iron dextran (Dexferrum®)
HFeD_G	High molecular weight iron dextran; generic (Ironate®)
hkl	Miller indices
HMWID	High molecular weight iron dextrans
HO(s)	Heme oxygenase(s)
HRG-1	Heme responsive gene 1
ID	Iron deficiency
IDA	Iron deficiency anemia
IL-6	Interleukin 6
IQR	Interquartile range
IRE	Iron responsive element
IRP	Iron responsive protein
IS	Iron sucrose (=FeSuc; Venofer®)
ISS	Iron sucrose similars (generics of Venofer®)
IUPAC	International Union of Pure and Applied Chemistry
i.v.	Intravenous
KC	Kupffer cells
LDV	Laser Doppler velocimetry
LFeD1	Low molecular weight iron dextran (CosmoFer®)
LFeD2	Low molecular weight iron dextran (InFed®)
LIP	Labile iron pool
LMWID	Low molecular weight iron dextrans
MCH	Mean cell hemoglobin
MCV	Mean cell volume

MDA	Malonyldialdehyde
MDCI	Mobilizer dependent chelatable iron
MPS	Mononuclear phagocyte system (newer term for RES)
MRI	Magnetic resonance imaging
NaCl	Sodium chloride 0.9 % in water
NbCD	Non-biological complex drugs
NED	Nano electron diffraction
no.	Number
NP(s)	Nanoparticle(s)
NRAMP-1	Natural resistance associated macrophage protein 1
NSAIDs	Non-steroidal anti-inflammatory drugs
NTA	Nitrilotriacetic acid
NTBI	Non-transferrin bound iron
$O_2^{\cdot -}$	Superoxide radical
$^{\cdot}OH$	Hydroxyl radical
p.	page
pp.	pages
P.FeM1.13	Trial 1
P.FeM2.13	Trial 2
P.FeM3.13	Trial 3
P.FeM4.13	Trial 4
P.FeM5.13	Trial 5 (dose dependency)
PCC	Protein carbonyl content
PCFT	Proton coupled high-affinity folate transporter (=HCP-1/SLC46A1)
PCS	Photon correlation spectroscopy = DLS
PDI	Polydispersity index
RBC	Red blood cells
RE	Reticuloendothelial
RES	Reticuloendothelial system (older term for MPS)
RI	refractive index
ROS	Reactive oxygen species
SAED	Selected area electron diffraction
SD	Standard deviation
SEM	Standard error of the mean
SLN	Solid lipid nanoparticles
Steap3	Metalloreductase, encoded by Step3 gene
sTfR	Serum transferrin receptor
TEM	Transmission electron microscopy
Tf	Transferrin
Tf-Fe_2	Holotransferrin
TfR	Transferrin receptor
THP-1	Human leukemic monocytic cell line

TIBC	Total iron binding capacity
WHO	World Health Organization
XRPD	X-ray powder diffraction

1. Introduction and review on iron supplement drugs

1.1. The diversity of iron in nature, economy and biology

Iron in space and on our planet

Iron is a transition metal with the atomic number 26 and is located in the 8th subgroup of the periodic table. From point of frequency of occurrence, it is the 9th most abundant element in universe. The life span of a star ends with the production of the radioactive iron precursor-nuclide nickel-56. This is the consequence of the fact that the produced nickel-56 is the element with the highest atomic number for which the fusion is an exothermic reaction. In case of heavier elements, the reaction is endothermic and takes only place during a supernova explosion. Iron is the 2nd most common element on earth from point of mass fraction. Leaving aside the atmosphere, it is the most common element as the core of our planet is assumed to be mainly consisting of iron and nickel. The earth's crust contains iron with the 4th highest frequency of occurrence.

Meteorites that have been fallen on our planet were the first source of genuine iron for humankind long before iron extraction from ore was possible. Oldest founds of such iron containing items made by men are dated about 3100 B.C. The extraction from ore has been performed at least since 1300 B.C. The Iron Age started when superior iron replaced bronze as material for tools and weapons.

As pure iron is reactive to oxygen and water, it is rarely present in genuine state, but as alloying with nickel from meteorites or as reduction products in basalts (volcanic rock). The main sources of iron are ores such as the minerals magnetite (Fe_3O_4), hematite (Fe_2O_3), pyrrhotin (FeS), pyrite (FeS_2) and siderite ($FeCO_3$) and the rock limonite, which is a water containing mixture of different iron oxides / iron oxy hydroxides (FeOOH) e.g. goethite, lepidocrocite, and others.

Economic relevance of iron

The industry uses iron as pig iron (4-5% carbon, intermediate in the production of cast iron and steel), cast iron (2-6.7 % carbon, not plastically formable / forgeable) and steel (0.1-2.1 % carbon, forgeable), which is used as constructional or tool steel. Iron is beside cobalt and nickel a ferromagnetic metal that is important in the commercial use of electromagnetism. Iron compounds, especially iron (III) chloride and iron (II) sulfate, are industrially used e.g. as catalysts, coloring agents, agents for water purification, agents for sewage treatment, and reducing agents.

Iron in biology

Iron can be present in oxidation states between -2 and +6 with the most common states of +2 (ferrous iron) and +3 (ferric iron). Iron is an essential trace element for most creatures. Iron has the ability to change its oxidation states and the corresponding redox potential is varying dependent on the ligand it is bound to. These characteristics make it important for many enzymes and proteins (**Figure 1**). It can be present as central atom in the cofactor heme (cytochromes, myoglobin, hemoglobin, katalases), as iron sulfur clusters in iron sulfur (Fe-S) proteins (e.g. nitrogenases, dehydrogenases, aconitases, ferredoxin) or as iron in non-heme containing proteins (e.g. hemerythrine as oxygen transporter in case of marine invertebrates, ribonucleotide reductase in DNA synthesis, and methane monooxygenase in case of methanotropic bacterias). These proteins and enzymes are essential for metabolism (cytochromes and Fe-S proteins in citric acid cycle), oxygen transport (hemoglobin in blood, myoglobin in muscle), degradation of reactive hydrogen peroxide (katalases) and DNA synthesis (ribonucleotide reductase) in most creatures.

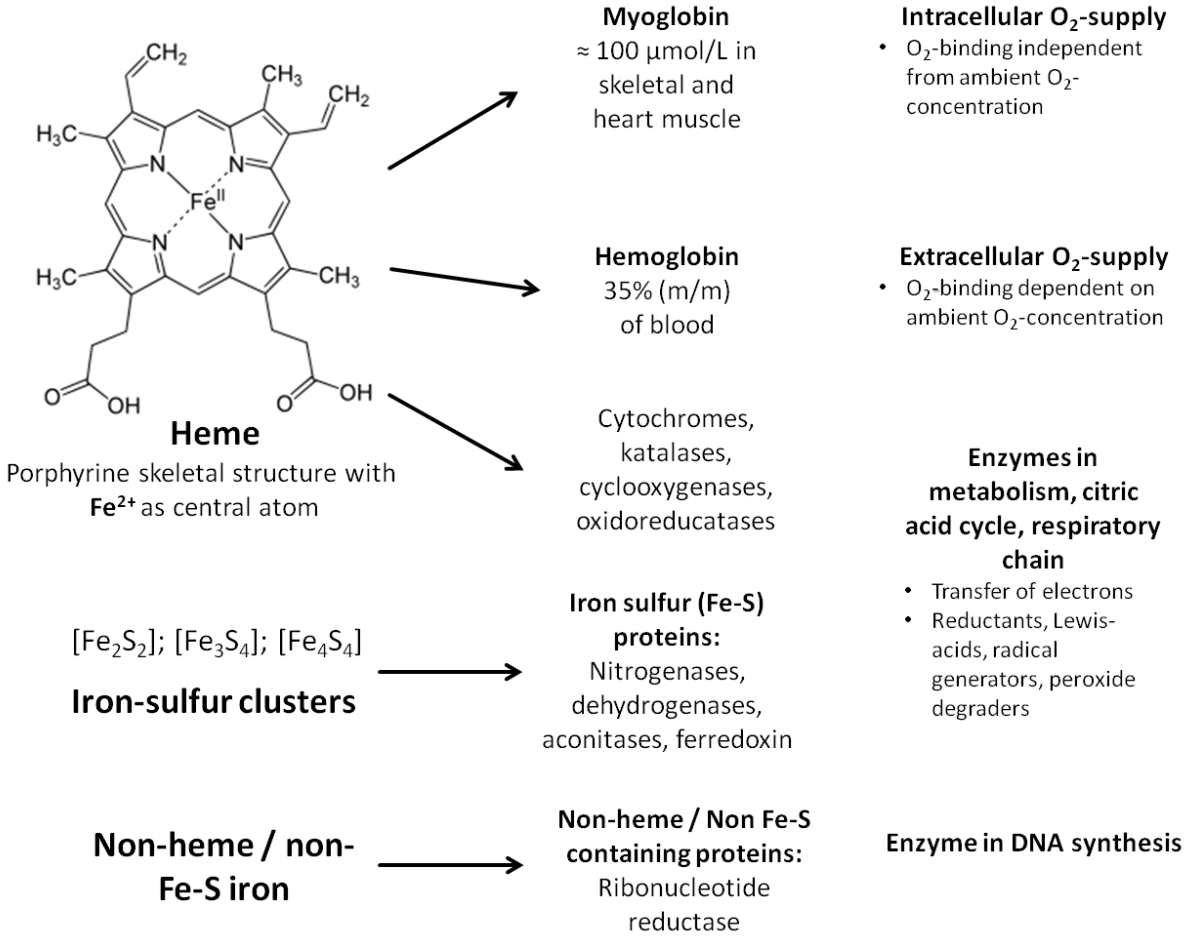

Figure 1 - Physiological importance of iron and iron containing proteins. Iron is key component of proteins in form of heme, iron sulfur (Fe-S) clusters and non-heme / non Fe-S iron. The ability of iron to change its oxidation states and the corresponding redox potential dependent on the ligand it is bound to makes it irreplaceable for most creatures. It thus exhibits systemic and local oxygen supply, catalyzes redox reactions, serves as Lewis acid, generates and degrades radicals, makes nitrogen physiological accessible and participates in energy supply as well as DNA and protein synthesis.

1.2. Iron homeostasis

1.2.1. Iron relevance and body distribution

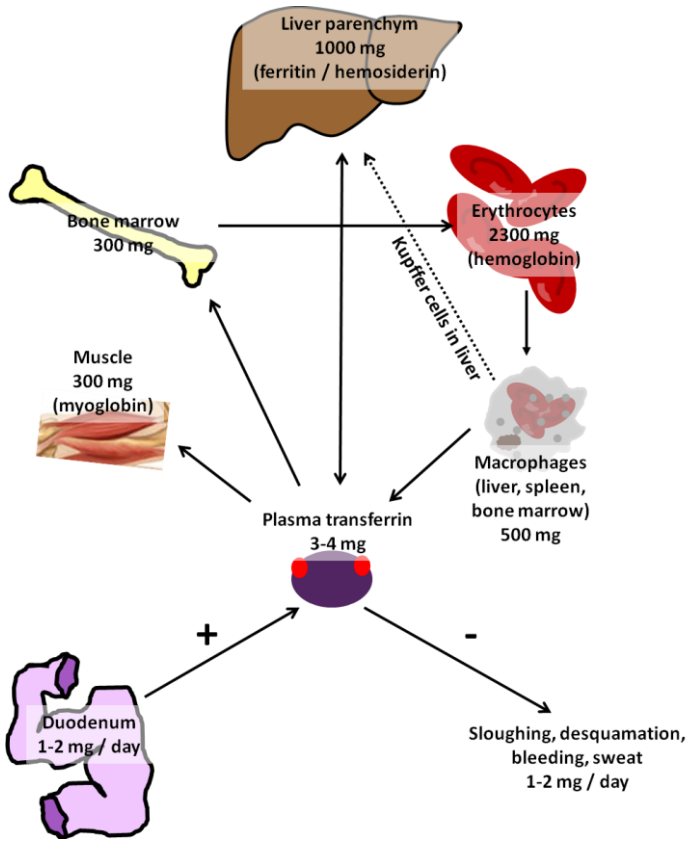

Figure 2 - Body iron distribution in adults. Arrows represent direction of iron transport. 1-2 mg of iron are absorbed in duodenal enterocytes, exported into plasma and bound to transferrin (Tf) - the systemic iron carrier. 1-2 mg are lost via sloughing of intestinal cells, bleeding, desquamation of skin and urinary epithelial cells and sweat. Ferritin and hemosiderin (1.2.8) in hepatocytes of the liver represent the main body iron store beside macrophages of the mononuclear phagocytic system (MPS). Most iron is functionally present in hemoglobin of red blood cells and myoglobin in muscle cells giving the muscle its typically red color. Only about 8 mg are present in other enzymes and proteins in body cells. Systemic iron homeostasis is strictly regulated by hepcidin (1.2.4) and on cellular level via the IRE-IRP (1.2.5) system which plays an important role in the body's elaborated mechanisms for iron uptake and assimilation.

Iron is a functional component of numerous proteins and enzymes e.g. for binding and transport of oxygen, redox reaction processes, ATP generation in the respiratory chain and DNA synthesis. However, it is rather limited in its biological availability and moreover it can be toxic in even low concentrations if it is not held in a redox inert state. Thus, it is a key challenge for the body to regulate the iron levels in circulation and total iron body levels (**1.2.4**; **1.2.5**). Low iron levels result in iron deficiency diseases. Symptoms are pallor, fatigue, learning and concentration disability, rhagades in the corner of the mouth, loss of hair, koilonychia (nail disease), smooth atrophic tongue and cognitive deficits. On the other hand, iron overload can occur in case of increased iron uptake or over the course of diseases e.g. in case of hemochromatosis. Iron overload in plasma is the consequence of exceeding the binding capacity (oversaturation) of the physiological transport protein transferrin (Tf) (**1.2.6**) and the ability of the cells to store iron as ferritin (Ftn) (**1.2.8**). Tf oversaturation can be the consequence of increased influx of iron into plasma or it can occur in case of low Tf levels (hypotransferrinemia). Thus, "free" iron is available which is toxic for the body (**1.2.7**) through the catalytic formation of dangerous free radicals. Additionally, "free" iron promotes bacterial growth [1, 2]. The low solubility of the naturally most common ferric iron (Fe^{3+}) at neutral pH values and the inability of controlled iron excretion are further challenges for the body. All these factors made it necessary for most organisms to develop a complex iron transport and management system in the course of evolution [3].

The body iron content in an average male adult is between 40 - 50 mg per kilogram body weight [4], in total between 3 - 5 g iron in the human body [5]. The dietary absorption is only 1-2 mg iron per day to compensate the similar valued iron loss with 1-2 mg per day by sloughing of intestinal epithelial cells, desquamation of skin and urinary cells, bleeding or sweat. In case of increased iron requirements during pregnancy or increased erythropoiesis, the absorption can be up-regulated [6]. The formation of erythrocytes requires about 20 mg per day [7] which is supplied by recycling of erythrocytes generating 20 - 25 mg iron per day. Plasma iron is in consequence turned over approximately every 2 h [8]. The most iron is present as heme in red blood cells (2300 mg), myoglobin of muscles (400 mg) and erythroid marrow (150 mg). Macrophages of the liver (= Kupffer cells; KC), spleen and bone marrow contain a fraction of 500 mg iron [4]. Parenchymal liver cells (hepatocytes) play a dual role in iron metabolism. They store iron in form of ferritin or hemosiderin with an amount of about 500-1000 mg (lower in case of growing children and menstruating women). On the other hand they play the key role in iron metabolism as they secrete the regulatory hormone hepcidin [3, 4, 6]. Cellular iron-containing proteins and enzymes are estimated to bind approximately 8 mg of iron [9]. Blood plasma contains 3-4 mg of iron bound to transferrin (Tf) (**Figure 2**).

1.2.2. Intestinal iron uptake from diet

Typical western diets contain 12-18 mg of iron present as heme iron (ferrous iron protoporphyrin IX) or inorganic non-heme ferrous iron (Fe^{2+}) and ferric iron (Fe^{3+}) iron, respectively. About 1 mg iron is absorbed per day in case of males and non-menstruating women and up to 6 mg per day in case of pregnant women in the last trimester [4]. Non-heme iron is delivered via inorganic iron salts and chelates supplying ferrous iron or ferric iron mostly from cereals (e.g. wheat bran, millet, oatmeal), vegetables (e.g. lentil, chanterelle, kidney bean, pea) and fruits (e.g. apricot, black currant, raspberry, strawberry) [10]. A third nutritional form of dietary iron beside heme and non-heme iron is the non-heme food ferritin (Ftn) which contains iron minerals in small absorbable iron complexes ([11], **1.2.8**).
Inorganic ferric iron is either reduced by ascorbic acid from food in the intestinal lumen or at the brush border of duodenal enterocytes by the membrane-associated ferrireductase DCYTB (Cybrd1) and other ferrireductases [12]. Consequently, the divalent metal transporter 1 (DMT-1: SLC11A2; also known as DCT-1: divalent cation transporter) absorbs the ferrous iron (**Figure 3**, [13]).

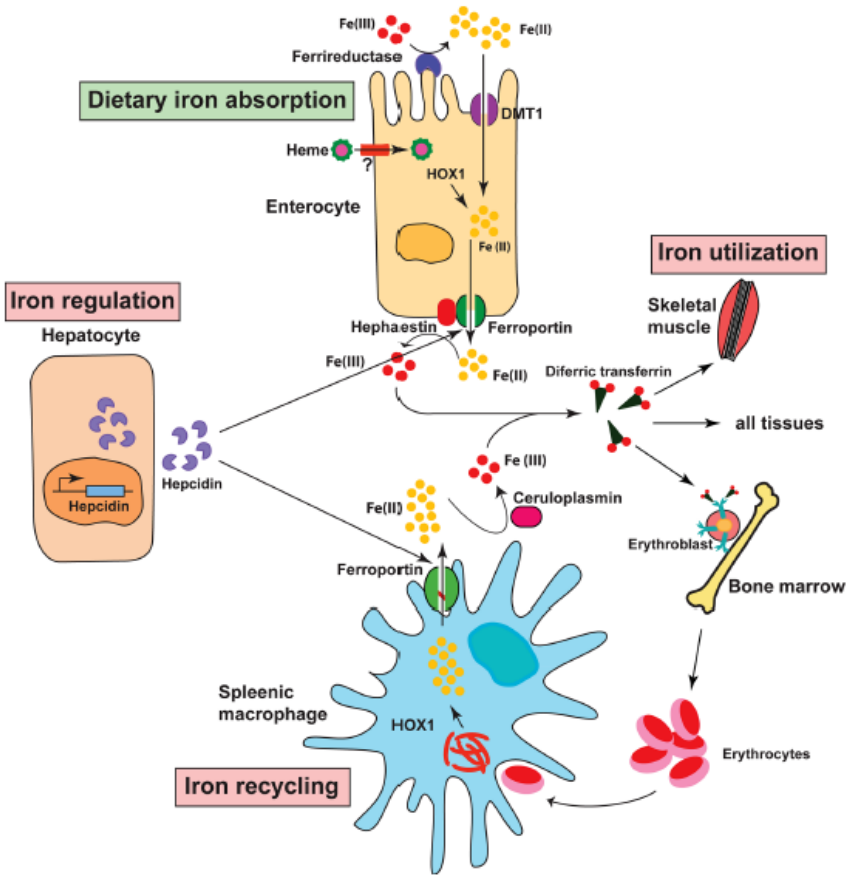

Figure 3 - Systemic iron metabolism. Reprinted from [9]. Enterocytes in duodenum absorb ferrous iron (Fe^{2+}) via the divalent metal transporter 1 (DMT-1) after reduction of ferric iron (Fe^{3+}) by membrane associated ferrireductases (e.g. DCYTB) or ascorbate in intestine lumen. Heme uptake is not completely clarified (see description in the text). After heme is taken up, the porphyrine structure is cleaved by hemoxigenase 1 (HOX1 / HO 1). Liberated and absorbed ferrous iron can be exported via Ferroportin (Fpn) into the plasma. Prior to binding to Transferrin (Tf), ferrous iron is oxidized to ferric iron by membrane associated hephaestin. Tf is the systemic iron carrier (1.2.6) supplying iron to places of storage (hepatocytes, macrophages) and regulation (hepatocyte) as well as iron utilization (bone marrow, muscles, other tissues). Ferrous iron obtained from recycling of old red blood cells (RBC) in spleenic macrophages can be exported via Fpn like in case of enterocytes. Subsequently, it is bound to Tf after oxidation to ferric iron via circulating ceruloplasmin - in contrast to membrane associated hephaestin in case of export from enterocytes. Hepatocytes secrete hepcidin, the key regulator in systemic iron uptake and cellular iron export by inhibition of Fpn export. Hepcidin transcription is directly controlled by the iron status in hepatocytes (1.2.4).

Heme iron is commonly believed to be the most important source of dietary iron in a typical western diet. Heme sources such as myoglobin and hemoglobin from meat deliver about two-thirds of the average person's iron store while just one-third of the ingested iron is present as non-heme iron. The mechanism of heme uptake is still uncertain but it is assumed to involve direct transport of heme or receptor mediated endocytosis [10]. Heme can be taken up by absorption through interaction with a specific transporter system at the apical site of the enterocyte. One transporter involved in heme uptake was identified as the heme carrier protein 1 (HCP-1, encoded by the gen SLC46A1) [14]. The affinity of heme to this protein is with a Ki of 125 µM by far not as good as the affinity to folic acid with a K_i of 0.6 µM. So, the name of the protein encoded by the gene SLC46A1 was amended to PCFT/HCP-1 (proton coupled, high-affinity folate transporter) by Qiu et al. (for review see [15]). Interestingly, PCFT/HCP-1 is part of a larger family of transporters known as the major facilitator superfamily (MFS). In this family, PCFT/HCP-1 well resembles a bacterial protein that transports the antibiotic tetracycline. Notably, there are similarities in structure between the planar heme ring and tetracycline-metal structures [16].

It is not known whether heme absorption is always coupled to folate or if there is another structure specific for the absorption of heme [11]. As already mentioned, endocytosis plays an important role [17] in the uptake of heme. Nevertheless, the mechanism, explicitly the binding structure for the activation of the endocytotic process is not yet determined. It has been suggested that PCFT/HCP-1 also plays an important role by binding of heme to the cell surface and internalization of the complex by receptor mediated endocytosis [14, 18]. After heme is taken up by an endocytotic pathway, it is present in the vesicle. From there, it has to be transported into the cytosol, where heme oxygenases (HOs) are located in the smooth and rough endoplasmatic reticulum (ER) [19]. The HOs cleave the organic porphyrine structure and liberate ferrous iron (**Figure 3**, **Figure 5**)**.** This transport may be realized through the peptide HRG-1 which is present in endosomes but not in lysosomes [20, 21]. In Caco-2 cells HO-1 mRNA and protein levels were found time- and dose-dependently induced by heme [22].

After inorganic ferrous iron is taken up via DMT-1 or liberated from heme via HOs, different pathways are possible: Export to plasma (**1.2.3**), storage in ferritin (described in sections **1.2.5** & **1.2.8**) or supply to mitochondria for the synthesis of endogenous heme (**1.2.5**).

Mitochondrially synthesized heme inside cells can be exported via the protein heme responsive gene 1 (HRG-1) located at the basolateral membrane of enterocytes and other body cells [19]. The heme exporter FLVRC1 (feline leukemia virus, subgroup c surface receptor) may also play a role in this context (**Figure 5**, [23]). Free heme in extracellular fluids is like "free", non-transferrin bound iron (NTBI) (**1.2.7**) a source of free radical formation and a major source of iron for invading pathogens [24]. Bacteria need heme as well as "free" iron for their metabolism. This makes free iron and free heme potential promoters of bacterial growth. For these reasons, the body necessitates a protection from free heme and "free" ionic iron. As transferrin (Tf), doing this in case of "free" iron, the 60 kDa serum protein hemopexin binds heme with high affinity (K_d < 1 pM) and delivers it to its targets via specific receptors [4, 25].

1.2.3. Systemic cellular iron uptake and export

After uptake or cleavage from heme, ferrous iron is present in duodenal enterocytes. It can be exported at the basolateral side of the enterocytes via the cellular iron exporter ferroportin (Fpn) [26]. Fpn can be inhibited by the iron regulator hormone hepcidin (**1.2.4**). The binding of iron to transferrin (Tf) necessitates previous oxidation of ferrous iron to ferric iron by the multicopper oxidase hephaestin. Hephaestin is present at the basolateral side of enterocytes in combination with Fpn.

In case of iron export from other cells involved in iron homeostasis like splenic macrophages, Kupffer cells and enterocytes, Fpn is also the executor. However, the necessary oxidation prior to binding to Tf is in this connection performed by circulating ceruloplasmin. Ceruloplasmin is homologue to hephaestin but not membrane associated. Tf binds ferric iron in plasma and maintains it in an redox inert state [9]. This prevents the generation of toxic radicals and iron can be delivered to all tissues (**Figure 3**).

Iron uptake into hepatocytes and erythroid precursors in bone marrow is performed via the binding of iron loaded Tf (Tf-Fe_2 / holotransferrin) to the Tf receptor 1 (TfR1). The Tf-TfR complex is subsequently internalized by endocytosis via clathrin-coated pits (**1.2.6**). The conformation of Tf is changed through the acidification of endosomes via proton pumps. The ferric iron is liberated and reduced to ferrous iron under the acidic conditions. DMT-1 or its homologue NRAMP-1 (natural resistance-associated macrophage protein 1) transport the ferrous iron from the lysosomes into the cytosol. DMT-1, introduced as uptake transporter in case of enterocytes, is also present in the membrane of hepatocytes and red blood cells. There, it facilitates the uptake of "free", non-Tf bound iron (NTBI) in case of Tf oversaturation.

In hepatocytes, the cytosolic ferrous iron is primarily stored in ferritin or hemosiderin after oxidation to ferric iron. Contrary, in erythroid cells the ferrous iron is predominantly transported into mitochondria where hemoglobin synthesis takes place [3, 4]. Red blood cell (RBC) recycling in macrophages is performed via endocytotic uptake of old RBCs. Heme is subsequently enzymatically cleaved by hemoxygenase (HO 1 and 2) and ferrous iron is liberated. Afterwards, it is transported via a DMT-1 homologue transporter (NRAMP1; [27]) into the cytosol. From there it can be hepcidin-controlled exported by Fpn and oxidized by ceruloplasmin to ferric iron, which is subsequently bound to Tf.

1.2.4. Systemic iron homeostasis - hepcidin

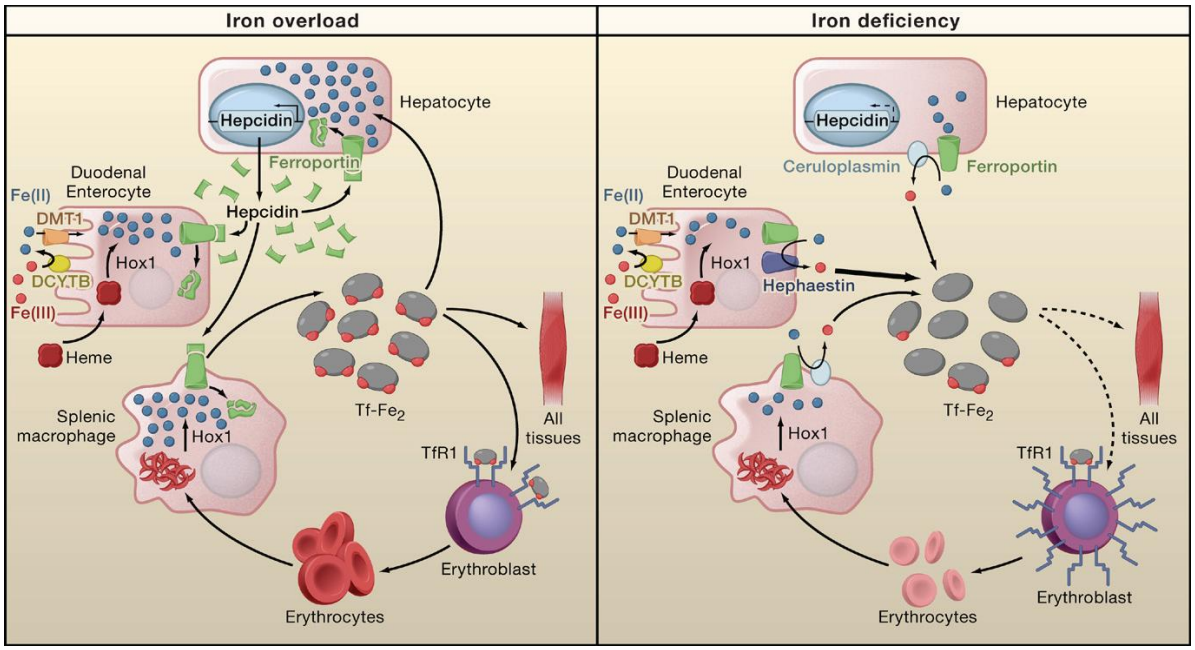

Figure 4 - Regulation of systemic iron homeostasis. Tissues and cells involved in systemic iron homeostasis are depicted. The duodenal iron absorption is described in Figure 3 and section 1.2.2. Macrophages recycle old erythroblasts or iron containing foreign materials like iron oxy hydroxide nanoparticles (FeOOH NPs), cleave heme, and export ferrous iron. Hepatocytes sense high Tf-Fe_2 levels and increase hepcidin transcription and export. Hepcidin binds to ferroportin (Fpn) and triggers its internalization, causing iron accumulation in enterocytes, macrophages, and hepatocytes themselves. Low holotransferrin (Tf-Fe_2) levels inhibit hepcidin production. Consequently, hepcidin levels are low and iron can be exported from the cells via Fpn. Reprinted and cited from [6].

As already shortly described, iron uptake from duodenum and iron recycling by macrophages of the mononuclear phagocytotic system (MPS) is controlled by the antimicrobial peptide hormone hepcidin (**hep**atic bacteri**cid**al prote**in**) (**Figure 4**). Hepcidin consists of 25 amino acids and is mainly produced in hepatocytes [6]. It is the key regulator of systemic iron homeostasis and inhibits iron export from enterocytes, macrophages and hepatocytes itself. Hepcidin exhibits this function by binding to ferroportin (Fpn), promoting its internalization and subsequent lysosomal degradation [28]. Iron consequently accumulates in enterocytes, macrophages and hepatocytes [6, 29]. Additionally, hepcidin inhibits the uptake in enterocytes by degradation of DMT-1 [30-32]. The hepcidin biosynthesis is controlled by three known mechanisms:

(I) high Tf-Fe_2 levels (in consequence of a high serum iron concentration) trigger hepcidin transcription by binding to Tf-receptor (TfR)-1 leading to a shift from HFE to TfR-2, followed by the internalization of the HFE-TfR-2 protein complex and activation of hepcidin m-RNA synthesis

(II) erythropoetic signals (hormones [GDF 15 and TWSG 1] released by erythroid precursors) inhibit hepcidin transcription

(III) inflammatory stimuli (Interleukin-6) trigger hepcidin transcription

Control mechanism (I) blocks the uptake of excess iron from duodenum and export from macrophages, enterocytes and hepatocytes to plasma. This circumvents oversaturation of Tf with possible toxic effects by NTBI. Mutations in TfR-2 contribute to iron overload in case of hereditary hemochromatosis (iron overload with low hepcidin levels). Mechanism (II) promotes iron delivery to erythroid precursors triggering hemoglobin synthesis in case of hypoxia. Dysfunction in mechanism II is a factor in "iron loading anemia" (too much iron in erythrocytes). The triggering of hepcidin transcription via inflammatory stimuli (III) represents a defense mechanism against (iron dependent) pathogens. High hepcidin levels with consequent iron deficiency occur in case of infections, malignancies, chronic kidney diseases or any type of inflammation and may lead to anemia of chronic diseases (ACD). (For details see [6])

1.2.5. Cellular iron homeostasis

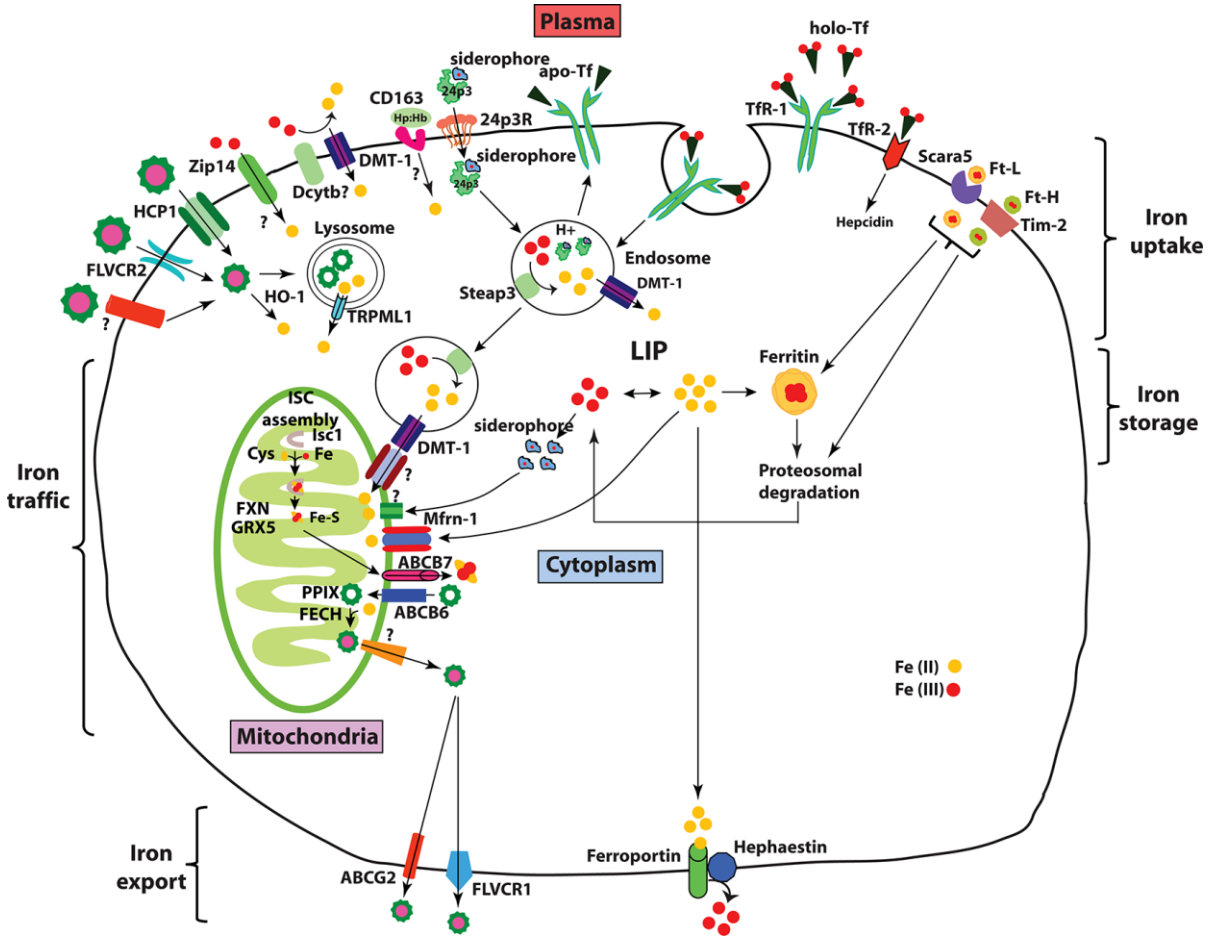

Figure 5 - Complex cellular iron metabolism. Body cells obtain iron by uptake of holo-Tf (top: black triangle with 2 red dot) via TfR1, followed by endocytosis via clathrin coated pits. Endosomes get acidified via proton pumps and the TfR-Tf-Fe_2 complex is consequently dissociated into the apo-Tf-TfR complex and ferric iron. The apo-Tf-TfR1 complex is recycled, transported back to the cell membrane and dissociated liberating apo-Tf (black triangle) back to circulation. The endosomal ferric iron (red dot) is reduced by the metalloreductase Steap3 and exported via DMT-1 into cytosol. Ferrous iron (yellow dot) contributes to the LIP (labile iron pool).
Additionally, NTBI, present as extracellular ferrous and ferric iron, can be imported via DMT-1 after oxidation of ferrous iron to ferric iron by membrane associated ferrireductases. (e.g. DCYTB; see 1.2.2 & 1.2.3) Other iron sources are heme (top left: green "sun" with pink dot), serum Ftn (top right "Ft-L") and siderophore-like molecules. Siderophores are low molecular weight proteins that are high efficiency iron chelators in prokaryotic cells. Current studies indicate the existence of siderophore-like molecules in mammalians possibly contributing to mitochondrial iron uptake. (see review [9])
The transcription of the systemic iron homeostasis hormone hepcidin (Figure 4) is triggered via Tf-Fe_2 binding to TfR1 and TfR2 (details in section 1.2.4 or literature [6]).
LIP ferrous iron is mainly transported to mitochondria for the synthesis of co-factors for enzymes and proteins (heme, Fe-S-clusters; synthesis described in literature, see [9] for details) but also supplies iron for storage in ferritin or export via Fpn. Heme produced by mitochondria is exported from cells or used for enzyme / protein formation. Ferritin can also be exported from the cell. Reprinted from [9].

Beside hepcidin at systemic level, the IRE/IRP system (**I**ron **R**esponsive **E**lement / **I**ron **R**esponsive **P**rotein) is a regulatory system to control cellular iron homeostasis. IRP1 and IRP2 are ubiquitously present in the cytosol. These proteins bind to the IRE at an untranslated region of mRNA which encodes various proteins participating in iron uptake (DMT-1, TfR), recycling, storage (apo-Ftn) and export (Fpn) [33-36]. DMT-1 plays a dual role as it participates in cellular as well as in systemic iron homeostasis. When cytosolic iron concentrations

are low IRP1 & 2 are able to bind to the IRE of mRNAs and the translation of peptides involved in iron homeostasis as DMT-1, TfR, Apoferritin, Fpn. In case of high iron concentrations, they are not able to bind to this IRE. Beside iron concentrations, the IRPs binding activities are also controlled by tissue oxygen levels, oxidative stress and nitrogen oxide levels. Iron dependent regulation is different between IRP 1 and 2. While IRP 1 conformation changes to a cluster containing the holo-form at high iron levels, IRP 2 is iron dependently (at high concentrations) degraded by proteasomes [32]. In case of low cellular iron content and increased translation of iron homeostasis peptides, cellular iron uptake is directly increased. This is achieved via DMT-1 up-regulation especially in enterocytes. In case of hepatocytes and erythroid precursors the TfR expression is up-regulated. Hence, endocytosis of Tf-Fe_2 increases with elevated endosomal ferric iron release. The ferric iron is reduced to ferrous iron by the metalloreductase Steap3 and exported from endosomes to cytosol via DMT-1 (**Figure 5**). The cytosolic iron is available for storage in Ftn, for the supply to mitochondria in order to synthesize heme as well as Fe-S clusters, and for the export via Fpn to plasma. Inside cells, iron distributes in three compartments [37]:

(I) "transit" compartment - LIP (intracellular **L**abile **I**ron **P**ool)
(II) functional compartment (esp. mitochondria for manufacturing of co-factors for proteins like heme, Fe-S clusters [38])
(III) storage compartment

1.2.6. Iron carriers

Transferrins (Tfs) are glycoproteins with a molecular weight of about 80 kDa, consisting of a single polypeptide chain of 680 amino-acid residues. The first member of the family, which was found in egg white and exhibited antimicrobial activity, was ovotransferrin. Plasma transferrin was found several years later. In human milk, the iron binding protein lactoferrin was identified to have the same antibacterial characteristics as ovotransferrin. The antimicrobial activity is performed by depriving bacteria of iron, contributing to immune defense of mammalians. Members of the Tf family have been found in many body fluids, including serum, breast milk, tears and saliva and are secreted by leukocytes (lactoferrin). The latest member of the family identified in case of mammalians was melanotransferrin. It was named this way as it is present anchored to the surface of melanocytes. In case of melanoma, this type of transferrin supplies the melanoma cells with iron via a receptor-independent but saturable pathway [39].

Tf is mainly secreted by liver, but varying amounts are also produced by lymph nodes, thymus, spleen, salivary glands, bone marrow and testis. Iron free Tf (apo-Tf) reversibly binds two molecules of ferric iron with high affinity ($K_d = 10^{-23}$ M) and is then named holofransferrin (Tf-Fe_2). Release as well as binding of iron is accompanied by a conformational change. The interaction between ferric iron and Tf is pH dependent. At pH values below 5, the strong interaction is abrogated (e.g. in endosomes). Hence endosomal liberation is possible (**Figure 5**).

At physiological conditions 3-4 mg iron is bound to the Tf plasma fraction giving a Tf saturation level of approximately 30 %. The total iron binding capacity (TIBC) is valued with 45-80 µM/L, about 12 mg in case of an average adult male [40]. As described in section **1.2.1** the formation of erythrocytes requires about 20 mg iron per day, turning over iron bound to Tf about 10 times a day. The high amount of unsaturated apo-Tf allows efficient buffering of increased plasma iron levels. In case of oversaturation with iron (> 75 % Tf saturation) non-Tf bound iron (NTBI) is present promoting iron toxicity [9]. Iron has to be present as ferric iron in order to bind to Tf as described in section **1.2.3.** Beside the multicopper complexes hephaestin (membrane associated at basolateral side of enterocytes) and ceruloplasmin (circulating in plasma), apo-Tf itself was found *in-vitro* to have oxidizing effects. Tf-Fe_2 uptake into cells via TfR is described under **1.2.3**. After endosomal dissociation of the TfR-Tf-Fe_2 complex, the TfR-apo-Tf complex returns to the cell surface were it is split in apo-Tf and membrane associated TfR [4, 9, 41].

1.2.7. Non-transferrin bound iron (NTBI) and iron toxicity

NTBI describes all forms of iron in plasma that are bound to ligands different from transferrin (Tf) [40, 42]. Tf has an total iron binding capacity (TIBC) of 45-80 µM/L at normal Tf saturation levels of approximately 30 %, providing a buffer capacity for entering iron.

In cases of iron overload, TIBC is saturated with the consequence of iron species binding to other ligands than Tf, like albumin, citrate [43, 44], or lipocalin24p3 [9] and do not correspond to heme or ferritin iron. The NTBI can be divided into two fractions: (I) a fraction that can be directly chelated by desferioxamine (DCI; **D**irectly **C**helatable **I**ron) and (II) a fraction that needs to be mobilized by e.g. nitrilotriacetic acid (NTA) or oxalate (MDCI; **M**obilizer **D**ependent **C**helatable **I**ron) [45].

In contrast to iron bound to Tf, NTBI conserves its ability to generate free radicals. Under physiological conditions no NTBI is detectable. However, it appears in iron overload syndromes, atransferrinemia or in case of parenteral iron administration [9, 46] even when the Tf saturation is less than 83% [47, 48]. NTBI is taken up by highly vascularized tissues like liver, heart, the endocrine system and endothelial cells by DMT-1 [49, 50]. Inside cells of these tissues it increases the LIP and thus may induce oxidative damage by reactive oxygen species (ROS) [51].

The primary ROS, superoxide radical ($O_2^{\bullet -}$), is commonly derived in vivo by metabolic processes or by irradiation. Under normal conditions, it is depleted by superoxide dismutase in conjunction with H_2O_2 removing catalases. The intracellular LIP consists of ferrous iron, which is known to participate in the Fenton reaction generating highly reactive hydroxyl radicals ($^{\bullet}\mathbf{OH}$):

$$\boldsymbol{Fe^{2+} + H_2O_2 \rightarrow Fe^{3+} + {}^{\bullet}OH + OH^-} \qquad \textbf{Formula 1}$$

The possibly present superoxide radical reduces the ferric iron again:

$$\boldsymbol{Fe^{3+} + O_2^{\bullet -} \rightarrow Fe^{2+} + O_2} \qquad \textbf{Formula 2}$$

The combination og both reactions yields the Haber-Weiss reaction

$$\boldsymbol{O_2^{\bullet -} + H_2O_2 \rightarrow O_2 + {}^{\bullet}OH + OH^-} \qquad \textbf{Formula 3}$$

Catalytic (low) amounts of iron are thus sufficient to produce high amounts of highly reactive hydroxyl radical, which can oxidize DNA, proteins, carbohydrates and lipids [52]. In normal cellular metabolism, those radicals are rapidly detoxified (by α-tocopherol, glutathione, superoxide dismutase, catalase, glutathione peroxidase, glutathione reductase). In case of higher radical levels e.g. by iron overload and Fenton chemistry or in case of low cytoprotective enzyme activity during cancer, these radicals can initiate cellular toxicity [4]. Additionally ROS can also release iron from stable forms like Ftn and heme worsening the conditions [46, 53-56].

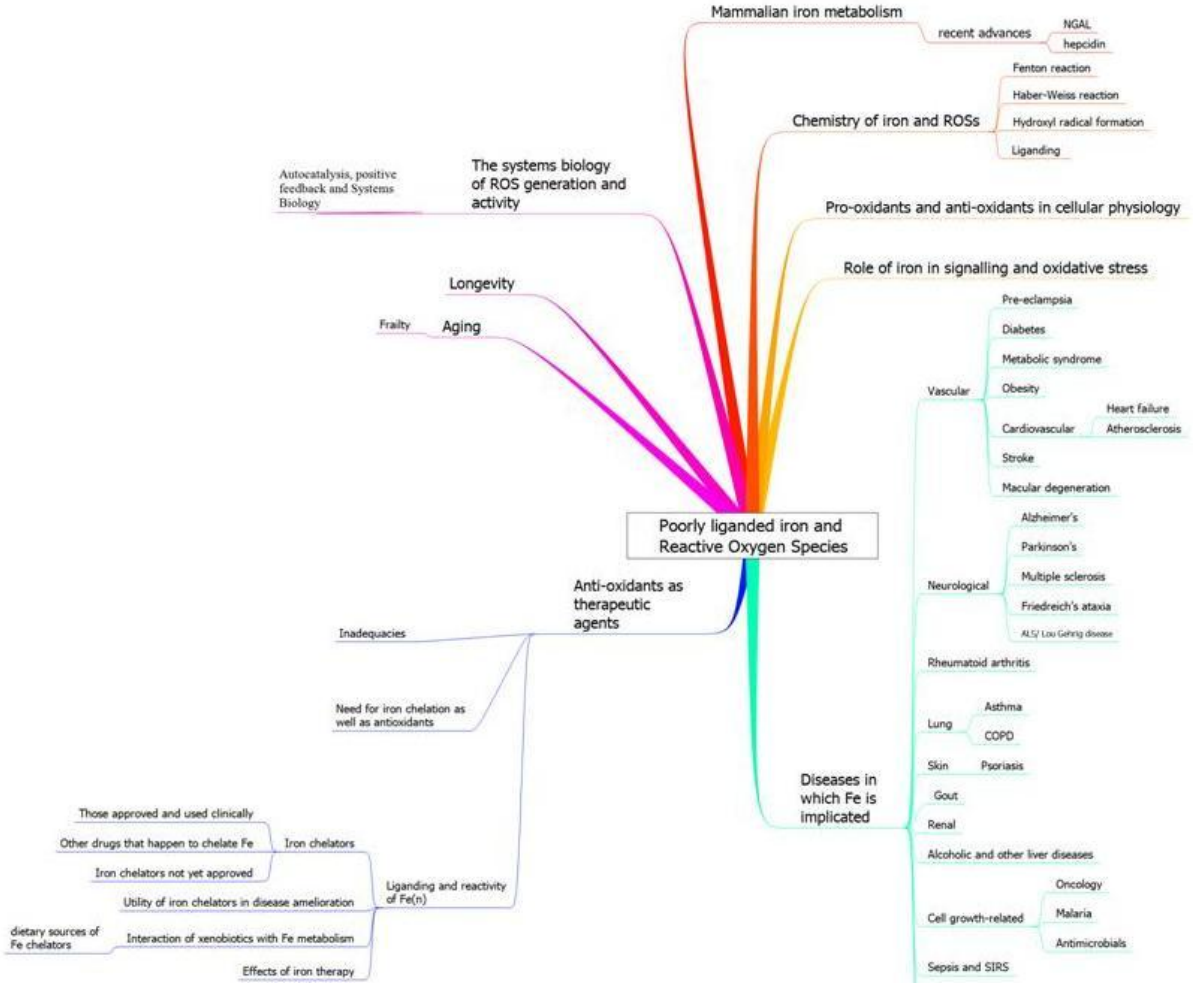

Figure 6 - Mind map by Kell et al. [56] summarizing chemistry, physiological effects, disease implications and therapy of poorly liganded Fe and ROSs.

Clinically relevant markers of oxidative stress are e.g.

(I) 8-oxo-7,8-dihydro-2'-desoxy guanosine (8-oxo-dG) & 8-oxo-dihydro guanine (8-oxo-Gua) as markers of DNA damage

(II) malonyldialdehyde (MDA), lipid hydroperoxides, and isoprostanes as markers of lipid-peroxidation

(III) advanced oxidation protein products (AOPP), advanced glycation end-products (AGE), and protein carbonyl content (PCC) as products of protein oxidation.

Diseases associated with oxidative stress are cardiovascular diseases (e.g. arteriosclerosis, ischemia), diabetes mellitus, renal diseases, cancer, neuronal diseases (inflammatory myopathy), neurodegenerative diseases (Alzheimer's, parkinsonism, amyotrophy), liver diseases (alcoholic cirrhosis, acute or chronic hepatic failure), metabolic syndrome, hypertension, obesity, rheumatoid arthritis, age related macular degeneration (AMD), psoriasis, gout, asthma, COPD, inflammatory bowel disease, and infections [32, 51, 56, 57](**Figure 6**).

1.2.8. The iron storage proteins ferritin (Ftn) and hemosiderin

As shortly broached, iron can be stored in form of ferritin or hemosiderin. Mammalian ferritin is a protein complex with a molecular weight of about 500 kDa with 24 similar or identical subunits. It builds up a hollow sphere with an external (internal) diameter of 12-13 nm (7-8 nm). Hence, it gives room to up to 4500 iron atoms in a water soluble, non-toxic, bioavailable form, present as a ferrihydrite (amorphous ferric iron oxy hydroxide) nucleus. Ferrous iron is taken up via hydrophilic threefold channels into the protein shell, where the H-chain Ftn accelerates oxidation to ferric iron by O_2 under production of H_2O_2. Ferric iron then migrates from the ferroxidase site to the side of nucleation where it is hydrolyzed to ferrihydrite [58].

Hemosiderin is found in conditions of iron overload and contains degradation products of apo-Ftn. Contrary to Ftn the water-insoluble hemosiderin is normally present only in low concentrations. Anti-Ftn immunoglobulin response of hemosiderin indicates that it is a lysosomal degradation product of Ftn [59] with increased iron to protein ratio. However, lysosome incubation with Ftn didn't yield hemosiderin *in-vitro* [60]. The iron in hemosiderin is present as amorphous ferrihydrite, similar to that in Ftn, but it is also found to be present as goethite (α-FeOOH) in case of patients suffering from hemochromatosis and thalassemia.

Iron can be readily mobilized from storage iron forms, whether Ftn or hemosiderin, via proteasomal degradation. Beside released iron from Ftn, small amounts of Ftn itself are transported into the plasma, dependent on the intracellular concentration. This serum Ftn represents an indirect reflector of the body's iron stores. Serum Ftn is thus a useful indicator for the iron status of patients (upper limit 800 µg/L) [37]. Intravenously applied Ftn is readily taken up into hepatocytes by endocytic pathways and it is subsequently degraded in lysosomes. Lysosomal degradation reutilizes the iron for hepatocyte Ftn synthesis [4, 9].

1.3. Iron deficiency

Iron deficiency is the most common deficiency disease worldwide with two billion people suffering from it, mainly in less developed countries [61]. It occurs when the absorbed amount of iron is not covering the demand of the body. This can either be caused by decreased uptake (poor availability of iron in diet or disorder in iron uptake) or by increased demand. In developed countries iron deficiency (ID) is mainly caused by blood loss. The consequence can be anemia with decreased oxygen capacity of the red blood cells [62]. Menstrual blood loss is the most common reason for iron deficiency anemia (IDA) in premenopausal women whereas blood loss in the GI tract causes most IDA in adult men and postmenopausal women. Reasons for IDA may be colonic or gastric cancer, use of non-steroidal anti-inflammatory drugs (NSAIDs), malabsorption, poor dietary intake, blood donation, gastrectomy, oesophagitis, coeliac disease, helicobacter pylori colonisation, hematuris and it is a secondary side effect of cancer and chemotherapy. The WHO defines IDA with hemoglobin (Hb) values below 13 g/dL in case of man respectively below 12 g/ dL in non-pregnant women and both over 15 years of age. IDA in pregnant women is present if Hb values are below 11 g/dL [63].

1.3.1. Symptoms and diagnostics

Typical symptoms of iron deficiency are pallor, fatigue, learning and concentration disability, rhagades in the corner of the mouth, loss of hair, koilonychia (nail disease), smooth atrophic tongue and cognitive deficits [64]. Diagnostics involve measurements of changes in red blood cells, like reduced mean Hb content (MCH) - hypochromia - and reduced mean cell volume (MCV) - microcytosis. Hypochromia and microcytosis are sensitive indicators for iron deficiency in the absence of chronic diseases or coexisting vitamin B_{12} or folate deficiency. The serum markers of ID are low ferritin, low Tf saturation, low iron, raised TIBC, raised zinc protoporphyrin and increased serum Tf-receptor levels (sTfR). Serum Ftn is the most powerful test in absence of inflammation. Levels lower than 12 - 15 µg / L indicate ID in case of absent inflammation whereas even levels of 50 µg / L refer to ID in case of inflammation. The sTfR concentration is a good marker of ID in healthy subjects and is good useable in combination with serum Ftn if inflammation is present [63].

1.3.2. Functional iron deficiency

Functional iron deficiency is present when the body iron storage is normal (normal or increased serum ferritin) but is not sufficiently supplied to the bone marrow. This occurs in patients with renal failure being treated with erythropoietin (EPO) [65, 66] and in case of anemia of chronic diseases (ACD). Such diseases are chronic inflammatory diseases like rheumatoid arthritis and inflammatory bowel disease, chronic infections, malignancies, and chronic kidney diseases (CKD). Serum Ftn and Tf levels are decreased [63] and hepcidin levels are increased by transcription induction via inflammatory cytokines, especially IL-6 (**1.2.4**). High hepcidin levels inhibit iron export from enterocytes, macrophages and hepatocytes and

are a defense mechanism of the body against bacterial infection [6]. In case of increased hepcidin levels, oral iron supplementation is not efficient, as iron uptake from intestine is additionally blocked by high hepcidin levels (**1.2.4**). Consequently parenteral iron supplementation is required in patients with ACD, especially when they are treated with EPO.

1.3.3. Treatment of iron deficiency

Oral iron

Ferrous iron (Fe^{2+}) salts are a very easy and also cheap way [67] for the treatment of iron deficiency (ID) in most patients. To increase the bioavailability it is usually orally administered to patients (in fasted state) as a gastro-resistant formulation to avoid oxidation in the acid gastric milieu. If the administration in the fasted state is not well tolerated because of gastro intestinal (GI) side effects, the iron can be also administered in the fed state. Additionally it is to advantageous to take oral iron in combination with ascorbic acid (e.g. with a glass of orange juice). This prevents the ferrous iron from oxidation to the ferric form which is not taken up by DMT-1 transporters at the brush border of the enterocytes. The kind of administered ferrous iron salt (sulfate, fumarate, gluconate, ascorbate, and succinate) has no considerable influence on the bioavailability [68]. Iron from ferrous iron sulfate is fast and in high amount absorbable resulting in increased NTBI (up to 6 µM / L) levels for 5 h at a dose of 100 mg [69-72]. Ferric iron-hydroxide polymaltose complex is a soluble nanoparticular ferric iron preparation and its efficacy is comparable to ferrous salts [32, 73-75].

Oral iron is not suitable for ID treatment when patients suffer from inflammatory diseases or other diseases that evoke increased hepcidin levels with consequent iron malabsorption (**1.2.4**). Oral iron is also not suitable if patients suffer from significant GI side effects or in cases where large doses of iron are required. This is relevant in case of EPO treatment [66, 76] as the physiological iron stores are relatively fast run out. Parenteral iron supplementation can save up to 75 % of EPO in this context [77, 78].

Parenteral iron

Parenteral iron therapy is indicated in patients suffering from ID and having iron related gastro intestinal (GI) side effects or if they do not respond to oral therapy in case of anemia of chronic diseases (ACD). Nanoparticular iron complex drugs for parenteral administration, beside erythropoietin stimulating agents, have an outstanding status in the treatment of iron deficiency anemia in patients, who are suffering from chronic kidney diseases (CKD) and require frequent hemodialysis treatment [79]. Sources of iron loss during hemodialysis (HD) treatment are usual blood drawings for laboratory tests, surgical procedures for vascular access and the HD itself [46, 80]. The average loss in iron in case of HD patients is counted with 1-2 g iron per year. Hörl et al. [81] numbered the average iron requirements due to blood loss with 1-3 g of elemental iron per year in case of HD patients. As in many patients the iron absorption is additionally reduced by inflammation (See **1.3.2**) or medication (e.g. gastric acid inhibitors, phosphate binders) [82, 83] the oral supplementation of iron is not yielding sufficient amounts of absorbed and bioavailable iron. Clinical study outcomes

showed higher increases in hemoglobin after parenteral iron administration in comparison to oral iron therapy as evidence for the superiority of parenteral administration [84-87].
Intravenous iron therapy is for that reasons from essential meaning in the treatment of iron deficiency. Beside this field of indication the use of parenteral iron as diagnostic, imaging agent or therapeutic has spread in other indication fields like gastroenterology [88], cardiology [89, 90], oncology [91], pre/post operatively [92], obstetrics', and gynecology [93, 94]. In some of those segments, care providers do not have frequent patient contact. This results in an increased demand for high dose administration of iron in a single clinical session [95].

1.4. Intravenous iron complexes: Structure, metabolism, toxicity and regulatory impacts

1.4.1. Nanoparticular drug carrier systems

Nanoparticles are particulate drug carrier systems beside liposomes and solid lipid nanoparticles (SLN).
Usually nanoparticles are described by the composition and morphology beside their size. Some particles can be spatially uniform with respect to the chemical composition of the polymers. Beside these homogenous particles, there are multi-component particles, which are inhomogeneous and consist of two or more components. Multi-component particles can be divided in core shell particles, inverted core shell particles, multilayered particles, occluded particles and partially engulfed particles (**Figure 7**; [96]).

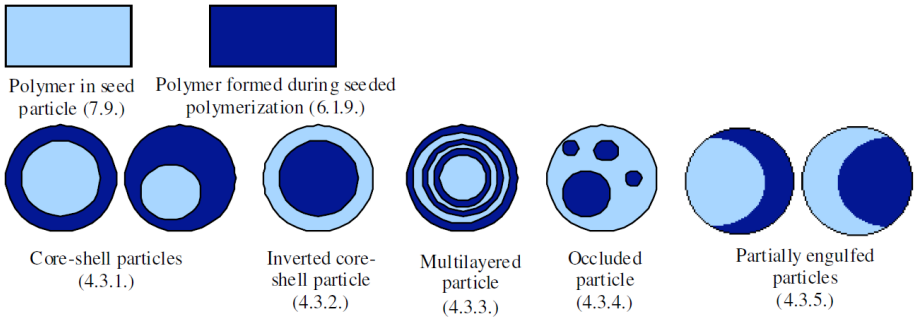

Figure 7 - Examples of multi-component particle morphology. From [96].

1.4.2. Iron containing non-biological complex drugs (Fe-NbCD)

Iron complexes are usually seen as core shell particles [97-99]. Typically, the synthesis of those particles is performed by precipitation of ferric (Fe^{3+})-(to synthesize Fe_2O_3 or FeOOH phase) and ferrous (Fe^{2+})-(Fe_3O_4-magnetite particles) iron in a molar relationship 2:1 (ferric iron: ferrous iron) present in form of salts (e.g. chloride, sulfate, nitrate). Rising of pH (adding of HCO_3^- or OH^-) leads to precipitation of $Fe(OH)_3$ / $Fe(OH)_2$ in presence of a carbohydrate (e.g. dextran, sucrose, gluconate, polymaltose, isomaltoside or hydroxyethyl starch). Alternatively, the carbohydrate solutions are added after precipitation, under influence of increased temperature and pH values between 9 and 14 (

Figure 8). The applied conditions (temperature, pH, the type of salts used, Fe^{2+} and Fe^{3+} ratio, pH and ionic strength of the medium) directly influence the properties of the resulting complex (magnetic properties, size, charge, shape, morphology)[100-102].

As the synthesis was not in the scope of this work and a diversity of synthesis variations is possible, closer information can be derived from literature and patents [103-106]. In the simplest case, the synthesis can be performed by the following reaction scheme:

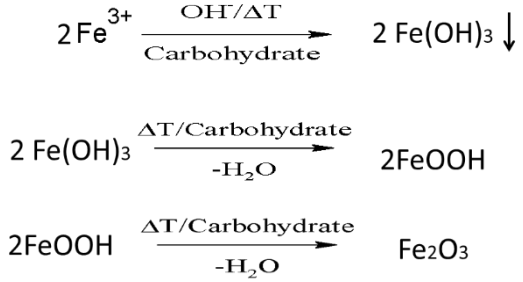

Figure 8 - Simpel reaction schema for *i.v.* iron oxide synthesis. (1) Ferric iron salt is dissolved in water and mixed with a carbohydrate before or after precipitation by pH-rising (2) Mixture of ferric iron and carbohydrate is heated and transferred to iron oxy hydroxide or (3) iron oxide by dehydration dependent on time and temperature being applied

The outcome is a complex of iron oxide or iron oxy hydroxide with the applied carbohydrate.

1.4.3. Structure of iron nanoparticles in *i.v.* iron supplement compounds

Parenteral iron drugs are categorized as iron containing non-biological complex drugs (Fe-NbCD). Synonyms used within this work and the literature are:

- Fe-NbCD
- intravenous (*i.v.*) iron preparation / agent / drug
- *i.v.* iron complex drug
- iron complexes
- nanoparticular iron formulations
- polynuclear iron formulations

Especially the term "iron complex" is not related to a classical chemical complex compound with a central particle and a ligand. The structure of parenteral iron supplement drugs in literature is related to polynuclear [32, 95, 107, 108] and describes nanoparticular drugs consisting of a carbohydrate fraction keeping the purely insoluble iron oxy hydroxide fraction in a soluble colloidal-disperse nano-suspension (***Table 1***).
The inorganic iron phase can be present in different modifications of the biphasic system between iron and oxygen, or the corresponding hydrolyzate. Different thermodynamic properties with influence on e.g. solubility are the result.
Iron oxide / oxy hydroxide modifications can theoretically be:

(I)	Goethite α-FeOOH
(II)	Akaganéite ß-FeOOH
(III)	Lepidocrocite γ-FeOOH
(IV)	Ferrihydrite 5 Fe_2O_3·x 9 H_2O (amorphous iron hydroxide)
(V)	Hematite α-Fe_2O_3
(VI)	ß-Fe_2O_3
(VII)	Maghemite γ-Fe_2O_3
(VIII)	Magnetite Fe_3O_4 ($Fe^{2+}Fe^{3+}{}_2O_4$ - spinel-like structure)
(IX)	Amorphous iron oxide

Iron nanoparticles, containing magnetite and maghemit are predominantly applied in the area of magnetic resonance imaging (MRI) of the reticuloendothelial system (RES; e.g. liver, spleen) where it is possible to visualize malignant tumors by their use. An example of such a superparamagnetic iron oxide nanoparticular formulation is ferucarbotran (Resovist®, Bayer Schering Pharma AG, , Berlin, Germany) which contains carbodextran coated nanoparticles with a hydrodynamic diameter of app. 63 nm. The inorganic phase consists of single nanocrystals of magnetite / maghemit with a size of 4.2 nm [109]. Formulations like this are not in the scope of this work as only preparations for the treatment of iron deficiency anemia were investigated. Therefor, they have not been further investigated and are thus only mentioned at this part of this work.

Table 1 - Overview on some commercial intravenous iron supplement formulations and characteristics from literature [110, 111]

IV iron complex	Lable	Brand name	Manufacturer / seller	Dosage [mg/ml]	Vial volume [5 ml]	Carbohydrate	Molecular wheigt [kDa]	Plasma half life [h]	Direct iron donation to Tf [%]	Maximum single dose [mg]
Sodium ferric gluconate	FeG	Ferrlecit®	Sanofi-Aventis; Frankfurt am Main; Germany	12.5 mg	5	Gluconic acid (monosaccharide) & Sucrose (disaccharide)	289 - 440	1	5-6	125
Iron sucrose	FeS	Venofer®	Vifor, Munich, Germany	20	5	Sucrose Disaccharide: α-D-Glucose & β-D-Fructose units; α,β 1,2-glycosidic	140-252	6	4-5	200
LMWID	LFeD	CosmoFer® / InFed®	Teva, Radebeul, Germany / Watson, Morristown, NJ, USA (MFR: Pharmacosmos, Holbaek, Denmark)	50	2 and 10	Dextran Polysaccharide: α-D-glucose units; α-1,6-& -1,3-glycosidic (1 branching/ 32 glucose units)	165	20	1-2	20 mg/kg
HMWID	HFeD	Dexferrum®	American Regent, Shirley, NY, USA	50	2	Dextran branched Polysaccharide: α-D-glucose units; α-1,6-& -1,3-glycosidic	265	60	1-2	20 mg/kg
Generic iron dextran	HFeD_G	Ironate®	HELP SA, Metamorfosi, Attika, Greece	50	2	Dextran branched Polysaccharide: α-D-glucose units; α-1,6-& -1,3-glycosidic	-	-	-	20 mg/kg
Iron isomaltosid 1000	FeIM	Monofer®	Pharmacosmos, Holbaek, Denmark	100	1, 5 and 10	Isomaltosid 1000 linear oligosaccharide: α-D-glucose units (3-5 units); α-1,6-glycosidic	150	20	<1	20 mg/kg
Ferumoxytol	FePSC	FeraHeme® / Rinso®	AMAG Pharmaceuticals, Cambridge, MA, USA	30	17	Polyglucose sorbitol carboxymethylether	750	15	<1	510
Ferric carboxymaltose	FeCM	Ferinject® / Injectafer®	Vifor, München, Germany	50	2 and 10	Carboxymaltose α-D-glucose units & α-D-gluconic acid; α-1,4 glycosidic	150	16	1-2	20 mg/kg max 1000
Iron hydroxyethyle starch	FeHES	Feramyl®	Serumwerk Bernburg AG, Bernburg, Germany	50	-	Hydroxyethyle starch branched polysaccharide: α-D-glucose units; α-1,6-& -1,4 glycosidic	-	-	-	-

1.4.4. Biological utilization of *i.v.* iron complexes

Stability of different iron complexes in circulation

Intravenously applied iron containing nanoparticles (NPs) are suggested to behave differently under physiological conditions (**Figure 9**, [32]). Complexes with low thermodynamic stability contain iron which is more associated than tightly bound to the carbohydrate fraction (e.g. FeSuc and FeG). Those complexes are predominantly dissociated in blood [112].

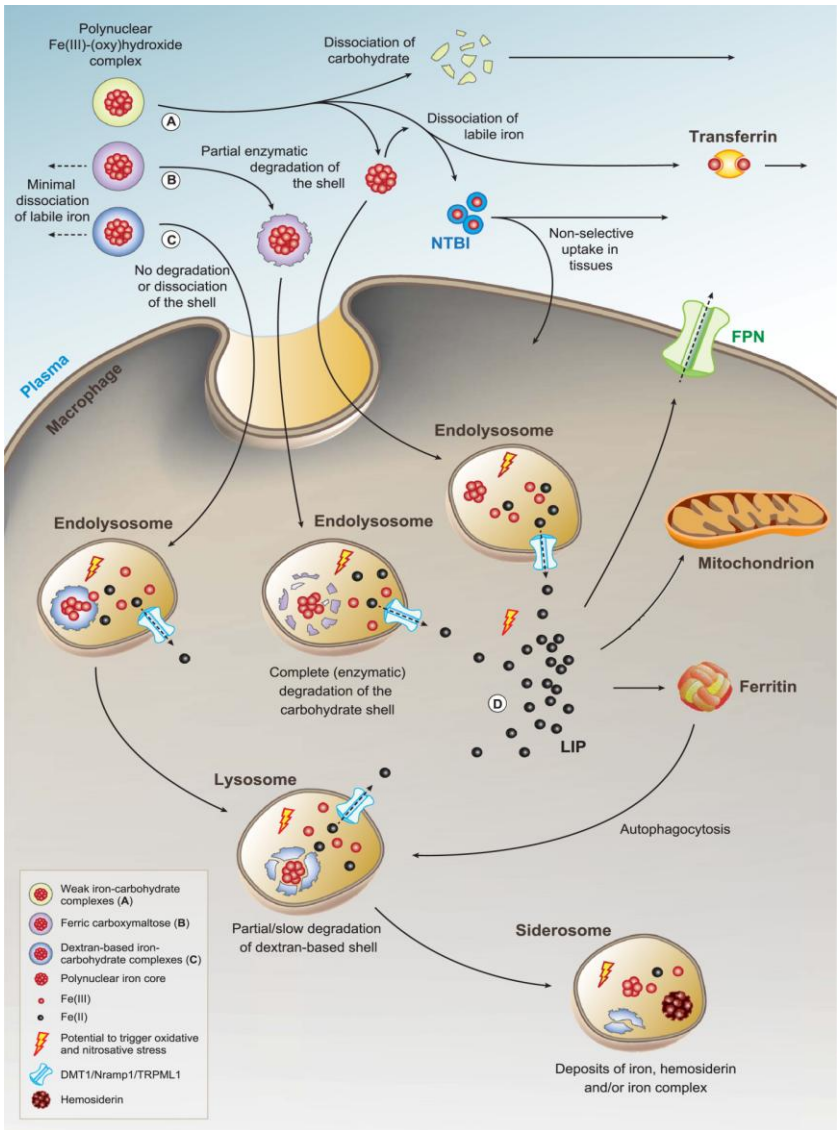

Figure 9 - The metabolism of intravenous iron complexes depends on their stability:
(A) Low stability complexes (e.g. FeSuc and FeG) may partially or totally dissociate in the plasma liberating loosely bound or free iron from the formulation that can directly bind to Tf. The carbohydrate fraction can be renally excreted. If the dose of the *i.v.* iron formulation is too high or the Tf concentration is decreased, NTBI can be present in plasma. The inorganic iron core can consequently be taken up by macrophages of the MPS (spleen, liver, bone marrow) via phagocytosis. Subsequently, the endosome fuses with lysosomes yielding endolysosomes. The particle enclosed iron core is degraded at reductive (Steap3 [113],and acidic (proton pump) conditions or in the presence of complexing agents (e.g. lactoferrin) [114, 115].
(B) Complexes with α-1,4 glycosidic connected carbohydrates as FeCM, FeIM and possibly FeHES (α-1,4 & 1,6 glycosidic) can be partially degraded by α-amylases in the blood. Subsequently, they can be taken up via phagocytosis.
(C) Dextran coated carbohydrates are taken up by endocytosis and - like particles with lower stable carbohydrate shell - degraded in endolysosomes by enzymes and complexing agent under acid and reductive conditions. Ferrous iron is then exported into cytoplasm via e.g. DMT-1 contributing to the intracellular labile iron pool (LIP, (D)). In case of highly stable complexes the lysosomal degradation step can be prolonged - proportional to the surface to volume ratio (smaller with rising size) [116] - leading to a slower increase of intracellular LIP. In case of very highly stable or non-bioavailable complexes, the particles may accumulate in lysosomes forming iron-laden siderosomes. The intracellular LIP, with ferrous iron present catalytically active, is a main trigger for oxidative stress via Fenton chemistry (1.2.7). Reprinted from [32].

The carbohydrate fraction is present unbound in blood and can be renally excreted. High amounts of loosely bound iron are liberated and can be bound or directly transferred from the circulating complex to transferrin (Tf). In case of high dose administration or physiological preexisting Tf deficiency, the relatively low total iron binging capacity (TIBC) of app. 12 mg (1.2.6) is possibly saturated, leading to the presence of non-transferrin bound iron (NTBI) which is non-selectively taken up by highly vascularized tissues like liver, heart, the endocrine system and endothelial cells.

Higher stability complexes may be partly and slowly degraded by α-amylases in the blood. Those particles show increase plasma half lives. Complexes of carbohydrates with α-1,4 glycosidic bounds, like maltodextrin (isomaltoside: FeIM) or its derivates (carboxymaltose: FeCM) may be less stable than complexes with partially α-1,4 glycosidic bounds like in case of starch derivates (hydroxyethyl starch: FeHES).

Particles consisting of dextrans (α-1,3 and 1,6 glycosidic: LFeD, HFeD, HFeD_G) are even more stable in terms of α amylase influence and not degraded in that way. A main influencing factor determining supply of iron to Tf is beside complex stability the plasma half life. Particles which are rapidly eliminated from plasma by the MPS/RES can liberate less iron than particles persisting longer in circulation.

Uptake and degradation

The cores, and persisting particles of low stability complexes, the partly degraded higher stable complexes, and the initially iron dextran complexes are opsonized dependent on their surface properties. Subsequently, macrophages of the mononuclear phagocyte system (MPS) e.g. the Kupffer cells in case of liver detect the particles [117-121]. The particles are then taken up by endocytosis [122] or as in case of dextran complexes via a receptor mediated pathway [123]. The endosomes subsequently fuse with lysosomes and the complex structures are cleaved enzymatically and pH-dependently. The iron phase is dissolved pH-dependently (≈ 4.5) due to the activity of proton pumps, redox-mediated possibly via Steap3 [113] and ligand-mediated possibly by lactoferrin. High stable complexes and big particles are only slowly degraded - proportionally to the surface to volume ratio (smaller with rising size) [116] - or may even be embed in siderosomes.

Iron utilization

Ferrous iron is exported into the cytoplasm via DMT-1/Nramp1/TRPML1 combined activity [124, 125] contributing to the intracellular labile iron pool (LIP).

Thus, the LIP is only slowly increasing preventing the formation of ROSs. The intracellular LIP is suggested to be the critical factor for the formation of $^{\bullet}OH$ [51, 126, 127] (**1.2.5**).

Ferrous iron from the LIP can be supplied to mitochondria for the synthesis of Fe-S clusters and heme, as cofactors for Fe-S proteins, myoglobin and hemoglobin. (**1.2.5, Figure 5**) If hepcidin levels are low it can also be exported into plasma via Fpn (**1.2.2, 1.2.3**) prior to oxidation to ferric iron and binding to serum Tf (**1.2.4**). In case of high hepcidin levels ferrous iron from LIP is predominantly stored in ferritin (**1.2.8**).

Iron overload

In conditions of iron overload, ferritin can be autophagocytosed in lysosomes, triggering the formation of ROSs. H_2O_2, which is omnipresent in macrophages, is transported into ferrous iron loaded lysosomes. $^{\bullet}OH$ can be consequently generated via Fenton reaction (Formula 1; **1.2.7**). This highly potent radical is able to peroxidate phospholipids of the lysosomal membrane resulting in rupture of the lysosomal membrane. The intracellular LIP is subsequently rapidly increased. This phenomenon is also relevant in case of non-selective uptake of NTBI iron in other kind of cells. Iron uncontrolledly released by rupture of lysosomes or taken up as NTBI from the plasma abruptly increases the LIP. Radicals can consequently be generated in cytosol, triggering cellular damage or even worse, inducing apoptosis and tissue necrosis [32].

1.4.5. Adverse drug events under the treatment with *i.v.* iron complexes

Free ionic iron shows toxicity e.g. mutagenity by Fenton reactions [128] and a potential increase of microorganism proliferation [1] (1.2.7). In order to reduce these effects, the use of oxy hydroxide nanoparticles (FeNPs) was introduced. Historically, the first FeNPs were uncoated and toxic. Toxicity was avoided by coating the iron core with a shell of carbohydrate [129]. Today, different iron containing non-biological complex drugs (Fe-NbCD) are marketed. Traditional iron sources used in these preparations are either iron dextrans such as Dexferrum® (HMWID; HFeD), Ironate® (generic iron dextran, HFeD_G), CosmoFer® (LMWID; LFeD1) and Infed® (LMWID; LFeD2) or other iron salts like sodium ferric iron gluconate-sucrose (Ferrlecit®; FeG) and iron sucrose (Venofer®; FeSuc). Infed® and Cosmofer® are the same product and only differ in their brand names, as Infed® is the brand for the US market whereas Cosmofer® is marketed in Europe. Later on, the NbCDs ferric carboxymaltose (Ferinject®), ferumoxytol (Feraheme®) and iron isomaltoside 1000 (Monofer®) followed containing complexes without dextrans as complex former. In the last couple of years, generic parenteral iron formulations like generic iron sucrose or iron dextran (Ironate® as a generic iron dextran introduced to the Greek market) have entered the market. Iron hydroxyethyl starch (Feramyl®) is an example for a new complex, which is at the stage of clinical approval.

Beside iron toxicity, another source of severe adverse reactions is the immunological response of the body to the carbohydrate fraction of the Fe-NbCD [129]. Especially in case of iron dextran formulations anaphylactic (antibody-mediated) or anaphylactoid (non-antibody-mediated) reactions are a risk to be considered. The difference of hypersensitivity adverse reactions between high molecular weight iron dextran (HMWID; Dexferrum®) and low molecular weight iron dextran (LMWID; Cosmofer® = Infed®(US-market)) is remarkable with 3.3 adverse drug events (ADEs) per 10^6 doses in case of LMWID vs. 11.3 ADEs in case of HMWID [111, 130-133]. This difference is not well reflected in many recent studies as they often only mention "iron dextran" without clarification whether LMWID or HMWID was investigated. Ironate® - an example of a generic iron dextran preparation - is intended to be marketed as generic to LMWID in Greece. The believe that non-dextran iron products are related with

lower incidents of anaphylactic / anaphylactoid reaction is not well substantiated[134]. It must be considered that generic compounds of iron sucrose (iron sucrose similars) as well as iron dextran have entered markets, giving rise to the question of interchangeability between originator and generic compounds (closer look inside this topic in section **1.4.7**).

Ferumoxytol (FePSC; Feraheme®/Rinso®) is somewhat outstanding in the field of Fe-NbCD as it is indicated in IDA and as contrast agent in magnetic resonance imaging (MRI). The rate of ADEs in FePSC was beside iron dextran preparations the highest of the *i.v.* iron compounds on the US market, as revealed by an investigation of reported ADEs [135]. FePSC has a comparable risk of immunological reactions as dextran complexes as previously reported [136] and shown in an *in-vitro* experiment [108] although the method and way of interpretation has raised critics [137]. Best benefit to risk ratio was assessed for ferric carboxymaltose (FeCM, Ferinject® / Injectafer®) with a potential single dose of 1000 mg in one infusion (independent from body weight). In connection with such high-dose infusions, events of hypophosphatemia as a severe ADEs have been reported [111, 138]. Iron isomaltoside 1000 (FeIM, Monofer®) has been categorized as iron(III) hydroxide dextran complexes (B03A C06 ATC code) by regulatory authorities. However, it was excluded from the requirement of a test dose in contrast to all other iron dextrans, as demanded at the time of approval. This reflects the unique properties of FeIM, consisting of a carbohydrate without anaphylactic potential [139, 140].

Today a test dose for iron dextrans is not demanded anymore, as a toleration of the test dose not proof a toleration of the whole dose. Instead, resuscitation facilities should be available when performing *i.v.* iron administration [141]. In general, the incidence of life threatening adverse drug events (ADEs) is lower in case of *i.v.* iron complex drugs (2.2 per 10^6 doses with 0.4 deaths) than of allogeneic blood transfusions (10 per 10^6 with 4 deaths) - the only alternative in many patients with perioperative blood loss [111]. Chertow et al. reported of 38 ADEs per million of administered doses and reasoned that *i.v.* iron therapy is save except in case of HMWID. The absolute rates of life-threatening ADEs were 0.6, 0.9, 3.3 and 11.3 per million for FeSuc, FeG, LMWID and HMWID, respectively [133]. In 2012 a study by Okam et al. found 32 ADEs in 619 patients who were treated over 2 years with *i.v.* iron (LMWID, HMWID, FeSuc, FeG). LMWID (2.5 % of the treated persons) and FeG (3.6 %) were identical and showed lower incidences of ADEs than FeSuc (11.5 %) (OR=5.7; 95% CI=1.6-21.3). HMWID was only administered in case of 9 patients and ADEs occurred in 4 of them (44.4 %). The authors concluded that LMWID should be used more often [142].

Most adverse reactions with symptoms like flushing, hypotension, vomiting, diarrhea and nausea are related to iron toxicity by release of labile iron [143, 144]. As free iron promotes proliferation of microorganism (**1.2.2**, **1.2.6**) it is expected that infection rates are increased under therapy with *i.v.* iron compounds. But contrary to that several studies have shown that patients under *i.v.* iron treatment show significant decreases in infection rates ($p < 0.001$) [145] and no increase of postoperative infections was observed. As final clinical data are missing so far, the authors quote nevertheless, that *i.v.* iron should be avoided at acute infection and when ferritin values are above 500 ng/mL [111]. Most of the studies investigating the risk of *i.v.* iron are retrospective, e.g. [133]. The general and increasing use of

i.v. iron in hemodialysis patients is raising questions to the benefits to risks ratio. Tissue iron overload is probable in hemodialysis patients and the consequences are barely understood and require a "well-powered study of sufficient duration to better define the role of intravenous iron" [46].

Investigations concerning the general safety of *i.v.* iron in different studies show that the different preparations are comparable safe when they are used at the recommended doses with the exception of HMWID [111].

Intranveous iron and oxidative stress

Studies investigating oxidative stress under the treatment of *i.v.* iron summarized Koskenkorva-Frank et al [32]. FeSuc without comparision to other products was identified to increase oxidative stress markers at a dose of 100 mg in hemodialysis (HD) patients and patients suffering from chronic kidney diseases (CKD) [146-148]. A comparison of FeSuc with FeG and LMWID in patients with HD and CKD showed increased markers for all preparations but significantly increased values for FeG in comparison to FeSuc and LMWID [149]. Stefánsson et al. found protein carbonyl and ascorbic free radicals in case of FeSuc but not in case of LMWID in HD patients [150]. A study investigating oxidative stress for FeSuc originator, FeSuc generics, FeG, LMWID and FeCM showed increased superoxide ($O_2^{\bullet -}$) radical levels in case of all preparations in HD patients. A summary of 55 Studies in rats show increased markers of oxidative stress in case of all complexes investigated in heart, liver and kidney. But the results seem to be inconsistent among the different non-clinical and clinical studies possibly as consequence of the use of different oxidative stress markers and as HD itself induces oxidative stress [32]. There have not been studies investigating oxidative stress in case of FeIM and FePSC so far. Oxidative stress is a consequence of tissue iron overload. A study by Rostoker et al. recently investigated tissue iron levels by magnetic resonance imaging. A strong correlation between hepatic iron storage and *i.v.* iron has been observed [151]. But it was not possible to distinguish whether iron was present in hepatocytes with possible toxic effects or in Kupffer cells. Similar results were found by Canavese et al. [152]. Post mortem analyses of tissues from patients being treated with iron - before EPO was used in combination with *i.v.* iron - showed increased iron accumulation in adrenal glands, lymph nodes and lungs but sparse in heart, kidney and pancreas [153]. Fishbane et al. reasoned that iron overload is probable in HD patients but tissue damage is not probable as even in case of genetic iron overload high doses of iron and several years are required to cause injury [46].

Iron and cardiovascular risk

Cardiovascular diseases (CVD) are very common in dialysis patients and negative impact of *i.v.* iron is relevant for that reason. Chronic volume expansion, anemia, disorders in calcium phosphate metabolism, hyperhomocysteinemia and oxidative stress are typical risk factors in dialysis patients [154]. There are some studies indicating a connection between iron status in humans and risk of cardiovascular effects [155-160]. Drueke et al. showed in a study with 79 dialysis patients under *i.v.* iron therapy that there was a correlation between serum ferritin levels, oxidative stress markers and intima-media thickness of the carotid artery - a marker for beginning atherosclerosis [161]. Other studies exclude connections between iron

status and cardiovascular risk [162-164]. Sullivan has written an interesting review about the connection between atherosclerosis and iron in arterial plaques. The iron hypothesis, described by Sullivan, means that decreasing body iron is protective and reduces the risk of suffering from ischemic heart disease. There is proof that depletion of iron is connected to increased plaque stability. Increased levels of hepcidin - associated in case of anemia of chronic disease (ACD) e.g. in chronic kidney disease (CKD) patients or inflammations - may impair the clearance of iron from macrophages in atherosclerotic plaques [165]. Lapice et al. recently reviewed several studies of the influence of body iron status on chrinic vascular diseases (CVD). They summarize that the iron status has a neutral effect on CVD. Extreme conditions of iron deficiency as well as iron overload are associated with a modestly increased CVD risk [166]. Thus, the risk for CVD may be increased in case of iron overload in heart as consequence of *i.v.* iron therapy of dialysis patients. (See section **0** for supplemental information and discussion)

1.4.6. Complex stability

Dependent on what kind of complex is administered iron containing non-biological complex drugs (Fe-NbCD) are associated with anaphylactic and/or anaphylactoid side effects. Anaphylactic ADEs are linked to an antibody-mediated depletion of mast cells in response to the presence of a complex [167]. Those ADEs are mainly reported in case of HMWID but also LMWID and FePSC. Anaphylactoid reactions are not antibody-mediated and they are linked to the presence of NTBI with local hypersensitivity, induced by depletion of mast cells caused by a chemical trigger. The consequences are acute reactions like flushing, chest pain, urticaria, hypotension, vomiting, diarrhea and nausea. Chronic reactions are associated with the induction of oxidative stress and iron stimulated growth of pathogens. They are a consequence of iron overload in tissues and NTBI in serum.
The presence of NTBI (**1.2.7**) is related to the dose of the administered *i.v.* iron complex, "free" non-complex bound iron in the formulation and the stability of the complex. The complex stability is relevant with regard to in vivo conditions as well as to the infusion solution medium (glucose, sodium chloride) in case of high dose administration. One factor determining the in vivo stability is the kind of carbohydrate (I). As described in **1.4.4** carbohydrates with α-1,4 glycosidic bounds are likely to be partly degraded in the blood by α-amylases. This makes them well biodegradable but may also contribute to iron release in plasma with the consequence of NTBI. Another influence factor is the type of the carbohydrate-iron interaction (II). Dependent on the carbohydrate and the manufacturing process (temperature, speed of pH increase etc.) the stabilizing effect of the carbohydrate on the inorganic phase may be differently pronounced. The crystallinity determines the thermodynamic stability and thus the solubility of the inorganic phase (III). Highly stable and large single crystals will dissolve much slower than amorphous material. The types of carbohydrate as well as the manufacturing process - especially terminal temperature increase - have influence on the stability of the inorganic phase (IV). The particle size has a main influence on the

dissolution rate as given with *Formula 10* and is dependent on the molecular weight of the carbohydrate as well as on the manufacturing process (V).

Figure 10 gives an overview of factors determining complex stability. All these properties together determine the efficacy of the drug in respect to increasing Hb levels and the safety in respect of preventing the generation of NTBI, oxidative stress and hypersensitivity reactions, respectively:

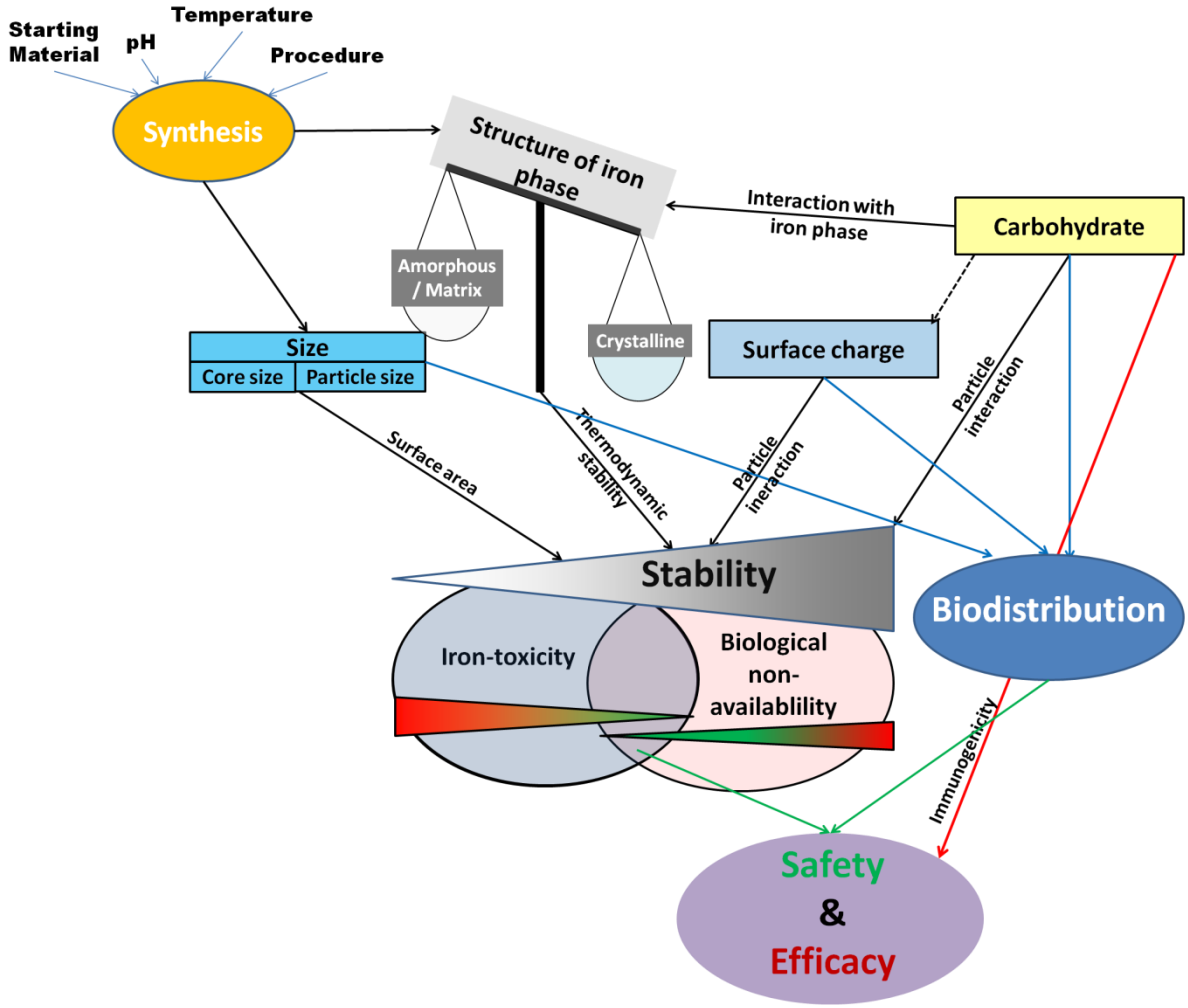

Figure 10 - A mind map summarizing the aspects of *i.v.* iron preparations influencing safety and efficacy in clinical use: The conditions during synthesis influence the size and the structure of the resulting complex. The size (surfac area), the structure (thermodynamic stability), the surface charge (particle interaction), and the kind of carbohydrate (particle interaction) directly influence the stability of the complex. The kind of carbohydrate as stabilizing component of the complex has influence on the structure (e.g. matrix structure), the surface charge and the particle interaction (hydrophilic interaction). Low stability of an iron complex drug increases iron-toxicity by liberation of "free" and labile iron in circulation. High stabile complexes show good safety profiles in this context but may accumulate in the cells were they cannot be degraded. The particle size, the surface characteristics, and the kind of carbohydrate of the particle influence the distribution in body compartments. The kind of carbohydrate is the most important factor regarding immunological side effects.

"Free" iron

Paffetti et al. classified “free" iron as low molecular weight iron not bound by high affinity plasma proteins [168]. Nilsson et al. classified “free" iron as iron loosely bound to a variety of biomolecules in body liquids in a way that it maintains its ability to catalyze the formation of reactive oxygen species (ROS) [169]. In general, it has to be distinguished between physiological conditions and the description of the pharmaceutical quality of an *i.v.* iron drug The term "free" iron is used within this work to describe the fraction of iron in the complex, which is readily dissolved from the complex, as it is either present as free iron in the formulation or loosely bound to the surface of the complex. Thus, it can be dissolved easily by dilution without the presence of reductive agents, acidic milieu or complexing agents. In the presence of transferrin (Tf), it is quickly bound to it, contributing to non-transferrin bound iron (NTBI) in case of oversaturation of Tf. "Free" iron can be determined *in-vitro* by dialysis in case of non-biological media. When determining it in plasma, mobilizing agents are required as "free" iron is bound to albumin and other serum proteins, which do not cross a dialysis membrane. The problem then is that the mobilizing agent (e.g. nitrilotriacetic acid (NTA)) may also directly dissolve iron from the complex, dependent on how tightly iron is bound to the complex and thus delivers higher results in case of low stability complexes.

Labile iron

The term labile iron is frequently used but it must be distinguished between labile iron in connection with intracellular iron metabolism forming the intracellular labile iron pool (LIP; **1.2.5**, **1.4.4**), labile plasma iron (=NTBI) [45, 48, 170] and the labile iron fraction present in a pharmaceutical preparation. They are termed "labile" because they potentially induce oxidative stress, as the iron is not kept in an inert redox state. Labile iron is available for Fenton reaction if ferrous iron is present in the complex or reducing agents are present (e.g. ascorbate in blood) to react with liberated ferric iron. This is from elevated relevance if the antioxidant capability of the body is decreased. The labile iron in an *i.v.* iron complex is the fraction of iron that includes the "free" iron in the complex and the fraction that can be readily and directly bound by Tf in vivo (without the step of biodegradation and transfer to Tf after export from macrophages)(**Figure 11**). The amount of iron that can be detected *in-vitro* by complexing/color agents, without previous treatment with e.g. acids and reductives (e.g. FerroZine®) is also referred to labile iron in the complex.

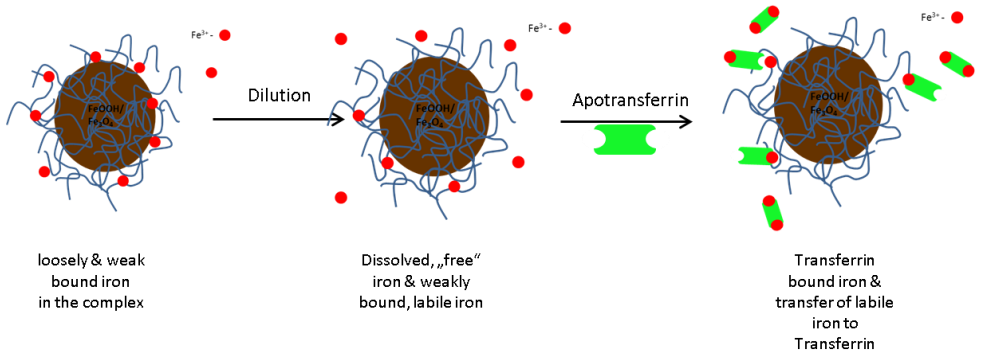

Figure 11 - Visualization of loosely and weak bound, "free", labile iron and transferrin bound iron.

Catalytically active iron (Bleomycin detectable iron)

Bleomycin detectable iron (BDI) is a method for the determination of NTBI [57] but may also describe all kinds of catalytic active forms including heme as Bonsdorff et al. showed that erythrocyte hemolysis interferes with the results of BDI assay [171]. The catalytically active iron either in the iron complex drug or present after dilution is theoretically equivalent to the labile iron fraction of the complex. They both describe the fraction of the iron in the complex that is capable of the generation of oxidative stress.

The terms used for the characterization of Fe-NbCD are partly the same as those used to describe conditions in vivo without the presence of *i.v.* iron complexes. Thus, it has to be distinguished whether the pharmaceutical quality of the drug is point of interest or if the physiological condition is described. The labile iron fraction in the complex directly contributes to the labile plasma iron, "free" iron in serum, NTBI, catalytically active iron. Those terms characterize in vivo the same or nearly the same fraction of iron.

1.4.7. Regulatory aspects

Health care systems are exposed to continuous pressure to safe costs. The exchange of expensive originator products with cheaper generic copies is thus relevant for the legislative and healthcare authorities. In the last couple of years, patent protection of several kinds of iron complexes ran out. This makes it likely for generic companies to copy the original active pharmaceutical ingredient (API) and market it. Examples are the generic iron dextran Ironate®, which was designated to copy LMWID (Cosmofer® / Infed®), and several iron sucrose (FeSuc / IS) preparations like FerMed® - so called iron sucrose similars (ISS) - copying Venofer®.

In case of classical orally administered drugs e.g. solid drugs (tablets, capsules, granulates, powders) or liquid drugs (solutions, suspensions, emulsions etc.) an reference and a test drug are assessed bioequivalent if they have the same active pharmaceutical ingredient (API) and show equivalent availability at the site of drug action when administered at the same dose. The two variables that are important for bioequivalence are the maximum concentration of the plasma concentration-time-curve (C_{max}) and the area under the curve (AUC) of the plasma concentration-time-curve. Two formulations are equivalent if the 90 % CI of $\frac{Cmax}{AUC}$ or AUC of a formulation is between 80 to 125 % of the other formulation. As only the outcome is interesting, it is not necessary that the excipients or manufacturing processes of the drug are identical between originator and generic. In case of intravenous administration of a chemical API, it is automatically bioequivalent when administered with the same dose if there are no excipients in the formulation influencing the pharmacokinetic profile. This makes it relatively easy for companies and authorities to proof whether two drugs are bioequivalent and thus can be exchanged without consequences in respect to efficacy and safety. In case of iron containing non-biological complex drugs (Fe-NbCDs) the critical question is: What is the API?

Is it the complexed iron or is it the complex itself?

As the carbohydrate influences the complex stability and directly determines the distribution of the complex in the body it is of essential relevance in this context. Therefore, the complex

must be the API and not the contained iron. The complex should fulfill the same criteria for assessment of bioequivalence as in case of a chemical API, which raises the second question: What are the criteria for bioequivalence of two Fe-NbCDs? Respectively: How is bioavailability defined in this case? Are AUC and C_{max} useable?
In case of *i.v.* administration of Fe-NbCDs the iron must be released from the complex to be bioavailable, which raises questions concerning complex stability (influence of manufacturing process). In case of Fe-NbCDs the bioavailable amount is the fraction that is available for utilization in the human body and at the place of hemoglobin synthesis (bone marrow). The way to this target is much more complicated than in case of a chemical API as a particular fraction of the complex may be very slow or not biodegradable and the liberation kinetic is thus from relevance. (See section **1.4.4**)
Borchard et al. generally discussed this matter [172]. While a chemical API is fully characterizable, biological or non-biological complex drugs are not. The starting material, reaction time and conditions (temperature, pH) directly influence the properties of the NbCD. Such properties like structure of the inorganic phase, size, size distribution and surface charge of the complex directly influence the thermodynamic stability, biodegradability and body distribution. Thus, efficacy and safety profiles may differ between two products although they contain the same amount of iron and the same amount and kind of the complexing carbohydrate. In fact, the manufacturing process has remarkable influence on the thermodynamic properties of a Fe-NbCD. If a complex is produced at lower temperature or less cycles of temperature changes, the iron phase may be transformed to a different modification directly influencing solubility. Faster pH rising may affect the interaction between carbohydrate and iron phase and the size of the resulting complex. Thus, iron may be released more likely to plasma, with higher possible non-transferrin bound iron (NTBI) values and higher rates of adverse events in case of a smaller or less stable complex type. Those differences have already been shown in case of ISSs [173-176].

Intended copies of NbCD have been approved according to generic paradigm [172]. But interchangeability is for the above-mentioned reasons not possible on that base. Evidence of equivalence must show that (I) the physicochemical properties additionally to those required by pharmacopoeia [177] (structure of the inorganic phase, size and size distribution of the complex, size of the cores, surface charge, labile and free iron content in the drug) are similar and do not exceed differences of batch to batch variation of the originator product. (II) The biological distribution and utilization is comparable between originator and intended copy. In this context, Borchard proposed the demonstration of equivalent biological utilization by isotope-labeled iron preparations. Schellekens et al. proposed in case of comparable pharmaceutical quality the validation of safety in rodents [177]. Another model in this context is the avian model used by Roth et al. [178] to show similar behavior in a biological system. However, as the iron metabolism of avian as well as rodents differ from that of humans, clinical studies may also be necessary to proof equivalence between Fe-NbCDs.

Current regulatory requirements

In reaction to the scientific and clinical impacts, regulatory authorities like the EMA (European Medicines Agency) have adapted approval requirements of intravenous iron nano-colloidal products. The 2013 draft reflection paper [179] gives an overview of analyses that have to be performed and it summarizes:

"For the comparison of iron-based nano-sized colloidal products developed with reference to an innovator medicinal product, current scientific knowledge and regulatory experience for characterization of nano-sized colloidal preparations indicate that quality characterization on its own, would not provide sufficient assurance of the similarity between the two products, even if the quality tests performed show similarity. In the context of such iron based preparations, a “weight of evidence approach” including data from quality, non-clinical and human pharmacokinetic studies is required".

Quality characterization includes:

- "quality standard for coating materials
- structure and composition of the carbohydrate
- identification and control of key intermediates in the manufacturing process
- particle size (and size distribution) and specific surface area of the iron core
- the fraction of labile iron released from the product when administered
- polymorphic form of the inorganic iron compound comprising the core
- impurities e.g. ratio of divalent and trivalent iron
- morphology e.g. microscopic evaluation of iron distribution in the iron complex (e.g. iron surrounded by a carbohydrate coat, iron distributed through a carbohydrate matrix)
- ratio of bound carbohydrate to iron
- particle size, size distribution
- charge, of the iron-carbohydrate complexes
- *in-vitro* iron release rate from the iron-carbohydrate complex in physiologically/clinically relevant media. Reliable and discriminating validated *in-vitro* release methods should be developed using models that represent the extracellular (plasma/serum) release of labile iron and acid degradation kinetics,
- degradation path for the carbohydrate and the iron carbohydrate complex
- stability on storage of the product
- in-use stability (including after re-constitution with recommended diluents for administration) with consideration to instructions for administration in the SPC (Summary of product characteristics) e.g. concentration"

Non-clinical studies should include:

- "validated analytical methods for the quantification of analytes in blood/plasma and tissue
- biodistribution studies in a relevant animal model with focus on RES, plasma and pharmaceutical (bone marrow) as well as toxicological target tissues (liver, heart, kidney, lung)
- development of additional analyses for the determination of degradation products is encouraged
- Toxicity studies (.) are not useful"

Clinical studies should show:

- comparison of pharmacokinetic behavior in respect to Tf bound iron (90 % CI of $\frac{Cmax}{AUC}$ or AUC is between 80 to 125 %)" [179]

The EMA furthermore states that minor differences between reference and test product in quality, non-clinical and human pharmacokinetic characteristics require a therapeutic equivalence study to show impacts on efficacy and safety. (For details see [179])

1.5. Aim of this work

The aim of this work was the characterization of commercial iron suplement drugs regarding the differences between the complexes with the possible impact on their clinical safety and efficacy profile. The aims can be summarized as follow:

- Finding physicochemical differences between different iron complexes regarding size (size of the inorganic phase by transmission electron microscopy [TEM], hydrodynamic diameter by dynamic light scattering [DLS]), charge (dispersion media dependent surface charge by ζ-potential), structure of the inorganic iron oxy hydroxide phase (electron & X-ray-powder diffraction)
- Comparing the stability (acidic hydrolysis in presence of a complexing agent) and the fraction of labile or loosely bound iron in human serum (FerroZine® assay) of the different complexes as indicators for the biological safety profile
- Assessment of the distribution of different complexes into pharmacological and toxicological target tissues
- Combination of the applied methods to estimate clinical safety and efficacy

2. Materials and Methods

2.1. Methodical background

2.1.1. Some basic aspects of crystallography

Crystals are omnipresent in nature as practically all naturally developed solid materials are present in a crystalline state. While a mountain consists of rocks, built up of different kinds of crystals, an iceberg is consisting of many similar small ice crystals. A crystal is an anisotropic, homogeneous corpus that consists of atoms, ions or molecules, which are not arranged randomly like in amorphous state, but in an ordered, three-dimensional periodical way. The crystalline state is the solid aggregate state with lowest energy [180]. The enthalpy of the crystal lattice is correspondingly high. Physicochemical characteristics like melting enthalpy or solubility are dependent on the enthalpy of the crystal lattice. Modifications of a substance with a higher level of crystal arrangement show worse solubility behavior than other modifications with a lower level of crystallinity. This phenomenon is called polymorphy.

The differentiation between amorphous and crystalline material is possible in various ways. One possibility is determination of the melting behavior as a melting point defines crystalline materials whereas amorphous substances have a sagging point. Another very helpful approach is the behavior against X-rays (**2.1.5**). The three-dimensional periodical arrangement of crystals causes interferences of the X-rays whereas amorphous materials cannot do this.

A space lattice is a mathematical model in crystallography, which describes the periodical arrangement inside a crystal with points and vectors. In contrast to limited crystals, the space lattice is defined unlimited. For that reason lattice planes and lattice straights are also unlimited (**Figure 12**).

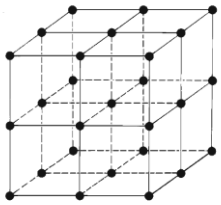

Figure 12 - Example for a space lattice [180]

Lattice straight

Starting from point 0 in **Figure 13** and shifting it by the vector $\vec{a}$ leads to point 1. By shifting with 2 $\vec{a}$ Point 2 is reached etc. This procedure is called symmetry operation and a lattice straight is yielded. Every point that can be added by shifting in the same manner is an identical or translatoric comparable point. $|\vec{a}| = a_0$ is the lattice constant and contains all information of this one-dimensional lattice.

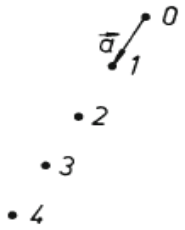

Figure 13 - Lattice straight with lattice constant: $|\vec{a}| = a_0$ [180]

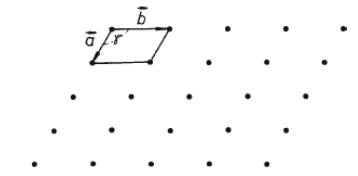

Figure 14 - Lattice plane being spanned by vectors $\vec{a}$ and $\vec{b}$. [180]

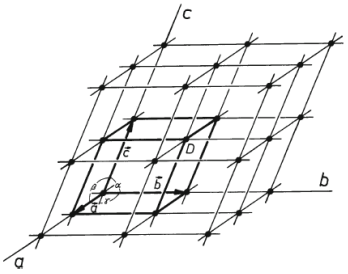

Figure 15 - Space lattice formed by factors $\vec{a}$, $\vec{b}$ and $\vec{c}$. [180]

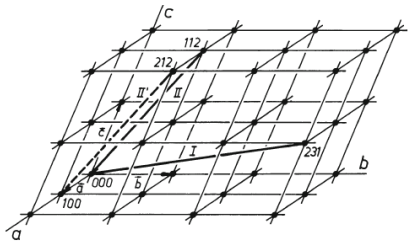

Figure 16 - Description of straights in the space lattice by the coordinates from the origin of the lattice to a point uvw by a vector [uvw]. (example from figure: I [231]; II [112]). [180]

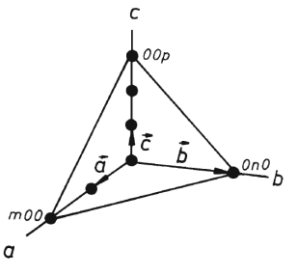

Figure 17 - A lattice plane with the Miller indices (362) [180]

Lattice plane

By introducing a vector $\vec{b}$ and shifting it to the lattice straight in **Figure 13** a two-dimensional lattice plane is spanned by vectors $\vec{a}$ and $\vec{b}$. (**Figure 14**)

Space lattice

Finally, introducing a vector $\vec{c}$ to the lattice plane, which is not coplanar with vectors $\vec{a}$ and $\vec{b}$, forms a space lattice, which is described by vectors $\vec{a}$, $\vec{b}$ and $\vec{c}$, with the corresponding lattice constants $|\vec{a}| = \boldsymbol{a_0}$, $|\vec{b}| = \boldsymbol{b_0}$ and $|\vec{c}| = c_0$. Vectors $\vec{a}$, $\vec{b}$ *and* $\vec{c}$ span an elementary cell. (**Figure 15**)

Each point in the lattice can be described by the vector from the 0-point (origin) to it, with $\vec{\tau} = u\vec{a} + v\vec{b} + w\vec{c}$ and the constants *a*, *b*, *c* with the absolute values a_0, b_o and c_0. Thus, the point can be described by *u*, *v* and *w* or shortly *uvw*. The straight from the origin to the point *uvw* is described by [*uvw*]. (**Figure 16**)

Lattice plane (hkl)

Planes are not only possible to be described by vectors $\vec{a}$ *and* $\vec{b}$. Planes can be spanned in the space lattice in a variable manner. This plane has intercepts with the axes a, b and c, described by the vectors $\vec{a}$, $\vec{b}$, *and* $\vec{c}$ (**Figure 17**). The intercepts with this axis give the points m (axis a), n (axis b) and p (axis c). The reciprocals of the coordinates are used to describe the plane. These are:

axis a: h ≈ 1/m

axis b: k ≈ 1/n

axis c: l ≈ 1/p

(hkl) are the Miller indices, which are the smallest integral numbers of the reciprocals and describe any plane inside the space lattice of a crystal.

Crystal structure

Inside a crystal, the points in the space lattice are occupied by atoms, ions or molecules. The Miller indices (hkl) and lattice straights [uvw] are not able to describe specific planes and straights inside an elementary cell. For this purpose it is necessary to use the coordinates x, y and z. For example x,y,½ describes all points that are situated on a plane which is parallel to the a,b-plane and cuts vector $\vec{c}$ at ½ the length [180].

2.1.2. Transmission electron microscopy (TEM) and Scanning-TEM (STEM)

Background

The resolution of optical microscopy methods is limited to about 200 nm by the light absorption in biological material at < 295 nm and the imaging physics. The resolution of microscopic technique is directly dependent on the wavelength of the applied radiation (visible light 380-780 nm). This relationship is formulated by the Rayleigh criteria:

$$\delta = 0.61 \cdot \frac{\lambda}{n \cdot \sin \alpha} \qquad \textbf{Formula 4}$$

The minimum distance δ between two points that is necessary to resolute these points as two different points is dependent on the wavelength λ of the applied radiation. α is the angle between the dipping and the reflected beam and n is the refraction index.
The limit can be overcome by imaging of thin samples (in vacuum) with electrons of short wavelength. The resolution of electrons is dependent on the accelerating voltage of the device (typically 80 keV-400 keV) as the de-Broglie wavelength (λ) is dependent on the mass (m_e) and the velocity (v) of a particle. h is the Planck constant:

$$\lambda = \frac{h}{m_e \cdot v} \qquad \textbf{Formula 5}$$

The higher the velocity of an electron the smaller is the de-Broglie wavelength and consequently the resolution (*Formula 5*) of the device. Additionally, a vacuum is necessary to circumvent the collision with air molecules and consequently deflection by them. The theoretical resolution of electron microscopy is about 0.05 nm but it is limited by aberration effects of the electromagnetic lens system to about 0.1-0.3 nm with modern devices and radiation damage of the sample.

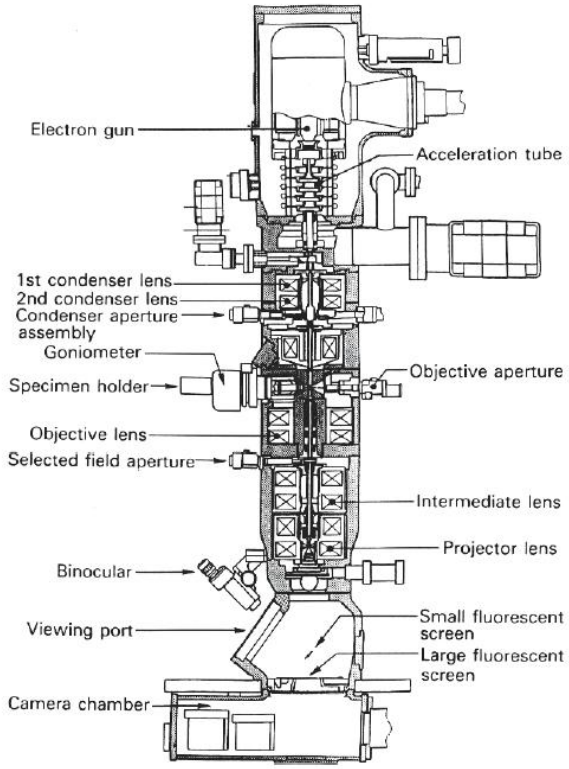

Figure 18 - Picture of a TEM from [181]

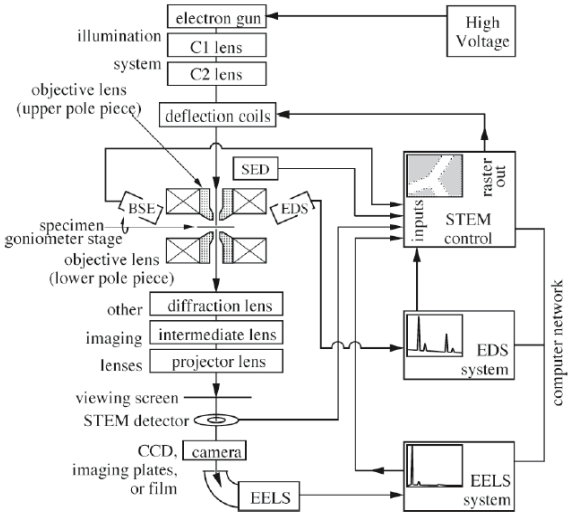

Figure 19 - Scheme of a TEM with possible STEM mode and electron disperse X-ray spectroscopic (EDS) and electron energy loss spectroscopic (EELS) element. From [181]

Instrumentation

In a TEM (**Figure 18, Figure 19, Figure 20**), electrons are emitted from an electron gun. A three- or four-stage condenser lens system makes it possible to vary the illumination aperture and the illuminated specimen. The electron intensity distribution behind the specimen is imaged with a lens system (3-8 lenses) onto a fluorescent screen. The picture is taken by a CCD (charge-coupled device) camera. The specimen must be very thin (5 - 100nm in case of 100 keV electrons) as the electrons are strongly interacting especially with atoms of high electron densities (higher atomic number).

In TEM, imaging is possible with the primary beam (bright field) or a Bragg-reflected beam on-axis (dark field). This gives rise to diffraction contrast, making it possible to image crystal defects. When Bragg-diffracted beams pass the aperture, crystal-structure imaging shows a projection of atomic rows (electron diffraction). The bright field (BF) detector is located on the optical axis of the TEM and detects the electrons after passing the specimen. The annular dark field detector (ADF) detects the electrons being scattered elastically. The high-angle annular dark field (HAADF) detector detects the inelastically scattered electrons. In BF, only the transmitted (undiffracted) electrons are detected whereas in dark field (DF), only the diffracted electrons are detected.

The wanted detection variant is performed by a specific location of an “objective aperture” to detect only the electrons that have been diffracted by a specific angle.

The difference in the yielded image is that regions of the specimen with high electron density are in BF imaging dark (high scattering of the electrons, electrons are not on the optical axis anymore) whereas in DF imaging these regions are bright. Regions with fewer electrons

are dark in DF as the detector (situated concentric around the optical axis) detects only scattered electrons.

Modern TEMs are able to form nanometer-sized electron probes with 0.2-10 nm diameter. This makes it possible for the instrument to work at scanning transmission mode (STEM) with a resolution dependent on the probe diameter. The advantage of this method is the possibility to image thick specimens and record secondary and backscattered electrons. It is possible to acquit a "chemical map" of the sample by spectroscopy work. Probes of diameters between 0.2 and 100 nm can be applied to perform microanalysis such as X-ray microanalysis by an energy dispersive Si(Li) or highly pure germanium detector. By this method reliable quantitative information about the elemental composition is provided (energy disperse X-ray spectroscopy - EDX) [181, 182].

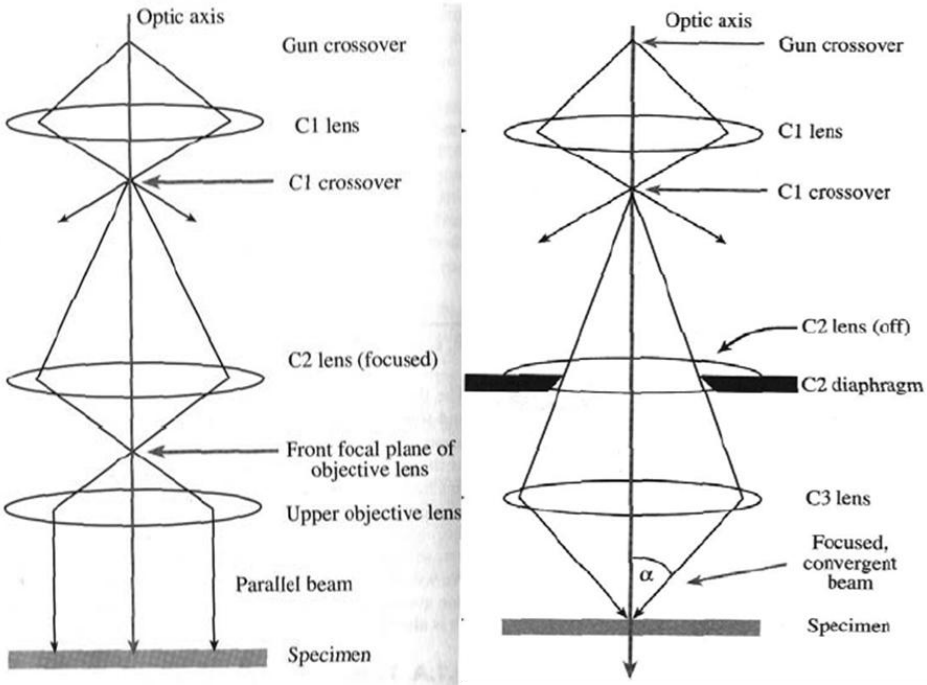

Figure 20 - TEM (left) versus STEM (right): TEM is working in a parallel beam mode yielding a homogenous illumination of the specimen. The contrast is, in comparison to STEM, lower but the resolution is higher. The enlargement in TEM is performed by adjusting of the lenses. In STEM an electron beam (electron probe), with a diameter of 0.1-10 nm makes it possible to analyze thicker specimens. The contrast is high but the area is limited making it necessary to scan the specimen with the beam. The magnification is dependent on the scanning area and the resolution of the screen. The data are collected digitally, which avoids aberration errors. [181]

2.1.3. Electron Diffraction

Beside imaging or spectroscopic investigations of the samples, a very helpful approach of TEM is the selected area electron diffraction (SAED). For this purpose, the specimen is first examined in image mode until a region of interest is found. Then the objective aperture is removed and an intermediate aperture is inserted, allowing the transmitted and all diffracted electrons to be sampled and the SAED pattern appears in the viewing screen (**Figure 21**).

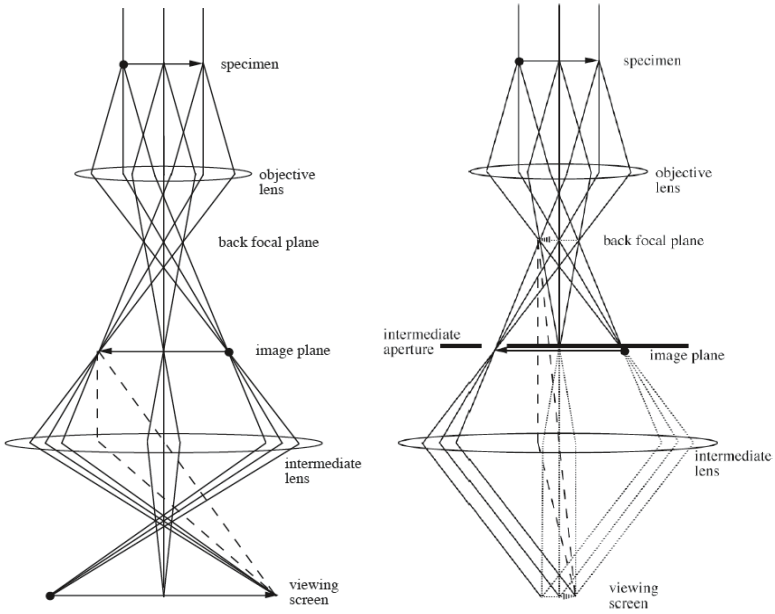

Figure 21 - Difference between image mode (left) and diffraction mode (right): In SAD mode an intermediate aperture is inserted allowing all diffracted and transmitted rays to be seen on the viewing screen (from [182]).

The application of SAED is limited to regions larger than 100 nm in diameter. For smaller areas, it is necessary to use a nano-beam allowing to analyze a single nano-crystal [182]. A diffraction pattern in nano electron diffraction (NED) thus can be obtained from a localized area as small as a single atomic column, which is very sensitive to local structure and probe positions [183, 184].

Scattered electrons

Electrons can be scattered coherently or incoherently. Coherent means that the phase relationships between incident and scattered wavelets are preserved. In case of incoherent scattering, there is a phase difference between incident and scattered wavelets. The consequence is that constructive and destructive interferences (sum of amplitudes of incident and scattered wavelet) are possible in case of coherent but not in case of incoherent diffraction.

The second differentiation is elastic or inelastic scattering. Elastically scattered electrons have the same energy as the incident electrons whereas in case of inelastic electrons the energy is changed.

In consequence, 4 kinds of scattering can be defined:

(I) coherent elastic (no change in phase and energy) → diffraction experiments

(II) coherent inelastic (no change in phase but in energy)
→ used in neutron scattering studies

(III) incoherent elastic (change in phase but not in energy)
→ caused by disorders in material (amorphous material)

(IV) incoherent inelastic (change in phase and energy)
→ spectroscopic investigations

While diffraction experiments generally require coherent elastic scattering, spectroscopic investigations often use incoherent inelastic scattering by measuring intensity versus energy.

2.1.4. Energy dispersive X-ray spectroscopy (EDX/EDS)

With the energy dispersive method the distribution of elements in the specimen can be detected. The requirement for EDX is the prevalence of incoherent inelastically scattered electrons. High-energy electrons can ionize nuclei by knockout of core-near electrons from the atom. The resulting gap is filled with electrons from an electron shell, more far away from the core. The energy differences between the different electron shells is emitted via characteristic X-rays (**Figure 22**). As the intensity of the emitted X-rays is dependent on the atomic order of the element and the number of the atoms, it is possible to conclude the chemical composition (quantitatively and qualitatively) of the material. The TEM has to be equipped with an EDX detector for this purpose [182].

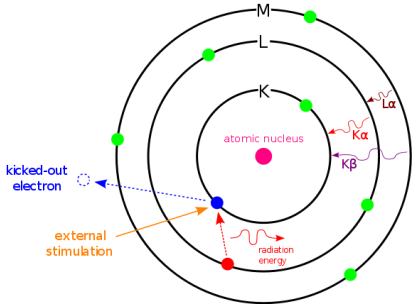

Figure 22 - Model of X-ray generation in EDX. Source: Wikipedia

2.1.5. X-ray powder diffraction (XRPD)

2.1.5.1. *Structure information*

X -ray powder diffraction (XRPD) is a useful tool for the quantitative and qualitative analysis of crystalline materials as well as for the determination of the structure and size of a crystal by analysis of the diffraction pattern.

The typical range of distances between lattice planes inside a crystal is with about 0.1 nm at the same range as the wavelength of X-rays (Cu K_α radiation; 1.54178 Å, generally: 1 pm-10 nm). Thus, the crystal works like a three-dimensional optical lattice for the X-rays and the X-rays are diffracted by the electron shells of the atoms (or ions) in the crystal. If the energy and the phase of the applied X-rays are preserved for two or more parallel diffracted X-rays (coherent elastic scattering), constructive or destructive interference will occur. The interference can only be constructive for a specific angle (θ) of the incident X-rays with a wavelength (λ) for the distance (d_{hkl}) between two and more lattice planes (hkl) (see **2.1.1**). This relationship is described by the Bragg equation:

$$n\lambda = 2 \cdot d_{hkl} \cdot \sin\theta \qquad n = 1, 2, 3 \qquad \textbf{Formula 6}$$

The intensity of the diffracted and constructively interfered radiation is then dependent on the repetition rate of this specific distance (d_{hkl}) in the measured sample, i.e. on the size of the crystalline domains. **Figure 23** graphically demonstrates how destructive interference occurs in case of mostly applied angles θ, related to a specific lattice plane (hkl). The phenomenon of constructive interference is demonstrated in **Figure 24**.

In case of highly crystalline materials compromised of large single crystals, the repetition rate is correspondingly high, yielding high levels of interferences with a small difference in θ (sharp diffraction patterns). In the diffractogram, the reflex is consequently sharp. In case of

low repetition rates for small single crystals, the yielded peaks are broadened in comparison to that. As the XRPD device illuminates the sample with a wide range of angles (usually between angles of 10° to 90°) a collection of reflexes is yielded for all possible lattice planes (hkl). This makes it possible to compare the calculated distances d_{hkl} with reference data from the ICDD (International Centre for Diffraction Data). This method allows the description of the specific physical and chemical structure if the crystallinity is sufficiently high, as the collection of d_{hkl} is specific for a compound and for every modification of it [182]. In case of initially liquid, then dried and powdered samples, the statistical distribution of crystalline particles without texture effects in or on the surface of the dried sample is achieved.

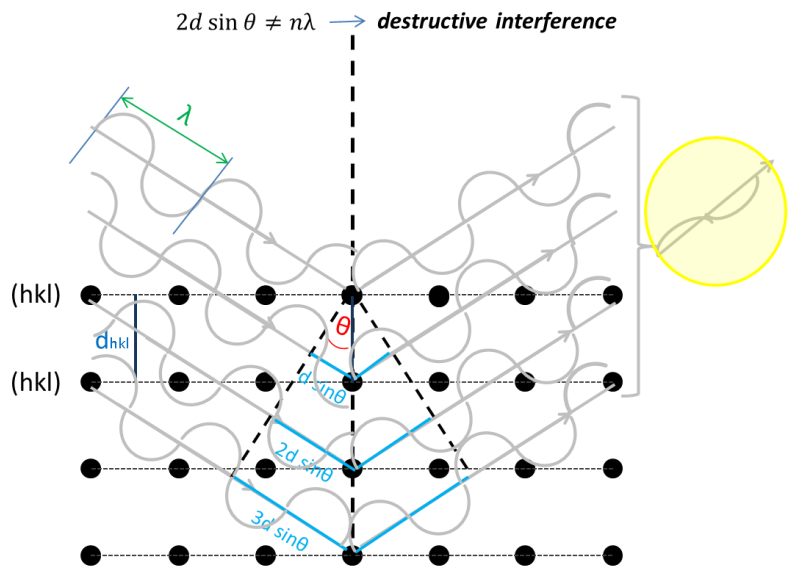

Figure 23 - Destructive interference: The used X-rays with the wavelength λ are applied at an angle θ. They are reflected by the electrons of atoms, ions or molecules, which form a lattice plane (hkl). In most cases the optical pass difference between parallel X-ray- waves/beams (x 2d sinθ - colored blue in the figure) reflected by the x-time repeated parallel lattice plane (hkl) is not a whole-number multiple (n) of λ. In this case, destructive interference is the consequence. The diffractogram does not show a reflex at 2θ, consequently.

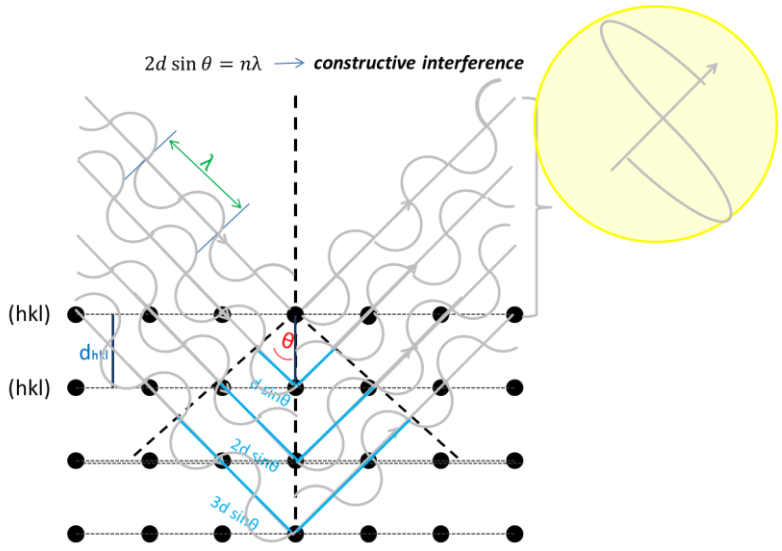

Figure 24 - Constructive interference: If the applied θ is changed, the optical pass difference will be an integral multiple (n) of λ. The consequence is constructive interference yielding a sharp reflex in the diffractogram at 2 θ. The graphic shows that a right triangle can be placed on the optical axis with the hypotenuse x d [distance between 2 parallel lattice planes (hkl)). x is the number of the repeated lattice plane (hkl). The opposite arm of the angle θ is equivalent to half of the total optical pass difference (as the reflected wave has to pass the same difference again). Thus, it is possible to use the sinus rule for determination of d (Bragg equation - see text).

2.1.5.2. *Size estimation by XRPD*

The statistical distribution of crystal-plane arrangements relative to the applied X-ray beams in combination with small crystals (smaller than app. 100 nm) with a low number of lattice planes leads to diffuse transitions from destructive to constructive interferences. The consequence is that diffraction peaks occur, which are broadened inversely dependent on the crystal size. By the use of this phenomenon, which was described by Paul Scherrer - a Suisse physicist - it is possible to calculate the mean size of single crystals. Therefore, it is necessary to measure the half width (β_m) of a reflex and calculate the mean diameter of a crystal with the help of the Scherrer equation:

$$d_k = \frac{k \cdot \lambda}{\beta_m \cdot \cos\theta}$$ **Formula 7**

d_k	mean diameter of a single crystal
k:	form factor ($k = 1$ in case of sqheric single csystals
λ	wavelength of the applied radiation
β_m	half width of a reflex
Θ	angle of the applied wavelength in radian measure

The minimum crystal size that is necessary to perform XRPD is about 2-3 nm as there have to be sufficient numbers of lattice planes to yield constructive interferences [185, 186].

2.1.6. Dynamic light scattering (DLS)

Nanoparticular colloidal disperse systems consist of particles in the nanometer range (< 100 nm) dispersed in a liquid medium - water in case of iron complex formulations for the parenteral administration. The particles are not classically dissolved in the medium, as they do not dissociate into molecules forming a molecular disperse system. In case of a colloids, the disperse phase is in the solid state forming a suspension in which the particles underlie Brownian motion.
Brownian motion is random and the consequence of the collision between the particles and dissolved molecules and atoms. The Brownian motion is faster in case of small particles than in case of larger particles as smaller particles have a lower mass than larger particles with the same composition and the velocity after a collision of two bodies is dependent on their mass and velocity before the collision (conservation of momentum).

Colloidal systems depict Rayleigh ($d < \lambda/10$) and Mie ($d \approx 2$ to $10 \bullet \lambda$) scattering: If particles are illuminated with light that has a great wavelength in comparison to the illuminated particles ($d < \lambda/10$), the light is scattered elastically in all directions. Samples investigated within this work are with an applied wavelength of 633 nm and particle sizes below 100 nm at the range of Rayleigh scattering. The scattered light of different particles interferes. The interferences lead to small fluctuations in the intensity of the scattered light determined by the Brownian

movement if coherent monochromatic laser light is used. This is the principle of dynamic light scattering (DLS), also called photon correlation spectroscopy (PCS).
The fluctuation of scattered light's intensity is correlated with the time yielding the diffusion coefficient, which is dependent on the hydrodynamic particle diameter (d_H) described by the Stokes-Einstein equation:

$$d_H = \frac{k_b \cdot T}{3 \cdot \pi \cdot \eta \cdot D}$$ **Formula 8**

k_B	Boltzmann constant
T	Absolute temperature
η	Viscosity of the solvent
D	Diffusion coefficient

Hydrodynamic diameter

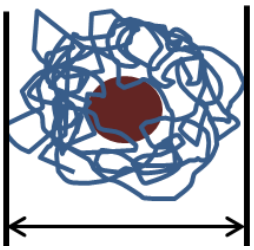

Figure 25 - DLS determines the hydrodynamic diameter of a sphere having the same diffusion properties as the NP.

Via DLS, the hydrodynamic diameter is determined. The hydrodynamic diameter is the equivalent diameter of a sphere having the same diffusion properties as particles of the investigated sample. In case of a iron nanoparticle (FeNP) surrounded by a carbohydrate shell, the whole particle's diameter is observed in the dispersion medium (**Figure 25**).
The raw data of size measurements received by DLS reflect the scattering intensities from particle classes. This is the consequence of the calculation of the diffusion coefficient by measuring the intensity fluctuation of an applied and scattered laser beam across microsecond time scales. The intensity distribution is weighted in respect to the scattering intensity of each particle, which is proportional to the square of the molecular weight and thus $I \sim d^6$ for spherical objects. The consequence is that a small amount of large particles can dominate the intensity distribution. For this reason, the method is very sensitive to larger particles. The Rayleigh approximation gives the correlation of scattered light intensity (I) to the diameter (d) of a particle with $I \sim d^6$ and $I \sim 1/\lambda^4$ (λ = laser wavelength).
The volume of a particle (V) is dependent on its diameter with $V \sim d^3$. For that reason the diameters obtained by intensity distribution (d_I), volume distribution (d_V) and number distribution (d_N) behave like (d_I) > (d_V) > (d_N) under assumption of spherical shapes particles (**Figure 26**). Different shaped particles like needles, hollow spheres and plates show divergent scattering behavior.

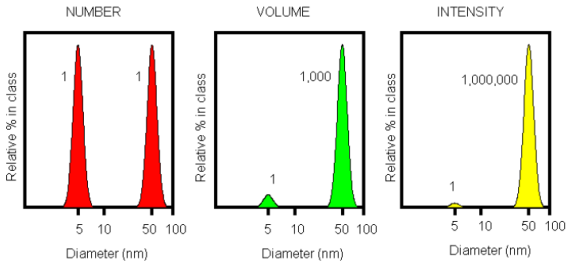

Figure 26 - Number, volume and intensity distribution of an equimolar mixture of two kinds of spherical, massive (not hollow) particles with 10-fold difference in size. Figure taken from[187].

The intensity distribution is the most secure interpretation as they do not include assumption of the particle shape and it is the raw data without the influence of the sample refractive index (RI) as long as the polydispersity index (PDI) is small enough. It is therefore used in case of quality control purposes to characterize the particles. The PDI gives information about the width of size distribution and is in this case not equivalent to the IUPAC defined dispersity which is calculated by the ratio of $\bar{M}_w/\bar{M}_N$ (with: $\bar{M}_w =$ mass-average molar mass; $\bar{M}_N =$ number average molecular mass) [188].
The PDI in case of DLS analysis is derived by cumulant analysis of the DLS measured intensity autocorrelation function, described in ISO 13321, and can be defined as relative variance.
In case of a monomodal distribution (PDI < 0.1), spherical particles, and the correct dispersant, the Z-average, which is intensity mean, gives a result comparable to other techniques. If these requirements are not fulfilled the Z-average is good for comparing samples among each other but does not reflect real size relations. In case of broader distributions (PDI > 0.5), Z-average is not useful anymore. In those cases, the application of the RI (when the particles are larger than 100-200 µm) and the transformation to volume or number weighted size distributions is possible to achieve a more realistic peak shape and mean size. In case of particles smaller than 100 nm, the RI does not have an influence on volume or number weighted distributions [189] and the RI of the particle is mostly unknown [190].

The PDI gives the following information:

PDI < 0.05	→	very narrow dispersion
0.05 < PDI < 0.15	→	narrow dispersion
0.15 < PDI < 0.25	→	wide dispersion
0.25 < PDI < 0.5	→	very wide dispersion
PDI > 0.5	→	polydisperse system (Z-average not reasonably suitable)

2.1.7. Zeta (ζ)-Potential

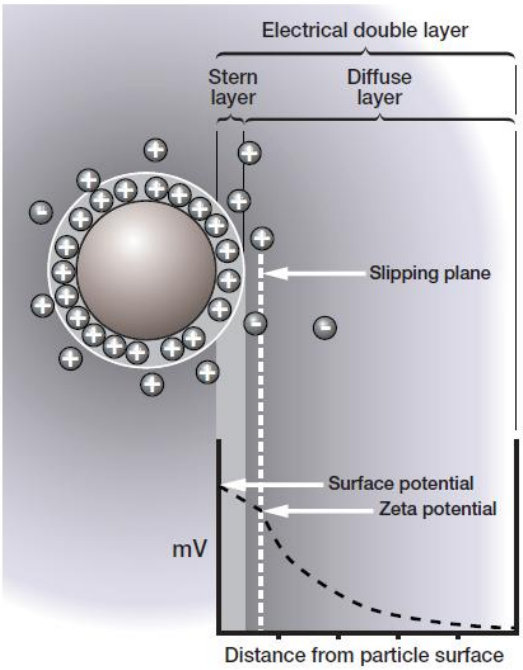

Figure 27 - Model of the Zeta (ζ)-potential from [189]

The Zeta (ζ)-potential describes the electrostatic interaction between a charged particle and the liquid in which it is dissolved, dispersed, or suspended. In case of disperse systems like suspensions or emulsions, the magnitude of the ζ-potential is an indicator of the stability of a colloidal system: If the ζ-potential is smaller than -30 mV or larger than +30 mV the stability is considered as high. This is due to electrostatic repulsions of higher charged particles and consequently less tendency of agglomeration. This plays an important role in case of lyophobic disperse phases where the binding between two particles is thermodynamically favored in comparison to the solvated form (e.g. emulsions where the lipophilic and the aqueous phase can be divided by coalescence or suspensions where a badly re-suspendable cake can be formed by agglomeration).
In case of nano-suspensions with a hydrophilic carbohydrate shell, the tendency of agglomeration is low. The ζ-potential consequently does not indicate stability in this context.

Particles can carry a charge dependent on their chemical composition. When charged particles are diluted in a solvent, which contains ions - either anions (negatively charged) or cations (positively charged) - contrary charged ions are adsorbed on the surface by Coulomb interaction. Contrary charged particles are strongly bound directly to the surface of the particle as the electrostatic force is influenced by the square of the distance between two charge carriers (Coulomb law). This inner region of strongly bound ions to the surface is called Stern layer. With rising distance from the surface, the electrostatic force on the ions decreases. This is determined by increasing the distance and compensation of the particle's charge by the contrarily charged ions. Ions are in consequence less firmly bound forming a diffuse layer. The consequence of this is an electrostatic double layer. While the ions inside the boundary of the Stern layer are carried with the particle when it is moving (e.g. by gravity), the less firmly bound ions beyond the boundary do not travel with the particle. This boundary is called surface of hydrodynamic shear or slipping plane and the potential at this boundary is the ζ-potential (**Figure 27**).

If an electrical field is applied to a dispersion of a charged particle with a ζ-potential, it is attracted by the opposite charge of the electrical field yielding a targeted movement. The velocity of particles (electrophoretic mobility) is dependent on the strength of the electrical

field, the ζ-potential, the viscosity and the dielectric constant of the medium. The Henry equation (*Formula 9*) can thus be used to calculate the ζ-potential from a measured electrophoretic mobility:

$$U_E = \frac{2 \cdot \varepsilon \cdot z \cdot f(k_a)}{3 \cdot \eta}$$ **Formula 9**

z : ζ-potential

U_E : Electrophoretic mobility

ε : Dielectric constant of the medium

η : Viscosity of the medium

$f(k_a)$: Henry's function (ratio between the particle radius to the thickness of the Stern layer)

Henry's function describes the ratio between the particle radius and the thickness of the electrical double layer (Stern layer) and is dependent on the dispersant and the kind of investigated particles. In an aqueous medium with moderate electrolyte concentration and particles larger than 0.2 µm the value is 1.5 and is referred to as Smoluchowski approximation. In case of small particles - as in this case -, low dielectric constant media or generally in non-aqueous media the Huckel approximation with 1.0 as Henry's function is used.

The electrophoretic mobility of the particle is measured by comparing a scattered beam with a reference beam yielding fluctuations of intensity. The rate of fluctuation is proportional to the velocity of the particle. This technique is the Laser Doppler Velocimetry (LDV) (**Figure 28**). The composition as well as the pH of the liquid are from elemental relevance for the ζ-potential. Thus the ζ-potential is an indicator for the charge of a particle and can be used for comparative characterization if the composition and pH of the dispersant used is considered.

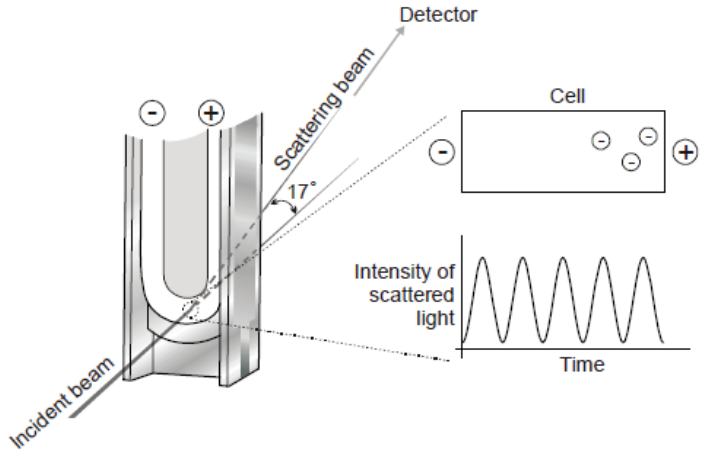

Figure 28 - Laser Doppler Velocimetry (LDV) technique for the determination of the electrophoretic mobility of a particle. From [189]

2.1.8. FerroZine® method

FerroZine® (3-(2-Pyridyl)-5,6-di(2-furyl)-1,2,4-triazine-5',5''-mono sodium salt) is an organic color reagent sensitive for copper (Cu^{2+}) and ferrous iron (Fe^{2+}) but not ferric iron (Fe^{3+}). Fe^{3+} has to be reduced to Fe^{2+} for that reason. Hem-iron is not detected by this method. FerroZine® (Fz) is very well water soluble and highly sensitive to iron and thus used in the determination of serum iron. It has been applied in many automated analyzers (e.g. Roche/Hitachi 912/917/MODULAR P/MODULARD). The complex between Fz and ferrous iron (**Figure 29**) is completely formed in aqueous solution at pH levels between 4 and 9 with a molar absorbance of 27900-28600 $cm^{-1}mol^{-1}$ at a wavelength of 562 nm dependent on the pH conditions. The Beer-Lambert law is followed to a concentration of 10 mg/l Fe at 1 mm path length. The Fz:Fe ratio in the complex is 3:1. The period of color reaction is given with 5 minutes between 10 and 45°C with an accuracy of ±2 % [191].

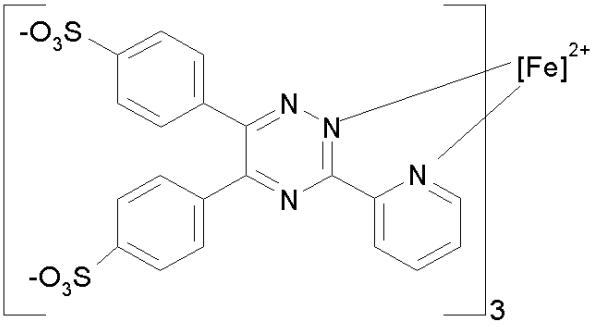

Figure 29 - FerroZine® complex with ferrous iron (λ_{Max}=562nm)

The test kid is used in this assay consists of two reagents. R 1 contains 200 mM citric acid for acidification of the sample and 115 mM thiourea, which builds a complex with copper and thus avoids disruption of the measurement by high serum copper levels. R 2 contains 150 mM sodium ascorbate as reductive agent for ferric iron and 6mM Fz. The method can be performed in presence of serum proteins. At acidic pH levels, ferric iron is liberated from transferrin and reduced to ferrous iron by ascorbate. Fz and ferrous iron build a violet-colored complex with color intensity proportional to Fe concentration. The recovery is ±10 % from the initial value. The measurement range is 0.9-179 µmol/L. The repetition accuracy is given with 1.2 % for human serum [192, 193].

2.2. Physicochemical characterization

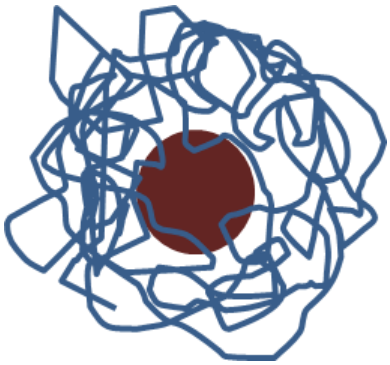

Figure 30 - Core-shell-model of the iron complex formulation
The inorganic iron oxy hydroxide/hydroxide is surrounded by an organic carbohydrate making the complex hydrophilic and water "soluble" and preventing the complexes from agglomeration.

The parenteral iron complex formulations are from a pharmaceutical point of view disperse systems with an aqueous dispersion medium and a nanoparticular disperse / colloidal phase. As consequence of the size in the nm range, with sizes below 100 nm, these complex formulations, and aqueous dilutions of it, are colloidal disperse systems. They consist of the solid nanoparticle (NP), underlying Brownian motion and showing the Tyndall effect - depending on the wavelength of the applied radiation.

These NPs are seen as an inorganic iron core consisting of iron oxide or iron oxy hydroxide (FeOOH) surrounded by one or more kinds of carbohydrate as an organic fraction of the complex. The carbohydrate fraction makes the complex hydrophilic and "soluble" in water. The core-shell-model is used to describe this kind of shape (**Figure 30, see 1.4.1**) [98, 99, 194].

2.2.1. Size determination

The size estimation on nano-scale parenterals is required for assuring medical safety (embolic risk) and for pharmaceutical analysis. The first characteristic coming to mind in describing a NP is the size of the complex. As the NPs are consisting of an inorganic phase of iron oxide or FeOOH (core) which is surrounded by one or more carbohydrates the diameter can be distinguished in the diameter of the core and the diameter of the whole particle (hydrodynamic diameter) (**Figure 31**).

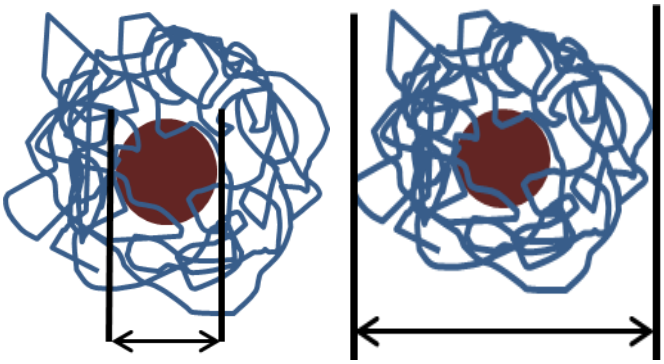

Figure 31 - Model of a particle with inorganic iron core (brown) and organic carbohydrate surrounding the core (blue). Difference between the diameter of the core (left) and the diameter of the whole particle (hydrodynamic diameter, right).

Information about the size of the core and its structure makes it possible to estimate the loading of a single particle with a specific mean diameter. Additionally it is possible to calculate the surface of one particle - which increases with higher diameter - but also the surface of all particles (inversely proportional to size) which is theoretically directly proportional to the dissolution rate as indicator for the complex stability. The Noyes-Whitney law in the modification by Nernst and Brunner (*Formula 10*) gives the dissolution rate (dm/dt) in dependency on the diffusion coefficient (D), the surface of the solid compound (A), the thickness of the diffusion layer (h), and the difference between the concentration of a saturated solution (C_S) and the concentration at a given point of time (C_t):

$$\frac{dm}{dt} = \frac{D \cdot A}{h}(C_s - C_t) \qquad \textbf{Formula 10}$$

In case of very small particles like NPs, another impact factor also influences the dissolution rate. Contrary to large particles for which the saturation concentration (C_S) is independent from size, it increases in case of small particles (< 2µm). This phenomenon is caused by an increased solution pressure (p) in consequence of an increasing radius of curvature. The solution pressure is inversely dependent on the particles radius (r) and directly proportional to the interface tension (solid-liquid; γ) expressed in the LaPlace equation:

$$\Delta p = \frac{2\gamma}{r} \qquad \textbf{Formula 11}$$

This is assumed in the Ostwald-Freundlich equation (C_S/C_{S_0}: ratio of the saturation concentration of very small (Cs) and very big (C_{S_0}) particles; R: general gas constant; T: absolute Temperature; V: molar Volume (Mw/density)) :

$$\frac{C_S}{C_{S_0}} = \exp\left((2 \cdot \gamma \cdot V)/(R \cdot T \cdot r)\right) \qquad \textbf{Formula 12}$$

Hence, C_S/C_{S_0} increases exponentially with decreasing size, which thus increases the dissolution rate in accordance with the Noyes-Whitney equation. Consequently small nanoparticles will show increased dissolution rates which potentially leads to lower stability under certain physiological or *in-vitro* conditions.

2.2.1.1. *Size of the core by TEM*

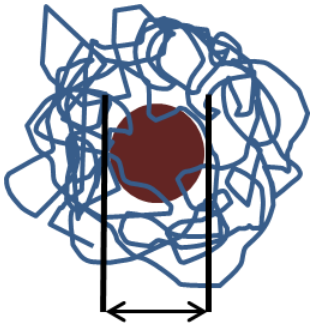

Figure 32 - Model of an iron nanoparticle with a carbohydrate fraction surrounding the inorganic FeOOH core with high electron density.

A precondition for TEM on the investigated material is as described in the background section (2.1.1) a high electron density. Elements with high atomic numbers fulfill this requirement.
Minerals like iron oxide or FeOOH have a sufficiently high electron density to be investigated by electron microscopy. The investigated complexes consist as previously described of an iron oxide or FeOOH core being surrounded / complexed by a carbohydrate. The electron density of the organic compound has in difference to the inorganic fraction a much lower electron density resulting in a inferior ability of being imaged by electron radiation.

At BF detection approach this leads to images where the inorganic core (phase) is dark/black (as most electrons are scattered, absorbed or reflected) and the surrounding carbohydrate is diffuse but notable brighter (as most of the electrons pass the atoms with lower electron density without being reflected). Consequently, the iron core can be visually separated and measured in the image. The diameter of the cores can be spherical but may also have the form of a needle or an oblong form. The equivalent spherical diameter of the core is determined by measuring the diameter at the shortest (d_s) and the largest dimension (d_l) and calculating the geometric diameter by Formula 13:

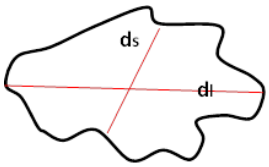

$$d_g = \sqrt{\frac{(d_s{}^2 + d_l{}^2)}{2}}$$ **Formula 13**

Materials

Iron complex drugs:

- Sodium ferric gluconate sucrose (**FeG**, Ferrlecit®, 12.5 mg Fe/mL in 3.2 mL ampoules; Sanofi-Aventis, Frankfurt, Germany)
- Iron (**Fe**) **s**ucrose (**FeSuc**, Venofer®, 20 mg Fe/mL in 5 mL ampoules; Vifor, Munich, Germany)
- **L**ow molecular weight **Fe d**extran (**LFeD**; CosmoFer®, 50 mg Fe/mL in 2 mL ampoules; Teva, Radebeul, Germany)
- **L**ow molecular weight **Fe d**extran (**LFeD;** Infed®, 50 mg Fe/mL in 2 mL vials; Watson, Morristown, NJ, USA)
- **Fe i**so**m**altoside 1000 (**FeIM**; Monofer®, 100 mg Fe/mL in vials; Pharmacosmos, Holbaek, Denmark))
- **H**igh molecular weight **Fe d**extran (**HFeD**; Dexferrum® 50mg Fe/mL in 2 mL vials; American Regent, Shirley, NY, USA)

- **H**igh molecular weight (See size results discussion **0**; p. **75**) **Fe d**extran, **g**eneric (**HFeD_G**; Ironate® 50mg Fe/mL in 2 mL vials; HELP SA, Metamorfosi, Attika, Greece)
- **Fe c**arboxy**m**altose (**FeCM**; Ferinject®, 50 mg Fe/mL in 2 mL vials; Vifor, Munich, Germany)
- **Fe**rumoxytol/ **p**olyglucose-**s**orbitol-**c**arboxymethylether iron oxide (**FePSC;** Feraheme®, 30 mg Fe/mL, in 17 mL vials; AMAG Pharmaceuticals, Cambridge, MA, USA)
-

Method

The dimension of the iron complex nanoparticle core was determined with an EM420 transmission electron microscope (FEI/ Philips, Oregon, USA) at 120 kV. All preparations (1 mg Fe/mL, double-distilled water) were deposited onto a hydrophilized copper grid (300 mesh, Ø 3 mm) and were allowed to dry under vacuum for at least 24 h. The median of the geometrical diameter was determined from at least 50 single particles (n = 50) (*Formula 13*). Measurement of d_s and d_l were performed with Adobe Photoshop CS5 Extended vs. 12.0 x32 (Adobe Systems Incorporated; CA, USA).

2.2.1.2. *Size of single nanocrystals by XRPD*

Diffractograms gained from XRPD (**2.2.3.1**) were used to estimate the mean size of single nanocrystals. The reflexes at an angle of about 36°2Θ were used in case of all XRPD diffractograms to measure half width of the peaks after smoothing to a gauss like curve. **Figure 33** demonstrates the procedure to yield the information for calculating the mean diameter of single nanocrystals corresponding to the Scherrer equation (**2.1.5.2**).

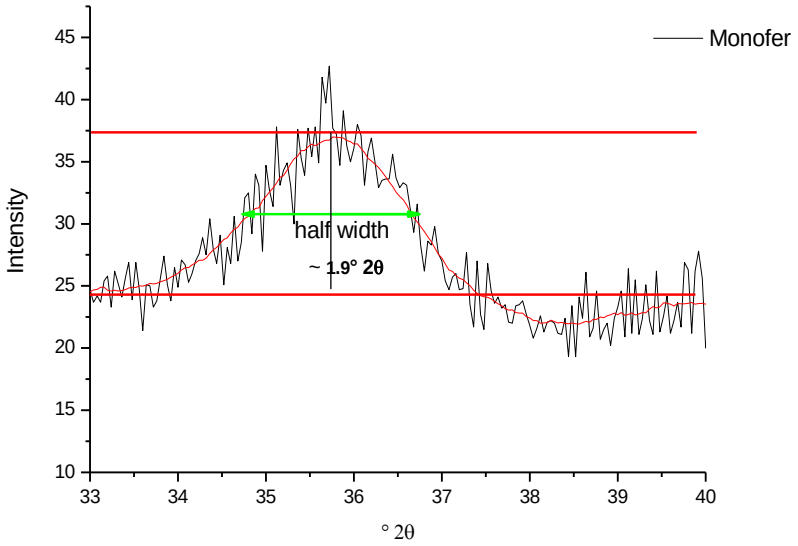

Figure 33 - XRPD reflex at 35.72° 2Θ of FeIM (Monofer®). The smoothed peak (Gauss fit) is measured for its half width β_m [1.9°x π/180°rad] at the peak position 35.72° 2Θ. The applied Cu Kα radiation had a wavelength of λ = 0.154178 nm yielding a mean diameter of single nanocrystals of about 5.7 nm. As it can be seen in mean single nanocrystal size is imprecise and is thus taken as an estimated value and indicator for the mean core the figure, the correlation between the peak and the fitted curve is not good with the consequence that the value for the size.

The **Figure 33** gives additional information about the structure the particle (iron isomaltosid in this case) and can be seen exemplarily for all the other investigated samples:
The diffuse peak with high basic scattering intensity is the consequence of high fractions of amorphous material in the sample. The single nancrystals are very small and have a big surface area. The complexing carbohydrate interacts with this surface area and builds up amorphous iron on that surface. This makes it difficult to receive valid size information from those nanoparticular complex formulations.

2.2.1.3. *Diameter of the whole particle by Dynamic light scattering (DLS)*

Materials

Iron complex drugs:

- Sodium ferric gluconate sucrose (**FeG**, Ferrlecit®, 12.5 mg Fe/mL in 3.2 mL ampoules; Sanofi-Aventis, Frankfurt, Germany)
- Iron (**Fe**) **suc**rose (**FeSuc**, Venofer®, 20 mg Fe/mL in 5 mL ampoules; Vifor, Munich, Germany)
- **L**ow molecular weight **Fe d**extran (**LFeD**; CosmoFer®, 50 mg Fe/mL in 2 mL ampoules; Teva, Radesbeul, Germany)
- **L**ow molecular weight **Fe d**extran (**LFeD;** Infed®, 50 mg Fe/mL in 2 mL vials; Watson, Morristown, NJ, USA)
- **Fe i**so**m**altoside 1000 (**FeIM**; Monofer®, 100 mg Fe/mL in vials; Pharmacosmos, Holbaek, Denmark))
- **H**igh molecular weight **Fe d**extran (**HFeD**; Dexferrum® 50mg Fe/mL in 2mL vials; American Regent, Shirley, NY, USA)
- **H**igh molecular weight **Fe d**extran, **g**eneric (**HFeD_G**; Ironate® 50mg Fe/mL in 2mL vials; HELP SA, Metamorfosi, Attika, Greece)
- **Fe c**arboxy**m**altose (**FeCM**; Ferinject®, 50 mg Fe/mL in 2 mL vials; Vifor, Munich, Germany)
- **Fe**rumoxytol/ **p**olyglucose-**s**orbitol-**c**arboxymethylether iron oxide (**FePSC;** Feraheme®, 30 mg Fe/mL, in 17 mL vials; AMAG Pharmaceuticals, Cambridge, MA, USA)
- **Fe h**ydroxy**e**thyl **s**tarch (**FeHES**, Feramyl®, 50mg Fe/ml in 2ml ampoules, clinical material, Serumwerk Bernburg AG, Bernburg, Germany)

Method

The size distribution of the whole particle - which consists of an iron oxy hydroxide core plus carbohydrate shell - was determined by DLS. The method is based on the theory described in section **2.1.6**. The diluted samples (0.4 mg Fe/mL double-distilled and sterile filtered water (0,2 µm cellulose acetate filter)) were measured, using a Zetasizer Nano ZS (Malvern Instruments Ltd; Worcestershire, UK), including a He-Ne Laser with a wavelength of λ=633 nm. The samples were illuminated and the scattering information was detected at an angle of 173° (Non-invasive back-scatter technology) after 30 seconds equilibration time and at a temper-

ature of 22 °C. The data were analyzed with the firmware, Zetasizer Software DTSv620 yielding size distribution data. Measurement settings were:
- Duration: automatic
- Number of measurements: 3
- Position method: seek for optimum position
- Automatic attenuation selection.

For the data evaluation, spherical particles were assumed, where the scaling of the intensity raw data (PSDI) to volume related data (PSDV) follows a $1/r^3$ law.

2.2.2. ζ-Potential as an indicator for the surface charge

Materials

Iron compounds: See section **2.2.1.3**

Method

The method is based on the background described in section **2.1.7.** ζ-Potential of diluted samples (0.4 mg Fe/mL double-distilled and sterile filtered water (0,2 µm cellulose acetate filter)) was measured in disposable folded capillary cells (DTS 1060, Malvern Instruments Ltd; Worcestershire, UK) with the Zetasizer Nano S (Malvern Instruments Ltd; Worcestershire, UK). In case of pH adjustment 0.1 N HCl or NaOH was added, respectively. The data were analyzed with the firmware Zetasizer Software DTS vs. 620. The Huckel approximation with 1.0 as Henry's function was used as all the investigated compounds contain NP smaller than 200 nm (see section **2.1.7.** for details). The further settings of the device were:

Dispersant Name:	Water
Dispersant RI:	1.330
Viscosity (cP)	0.8872
Dispersant Dielectric Constant	78.5
Measurement duration:	Automatic (Minimum 50; Maximum 120)
Measurement Position [mm]	2.00
Attenuator:	Automatic
Temperature:	25°C; 30 seconds equilibration
Voltage:	Automatic
F(Ka) selection	1.0 (Huckel)

2.2.3. Structure of the inorganic iron phase

One factor determining the stability of the complex is the structure of the iron oxide or FeOOH phase in the formulation. In nature, there are several iron oxide and oxy hydroxide structures with different thermodynamic stabilities. Structures with lower thermodynamic stability may dissolve more rapidly and consequently be more toxic depending on the doses administered. The complexes that include modifications with high stability may on the other hand lead to slow degradation with a potential low bioavailability of the complexed iron.

General materials

Omnifix® syringe 2 ml	B. Braun Melsungen AG, Melsungen, (Germany)
Reaction tubes, polypropylene, 1.5 ml	Greiner-Bio-One, Kremsmünster (Austria)
Sterican® cannulas, 20 Gx1½ "	B. Braun Melsungen AG, Melsungen, (Germany)
Tubes with screw cap, polypropylene 10 & 50 ml	Greiner-Bio-One, Kremsmünster (Austria)
Syringe filters, cellulose acetate, 0.2 µm, Ø 25 mm	VWR International Radnor (USA)

2.2.3.1. *X-ray powder diffraction (XRPD)*

Materials

Iron compounds: See section **2.2.1.1**

Method

The formulations were allowed to dry at room temperature for 24 h, or at 30 °C in a drying chamber (Ecocell 55; MMM Group GmbH, Planegg, Germany) for 72 h in case of the non-pulverized Ferrlecit® and Venofer® samples. Subsequently the dried samples were pulverized in an agate mortar. By preparing the sample in this manner, a statistical distribution of crystalline particles without texture effects in or on the surface of the dried sample was achieved. Additionally, for Ferrlecit® and Venofer® the dried sample at 30°C was not pulverized in order to emphasize the iron oxy hydroxide signal at the expense of the sucrose signal in XRPD. X-ray powder diffraction (XRPD) was carried out at the Institute for Geoscience in Mainz with a XRD 3000 TT (Seifert, Ahrensburg, Germany) using Cu Kα radiation (λ = 0.154178 nm, 40 kV, 30 mA) in Bragg-Brentano configuration (automatic divergence slit, irradiated sample width: 10mm; specified measuring range: 5-65° 2θ; angular rate 0.04° 2θ, measuring time 10 s/step). Measured angles (θ) can be converted to the d-distance (d) by the Bragg equation (*Formula 6***;** section **2.1.5**):

$$d = \frac{0.154178\ nm}{2 \sin \theta}$$

The diffractograms were compared with diffraction data of standard iron oxide and oxy hydroxide phases from the ICDD (International Centre for Diffraction Data) using software version 2.16 (ICDD, Newstown Square; PA; USA).

2.2.3.2. *Electron diffraction (ED)*

Materials

Iron compounds: See section **2.2.1.1**

Method

Dilutions were prepared with double distilled water with a concentration of 1 mg Fe/mL and a drop of it was placed on hydophilized (plasma cleaner) copper grids coated with amorphous carbon. The grids were immediately put in a vacuum chamber, dried overnight and analyzed the following day. Transmission Electron Microscopy (TEM) measurements were carried out with a FEI TECNAI F30 S-TWIN transmission electron microscope (FEI, Hillsboro, Oregon, USA) equipped with field emission gun and working at 300 kV. Selected Area Electron Diffraction (SAED) patterns were collected with a 40 µm aperture allowing the collection of diffraction rings obtained by the simultaneous diffraction of thousands of nanocrystals. Scanning Transmission Electron Microscopy (STEM) images and Nano Electron Diffraction (NED) patterns were collected with a mild illumination setting. STEM images were obtained by a FISCHIONE High Angular Annular Dark Field (HAADF) detector (E.A. Fischione Instruments, Export, PA, USA) and acquired by Emispec ESVision software (Emispec Systems Inc., Tempe, AZ, USA). NED was performed employing a 50 nm beam and a semi-parallel illumination of the sample, allowing diffraction patterns from single nanocrystals. SAED and NED patterns were taken with a Charge-Coupled Device (CCD) camera (14-bit GATAN 794MSC, 1024×1024 pixels) and acquired by Gatan Digital Micrograph software (Gatan Inc., Pleasanton, CA, USA). Elemental analysis was done by Energy-Dispersive X-ray (EDX) spectroscopy and quantified by Emispec ES Vision software. Crystallographic projections for each sample were calculated based on known iron oxide/oxy hydroxide structures using standard transformations [195].

2.3. Pharmacological safety

2.3.1. FerroZine®-assay for the detection of labile iron

2.3.1.1. *Reagents, Materials and Devices*

Reagents

Iron reaction kit "IRON2": - (R1, 6x64 ml; R2, 6x16 ml, Roche/Hitachi Cobas Integra®, Ref. No.: 03 183 696 122; Roche Diagnostics GmbH, Mannheim, Germany)

R 1: - Citric acid: 200 mMol; thiourea: 115 mMol; detergent

R 2: - Sodium ascorbate: 150 mMol; FerroZine®: 6 mMol; preservative

Materials

Iron compounds: See section **2.2.1.3**

General materials:

Human srum, pooled, off the clot (C-37548) Batch No.:07372174	PromoCell GmbH, Heidelberg (Germany)
Iron atomic absoption spectrometry standard 1000 µg/ml in 2% HNO_3	Sigma Aldrich
Omnifix® syringes 2 ml	B. Braun Melsungen AG, Melsungen, (Germany)
Reaction tubes, polypropylene, 1.5 ml	Greiner-Bio-One, Kremsmünster (Austria)
Sterican® cannulas, 20 Gx1½ "	B. Braun Melsungen AG, Melsungen, (Germany)
Tubes with screw cap, polypropylene 10 & 50 ml	Greiner-Bio-One, Kremsmünster (Austria)
Disposable semi-micro cuvettes (1.6 ml), polystyrene	Carl Roth GmbH & Co KG, Karlsruhe (Germany)
Parafilm® M	Carl Roth GmbH & Co KG, Karlsruhe (Germany)

Method

The Method was performed based on the FerroZine® method described in **2.1.8**.

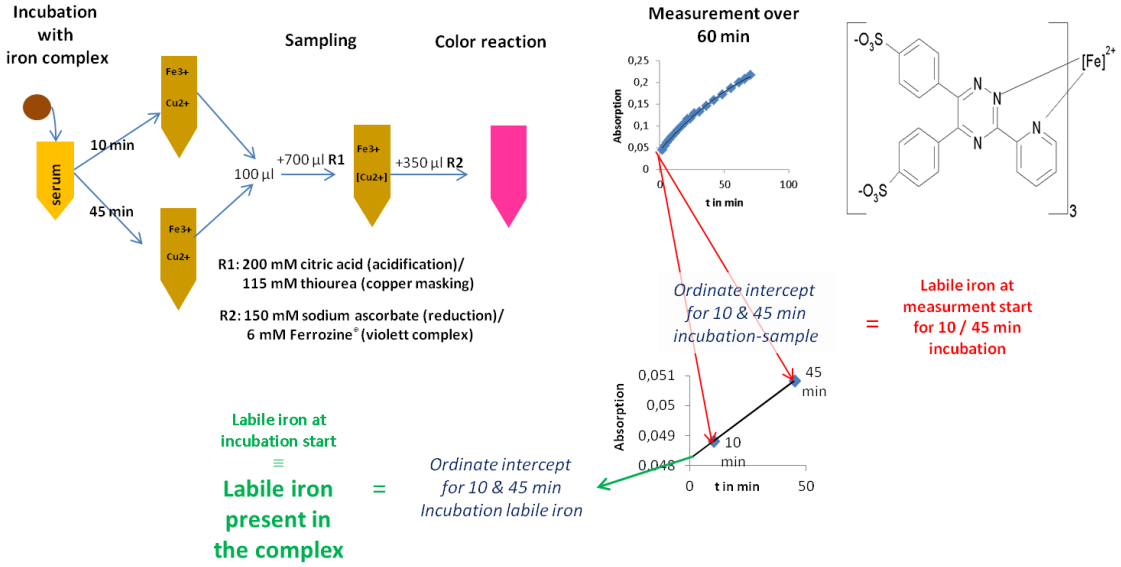

Figure 34 - Schema of the FerroZine® assay: The starting point is the upper left side:
Incubation with iron complex: Calculated volume of iron complex is added to human serum at room temperature (22 °C) yielding concentrations of 66.7 µg/ml (equivalent to a 200 mg dose) or 166.7 µg/ml (equivalent to a 500 mg dose);
Sampling after 10 and 45 min: 100 µl of incubated serum are sampled and transferred in a disposable semi-micro (1.5 ml) cuvette with provided 700 µl of R1;
Color reaction: 350 µl R2 are subsequently added and the cuvette is closed with Parafilm® avoiding evaporation;
Measurement of absorption at 562 nm wavelength for at least 60 min and fitting of the absorption versus time curve to a second order polynomial with an intercept on the ordinate indicating the labile iron amount in the incubated serum sample at the beginning of the measurement of the sample;
Determination of labile iron in the complex: labile iron amount at the beginning of measurement after 10 and 45 min incubation sample is extrapolated to hypothetical 0 min incubation by linear regression. The obtained intercept with the ordinate in this case gives the labile iron present in the complex at the point of time when the incubation was started.

The schema of the assay is demonstrated in **Figure 34**. R1 and R2 were equilibrated at room temperature app. 2 h prior to starting the assay. Human serum was taken from the freezer at -21 °C to a water bath at 37°C for 1h and stored again for 1h at room temperature allowing equilibrating. A sufficient amount of serum was put (at least 250 µl) in a 1.5 mL reaction tube first to obtain 100 µl sample volumes after 10 and 45 min incubation time each at room temperature, 22°C. The iron complexes were added yielding concentrations of 66.7 µg/mL or 166.7 µg/mL. This is equivalent to doses of 200, or 500 mg Fe in the complexes in case of a person with a body weight of 70 kg. This is a consequence of a blood volume of 0.07 L per kg and a serum fraction of 60 % of the blood volume, yielding a total serum volume of approximately 3 L in this case [196]. Incubation started at the moment of complex addition to serum. After 10 min of incubation, a first 100 µl sample of the serum-iron complex mixture in the reaction tube was transferred into a 1.6 ml semi-micro cuvette already filled with 700 µl of R1. 350 µl of R2 were subsequently added. The cuvette was closed with Parafilm® to avoid excessive evaporation and consequently an absorbtion drift during the measurement. The absorbance of the violet Fz-Fe complex was measured with a UV/Vis spectrometer (PERKIN ELMER Lambda 20; Perkin Elmer Inc, Waltham, MA; USA) at λ_{max}=562 nm for at least 60 to 80

min starting at 5 min after addition of R2. As the first 5 min absorption increase can be related to color reaction, it is helpful to regard only the absorption vs. time from 5 min on. The same procedure was performed with the 100 µl sample after 45 min of incubation. Calibration was performed using Fe standard solution with a concentration of 1000 µg/ml in 2 % nitric acid being diluted with serum to concentrations between 2.51 and 18 µg/ml. The dilutions were treated the same way as the samples. Absorption values of the Fz-Fe complex were taken after 5 min as the main color development was finished 5 min after addition of R2. Absorption vs. concentration was plotted yielding the specific absorption related to an iron solution of 1 µg/ml, which was used to calculate the labile iron from absorption values.

The absorbance vs. time curve was plotted for each incubation time and the resulting curve was fitted to a second-order polynomial. The intercept of the fitted function with the ordinate is equivalent to the amount of labile iron at the start of the UV/Vis measurement after 10 and 45 min incubation. The labile iron at a hypothetical incubation time of t=0 is yielded by linear regression of the ordinate intercepts of the second order polynomial of UV/Vis measurement curves for 10 min and 45 min incubation. This labile iron at hypothetical incubation time t=0 is the labile iron pool present in the pure complex formulation.

2.3.2. FerroZine® reaction kinetics

As described in **2.1.8** the Fz:Fe color complex development needs 5 min at a temperature range between 10 to 45°C. The color reaction is for this reason the rate-determining step in this period of time. The kinetic of color development in human serum over at least 60 min can be theoretically divided into the following steps:

Dissociation:	Liberation of transferrin bound iron
Reduction:	Reduction of ferric ironto ferrous iron
Color reaction:	Binding of ferrous iron to Fz
Liberation:	Acidic (citric acid), reductive (ascorbate) and ligand (Fz & citric acid) mediated dissolution of iron from the NPs

In the first 5 min, steps 1-3 are the rate-determining steps whereas afterwards the liberation from the complex is rate-determining.

The liberation is a direct indicator of the stability of the complex under (a) acid, (b) mild reductive conditions in presence of (c) complexing agents / ligands. The corresponding reaction to the liberation process form the iron phase can be thus formulated as follows [197]:

$$FeOOH + H_3O^+ \rightarrow Fe(OH)_2^+ + H_2O$$
$$FeOOH + 3H_3O^+ + e^- \rightarrow Fe^{2+} + 5H_2O$$
$$FeOOH + nL^- + 3H_3O^+ \rightarrow [FeL_n]^{3-n} + 5H_2O \quad (\text{“L”= ligand})$$

Alternatively, corresponding to that in case of magnetite as iron phase:

$$Fe_3O_4 + 4H_3O^+ \rightarrow 2Fe(OH)_2^+ + Fe^{2+} + 4H_2O$$
$$Fe_3O_4 + 8H_3O^+ + 2e^- \rightarrow 3Fe^{2+} + 12H_2O$$
$$Fe_3O_4 + 2nL^- + 8H_3O^+ \rightarrow 2[FeL_n]^{3-n} + Fe^{2+} + 12H_2O$$

Factors like weak/strong bound iron, diffusion through the carbohydrate fraction and size decrease determine the liberation rate. Hence, the second-order polynomial can be a helpful and very easy model to describe the kinetics. In terms of labile iron quantification, this model was used. As the first 5 min absorption increase can be related to color reaction, it is helpful to regard only the absorption vs. time from 5 min on.
The second-order polynomial is in fact suitable for the determination of the point for t=0 (intercept with ordinate) but not very helpful to describe the liberation kinetics. Thus, the absorption-versus-time curves were investigated in respect of the liberation kinetics. The aim was to observe a mathematical model, making it possible to compare all the complexes for their liberation behavior, and to obtain comparable stability information.

Possible kinetics are [198]:

- Zero order $\boldsymbol{C_t = kt}$ **Formula 14**

- First order $\boldsymbol{-ln\,(1 - \frac{C_t}{C_{max}}) = kt}$ **Formula 15**

- Square root
  - dose dependent
  (Higuchi, 1963) $\boldsymbol{\frac{C_t}{C_{max}} = k \cdot \sqrt{t}}$ **Formula 16**

- Cube root $\boldsymbol{\frac{C_t}{C_{max}} = k \cdot \sqrt[3]{t}}$ **Formula 17**

- RRSWB-equation $\boldsymbol{\log\left(-\ln\left(1 - \frac{C_t}{C_{max}}\right)\right) = b \cdot log(t) - \log a}$ **Formula 18**

t	-	Time
k	-	Constant of liberation from the complex
C_t	-	Concentration of Fz detectable iron
C_{max}	-	Concentration of the complex
b	-	Shape parameter
a	-	Scaling factor

2.4. Biological distribution in turkey embryos

2.4.1. Iron compounds

- Iron (**Fe**) **s**ucrose (**FeSuc**, Venofer®, 20 mg Fe/mL in 5 mL ampoules; Vifor, Munich, Germany)
- **L**ow molecular weight **Fe d**extran (**LFeD**; CosmoFer®, 50 mg Fe/mL in 2 mL ampoules; Teva, Radesbeul, Germany)
- **Fe**rric **c**arboxy**m**altose (**FeCM**; Ferinject®, 50 mg Fe/mL in 2 mL vials; Vifor, Munich, Germany)
- **Fe h**ydroxy**e**thyl **s**tarch (**FeHES**, Feramyl®, 50mg Fe/ml in 2 ml ampoules, clinical material, Serumwerk Bernburg AG, Bernburg, Germany)

2.4.2. Study design

Table 2 - Study design

Aim of the trial	Sub-trial name	Incubation time	Applied complexes	Applied dose	Control	Applied volume	Tissue sampling	Starting date	End date
Influence of complex type	P-FeM1.13	24 h	FeD, FeS, FeCM, FeHES	600 µg	Negative & 0.9% NaCl	60 µl	Liver Heart Kidney	22.01.2013	23.01.2013
	P-FeM2.13	120 h	FeD, FeS, FeCM, FeHES	600 µg	Negative & 0.9% NaCl	60 µl	Liver Heart Kidney	22.01.2013	27.01.2013
	P-FeM3.13	24 h	FeD, FeS, FeCM, FeHES	600 µg	Negative & 0.9% NaCl	60 µl	Liver Heart Kidney Muscle (upper leg)	03.04.2013	04.04.2013
	P-FeM4.13	120 h	FeD, FeS, FeCM, FeHES	600 µg	Negative & 0.9% NaCl	60 µl	Liver Heart Kidney Muscle (upper leg)	03.04.2013	08.04.2013
Influence of different doses	P-FeM5.13	24, 120 h	FeHES	300, 450, 600 µg	Negative	60 µl	Liver Heart Kidney Muscle (upper leg)	24.04.2013	25./29.04.2013

The whole study was divided in 5 sub-trials as time management played an important role and only about 100 eggs were possible to be treated simultaneously (application). A pilot trial was performed to estimate the fraction of the incubated eggs that can be used for intravenous chorioallantoic membrane (CAM) application. Turkey eggs have a hatching period of 28 days. Only those eggs were chosen on day 19 of incubation, that had a CAM with veines - not artery - which had diameters at the range of or larger than the cannula thickness (0.3 mm) to avoid excessive bleeding. 300 eggs were ordered in total to achieve group sizes of at least 7 individual eggs on the day of tissue sampling (day 20 or day 24).

The sub-trials were named P.FeM1 (or 2, 3, 4 and 5).13 (***Table 2***). Sub-trials P.FeM1.13 and P.FeM2.13 as well as P.FeM3.13 and P.FeM4.13 were started on the same day to achieve

incubation times of 24 and 120 h, respectively. ***Table 2*** gives an overview of the study design. To investigate the influence of the application method (*i.v.* administration) on the iron distribution two different control groups were discriminated. There was a negative control group ("Negative") which did not undergo intravenous treatment but was apart from that treated in the same way as the intervention groups before and after treatment. The second control group ("NaCl") was treated with 60 µl pure 0.9 % sodium chloride solution. The sodium chloride solution was also used to dilute the iron complex drugs. The application of pure sodium chloride solution as control group - next to negative control group without *i.v.* treatment - was performed to display the changes in iron levels that could possibly be determined by e.g. blood loss in consequence of *i.v.* application method.
The different complexes were investigated for their distribution in pharmacological and potentially toxicological target tissues (liver) or potential toxicological target tissues (kidney, heart) after incubation times of 24 and 120 h [199]. For cross-comparison between heart and an additional kind of tissue, upper leg muscle was included in sampling after the subtrials P.FeM1.13 and 2.13 had been evaluated. Intervention groups were treated with 600 µg iron containing complex dilutions with a constant volume of 60 µl. The dose was stated with 600 µg, as pretests showed no obvious toxic effects but good iron resonance in the target tissues. P.FeM5.13 was additionally performed to investigate the influence of different doses on iron levels in the tissues.

2.4.3. Procedure

Prearrangements

Turkey eggs with pointed end to the top in an egg carton

Turkey eggs were purchased from a hatchery (Heidemark Mästerkreis GmbH & Co. KG, Großenkneten, Germany), checked for damages by candling, weighted and numbered after receipt. Eggs lighter or heavier than 10 % of the average weight, as well as those with damages were excluded. Eggs were stored in a cold storage room over 4 °C until the trial started.
Turkey eggs have a total hatching period of 28 days.

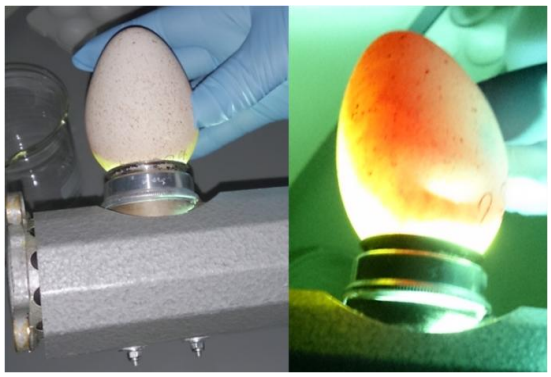

Checking for vitality on day 11 with a candling lamp

On hatching day 0 the eggs were stored for about 2 h at room temperature prior to storing on hordes in an incubator (Ehret BSS 300 or 420, Grumbach Brutgeräte GmbH, Asslar, Germany) at 37.5 °C and 65 % humidity. The eggs were turned-over 4 times a day and the room in which the incubator was located was darkened until the end of the trial.

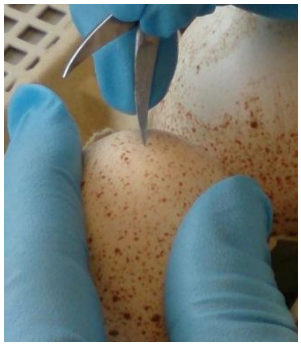

Piercing of the egg with a pair of scissors at the pointed end.

On day 11 the eggs were checked for vitality with a candling lamp (universal candling lamp Blohm 770, BruJa, Untertuttwil, Switzerland). Vital eggs were then placed with the pointed end upside into an egg carton, disinfected with a swab soaked with 70 % (V/V) ethanol and pierced with a pointed pair of scissors app. 5 mm deep into the top of the egg.

This was repeated by turning the blades 90° receiving a "x"-formed small whole which was closed with adhesive tape (Leukosilk®) immediately. Afterwards the eggs were placed in the incubator again but were no longer turned-over enabling the air pocket to move from the blunt end of the egg to the pointed end of the egg between the chorioallantoic membrane (CAM) and the inner eggshell.

Application

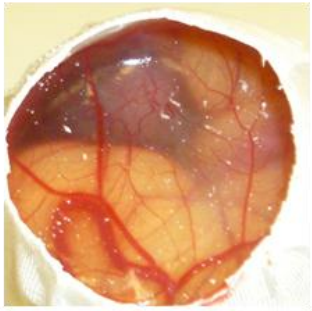

Look on the CAM with suitable blood vessels for iv-injection.

On day 19, the eggs were taken from the incubator in small groups and opened with a pair of scissors at the top of the egg by piercing through the taped “x”-formed whole. The whole was carefully widened subsequently until it was large enough to examine whether the CAM contained suitable blood vessels for injection.

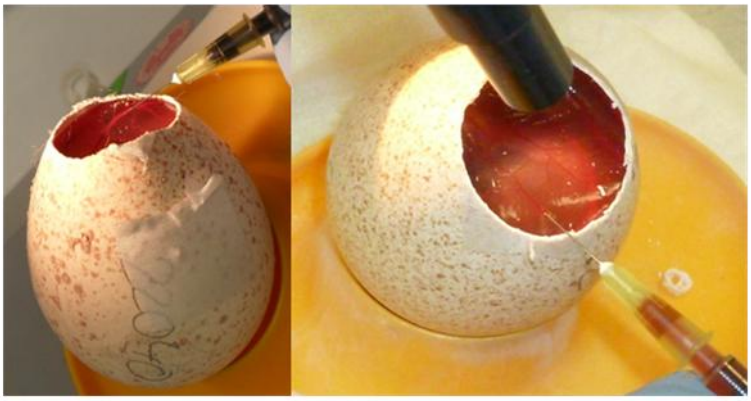

Injection of 60 µl complex-dilution in 0.9% sodium chloride solution containing 600 µg iron Suitable blood vessels were chosen circumventing excessive blood loss.

If the egg was not suitable for injection it was accurately closed with a glass and adhesive tape and used as negative control or abandoned by closing with adhesive tape and freezing at -20 °C, alternatively.

60 µl of complex-dilutions in 0.9 % sodium chloride (B. BRAUN MELSUNGEN AG, Melsungen, Germany) containing 600 µg of iron complex were applied. In case of FeHES, additional doses of 300 µg and 450 µg iron were administered. Dilutions were prepared immediately before application in autoclaved vials and filled in 1 ml syringe (cannula 30 G, 0.3 x 12 mm) without bubbles of air.

Egg after injection being closed with a glass and adhesive tape and labeled before putting it into the incubator

The correct application volume was adjusted under a binocular microscope prior to careful injection in suitable blood vessels under circumvention of the application in arteries or big veins to prevent excessive blood loss. Subsequently, the eggs were carefully closed with a glass and adhesive tape, the application time was noted, and the eggs were randomly placed in the incubator.

Tissue sampling

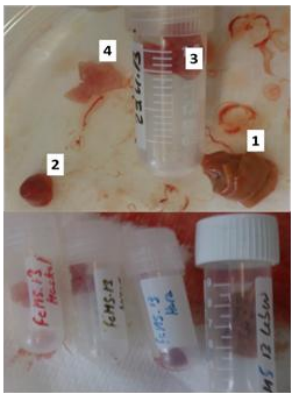

Tissue freshly taken from embryo and weighted into cryotubes
1 - Liver;
2 - heart;
3 - kidney;
4 - upper leg muscle

The incubation was stopped after 24 h or 120 h, respectively. Eggs were opened with a pair of scissors, the embryos were weighted and tissue samples were taken. In the case of heart, liver and kidney the whole organ was removed, whereas in the case of upper leg muscle only a fraction was sampled. The tissues were weighted in cryotubes, closed, labeled and subsequently frozen in liquid nitrogen before stocking at -80 °C in a freezer.

Tissue homogenization

Prior to iron quantification tissues were diluted with de-ionized water 1:5 (m_{tissue}: m_{water}) in case of heart, kidney and muscle or 1:10 in case of liver. Tissue dilution in case of liver was outstanding. Liver samples were filled with 2 ml water prior to homogenization, limiting the total volume in the tube to circumvent splashing and overflow. The rest of the water completing the final dilution of 1:10 was added subsequently.

Homogenization in case of all kind of tissues was performed with a TissueRupter®, using one disposable probe (QIAGEN, Hilden, Germany) for every single sample. Tissue dilutions were treated for app. 15 s at 10.000 rpm at the beginning, followed by maximum power at 33,000 rpm for 2-3 min in case of liver and for 1-2 min in case of heart, kidney and muscle, respectively. Dilutions were vortexed subsequently for 30 s and fixed volumes of homogenized tissue dilutions were transferred into 2 ml reaction tubes with screw cap and O-ring.

The transferred volume was dependent on the minimum resulting total dilution volume of all sampled probes for one particular kind of tissue in case of each sub-trial. This was done to yield the same volume of tissue dilutions for each single egg. Thus, it was possible to handle the samples blinded and randomly after numbering. As the mass of the tissue increases with longer growing time, a higher total volume is achieved after 120 h incubation. The transferred volumes were 600 µl in case of liver or 300 µl in case heart and muscle as well as in

case of kidney after 120 h incubation. In case of kidney after 24 h incubation 250 µl homogenate were transferred. For two probes of negative control of 24 h kidney it was necessary to take 125 µl instead of 250 µl and dilute it to 250 µl as the volume of the tissue dilution was to low. This additional dilution step was noted and considered at the evaluation. The reaction tubes with the adjusted volumes were subsequently closed, marked, and frozen at -80 °C at least for one night. The rest of the homogenized tissues was frozen and stored at -80° C as well for possible re-investigations.

Homogenate extraction

Iron quantification was performed using a modified version of the method published by Rebouche et al. [200]. The method does not discriminate between iron biologically liberated from the complex and iron present in the applied complexed shape. However, it does not spot on heme-iron, e.g. in hemoglobin or myoglobin. The reaction tubes with the adjusted volume were taken from the freezer and allowed to defrost at room temperature for 30 min. Then they were mixed with a shaker (Vortex VM 300, Heidolph GmbH & Co. KG, Schwabach, Germany) for 1 min prior to adding the same volume of protein precipitation solution (10 % [m/m] trichloroacetic acid in 1N hydrochloric acid in de-ionized water). These were 600 µl in case of liver, 300 µl in case of kidney after 120 h incubation, heart, and muscle or 250 µl in case of kidney after 24 h incubation. The reaction tubes were carefully closed, shaken for 2 min at room temperature (Thermomixer comfort, Eppendorf AG, Hummelsbüttel, Germany) and placed in a heating block (TB2, Biometra GmbH, Göttingen, Germany) at pre-adjusted 95 °C for 1 h. The mixture was then allowed to cool down at 4 °C (Thermomixer comfort) for 1 min followed by shaking for 2 min at 1400 rpm. Subsequently, the freshly shaken mixture was centrifuged (5415R, Eppendorf AG, Hummelsbüttel, Germany) at 16,000 g for 10 min at 20 °C. The clear supernatant was transferred into 1.5 ml reaction tubes and diluted 1:6 in case of liver intervention samples or further used undiluted in case of kidney, heart, muscle and NaCl- / negative control liver samples.

Iron quantification

Standard solutions were freshly prepared, using iron atomic absorption standard solution (1,000 µg Fe/ml in 1% [m/m] hydrochloric acid; Sigma Aldrich) and protein precipitation solution diluted with de-ionized water 1:1 (V/V). Concentrations of 1; 2; 4; 6; 8; 10 and 12 µg Fe/ml in case of liver samples or 0.5; 1; 2; 4; 6; 8 and 10 µg Fe/ml in case of kidney, heart and muscle samples were yielded. 100 µl of diluted or respectively undiluted supernatants were placed in quadruplicate (liver) or duplicate (heart, kidney, muscle) on different 96-well plates for either chromogenic (with FerroZine®) or blank (without FerroZine®) measurements. Each 96-well plate was loaded with 200 µl de-ionized water for blank measurement and 100 µl standard solutions with fourfold repetition. For the color reaction 100 µl chromogenic solution (1.016 mmol 3-[2-Pyridyl]-5,6-diphenyl-1,2,4-triazine-4',4''-disulfonic acid sodium salt [FerroZine®], 1.5 M sodium acetate, 0.24 % [V/V] thioglycolic acid in de-ionized water) were added to the standard solutions and the prepared supernatants, respectively supernatant dilutions. A total volume of 200 µl was yielded in each well. The probes on the reference

plate were treated with 100 µl blank solution (1.5 M sodium acetate, 0.24 % [V/V] thioglycolic acid in de-ionized water) also yielding total volumes of 200 µl. The plates were incubated for 30 min at room temperature and the absorption of the violet ferrous iron-FerroZine® complex and the blank probes were measured at 570 nm wavelength with an ELISA reader (Microtiter plate Reader MRX, Dynex Technologies Inc., Pewaukee, WI, USA) and analyzed with Relevation 4.25 software (Dynex Technologies Inc.).

The absorption values of the chromogenic treated probes were corrected with the absorption values of the same probe being treated with blank solution.

The equation of the regression line determined from standard curve was used to calculate the corrected absorption into the corresponding iron concentration. The iron content of the tissues was calculated back by consideration of the dilution factors. E.g. in case of liver samples of intervention groups: Fe content measured [µg/ml] x 10 (dilution of the homogenate) x 2 (dilution by adding the same volume of protein precipitation solution) x 6 (dilution of the supernatant after centrifugation).

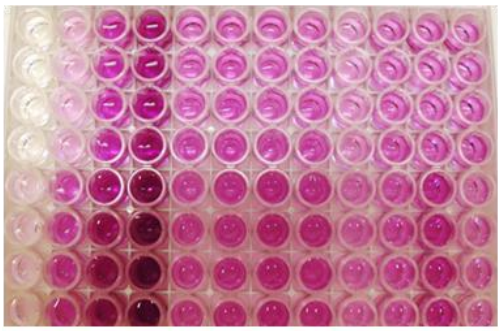

Example for a plate treated with chromogenic solution. Wells of column 1-4 from left contain the standard solutions with fourfold repetition. The upper four wells of row 1 contain 200 µl of deionized water. The other rows contain probes.

Recovery of iron in the complex

The iron complexes were investigated for the recovery of contained iron by the applied method of iron quantification in a separate experiment. For this purpose dilutions of the complexes containing 12, 18 and 24 µg/ml iron were made with sodium chloride solution 0.9 % and treated the same way as tissue homogenates (addition of the same volume of protein precipitation solution, mixing, incubation at 95 °C, mixing at 4 °C, centrifugation, iron quantification).

2.4.4. Statistical evaluation

Statistical evaluation and identification of extreme outliers was performed with SPSS software version 21.0.0.1 (IBM). Prior to comparison between treatment with different complexes, iron levels in the different tissues were compared for each kind of treatment looking for aggregation of the single sub-trials. Comparison between treatments with different complexes was performed for each complex type with aggregated results if differences between single sub-trials were not significant ($p > 0.05$). Prior to group-wise investigations for statistical significance of differences or test for aggregation, groups were investigated for normal distribution by Kolmogorov-Smirnov-test. The purpose was to decide whether tests have to be performed parametrical (t-test; ANOVA) or non-parametrical (Mann-Whitney-U-test; Kruskal-Wallis-test). In case of mean levels the standard error of the mean (SEM) was calculated and used for the error bars in the listed figures.

3. Results and detail discussion

The results (Transmission electron microscopy [TEM], electron diffraction [ED], X-ray (powder) diffraction [XR(P)D], dynamic light scattering [DLS], Zeta-potential, labile iron assay) of most presented *i.v.* iron complexes within this work are already published in three publications. In this chapter, these published results have been updated and combined with results received by additional experiments:

- Fütterer, S., Andrusenko, I., Kolb, U., Hofmeister, W., & Langguth, P. (2013). Struktural characterization of iron oxide / hydroxide nanoparticles in nine different parenteral drugs for the treatment of iron deficiency anaemia by electron diffraction (ED) and X-ray powder diffraction (XRPD). Journal of pharmaceutical and biomedical analysis, 86, 151-160.

- Jahn, M. R., Andreasen, H. B., Fütterer, S., Nawroth, T., Schünemann, V., Kolb, U., Hofmeister, W.; Munoz, M.; Bock, K.; Meldal, M.; Langguth, P.; (2011). A comparative study of the physicochemical properties of iron isomaltoside 1000 (Monofer®), a new intravenous iron preparation and its clinical implications. European Journal of Pharmaceutics and Biopharmaceutics, 78(3), 480-491.

- Jahn, M. R., Nawroth, T., Fütterer, S., Wolfrum, U., Kolb, U., & Langguth, P. (2012). Iron oxide /hydroxide nanoparticles with negatively charged shells show increased uptake in Caco-2 cells. Molecular Pharmaceutics, 9(6), 1628-1637.

3.1. Physicochemical characterization

3.1.1. Size determination

3.1.1.1. Size of the core - TEM & XRPD

The results of the size determination performed in accordance with the method described in section **2.2.1.1** and **2.2.1.2** are listed in ***Table 3***.

Table 3 - XRPD and TEM diameters: Diameters of nanoparticle "cores" and from high density regions of "particles" (FeOOH-carbohydrate matrix) determined from TEM-images (see section 3.2.2.1) and "mean nanocrystal size" determined by XRPD. High density cores with an adequate number were found in case of LFeD1 & 2, FeIM, HFeD, HFeD_G, FePSC and FeCM. Pure "cores" are generally not the main fraction of the contained iron. FeIM, FeG and FeSuc show only very small cores with high density ("ultra-small cores"). The number of those cores was very low in case of FeSuc and FeG and does not reflect the mainly amorphous structure of the FeSuc and FeG particles. Contrary to that one FeIM-particle seems to mainly consist of a high number of such "ultra-small particles" being bedded in a carbohydrate matrix.

	XRPD*	TEM		
Complex	**mean single crystal Ø [nm]**	**ulta-small cores-Ø [nm]**	**core-Ø [nm]**	**particle-Ø [nm]**
FeG	*4.7*	1.9 ± 0.8	-	**4.1** ± 1.7
FeS	*4.9*	1.1 ± 0.5	-	**5** ± 0.8
LFeD1	*6.2*	1.8 ± 0.6	5 ± 2.1	**12.6** ± 1.5
LFeD2	*6.4*	2* ± 1	4.8 ± 1.5	**14.9** ± 3.1
FeIM	*5.7*	0.9 ± 1.3	-	**6.3** ± 1.2
HFeD	*8.8*	2.1 ± 1.5	8.7 ± 1.9	**17.1** ± 4
HFeD_G	*7.2*	1.2 ± 0.8	7.5 ± 1.6	**17.5** ± 5.1
FePSC	*7.5*	0.7 ± 0.4	6.6 ± 2.5	**16.7** ± 3.5
FeCM	*7.7*	1.4 ± 0.7	5.9 ± 1.9	**18.6** ± 5
FeHES **	-	***		***28.2*** *± 14.2*

very low Number / Fraction

** XRPD sizes are estimated values: inadequat correlation with gauss-curve*

*** FeHES size is based on image provided from company Serumwerke Bernburg (not presented)*

**** not possible (different device & method of imaging with lower resolution)*

Three different kinds of particles / part of particles were assessed. "Particles" (column 4) are referred to as all shapes of structures that were possible to be recognized as well-defined and had an electron density lower than e.g. iron oxy hydroxide (FeOOH) cores but showed varying grades of electron density. This indicates an altering fraction of iron present as a mixture (most probable amorphous kind of structure) with the carbohydrate fraction. Those particles contained pure FeOOH cores (column 3: "core") in some cases. "Ultra small cores" (column 2) were purely inorganic cores, which were distributed inside the particles and were present homogenously distributed (e.g. FeIM, FePSC) or clustered to a quasi-core. The size of those ultra-small cores were at the range of image resolution and could not be recognized in the FeHES image, which is not presented here as it was provided by the manufacturer and obtained by a different method (cryo-TEM) with lower resolution. Ultra small cores were present in every sample but in a high amount only in case of FeIM, FePSC and FeCM.

Size information obtained from XRPD reflexes by Scherrer equation are additionally listed in ***Table 3*** column 1 and represent the mean size of single nanocrystals which are the source of XRPD patterns.

The increasing order of particle diameters determined from TEM images was FeG ≈ FeSuc ≈ FeIM < LFeD1 ≈ LFeD2 ≤ FePSC ≈ HFeD ≈ HFeD_G ≈ FeCM << FeHES. Pure high electron density FeOOH cores with increasing size were found in case of LFeD1 ≈ LFeD2 ≤ FeCM ≤ FePSC ≤ HFeD_G ≤ HFeD. Pure cores in case of all complexes are present in a relatively low amount in respect to the total amount of iron present in the formulation. This and the varying density of the lower density phase indicate that a specific fraction of the contained iron may be present in a more amorphous kind of structure.

This amorphous fraction as well as a possibly present ultra-small-core-fraction is neglected in XRPD size analysis by Gauss fitting and half-width survey of a single reflex and calculation by the Scherrer equation (**2.1.5.2**). The increasing order of estimated mean nanocrystal size is FeG ≈ FeSuc< FeIM ≤ LFeD1 ≈ LFeD2 ≤ HFeD_G ≈ FePSC ≈ FeCM < HFeD and is comparable to the order of core diameters determined from TEM with differences for HFeD_G, FePSC and FeCM. The different order there can be referred to the SD in case of TEM results and the inaccuracy of the XRPD size determination.

As a minimum crystal size of about 3 nm is necessary to yield constructive interference in XRPD measurements (see section **2.1.5.2**), the ultra-small cores are not contributing to this mean size (as they are smaller than 3 nm) - in difference to the mean size of core diameter determined from TEM images. Another and more relevant disadvantage - which is the reason why the diameters obtained by XRPD are termed "estimated values" - is that the fitted Gauss curve is not well correlating with the actual reflex peak. Thus, the width survey is imprecise with consequent defective size values. Nevertheless, the values presented in ***Table 3***. show very good accordance with the core size results from TEM measurement in case of LFeD1, LFeD2, HFeD, HFeD_G, FePSC and FeCM. In case of FeG, FeSuc and FeIM where no pure cores were recognized in the images the particle diameter value is very close to XRPD size. FeIM seems to be for thus outstanding as the XRPD pattern was obtained by the same sample preparation method as all other samples in difference to FeG and FeSuc. In case of these samples, it was not possible to receive reliable XRPD patterns even by different sample preparation methods (see results and discussion XRPD structure section **3.2.1**). Thus, it is likeable that FeG as well as FeSuc are mainly amorphous complexes whereas FeIM has an ordered structure, which is different to the other complexes.
The disadvantage of core size determined from TEM images is that there is a subjective impact and the possibility of statistical mistakes. The particle survey from the images may contribute to that, as one or also two images may show regions that do not represent a statistical cross section of the sample. This was circumvented by measuring single cores/particles from at least three images except in case of FeHES where only one figure was available which was moreover obtained by another method (CryoTEM) with a different sample prepa-

ration method and lower image resolution. Hence, it was not possible to measure reliable core diameters which is why they are not presented in ***Table 3***.
The TEM images of all complexes including the detailed evaluation of different kinds of particle shapes are presented in section **3.2.2.1**.

3.1.1.2. *Hydrodynamic diameter - DLS*

Results of DLS measurements can be seen in ***Table 4***. PDI was smaller than 0.25 in case of every kind of complex, which makes the Z-average a useful parameter to compare the different complexes. The increasing order of mean intensity weighted diameters (Z-average) is FeSuc < FeIM ≈ FeG ≤ LFeD2 ≈ LFeD1 << HFeD_G < FeCM < FePSC < HFeD <<< FeHES.

Table 4 - Results of DLS measurements. The mean Z-average results and the mean polydispersity indexes (PDI) are presented. The complexes can be assumed as monodisperse as PDI < 0.25 in every case. Only in case of FeG, FePSC, and FeSuc PDI was larger than 0.15 which indicates a broader size distribution.

Complex	*n*	**mean Z-average [nm]**	mean PDI
FeS	*7*	**11.73 ± 0.12**	0.185 ± 0.007
FeIM	*5*	**13.34 ± 0.14**	0.142 ± 0.007
FeG	*12*	**13.64 ± 1.18**	0.230 ± 0.026
LFeD2	*6*	**14.79 ± 0.32**	0.135 ± 0.013
LFeD1	*11*	**15.32 ± 0.62**	0.133 ± 0.042
HFeD_G	*6*	**23.93 ± 0.27**	0.082 ± 0.007
FeCM	*8*	**27.51 ± 0.94**	0.100 ± 0.047
FePSC	*8*	**29.92 ± 1.50**	0.202 ± 0.031
HFeD	*6*	**30.99 ± 0.25**	0.104 ± 0.008
FeHES	*3*	**63.31 ± 0.22**	0.112 ± 0.005

The mean values of volume and number weighted sizes can be seen in ***Table 5***. As scattering of light is overemphasized by larger particles ($I \sim d^6$; section **2.1.6**) and a single particle's volume is proportional to d^3, the mean size decreases by transforming intensity weighted size distribution to volume and number weighted distributions. The order of the complexes in respect to size only changes in case of FeG and FePSC. These complexes show the highest peak widths (PDI). Thus the diameter is overemphasized in case of intensity and less distinctive volume weighted distribution.

Table 5 - Mean values of volume and number weighted size distributions derived by calculation from intensity weighted size distribution data.

Complex	*n*	Mean diameter: volume distribution [nm]	Mean diameter: number distribution [nm]
FeS	*7*	8.17 ± 0.15	6.04 ± 0.17
FeIM	*5*	9.88 ± 0.13	7.50 ± 0.21
FeG	*12*	10.10 ± 1.54	5.89 ± 0.23
LFeD2	*6*	11.51 ± 0.25	8.92 ± 0.31
LFeD1	*11*	14.22 ± 3.73	9.59 ± 0.64
HFeD_G	*6*	20.96 ± 0.29	17.68 ± 0.27
FeCM	*8*	23.13 ± 0.81	19.02 ± 1.44
FePSC	*8*	21.97 ± 0.94	15.97 ± 1.09
HFeD	*6*	27.38 ± 0.51	22.85 ± 0.67
FeHES	*3*	55.35 ± 0.08	44.20 ± 0.33

Figure 35 depicts the peaks of the volume weighted size distributions for all complexes. Similarities can be seen between FeG and FeSuc as well as LFeD1 & 2 with similar distribution peaks. The tails in case of FeG, FePSC, FeSuc, and less defined for LFeD1 & 2 show relative higher dispersity than for the other complexes and is parameterized by the PDI in ***Table 4***.

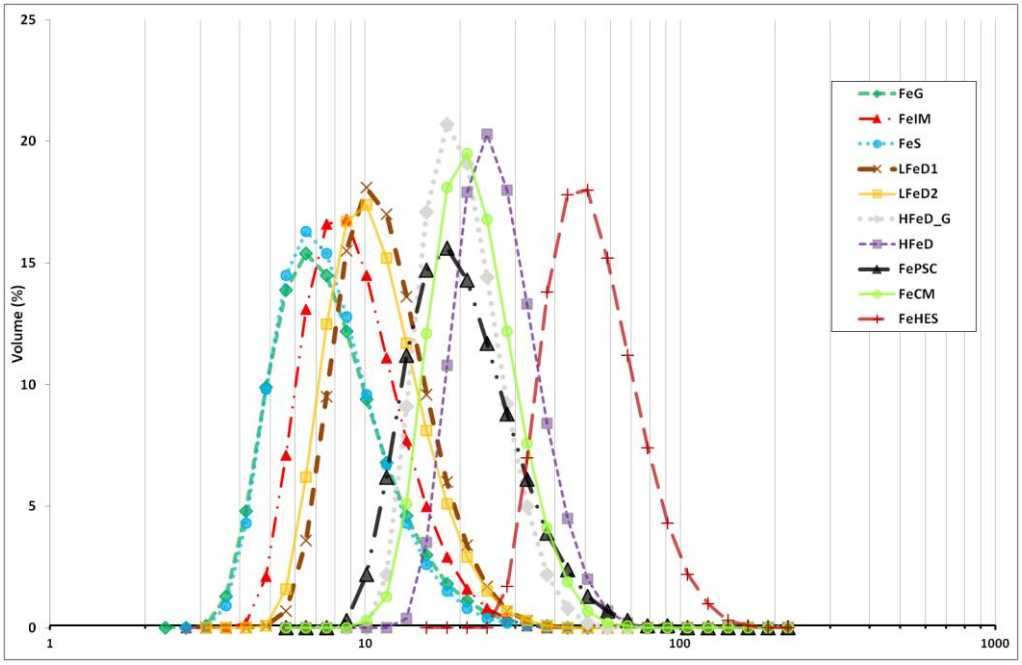

Figure 35 - Overview of the mean volume weighted size distributions of the different complexes without standard deviations in case of the single data points determined by DLS. The size distribution peaks of FeG (dark green) and FeSuc (light blue) as well as LFeD1 (brown) and LFeD2 (orange) show rather similarities. Peaks of FeG, FeSuc and FePSC (black) and less defined of LFeD1 & 2 show small tails indicating broader distribution than in case of HFeD (violet), HFeD_G (grey), FeCM (light green) and FeHES (red-brown). Mean volume distribution size values listed in Table 5 represent the sizes where the area of the size distribution peaks is halved.

3.1.2. Size discussion

Table 6 - Results of gel permeation chromatography (GPC) and mean volume weighted size distribution data by dynamic light scattering (DLS) published by [95]. The DLS data of FeG (sodium ferric gluconate), FeSuc (iron sucrose), LFeD1(LMW iron dextran / CosmoFer®), FePSC (ferumoxytol), and FeCM (ferric carboxymaltose) are part of the DLS data listed in Table 4 and Table 5.

Iron complex	MW [kDa]	Calculated Shell-Ø[nm]*	Shell-Ø [nm]	
	GPC		DLS	
Sodium ferric gluconate	164.1	20.3	8.6[a]	0.244[b]
Iron sucrose	140.1	19.1	8.3[a]	0.192[b]
LMW iron dextran	165.0	20.7	12.2[a]	0.149[b]
Iron isomaltoside	150.0	20.5	9.9[a]	0.182[b]
Iron carboxymaltose	233.1	23.8	23.1[a]	0.07[b]
Ferumoxytol	275.7	26.3	23,6[a]	0.143[b]

[a]median-Ø
[b]Polydispersity index
*The most frequently found particle diameter in the distribution.

The method of size determination by TEM (geometrical diameter of 50 particles from a TEM image) is mostly comparable with the mean number weighted DLS measured diameters. However, the number weighted distribution is derived from intensity weighted distribution data under the assumption of a monomodal dispersion, an unknown sample refractive index and light absorption. Those characteristics are consequence of the particle composition and the particle shape. For a number weighted as well as volume weighted evaluation of DLS raw data (intensity weighted) spherical particles are assumed. This is not applicable as can be seen in particle morphology chapter **3.2.2**. Thus, these results are less valid and stable than the Z-average data. The disadvantage is the minor possibility of comparing the values with sizes determined from other methods (e.g. GPC, TEM) as the intensity-weighted distribution is strongly influenced by larger particles and overemphasized for that reason.

The disadvantage of transmission electron microscopy (TEM) results derived from a number of TEM images is that there is a subjective influence when the particles are measured (single and defined particles are preferred in comparison to agglomerates and diffuse particle boarders). Additionally, in those images it is not sure that a representative composition of the formulation is depicted and sample preparation method may negatively influence sample composition on the copper grid.

TEM results of the less dense particles probably consisting of a mixture of carbohydrate with FeOOH show similarities to the number weighted distribution data except in case of LFeD1 & 2 (**Table 3**. vs. ***Table 5***). Already published data of gel permeation chromatography (GPC) in case of FeSuc, FeG, LFeD1, FeIM, FeCM and FePSC indicate higher accordance to Z-average data than to TEM / number weighted DLS data although all values are larger in case of GPC measurements (***Table 6***; [95]). Hence, the similarities between TEM results and number

weighted mean sizes of DLS might be misleading. The higher level of accordance of GPC data to Z-average than to TEM might be a consequence of a pure carbohydrate shell that cannot be seen in TEM images. Another reason for the overall higher size in case of GPC in comparison to DLS is assumed to be a consequence of an electrostatic interaction between the particles and the GPC-column [95]. As TEM core sizes are not present in case of all samples, mean size of a single nanocrystal was used, beside DLS Z-average size, for the purpose of size-stability correlation (**4.3**). The use of XRPD size data in this context has the disadvantage that the method is relative imprecise, as the surveyed reflex-peaks were very diffuse (**3.1.1.1**, p. **71**). These diffuse signals are consequence of small single crystals with low repetition rates of crystalline domains. Additionally, XRPD diffractograms bring evidence that the fraction of amorphous material is relative high. The small size of the particles and especially the small size of the pure iron phase combined with the high interaction area between carbohydrate and inorganic iron phase explains this phenomenon. From XRPD diffractograms the high fraction of amorphous material can be concluded from the high baseline intensity of scattered X-rays. This baseline signal has in all cases a relatively high intensity and is strongest in case of the small particles FeSuc and FeG. This made it extremely difficult to yield valid size information by Scherrer equation.

The intended iron dextran copy Ironate® is in consequence of the results of the size investigations with fundamental differences to the LMWIDs (LFeD1 & LFeD2; CosmoFer® & InFed®) and more similarities to HMWID (HFeD) referred to as a generic HMWID (HFeD_G) in the rest of this work.

3.1.3. ζ-Potential

3.1.3.1. *Results*

Table 7 gives an overview of the results of the ζ-potential measurements. The nature of the complexes makes high quality results very difficult to achieve. In most cases the software intern quality report classified the phase data as good but the distribution data as poor (**Figure 36**). As concentration variation and measurement settings did not yield results that met the quality criteria, but the results were reproducible with a good SD in most cases, the method was considered suitable to characterize the relative, medium dependent charge of the different NP in the complexes.

Results indicate that most of the complexes carry negative charge at the pH determined by the product composition. FeCM and FeHES are the only complexes that have a positive ζ-potential when the pH is not changed. The pH of these two compounds is comparable and the ζ-potential is more positive in case of FeHES.

The increasing order - from negative to positive - of the complex ζ-potential at unchanged pH was determined with FePSC < FeG ≈ FeSuc ≤ FeIM ≈ HFeD < LFeD1 ≈ LFeD2 < HFeD_G (all negative) < FeCM < FeHES. The results also show that the ζ-potential is increasing to more positive or less negative values, respectively, dependent on the media's pH values. Higher acidity leads to more hydronium cations in the medium and consequently a higher potential at the boundary of the Stern layer. The contrary effect can be seen at increasing pH values.

Table 7 - ζ-potential of the complexes with corresponding pH values

Complex	pH	n	ζ-potential [mV]		
FeG	8.4*	*5*	-43.4	±	1.56
	10.5	*2*	-44.4	±	0.14
	7.4	*2*	-44.5	±	0.64
	4.4	*2*	-24.8	±	1.20
FeS	10.8*	*4*	-39.3	±	3.60
	7.4	*2*	-39.3	±	0.57
	4.5	*2*	-21.4	±	0.57
LFeD1	6.4*	*6*	-25	±	2.75
	11.8	*2*	-23.6	±	7.04
	7.3	*2*	-25.9	±	0.99
	3.0	*2*	-5.34	±	1.10
LFeD2	6*	*2*	-27.6	±	3.89
HFeD_G	5.8*	*2*	-12.8	±	9.10
HFeD	6.7*	*3*	-31.1	±	6.45
FePSC	7*	*4*	-58.5	±	10.90
	10.4	*2*	-51.6	±	1.13
	7.4	*2*	-45.8	±	0.50
	3.4	*2*	-18	±	0.71
FeIM	6.3*	*2*	-33	±	2.26
	11.5	*2*	-39.6	±	1.27
	9.0	*2*	-43.4	±	1.13
	7.4	*2*	-31.6	±	1.70
	3.3	*2*	-5.96	±	0.16
FeCM	5.36*	*4*	+5	±	0.66
	9.5	*2*	-24.6	±	0.99
	7.3	*2*	-12.8	±	0.21
	3.3	*2*	+14.1	±	1.34
FeHES	4.86*	*8*	+17.5	±	0.61

*** no pH adjustment**

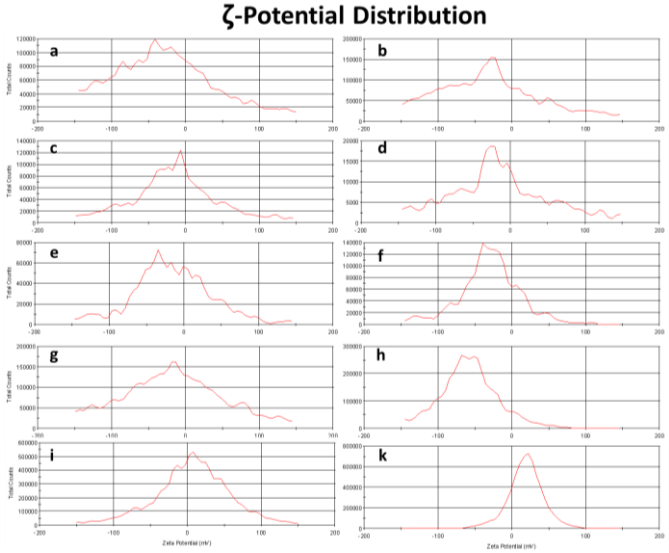

Figure 36 - ζ-potential distribution of one sample of each of the investigated compounds: (a) FeG; (b) FeSuc; (c) LFeD1; (d) LFeD2; (e) HFeD_G; (f) HFeD; (g) FeIM; (h) FePSC; (i) FeCM; and (k) FeHES. The total counts are plotted against the ζ-potential.

3.1.3.1. *ζ-potential discussion*

The ζ-potentials of the different Fe-NbCD indicate surface charge of the different NPs. The potential at the Stern Layer is not only dependent on the surface charge, as described in **2.1.7,** but also on the composition of the media in which the particles are dispersed. Thus, it is directly influenced by the pH, electrolytes in the applied dilution media, and charged excipients in the formulation itself. The influence of the medium was circumvented using double distilled, sterile filtered water in every case. In cases where the pH was adjusted, hydrochloric acid and sodium hydroxide had been added. Thus, the pH values were ideally at the same range but the medium composition was minimally different in respect to chloride and sodium ions. The pH value is a direct consequence of the iron complex formulation's characteristics and it influences the electrolytic composition of the dilution containing 0.4 mg of complexed iron. FeSuc, FeG, LFeD1, FeCM, FeIM, and FePSC can be directly compared independent from pH influence as they were adjusted to a physiological pH value of about 7.4. All the complexes showed negative ζ-potentials with a decreasing order of absolute values for FePSC ≈ FeG ≥ FeSuc > FeIM > LFeD1 >> FeCM. The values of HFeD, HFeD_G, LFeD2 and FeHES at non-adjusted pH values indicate that LFeD2 is at the range of LFeD1, which is likely as it is another batch of the same product and differences here can be referred to batch-to-batch variations. HFeD is comparable to LFeD2 and LFeD1 from point of ζ-potentials at non-adjusted pH. The pH is minimal higher with a influence on the absolute negative value and additionally, the SD is higher, too. Although the pH is minimal lower in case of HFeD_G with consequently minimal lower resulting value for the ζ-potential, it seems that it is different to LFeD1 & LFeD2 as well as HFeD with lower absolute value of negative potential. The result of FeHES at a minimal lower pH of the non-adjusted dilution in comparison to FeCM shows a higher positive ζ-potential. This potential is even higher positive than the potential of FeCM with a 1.6 pH units (≈ 40 times higher proton concentration) lower pH (3.3 vs. 4.9) indicating that at physiological pH the potential is intended to be neutral or even still positive. Possible different surface charges, indicated by different ζ-potential, might result in different uptake in macrophages of the MPS as the cellular uptake of particles seems to underlie surface charge influence, beside size influence [201-203].

3.2. Structure investigations

3.2.1. XRPD and ED results

Table 8 - Overview of analytical methods applied during XRPD and ED analyses, results obtained by those methods for the different samples, and the final assessment of the analyses.

Sample	XRPD/XRD	STEM	Size (STEM)	EDX	SAED	NED	Final assessment
FePSC	Magnetite/ Maghemite	✓	≤10nm <200nm[3]	Fe; O	Magnetite	Magnetite	**Magnetite[5]**
FeG	Ferrihydrite/ Lepidocrocite[2]	✓	<< 10nm	Fe; Na; O	n/a	Lepidocrocite/ Akaganéite	**Lepidocrocite or Amorphous[6]**
FeSuc	Ferrihydrite/ Lepidocrocite[1]	✓	<< 10nm	Fe; O	n/a	Various	**Lepidocrocite or amorphous[6]**
LFeD1	Akaganéite	✓	≤ 10nm	Fe, Cl, Ni[4]	n/a	Akaganéite	**Akaganéite**
FeCM	Akaganéite	✓	≤ 10nm	Fe, Cl, O, Ni[4]	Akaganéite	n/a	**Akaganéite**
FeIM	Akaganéite[2]	✓	< 10nm	n/a	n/a	Akaganéite	**Akaganéite**
HFeD	Akaganéite	✓	≈ 20nm < 50nm[3]	n/a	n/a	Akaganéite	**Akaganéite**
HFeD_G	Akaganéite	✓	≈ 20nm < 50nm[3]	n/a	n/a	Akaganéite/ Lepidocrocite	**Akaganéite**
LFeD2	Akaganéite	✓	≤ 10nm	n/a	n/a	Akaganéite	**Akaganéite**

n/a - no interpretable results

[1] XRPD without previous powdering was performed for Ferrlecit® and Venofer®; preferred orientation is possible

[2] with a shift of 0.002-0.006 nm

[3] agglomerates

[4] Nickel signal determined by EDX cannot provable be associated to the sample as it is possibly generated by the holder tip; Ni:Fe ≈ 1:100

[5] Maghemite can be excluded because some characteristic strong peaks are not present in Feraheme® (Ferumoxytol)

[6] comparison of TEM and XRPD results with the obvious difference to the akaganéite-like samples in XRPD measurements implies a lepidocrocite-like structure; difficulty to receive XRPD patterns makes amorphous kind of structure likely

Feraheme® (Ferumoxytol; FePSC)

XRPD measurements of the dried and pulverized sample yielded the diffractogram shown in **Figure 37.** The arrows label the crystalline, superimposing carbohydrate that was identified as δ-D-mannitol. The sugar alcohol δ-D-mannitol is used as a pharmaceutical excipient in the formulation but not part of the iron complex itself. In this case, the iron phase signal is sufficiently strong to be recognized as magnetite or maghemite (characteristic peaks at 0.296, 0.253, 0.162 and 0.148 nm).

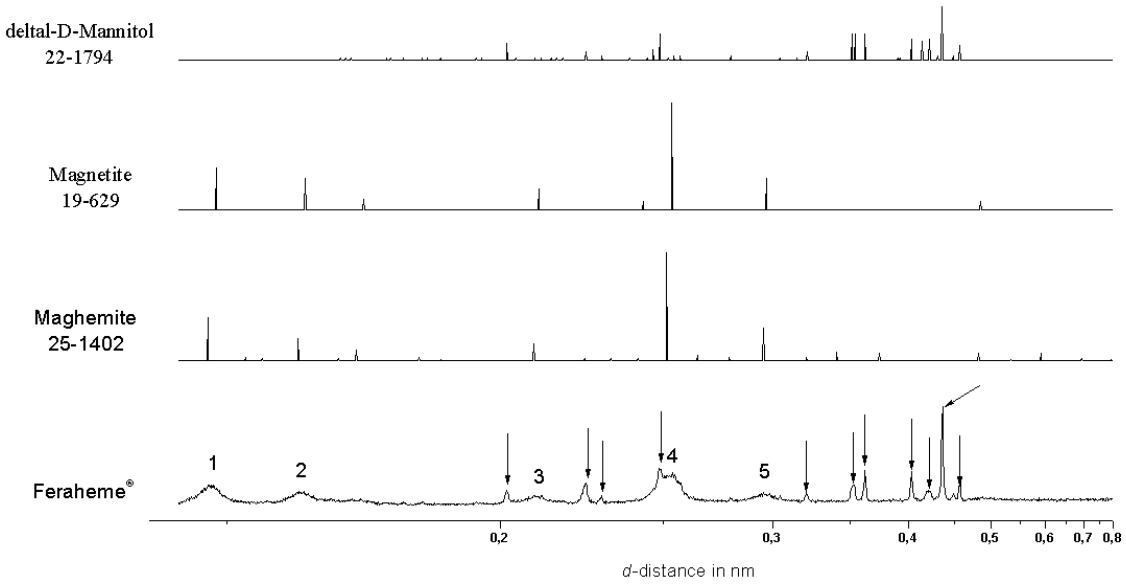

Figure 37 - XRPD pattern of FePSC (Feraheme®) with connected standards maghemite, magnetite, and the carbohydrate fraction δ-D-mannitol. The arrows label peaks associated with δ-D-mannitol. The numbered peaks from 1 to 5 can be referred to the iron oxy hydroxide maghemite and the iron oxide magnetite. Although the reference peaks for magnetite and maghemite show small differences of about 0.001-0.002 nm to each other, these differences cannot be imaged, as the peaks of the FePSC sample are broadened as consequence of relative small crystal sizes.

EDX analysis shows the presence of iron and oxygen only (Table 8). SAED patterns show nine characteristic *d*-distances of 0.301, 0.256, 0.212, 0.170, 0.164, 0.151, 0.130, 0.110 and 0.086 nm (**Figure *38***). They are in good agreement with the strongest peaks of magnetite with a maximum shift of up to 0.004 nm. Listed values from ICDD standards are: 0.297 nm (30% Intensity), 0.253 (100%), 0.210 (20%), 0.162 (30%), 0.148 (40%), 0.109 (12%) and 0.086 (8%). Maghemite is excluded because some characteristic strong peaks are not present in SAED patterns.

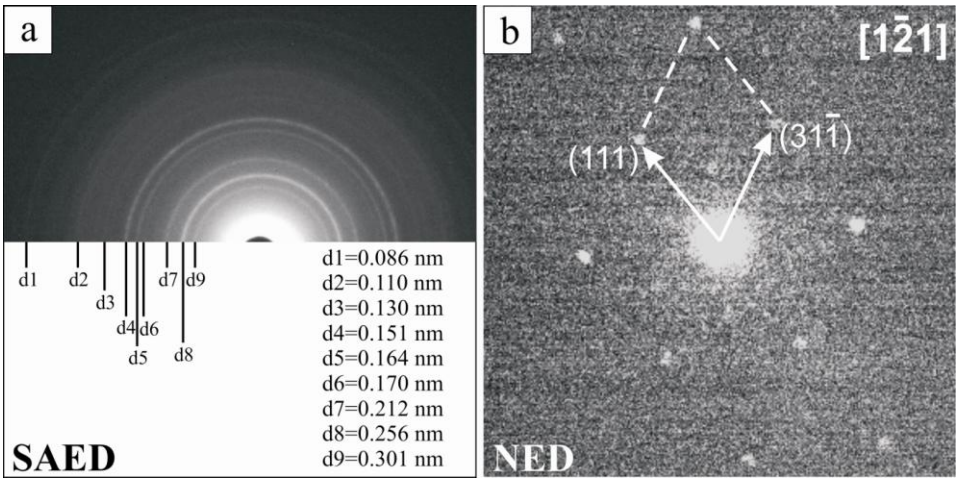

Figure 38 - SAED (a) and an exemplary NED (b) pattern of FePSC (Feraheme®) The NED pattern was collected on a single nanocrystal and shows two equivalent d-distances of about 0.25 nm and an in-between angle of about 58.5°. This pattern agrees well with [1-21] projection for magnetite. [195]

Ferrlecit® (Sodium ferric gluconate sucrose; FeG)

When XRPD patterns were collected from the pulverized sample, it was not possible to record a signal that can be referred to any standard iron oxy hydroxide. The reason is a very strong signal of the carbohydrate component, sucrose overlaying any possible iron oxy hydroxide signal. This makes it impossible to refer the sample to any standard iron oxy hydroxide although the presence of a more amorphous iron phase can be derived from the diffuse baseline signal. (**Figure 39**)

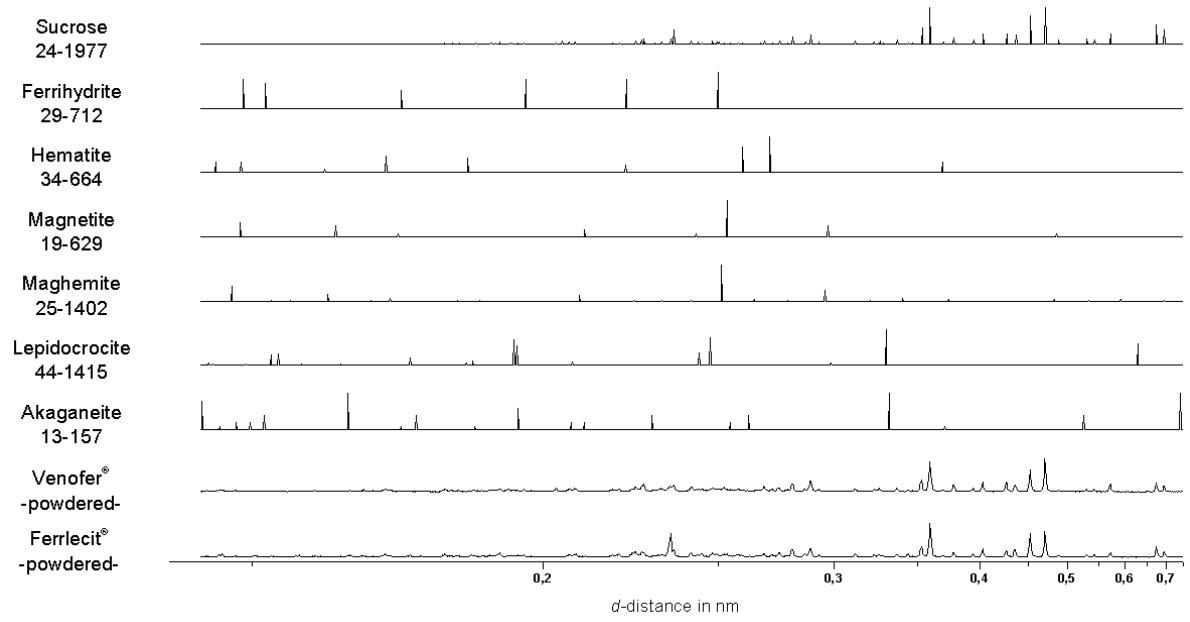

Figure 39 - XRPD patterns of powdered FeG (Ferrlecit®) and FeSuc (Venofer®) with standard iron oxides / oxy hydroxides and the carbohydrate sucrose. All relevant peaks determined for both samples can be associated to sucrose standard peaks.

In order to emphasize iron oxy hydroxide / hydroxide signal, XRPD measurements were done on a non-pulverized dried sample, resulting in the diffraction pattern shown in **Figure 40**.

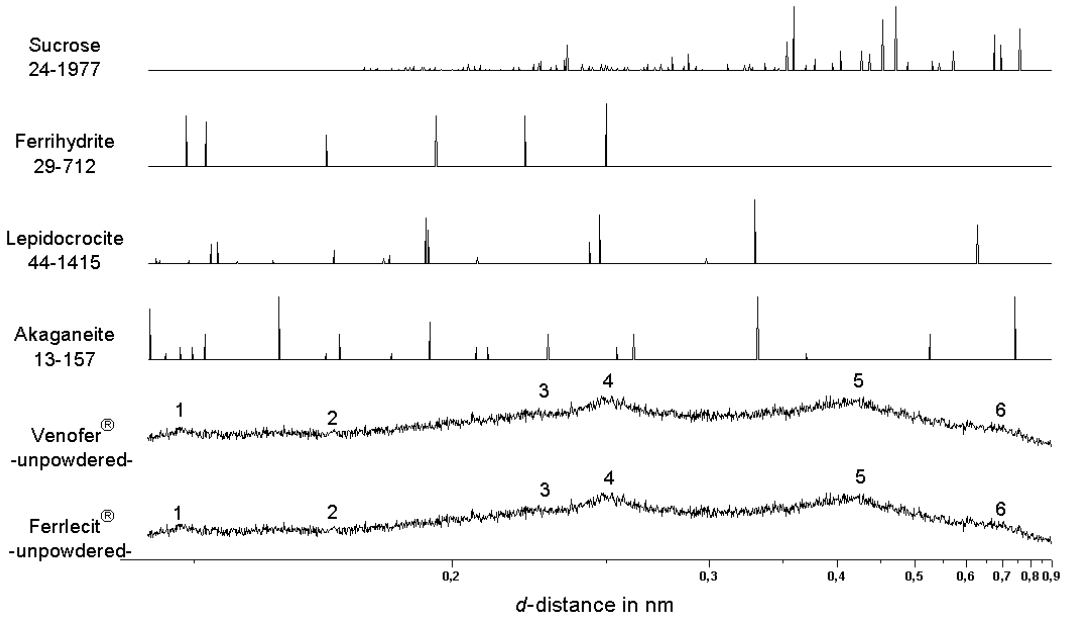

Figure 40 - XRD patterns of FeG (Ferrlecit®) and FeSuc (Venofer®) without previous pulverization. By evaporation during the drying process the intensity of some particular lattice planes is enhanced leading to texture effects and consequently to better interpretable diffraction data. Additionally, the sucrose signal is suppressed indicating a more amorphous sucrose structure. Peak 1 can be referred best to ferrihydrite with a small shift. Peak 2, which is relatively small, at about 0.175 nm can only be referred to lepidocrocite. Peak 3 is also small and can be referred to ferrihydrite, too. Peak 4 can fit ferrihydrite and lepidocrocite. Peak 5 does not match any iron oxide / oxy hydroxide reference very well and may be associated to sucrose. Peak 6 is weak and can be referred to lepidocrocite or sucrose. Akaganéite does not fit the diffractogram very well.

XRPD measurements were additionally done on a non-pulverized dried sample, resulting in the diffraction patterns shown in **Figure 40**. Interestingly, the diffractogram does not show the strong signal of sucrose and complies with structures of ferrihydrite and lepidocrocite, respectively. The suppression of the sucrose peaks indicating an amorphous sucrose structure is a very interesting effect. This can be explained by enhanced temperature during the drying process and/or the longer drying time. By evaporation during the drying process the intensity of some particular lattice planes is enhanced leading to texture effects and consequently to better interpretable diffraction data. By grinding the samples with the mortar this partial intensity enhancement is suppressed. The signal from flat iron oxy hydroxide crystals may therefore be emphasized by the sample preparation method. Independent from the sample preparation technique ICDD standards gluconic acid sodium- *[10-505]* and iron- *[5-527]* salt in contrast to sucrose were not identified in the diffraction pattern (**Figure 41**).

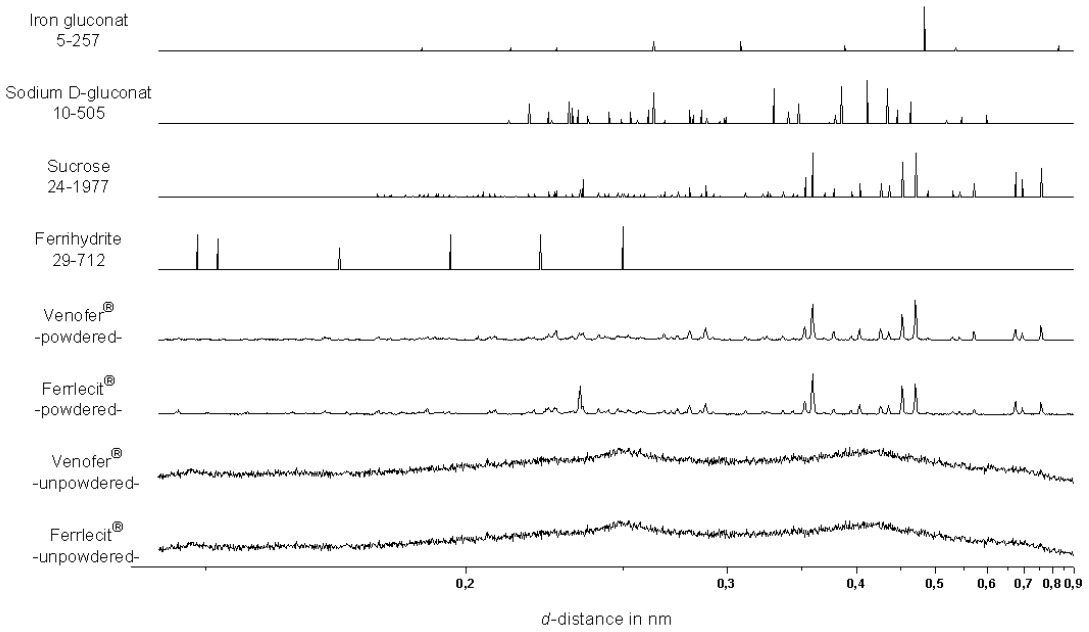

Figure 41 - XRPD patterns of FeSuc (Venofer®) and FeG (Ferrlecit®) - powdered and unpowdered - in comparison to the standard ICCD data of sucrose and the gluconic acid sodium- and iron- salt. The sucrose standard peaks can be very clearly recovered in the case of the powdered samples. Gluconic acid sodium- and iron salt signals have not been found for the FeG (sodium ferric gluconate sucrose) sample.

STEM analysis of FeG identified crystals with diameters <10 nm (**Figure 63 b**), thus producing only poor electron diffraction patterns (**Figure 42 a**). EDX analysis showed the presence of iron, sodium and oxygen.

Particles were so small that ED patterns cannot come from a single nanocrystal, but only from polycrystalline areas. In NED only three characteristic *d*-distances of 0.320, 0.194 and 0.148 nm were identified (**Figure 42 a**). These *d*-distances are in good agreement with lepidocrocite (listed values ICDD: 0.329 (100%), 0.194 (72%), 0.148nm (30%)) or akaganéite (Listed values ICDD: 0.331 (100%), 0.194 (60%), 0.148nm (20%)).

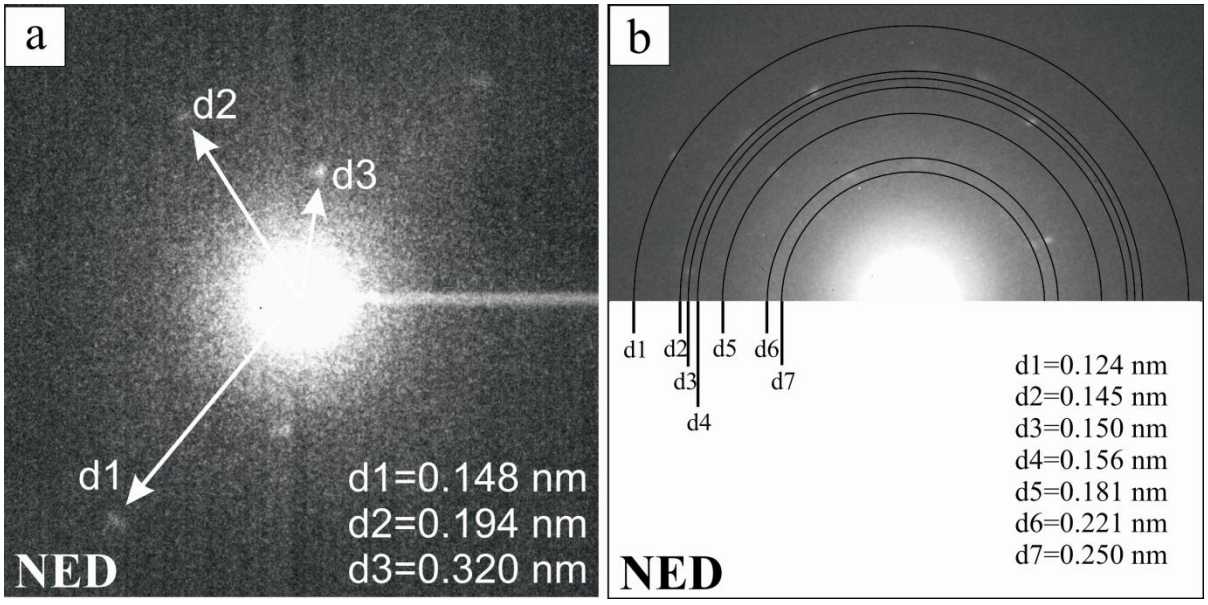

Figure 42 - NED patterns from polycrystalline areas: (a) FeG (Ferrlecit®); (b) FeSuc (Venofer®)

Venofer® (Iron sucrose, FeSuc)

The XRPD diffractogram pattern obtained for the pulverized sample is very similar to that obtained for FeG sample (**Figure 39**). The overlying sucrose signal hides the iron oxy hydroxide signal, preventing any reliable identification of FeNP phase. As for FeG, this was circumvented by performing XRPD on the dried sample without pulverization (**Figure 40**). The diffraction pattern does not show the strong signal of sucrose and fits with ferrihydrite and lepidocrocite. XRPD data from FeSuc and FeG are undistinguishable.
EDX analysis shows only the presence of iron and oxygen (***Table 8***).
As for FeG, NED patterns come from polycrystalline areas and show seven characteristic *d*-distances: 0.250, 0.221, 0.181, 0.156, 0.150, 0.145 and 0.124 nm **(Figure 42 b).** These distances are in accordance with different iron oxides and iron oxy hydroxides.

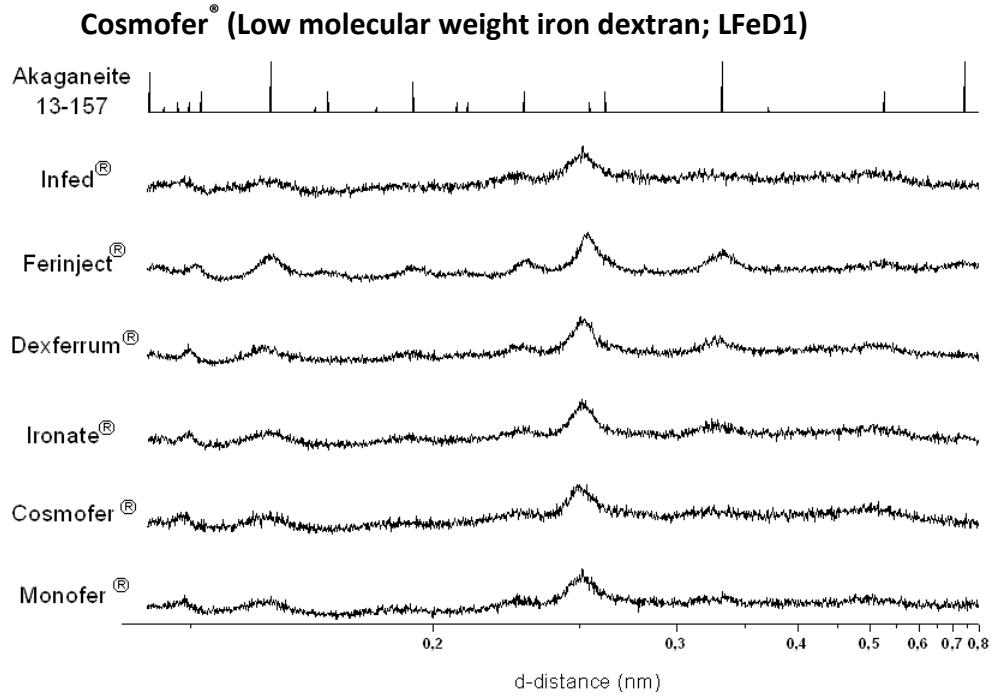

Figure 43 - XRPD patterns of FeIM (Monofer®), LFeD1 (CosmoFer®), HFeD_G (Ironate®), HFeD (Dexferrum®), FeCM (Ferinject®) and LFeD2 (Infed®) with akaganéite standard diffractogram. There is a high conformity between the samples and in relation to akaganéite standard d-distances.

The diffractogram of the XRPD analysis shows good agreement with akaganéite only (**Figure 43**). EDX analysis showed the presence of nickel and chloride besides iron and oxygen (***Table 8***). This composition is consistent with akaganéite only. The ratio Ni:Fe was in fact in the order of 1:100 and the Ni signal might have originated from the holder tip.
NED patterns from a polycrystalline area (**Figure 44 a**) displayed six characteristic *d*-distances (0.325, 0.251, 0.226, 0.191, 0.161 and 0.149 nm) that fit well to akaganéite. The listed *d*-distances for akaganéite in this range are 0.331 (100%), 0.254 (80%), 0.229 (40%), 0.194 (60%), 0.164 (100%) and 0.152 nm (40%).

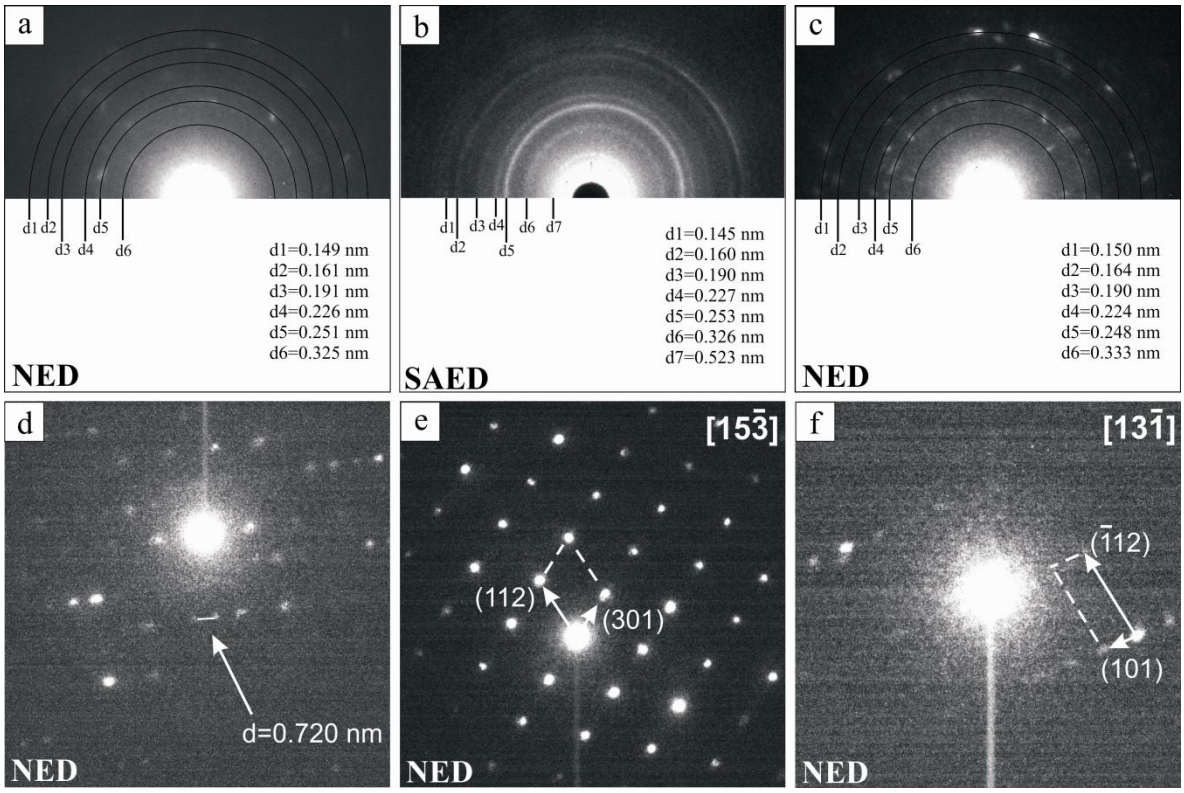

Figure 44 - NED (a, c-f) and SAED (b) patterns of akaganéite-like structures: (a) LFeD1 (Cosmofer®); (b) FeCM (Ferinject®); (c) FeIM (Monofer®); (d) HFeD (Dexferrum®); (e) HFeD_G (Ironate®); (f) LFeD2 (Infed®). NED patterns (a, c) come from polycrystalline area, while NED patters (d-f) come from single nanocrystals

Ferinject® (Ferric carboxymaltose; FeCM)

The diffractogram of the XRPD analysis shows good agreement only with akaganéite (**Figure 43**). EDX analysis showed the presence of iron, nickel, chloride and oxygen, consistent with akaganéite (***Table 8***). The ratio Ni:Fe was in fact in the order of 1:100 and the Ni signal might have originated from the holder tip. SAED patterns showed seven characteristic *d*-distances: 0.523, 0.326, 0.253, 0.227, 0.190, 0.160 and 0.145 nm (**Figure 44 b**). All distances are in good agreement with akaganéite.

Monofer® (Iron isomaltoside; FeIM)

The diffractogram of the XRPD analysis shows good agreement only with akaganéite (**Figure 43**). NED patterns from a polycrystalline area (**Figure 44 c**) showed the following six *d*-distances: 0.333, 0.248, 0.224, 0.190, 0.164 and 0.150 nm. These distances are in good compliance to the ICDD standard values of akaganéite with a small shift of 0.002-0.006 nm.

Dexferrum® (High molecular weight iron dextran; HFeD)

The diffractogram of the XRPD analysis shows good agreement only with akaganéite (**Figure 43**). NED patterns coming from single nanocrystals show *d*-distances of 0.720 nm, consistent only with akaganéite (**Figure 44 d**).

Ironate® (High molecular weight iron dextran; HFeD_G)

The diffractogram of the XRPD analysis shows good agreement only with akaganéite (**Figure 43**). Good quality NED patterns could not be collected due to the high dispersion of FeNP. In the best pattern two *d*-distances of 0.250 and 0.330 nm with an in-between angle of about 67.5° were observed (**Figure 44 e**). Nevertheless, this geometry is consistent with different iron oxides and oxy hydroxides. The similarity of HFeD_G XRPD pattern with the patterns of LFeD1, FeCM, LFeD2 and HFeD may imply that also this compound contains mostly akaganéite. In this case, the above-mentioned NED patterns represent the *[15-3]* projection of akaganéite [195].

Infed® (Low molecular weight iron dextran; LFeD2)

The diffractogram of the XRPD analysis shows good agreement only with akaganéite (**Figure 43**).

NED patterns from single nanoparticles (**Figure 44 f**) are consistent with akaganéite.

3.2.1.1. *Product comparison*

Iron dextran products

XRPD and TEM results show that the iron dextran products Dexferrum®, Infed®, Cosmofer® and Ironate® have an akaganéite or an akaganéite-like structure. All of the iron dextran products show similar XRPD profiles (**Figure 43**). The quality of the diffraction data seems to correlate with the size of the complexes. TEM results substantiate this observation.

New iron products

In contrast to the iron dextran products, the new complexes Feraheme®, Ferinject® and Monofer® do not show similarities between each other. XRPD and TEM data for Monofer® and Ferinject® indicate that the FeNP fraction of the complexes is akaganéite-like. The XRPD profile of these three samples is similar to that of the iron dextran products. The observation of nickel (Ni) in the Ferinject® sample, which was also found for Cosmofer® in the ratio of 1:100 (Ni:Fe) in both cases seems to have originated from the holder tip. Although natural akaganéite is known to host small amounts of Ni in its structure, pharmaceutics are not intended to contain Ni, as they are not generated from natural akaganéite but from solutions of $FeCl_3$. If Ni was impureness in the case of Cosmofer®, Infed® should also contain Ni, as they are in fact the same product. Ni is a dietary mineral, which can cause contact dermatitis and is considered carcinogen in humans as it leads to oxidative stress [204]. Symptoms for intoxication with nickel at plasma levels of 3 mg Ni/L are nausea, vomiting, weakness, headache, and palpitation [205].

The Feraheme® sample was identified as magnetite or maghemite (**Figure 37**). Magnetite with the molecular formula Fe_3O_4 or $Fe^{II+}(Fe^{III+})_2O_4$ has a spinel-like structure with the general formula AB_2O_4 [206]. The ferrous iron content of magnetite may have an influence on side effects in clinical use if the stability of the complex is not high enough. The fraction of iron that is loosely bound to the complex or already present in the formulation leads to free iron in form of ferric iron (Fe^{3+}). This is liberated by the complex in serum after application and bound to transferrin. Ferrous iron (Fe^{2+}) with a logK_a of 3.2 has a lower binding affinity to transferrin than Fe^{3+} (logK_a20.2) [207] and may be present as a toxic "free" state in serum for a short period of time. It is known to lead to the formation of active oxygen species by Fenton reaction, which may lead to free radical-mediated DNA and protein damage [208]. But for the reason that Feraheme® is a very stable complex with low free iron content [196] this may not play an important role. Maghemite $(Fe^{III})_2O_3$ also has a spinel-like structure where the ions are more or less randomly ordered in a similar way as for magnetite. The charge balance is maintained by site vacancies or lattice defects but no ferrous iron is included. [206] We exclude maghemite as a before mentioned possible structure [95] because some characteristic strong peaks are not present in SAED patterns.

Venofer and Ferrlecit

For Venofer® and Ferrlecit® previous investigations identified the FeNP cores as 2-line ferrihydrite (XRPD, TEM) [209, 210] and akaganéite, respectively (XRPD) [98] and suggested a possibly mixed structure [95].

Our analysis indicates that the iron oxy hydroxide in Venofer® and Ferrlecit® may be related to akaganéite or lepidocrocite. The XRPD patterns for Ferrlecit® and Venofer® are very similar.

Comparing TEM and XRPD results with the obvious difference to the akaganéite-like samples (Infed®, Ferinject®, Dexferrum®, Ironate®, Cosmofer®, Monofer®) in XRPD measurements implies that lepidocrocite seems to be the best possible interpretation. The data derived from the powdered sample are indicating that a non-crystalline, amorphous structure is possibly present in these two Fe-NbCDs.

Concerning the quality of the results it must be mentioned, that this interpretation is rather speculative. The influence of sample preparation leading to emphasized iron oxy hydroxide signals at the expense of crystalline sucrose signal is another disadvantage of this interpretation.

3.2.1.2. *Size influence on structure results*

In general, for XRPD analysis it was observed that the peaks of the iron phase are relatively broadened. Ironate®, Dexferrum® and Ferinject® show sharper and stronger peaks than the other three akaganéite samples Cosmofer®, Infed® and Monofer®.
This effect may be caused by the small diameter of the single nanocrystals and as a consequence by a low repetition rate of the single lattice planes and small areas of coherent scattering capability. This results in a low level of interferences, which superposes with the interference signal of a different nanocrystal and leads to low intensities of the measured signals as well as broadened and diffuse peaks. The correlation between size of the nanocrystals (size of the particle) and quality of the diffraction data can be seen in **Figure 43**. Size measurement results show bigger core sizes for Ferinject® and Dexferrum® as high molecular weight iron dextrans in comparison to Monofer® and CosmoFer®. The peaks of the smaller particles Monofer®, CosmoFer® and Infed® are broadened and small in comparison with Dexferrum®, Ferinject® and Ironate®. Larger nanocrystals lead to higher numbers of lattice planes and as a consequence to better quality diffraction data (**2.1.5.2**). This implies that there is a difference in size between Monofer®, Infed® and CosmoFer® with wide peaks and Dexferrum®, Ironate® and Ferinject® with stronger, less broadened peaks. With a diameter of about 5-10 nm (**Table 3**).
) of a single crystal and distances of about 1 nm between the lattice planes at smaller diffraction angles a typical long-range order of a crystal is hardly possible for all of the samples. This leads to a quality of the diffraction data for ED as well as XRPD analysis where it is partly not possible to refer them to one particular standard iron oxide / iron oxy hydroxide.

3.2.2. Structure information yielded from TEM (bright field) and STEM (dark field)

3.2.2.1. *TEM*

Iron sucrose (FeSuc)

Figure 45 & Figure 46 show TEM images of FeSuc. The sample contained mainly homogenous particles without high density FeOOH cores. The FeOOH cores found in some cases are at closer view (**Figure 45 right**) consisting of ultra-small particles that build a quasi core. The main fraction (**Figure 46)** of the contained Fe is present in a more complexed shape were the inorganic phase is homogenously distributed in the carbohydrate fraction building predominantly amorphous NPs.

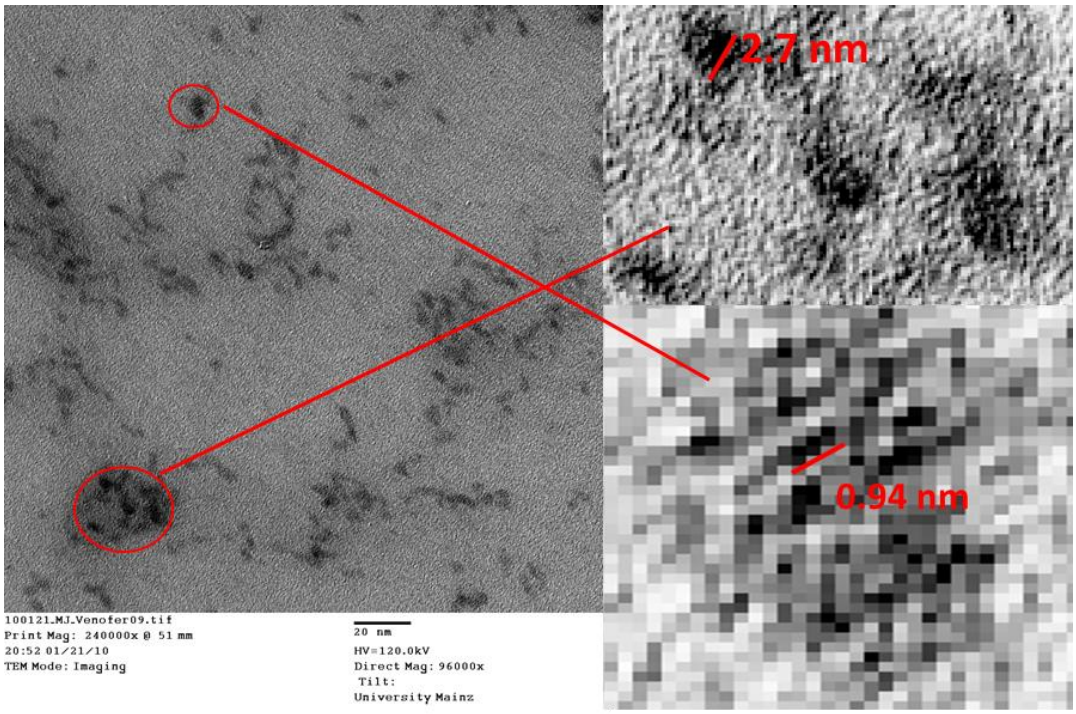

Figure 45 - TEM image of FeSuc (iron sucrose). Right side shows details of overview picture. Dark regions (high electron density) represent FeOOH-rich regions. Closer zooming in the electron rich "cores" discloses that in most cases no dense cores are present. The "cores" consist of super small FeOOH fragments mainly at the range of 1 nm in size. The most iron seems to be present in a complexed shape without a sharp boundary between the carbohydrate and inorganic Fe phases.

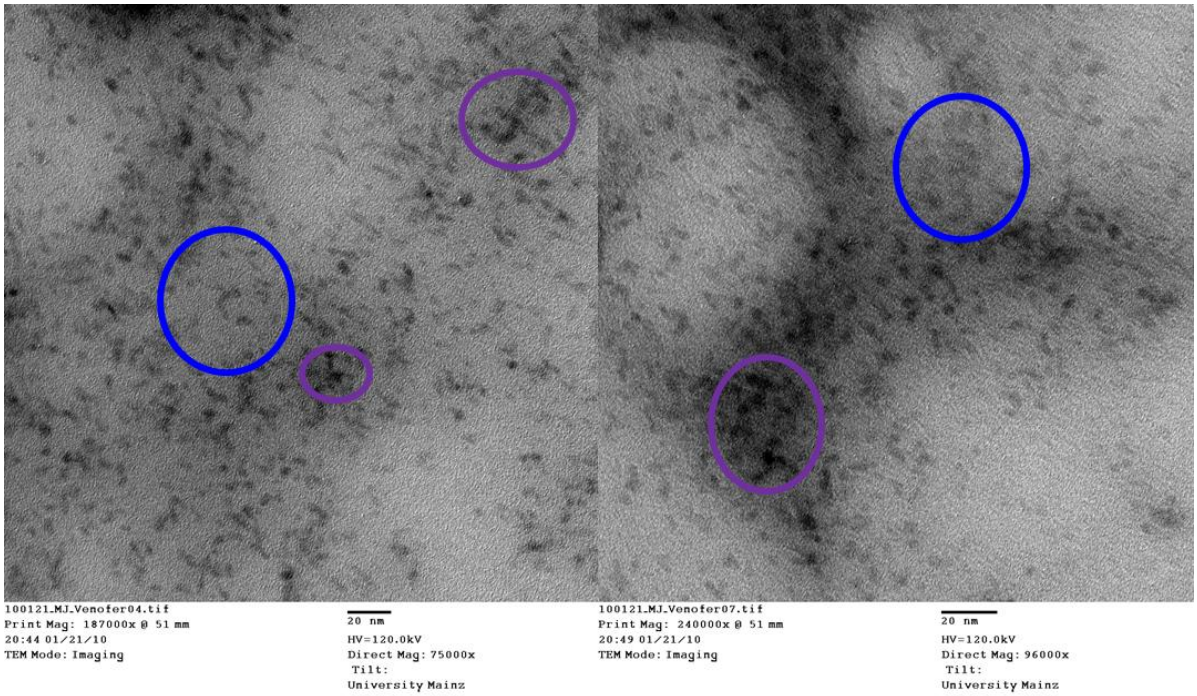

Figure 46 - TEM images of FeSuc (iron sucrose) indicating two different shapes of the complexed iron. Blue encircled particles seem to be homogeneous without a core and are the main fraction of the compound. The density is not high enough to conclude that there is a crystalline phase present. An amorphous phase is more probably forming monophasic particles with a mainly homogenous distribution of inorganic iron phase and organic carbohydrate. Violet encircled complexes consist of a very dark electron rich region indicating ultra small FeOOH particles clustered in a quasi-core and forming a multiple-core particle (Figure 45).

Sodium ferric gluconate (FeG)

FeG has similarities to FeSuc but consists partly of more spherical particles (**Figure 47**), which contain small cores of FeOOH, but not in most cases. The agglomerated form is the probable consequence of the sample preparation method with a drying step after dilution of the sample. The main fraction is - as in case of FeSuc - consisting of homogenous particles without a core, which may consist of a mixture of inorganic and organic material forming an amorphous particle.

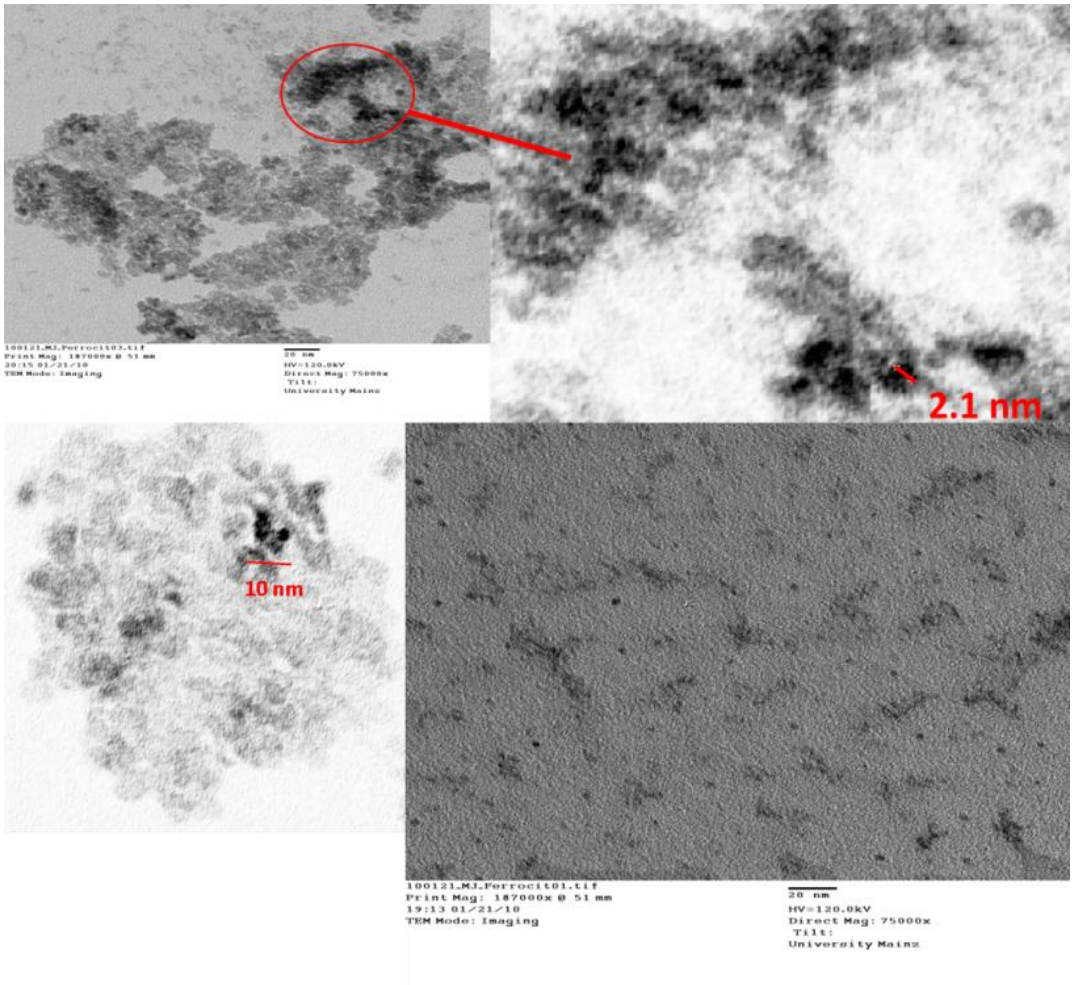

Figure 47 - TEM images of sodium ferric gluconate (FeG). Top left is an image showing clustered particles with very small, dark (electron rich) regions at the range of 2 nm consisting of inorganic material forming a core surrounded by material with decreasing density with more distance from the core (shell) - top right. Those core-shell particles are present in only a low number. Bottom left shows a uniform distribution of more homogenous particles representing the main appearance of complexed iron in the sample.

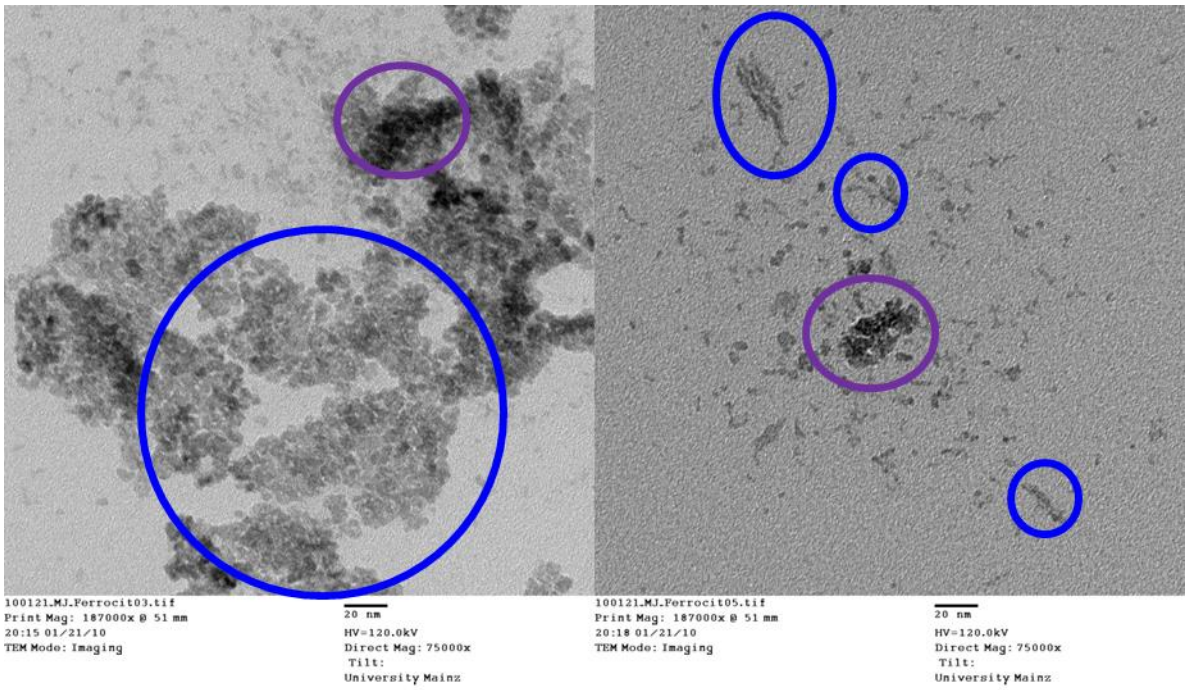

Figure 48 - TEM images of sodium ferric gluconate (FeG) showing two different kinds of particles: Blue encircled homogenous monophasic particles with a probable more amorphous shape. Violet encircled particles consisting of ultra small FeOOH cores clustered in a quasi-core and forming multi-core particles (Figure 47).

Ferric carboxymaltose (FeCM)

The TEM results of FeCM (**Figure 49 & Figure 50**) show differences to FeSuc and FeG with spherical particles consisting of inorganic material. Closer zoom on the particles indicate that they are not uniformly dense (**Figure 49**). Beside this there are mainly larger particles containing material with lower electron density indicating a lower content of inorganic material. A mixture of FeOOH and carbohydrate is probable in this connection. Inside those particles there are at some areas including ultra-small FeOOH cores at the range of 1 nm. Four different kinds of structures can be seen in **Figure 50** with spherical particles with high FeOOH content (red encircled), needle-formed particles with relative high Fe content (green encircled), lower density material probably of more amorphous structure that contains a mixture of FeOOH with carbohydrate (blue encircled), and particles that contain ultra-small particles. These are bedded in a carbohydrate matrix (violet encircled).

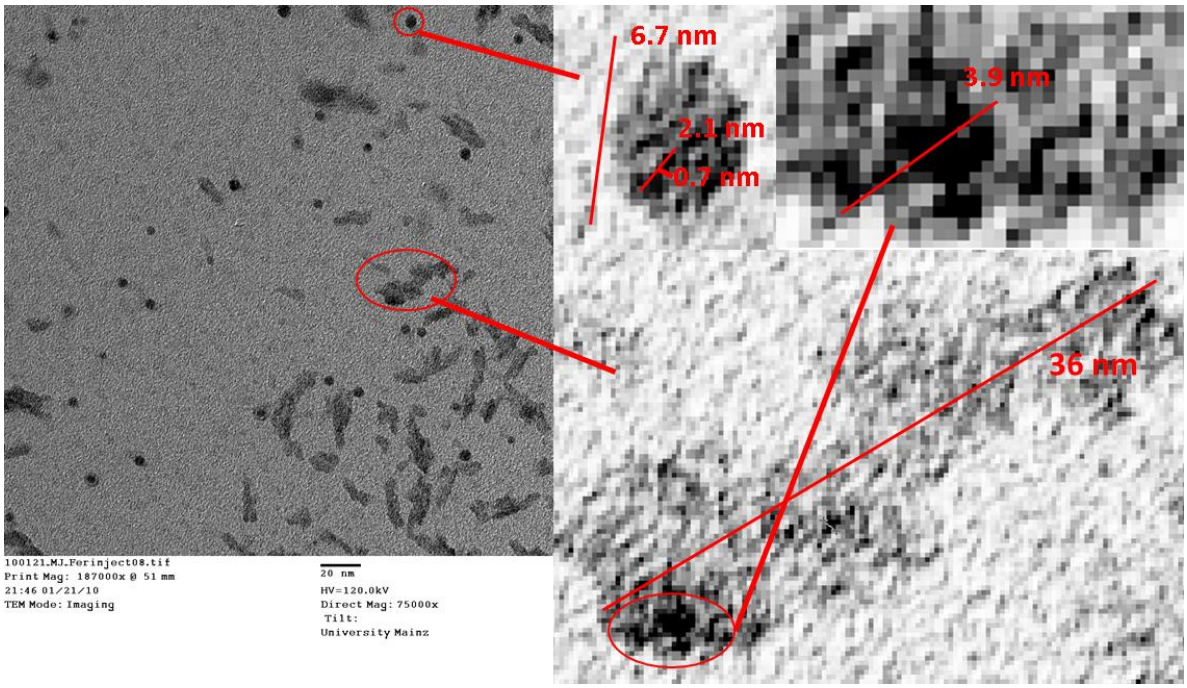

Figure 49 - TEM image of ferric carboxymaltose (FeCM) shows different shaped particles/cores. One kind is spherical and dark indicating high Fe content. By zooming closer in the particles (at the top) it can be seen that it is sharply bordered which indicates a core shell NP. Inside this core, it can be seen that it is not homogenously dense. There are regions at the range of 1 nm in size with dark-black (higher iron content) appearance indicating the presence of higher iron content than in the rest of the core. The second shape is a larger, geometrical undefined and less dense kind of particle (at the bottom) with a mainly homogenous appearance and partly also a kind of core (top right) or ultra-small core. These particles may also form needles (Figure 50).

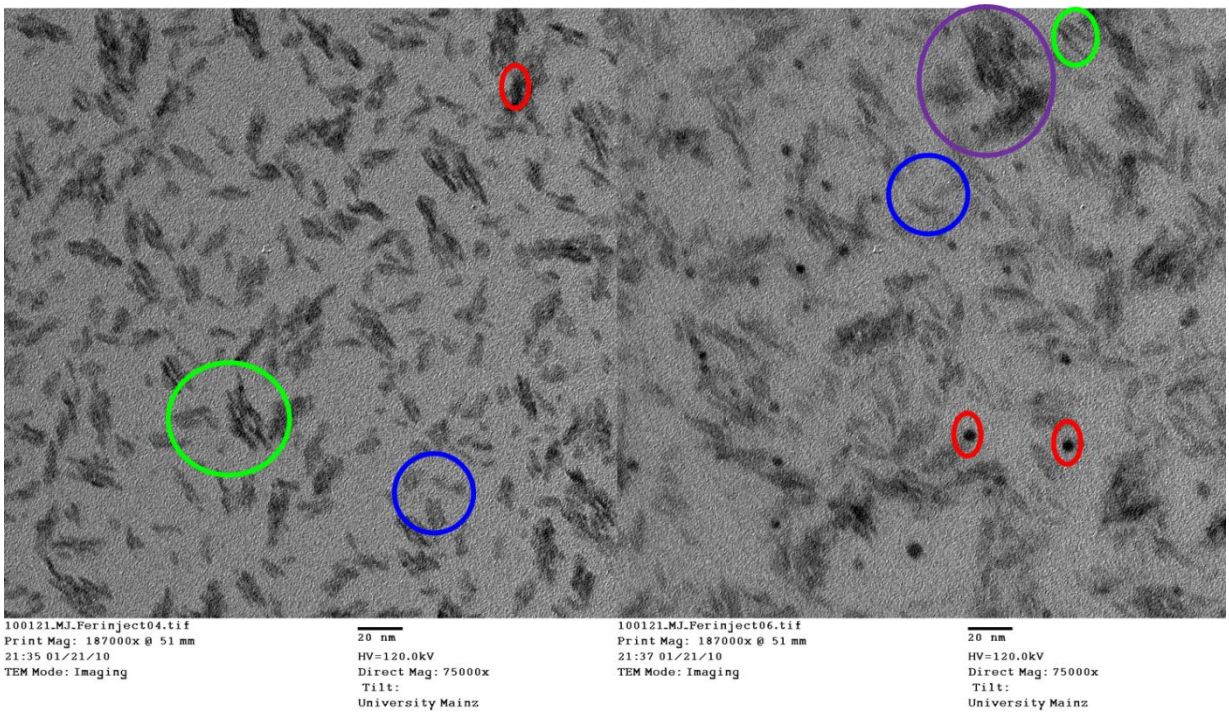

Figure 50 - Two TEM images of ferric carboxymaltose (FeCM) showing different kinds of iron containing NP. Blue encircled are particles without a core and relatively low density indicating a lower content of iron. Red encircled regions represent high iron density (FeOOH cores). Green encircled particles are forming needles with partly higher density. The violet encircled regions show particles, which contain ultra-small FeOOH cores at the range of 1 nm, which are bedded in a carbohydrate matrix (Figure 49).

Iron isomaltoside (FeIM):

TEM images of FeIM (**Figure 51 & Figure 52**) show particles mainly consisting of ultra-small FeOOH cores homogenously bedded in a carbohydrate matrix (bottom left in **Figure 51**; encircled violet in **Figure 52**) without contained big FeOOH cores. Only one big core can be seen, which seems to be an agglomerate of these ultra-small cores but is not characteristic for other regions of FeIM samples (**Figure 52** encircled red). Beside these matrix NPs there are homogenous particles with lower density indicating a homogenous mixture of carbohydrate with inorganic material (encircled blue). The needles as the third main fraction also partly consist of ultra-small cores being clustered to a big core inside a less dense shell with decreasing iron content (encircled green).

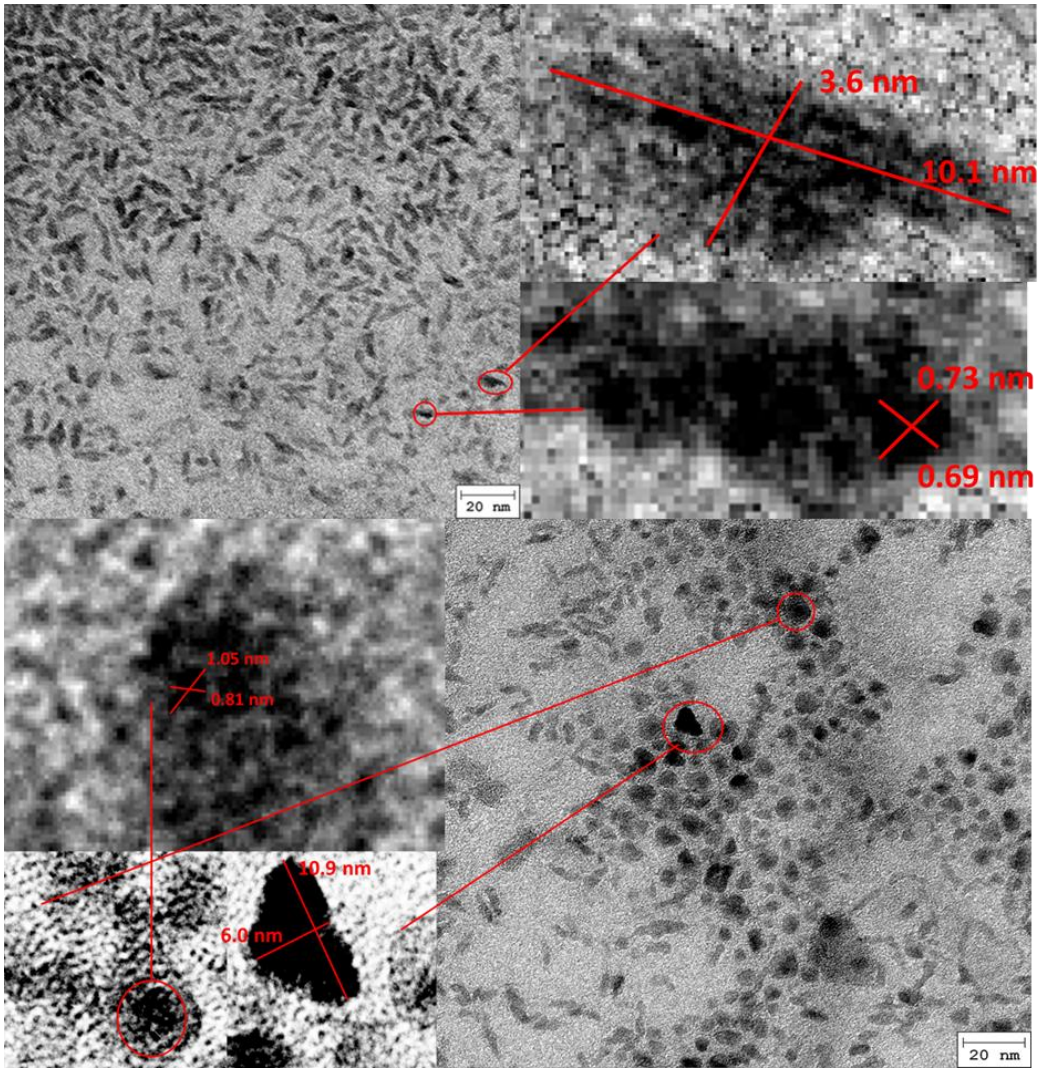

Figure 51 - TEM images of iron isomaltosid 1000 (FeIM). Top right shows mainly needles which contain a big electron dense region that is formed by clusters of ultra-small FeOOH cores (top right). The image (on the bottom) right shows particles consisting of ultra-small particles, which are homogenously distributed inside a carbohydrate fraction without forming a typical core. Bottom left shows a quasi-core, which is not characteristic for the sample as it was not found a second time in other images and seems to be originated by clustering of such ultra-small particles.

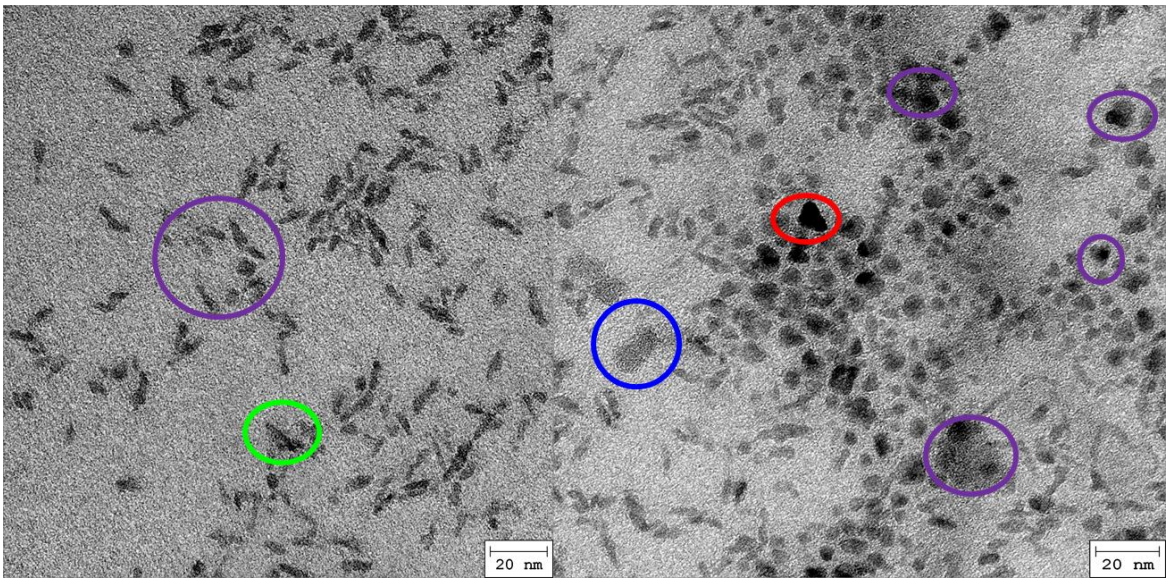

Figure 52 - TEM images of iron isomaltosid 1000 (FeIM) show mainly two different shapes of particles: Blue encircled are low-density regions with a more amorphous phase. Violet encircled are particles that contain ultra-small FeOOH core bedded in the carbohydrate. The red encircled high-density core is not characteristic for the sample as a core like this has not been present in another image again. It may be generated by clustering of ultra-small FeOOH cores.

Ferumoxytol (FePSC):

The TEM images of FePSC (**Figure 53 & Figure 54**) show particles containing ultra-small iron containing cores, bedded in a carbohydrate matrix and forming a quasi-core in some cases (**Figure 53;** encircled violet in **Figure 54**). Beside this, pure inorganic cores are present in low amounts and they are surrounded by lower density material (encircled red). The main fraction is build by particles with lower density and a homogenous shape probably formed by a mixture of iron oxide and carbohydrate with amorphous structure in which the inorganic cores are included in some cases (encircled blue).

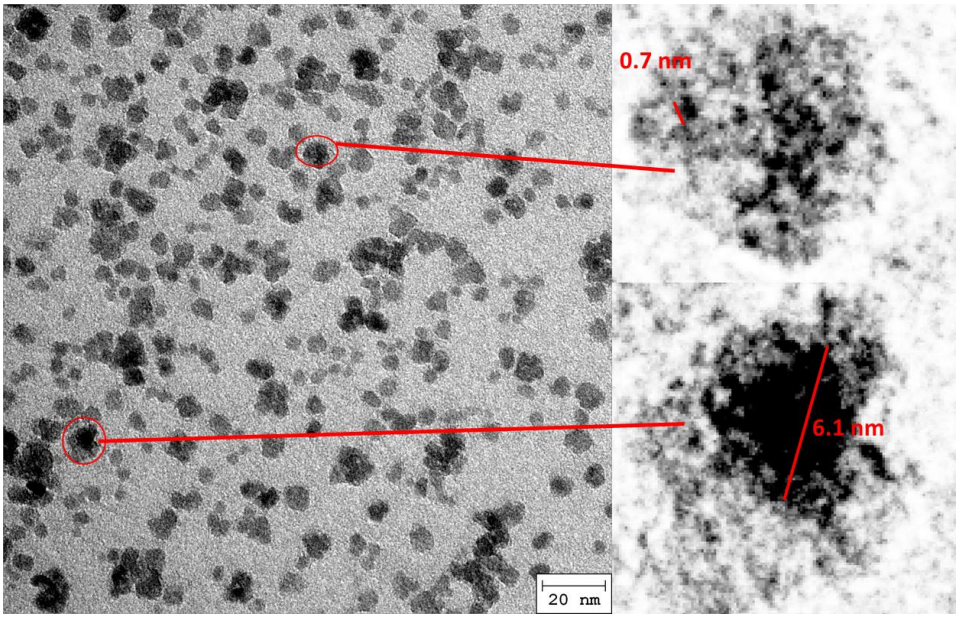

Figure 53 - TEM image of ferumoxytol (FePSC) with relatively high density particles consisting of ultra-small inorganic cores bedded in the carbohydrate mainly homogenously but partly forming clusters of cores which build a bigger quasi-core (bottom right).

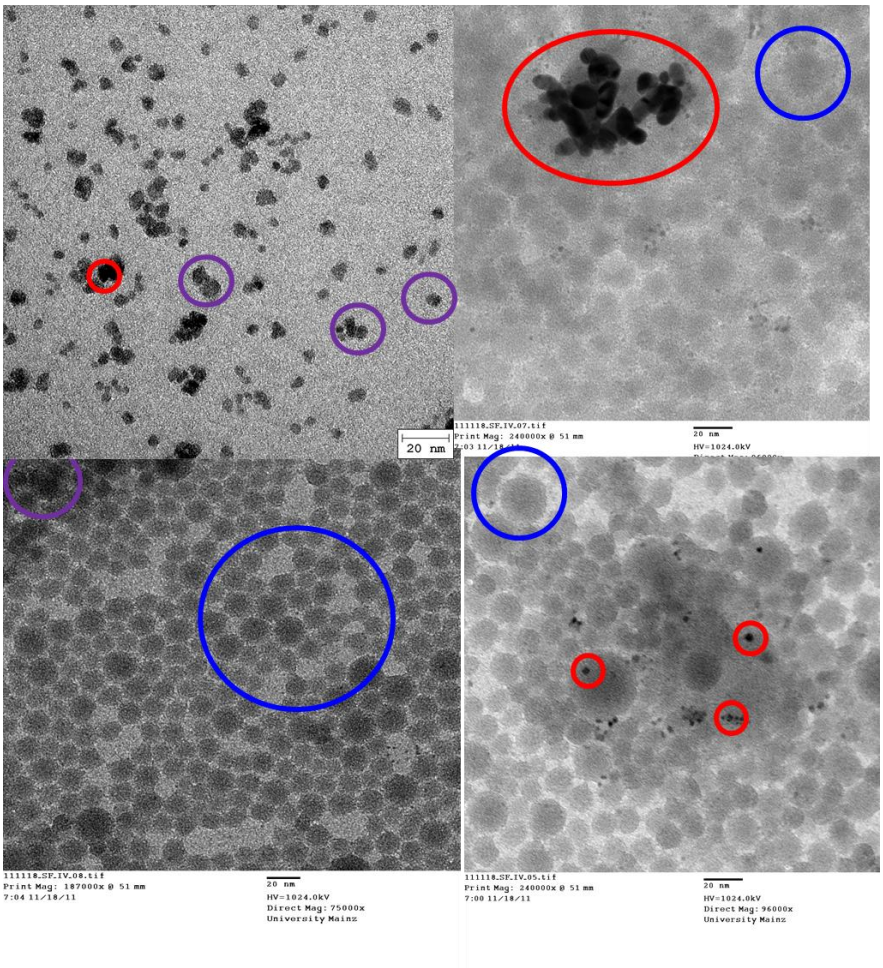

Figure 54 - TEM images of ferumoxytol (FePSC) with three different forms of complexed iron: Red encircled regions show high-density cores of purely inorganic iron containing cores. Blue encircled regions show lower density homogenous particles possibly consisting of a mixture between carbohydrate and iron phase. Violet encircled regions show particles in which ultra-small cores of iron oxide are uniformly bedded in the carbohydrate fraction (Figure 53).

High molecular weight iron dextran-original (HFeD):

The TEM images of HFeD (**Figure 55 & Figure 56**) show different shapes of iron containing NPs. Particles with ultra-small cores can be found only in a low number (**Figure 55;** encircled violet in **Figure 56**). In the TEM images presented in **Figure 56** some needle-formed particles with high density in relation to the ambient particles can be seen (encircled green). Beside this, high-density FeOOH cores can be seen in a high number (encircled red). As in case of the other compounds, homogenous particles with a less dense phase are present in high number. In some cases small FeOOH cores are embedded in those homogenous particles (encircled blue). These particles may consist of carbohydrate and, for the reason that their electron density is differing, complexed iron in a more amorphous state (alternating darkness because of different FeOOH content).

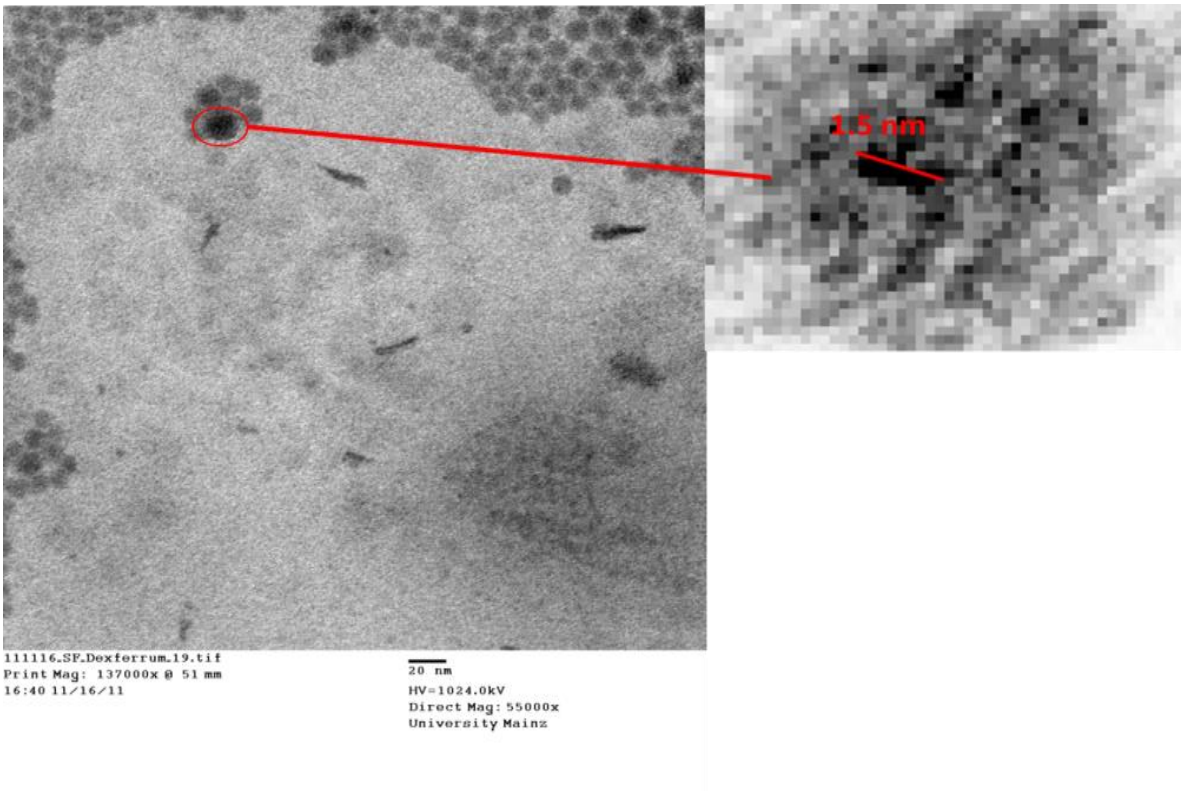

Figure 55 - TEM image of high molecular weight iron dextran (HFeD) showing a particle, which contains small FeOOH cores being embedded in the carbohydrate.

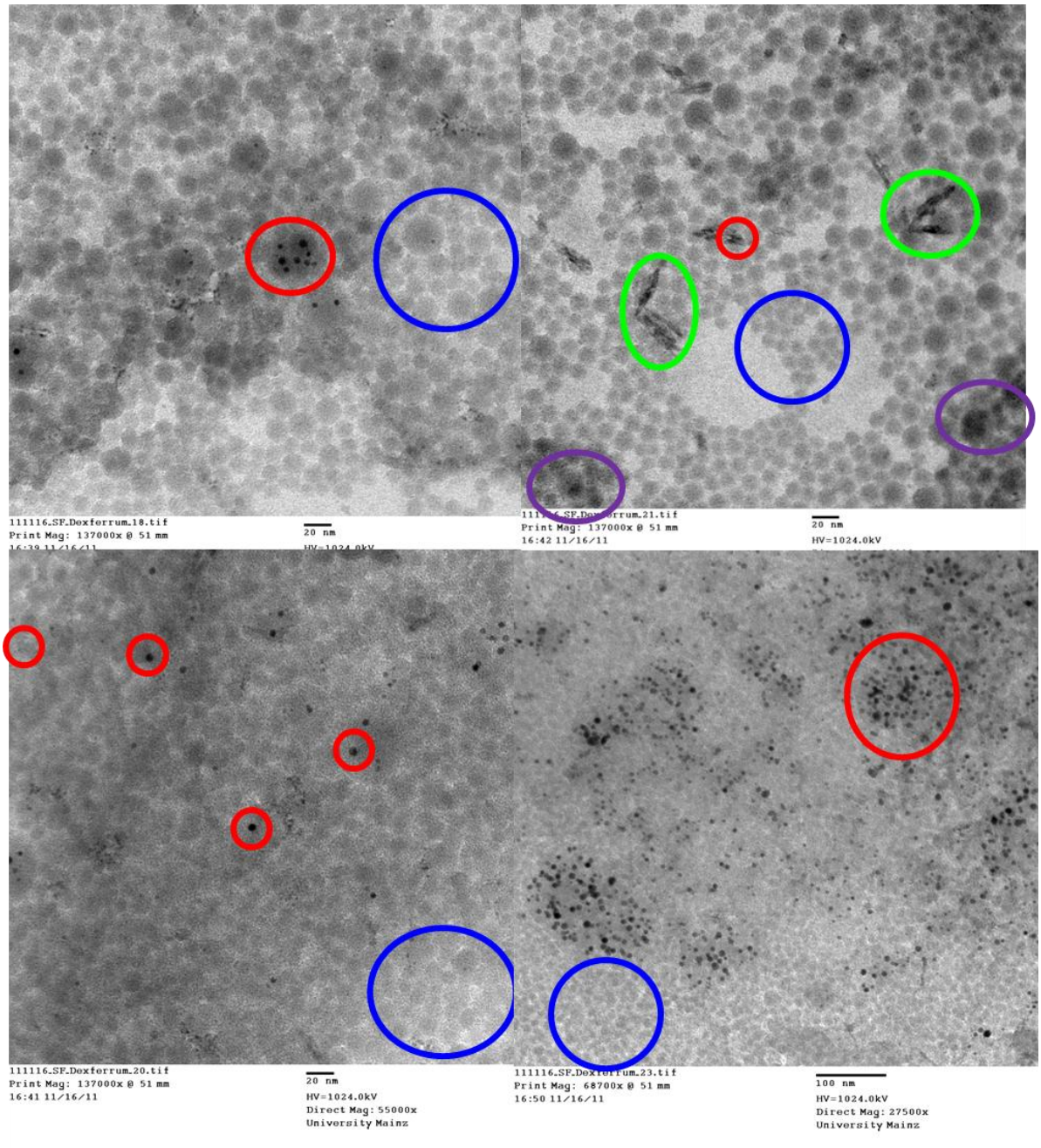

Figure 56 - TEM images of high molecular weight iron dextran (HFeD) presenting four different shapes. Red encircled regions contain high-density FeOOH cores. Green encircles particles have a needle form containing relatively high content of iron (darker than surrounded particles). Blue encircled regions contain lower density particles, which have a small core in some cases but are mainly consisting of a homogenous phase of a mixture between iron and the carbohydrate. Violet encircled particles seem to consist of ultra-small FeOOH cores but are not widely spread in the samples.

Low molecular weight iron dextran (Cosmofer®; LFeD1):

The TEM images of LFeD1 in **Figure 57 & Figure 58** show predominantly homogenous particles with relatively low density (encircled blue in **Figure 58**) and big cores only in some cases (encircled red). These particles appear similar to the particles found in the other compounds. By zooming in a higher electron region (**Figure 57**: bottom right) some ultra-small FeOOH cores can be seen with a size at the range of 1 nm. Such particles are present only in a low number (encircled violet).

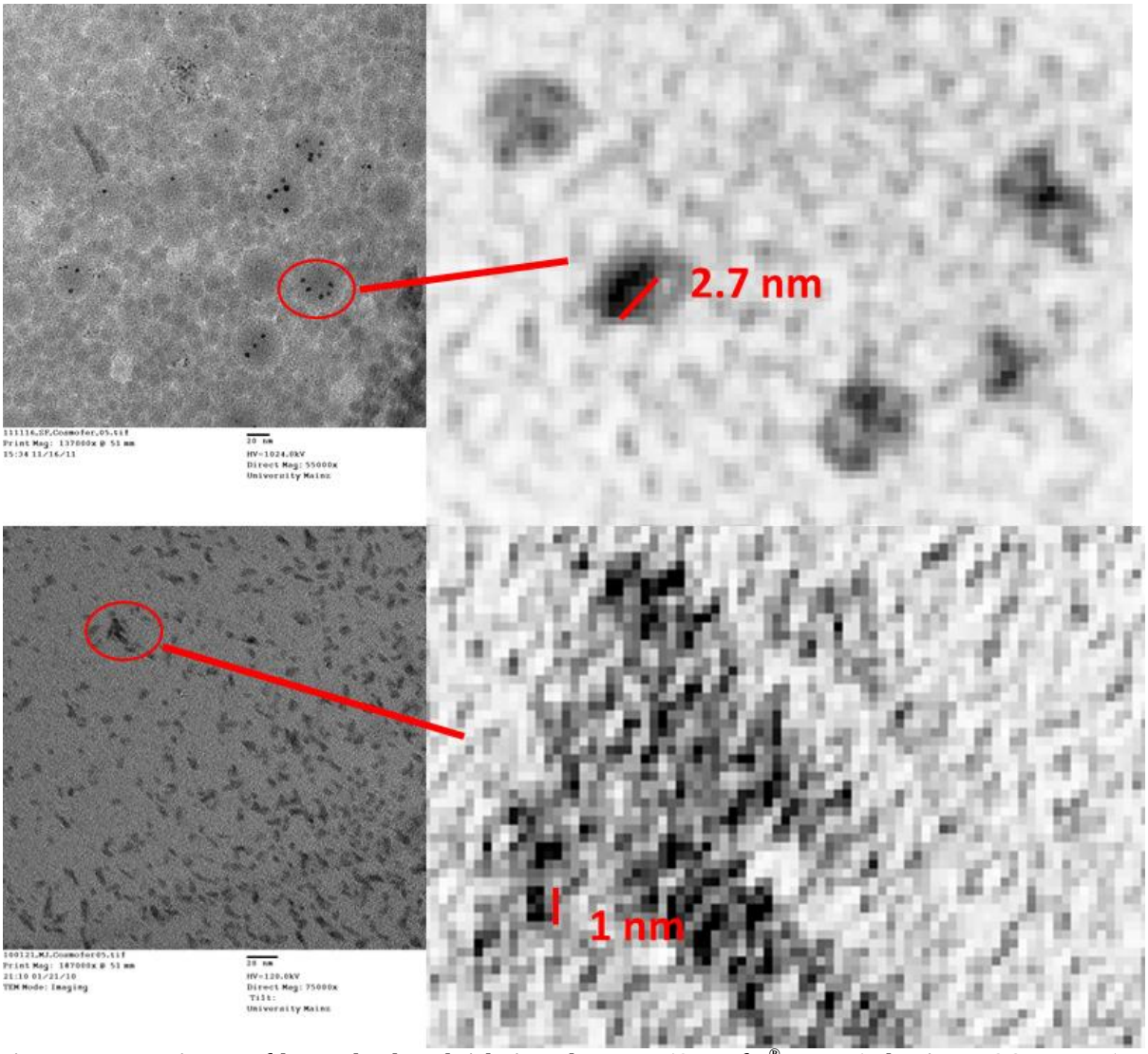

Figure 57 - TEM images of low molecular wheight iron dextran 1 (Cosmofer®, LFeD1) showing FeOOH cores (top right) and particles consisting of ultra-small FeOOH cores (bottom right).

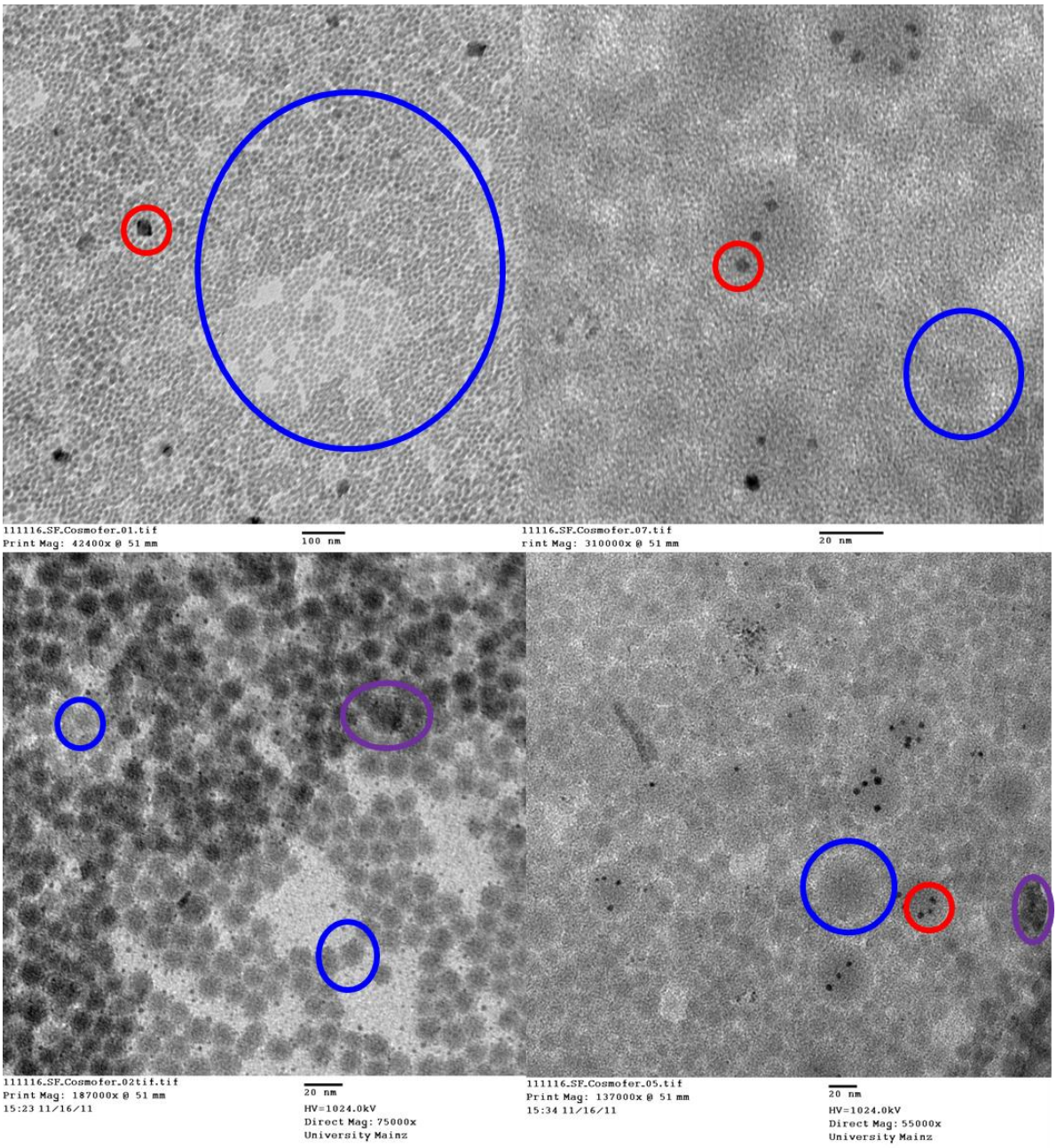

Figure 58 - TEM images of low molecular wheight iron dextran 1 (Cosmofer®, LFeD1) showing different kinds of structures. Red encircled regions contain high-density FeOOH cores. Blue encircled regions contain lower density particles, which have a small core in some cases but are mainly consisting of a homogenous phase of a mixture between FeOOH and the carbohydrate. Violet encircled particles seem to consist of ultra-small FeOOH cores but are not widely spread in the samples.

Low molecular weight iron dextran (Infed®; LFeD2):

The TEM images of LFeD2 show high similarities to LFeD1 (**Figure 59 & Figure 60**) with a major fraction of homogenous particles probably consisting of a more amorphous phase of carbohydrate mixed with FeOOH (encircled blue in **Figure 60**). In some cases, pure FeOOH cores are included in such particles (encircled red). Particles with ultra-small particles bedded in the carbohydrate are present in a low amount as in case of the LFeD1 sample (encircled violet).

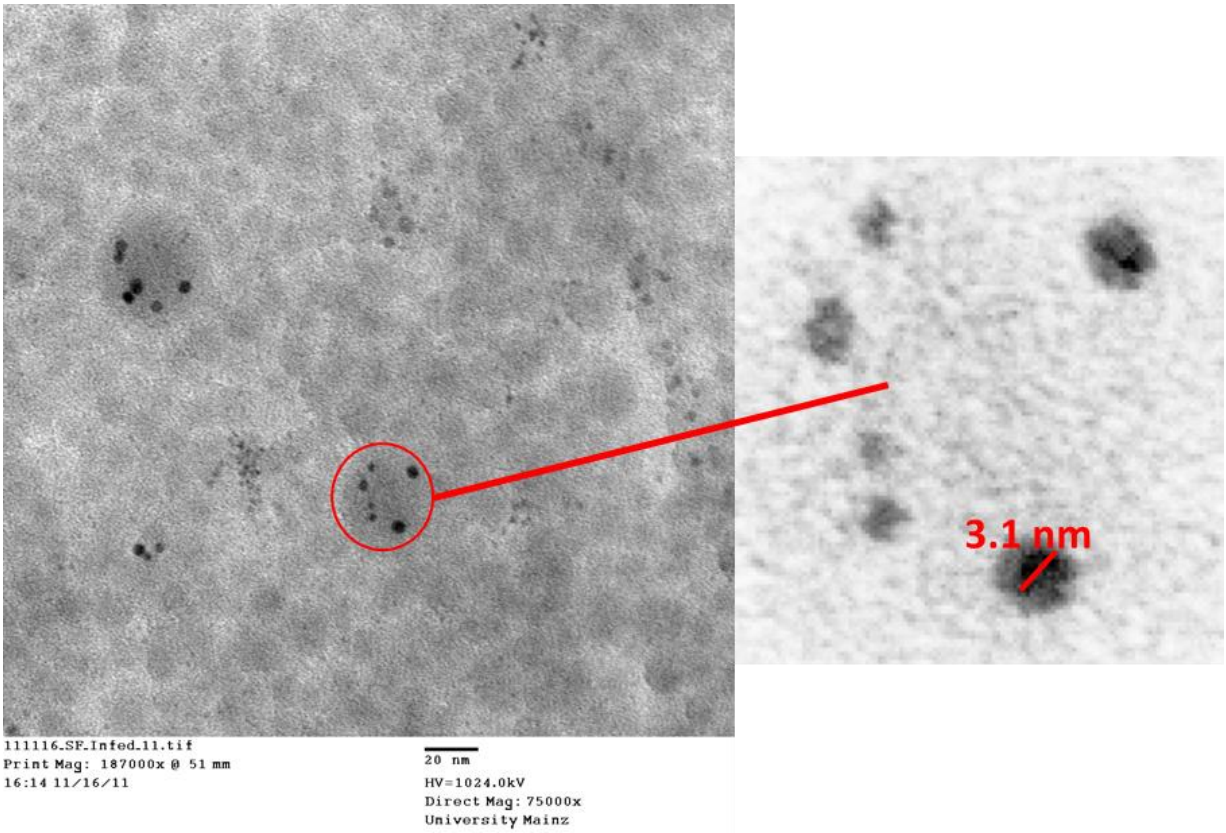

Figure 59 - TEM images of low molecular weight iron dextran (Infed®; LFeD2) showing NPs with included cores.

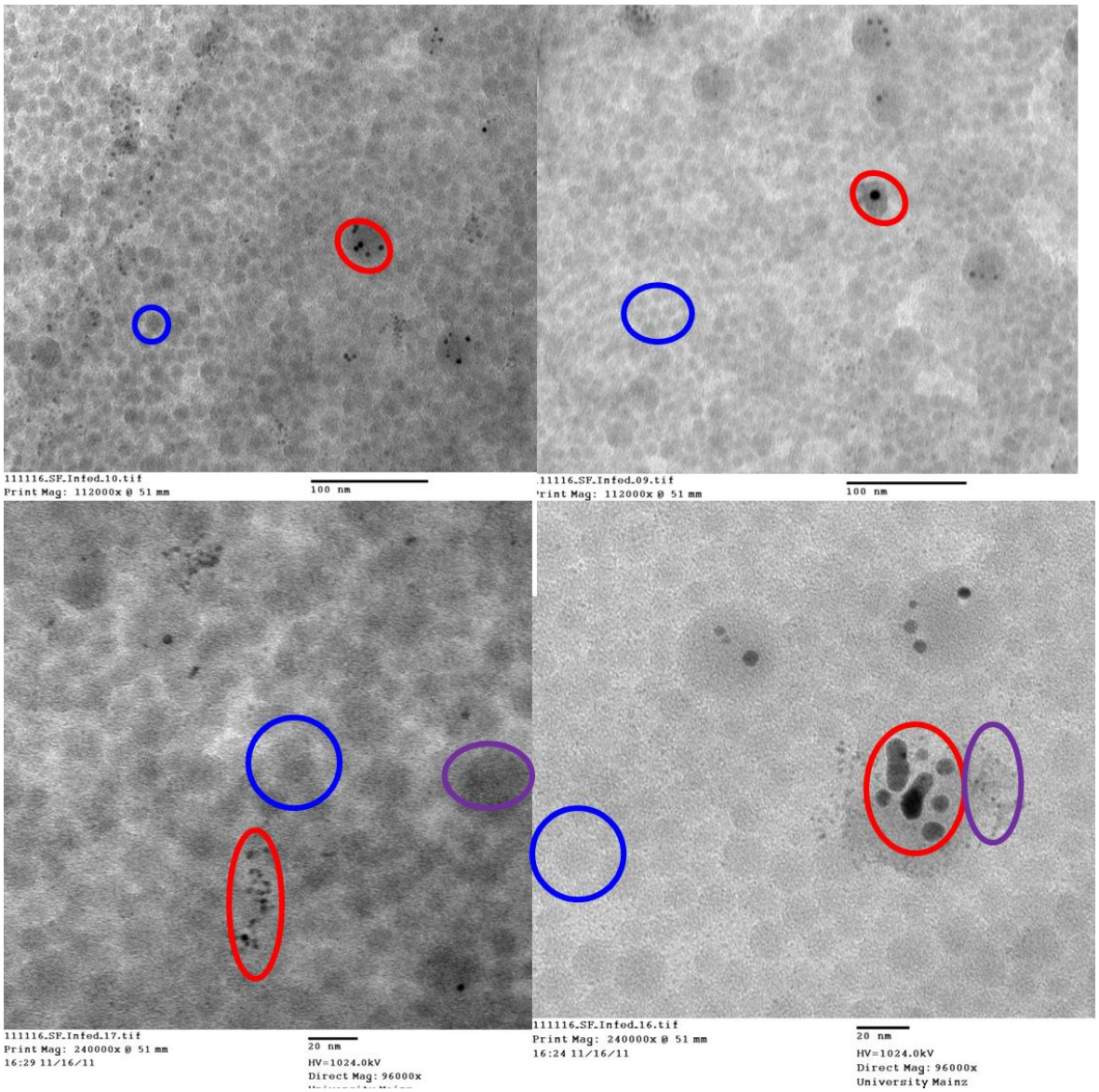

Figure 60 - TEM images of ow molecular weight iron dextran (Infed®; LFeD2) showing different kinds of iron containing NPs. Red encircled particles contain a dense FeOOH core. Blue encircled regions contain lower density particles, which have a small core in some cases but are mainly consisting of a homogenous phase of a mixture between FeOOH and the carbohydrate. Violet encircled particles seem to consist of ultra-small FeOOH cores, but are not widely spread in the samples.

High molecular weight iron dextran-generic (HFeD_G)

The TEM images of HFeD_G show best accordance with HFeD and less similarities with the LFeD samples (**Figure 61 & Figure 62**). The outstanding characteristic is a high amount of needle-formed particles with contained FeOOH cores in some cases (encircled green in **Figure 62**). Homogenous particles probably consisting of an amorphous mixture of carbohydrate with FeOOH are the main fraction beside this (encircled blue). In some cases, one or more pure FeOOH cores are included in such particles.

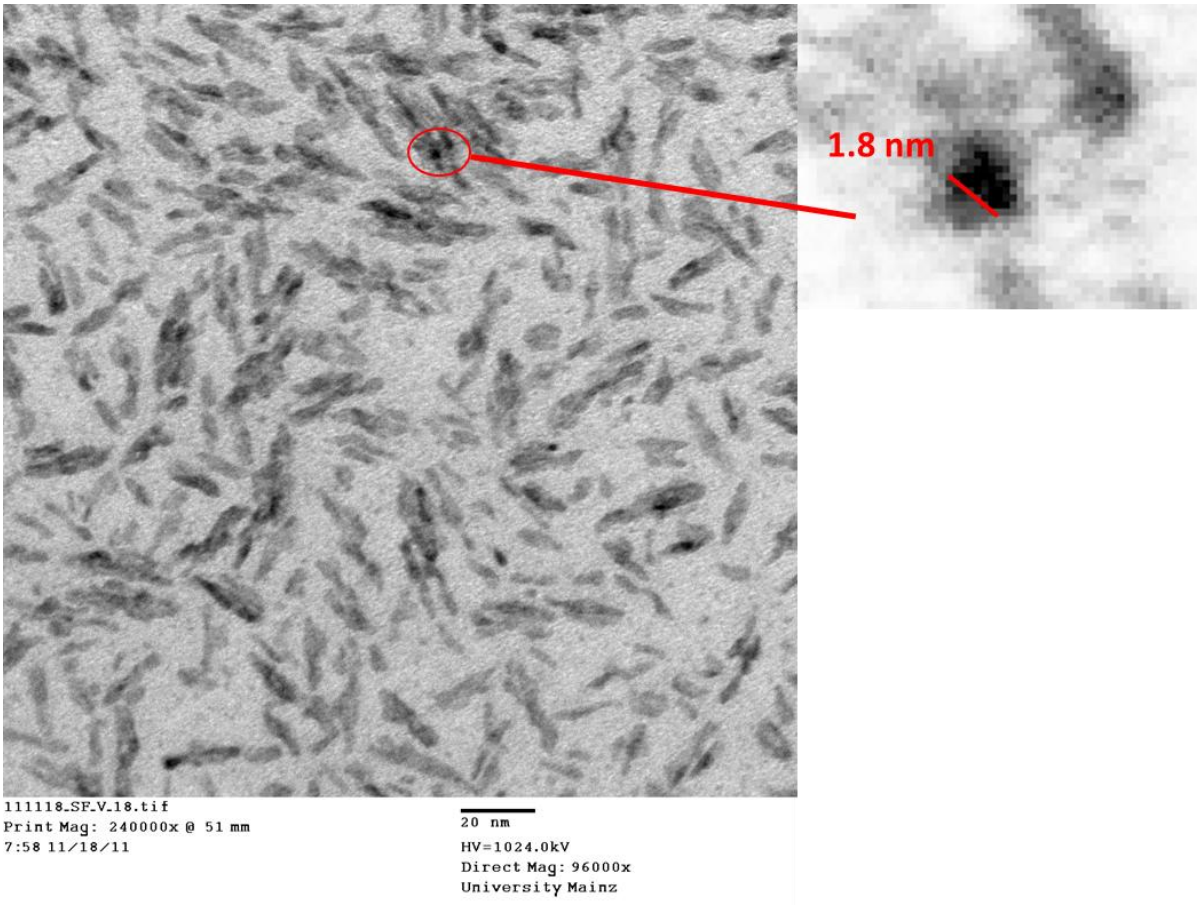

Figure 61 - TEM image of generic high molecular weight iron dextran (HFeD_G) showing particles with the shape of needles and partly containing FeOOH cores.

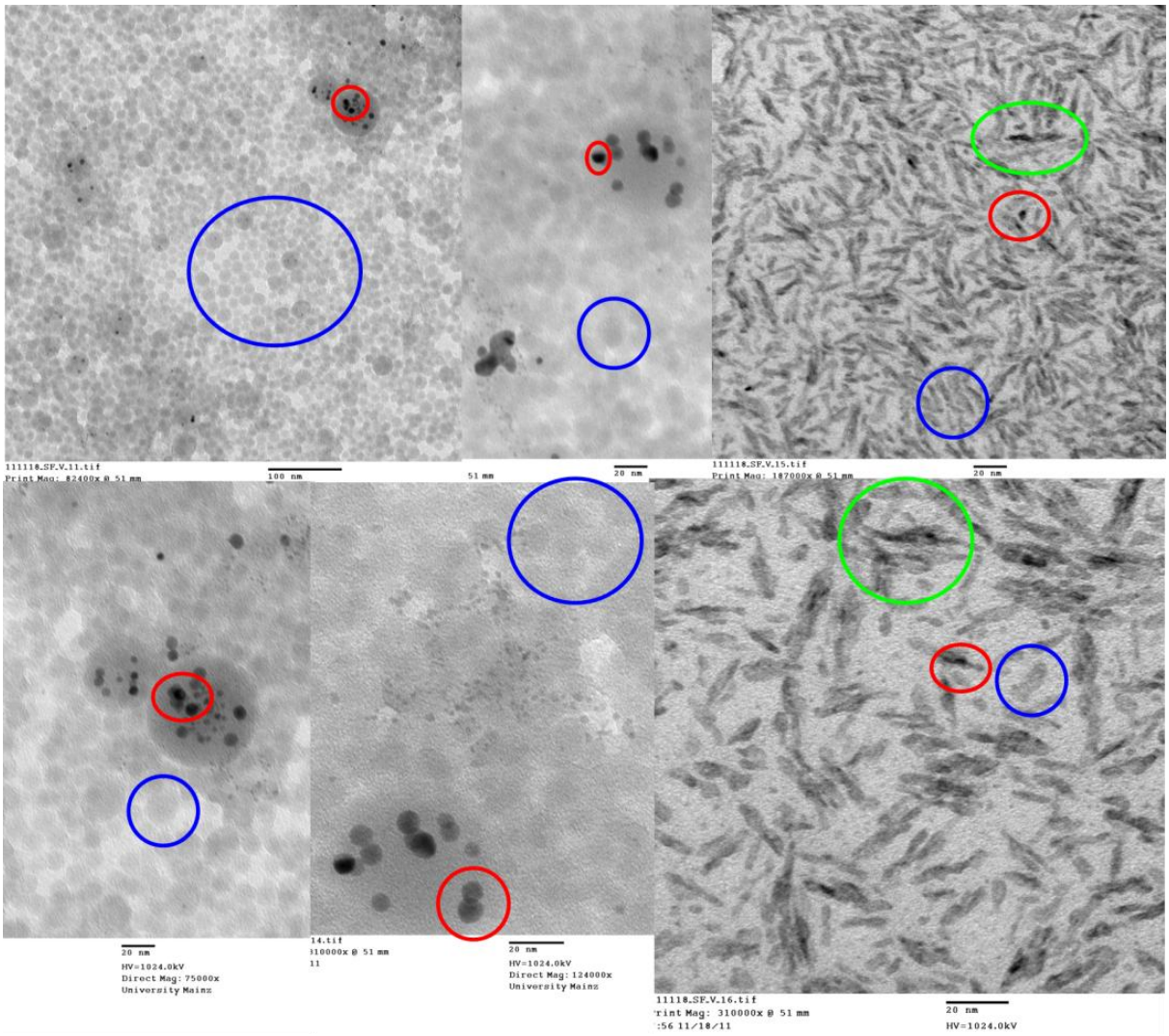

Figure 62 - Different TEM images of generic high molecular weight iron dextran (HFeD_G) that show the four different kinds of iron containing NPs: Red encircled regions contain high-density FeOOH cores. Green encircled particles are widely spread in the sample and have a needle form containing relatively high amounts of iron (darker than surrounded particles). Blue encircled regions contain lower density particles, which have a small core in some cases but are mainly consisting of a homogenous phase of a mixture between iron and the carbohydrate. Violet encircled particles seem to consist of ultra-small FeOOH cores, but are not widely spread in the samples.

3.2.2.2. *STEM*

STEM overview images obtained before the performance of electron diffraction investigations are presented in **Figure 63**.

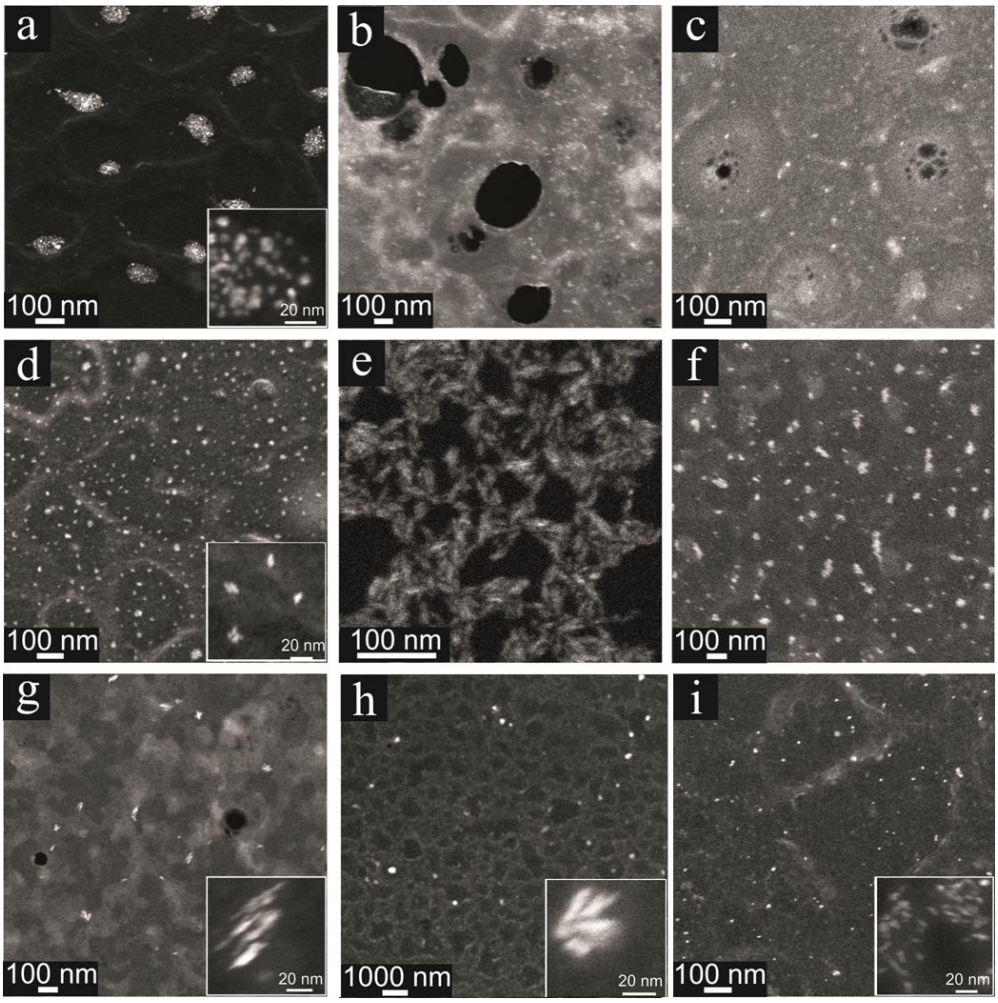

Figure 63 - STEM images of different samples: (a) Feraheme®; (b) Ferrlecit®; (c) Venofer®; (d) Cosmofer®; (e) Ferinject®; (f) Monofer®; (g) Dexferrum®; (h) Ironate®; (i) Infed®

FePSC:

STEM analysis of the FePSC sample shows that FeNPs agglomerate forming clusters up to 200 nm of about 100 units. Some isolated single particles can be recognized as well (**Figure 63 a**). The size of the single particles is less than 10 nm.

FeG:

STEM analysis of FeG showed crystals with diameters <10 nm (**Figure 63 b**).

FeSuc:

STEM analysis shows that the sample consists of crystals smaller than 10 nm (**Figure 63 c**).

LFeD1

STEM analysis of LFeD1 show that the sample consists of prolonged crystals smaller than 10 nm (**Figure 63 d**).

FeCM

STEM analysis shows that the sample consists of crystals less than 10 nm (**Figure 63 e**).

FeIM

STEM analysis shows that the sample consists of crystals smaller than 10 nm (**Figure 63 f**).

HFeD

STEM analysis shows that the sample mostly consists of prolonged particles around 20 nm in length, which often stay in agglomerates up to 50 nm in size (**Figure 63 g**).

HFeD_G

Result of STEM analysis of HFeD_G sample is very similar to HFeD and shows prolonged particles around 20 nm in lengths often agglomerated in clusters of more than 50 nm (**Figure 63 h**).

LFeD2

STEM analysis shows that most of the sample consists of small crystals smaller than 10 nm and prolonged particles approximately 10 nm in length with lower levels of agglomeration than HFeD_G and HFeD and high similarity to LFeD1 (**Figure 63 i**).

3.2.2.3. *Particle morphology summary*

Transmission electron microscopy (TEM)

Regarding the high total amount of iron in the formulations and the partly very low number of particles where an iron oxy hydroxide core can be seen in the TEM pictures the iron is possibly not only present as a so called core (**Figure 64 a**).

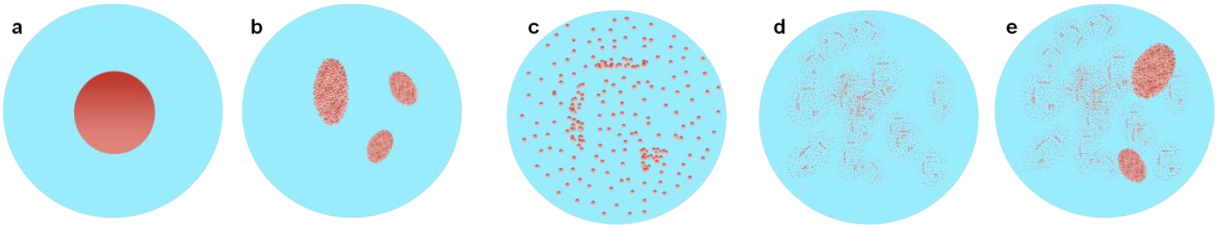

Figure 64 - Possible types of nanoparticles (NPs) from left to right:
(a) Classic core shell model as previously assumed [98, 194, 211] (LFeD 1 & 2, HFeD, HFeD_G, FePSC); (b) Polynuclear core of ultra-small cores which are agglomerated forming a quasi-core and surrounded by carbohydrate (compare to (e)): Present in case of FeCM, FePSC, FeIM (high incidence) / LFeD, LFeD2, HFeD, HFeD_G, FeG and FeSuc (low incidence); (c) Matrix like particles: FeIM, FePSC; (d) Homogenous particles with a more amorphous kind of structure (prevalent in case of all kind of complexes [encircled blue in Figure 46, Figure 48, Figure 50, Figure 52, Figure 54, Figure 56, Figure 60]); (e) Particles with cores or quasi-cores (like b) bedded in a more amorphous fraction which may be consisting of a mixture of carbohydrate and iron oxy hydroxide (like d): This kind of particle seems to be more realistic than (b) in case of complexes b as ultra-small cores can be recognized in most of those particles.

It is much more realistic, that the major fraction of the iron was present in a different form. A hint for that was the relatively high number of homogeneous particles without a core. In those particles, the structure may be either completely organic composed (carbohydrate without inorganic fraction) or a biphasic system where inorganic material is embedded into the carbohydrate structure to build up an homogeneous conformation (**Figure 64 d**). Concerning the high total content of iron, the biphasic system, where iron is bedded in the carbohydrate fraction, is very realistic. Those homogenous particles formed needles in some cases (HFeD_G, HFeD, FeCM, and FeIM) and contained cores with low prevalence (**Figure 64 e**). Especially in case of FeIM and FePSC a high fraction of particles was present, not consisting of a single (or small number of) core(s) but of a high amount of ultra-small cores which were bedded into the carbohydrate (or mixture of carbohydrate with iron phase). No such cores were found in case of FeG, FeSuc and FeIM. FeG and FeSuc were showing only a low amount of ultra-small cores and seem to tended more to an amorphous kind of structure (**Figure 64 d**). In case of FeIM and with lower incidence FePSC these ultra-small cores were present in high amount and they only barely clustered to a quasi-core. However, they were more homogenously distributed in a kind of matrix structure (**Figure 64 c**). Similar particles may have also been present in case of the other particles (encircled violet in the images) but were not of the same characteristic and homogenous shape as in case of FeIM and also FePSC. Pure inorganic cores were present in case of the dextran products LFeD1, LFeD2, HFeD, and HFeD_G as well as with lower incidence in case of FePSC, FeIM and FeCM. The bigger pure cores in case of FeIM and FeCM seem more to have been generated by agglomeration of ultra-small FeOOH cores (**Figure 64 b**) when the high-density details of the images are zoomed in. Whereas the bigger sized cores in case of FePSC and all dextran samples

seem to be generated during the manufacturing process as they seem more homogenous and dense (shape like **Figure 64 b** but core structure more like **a**).

Scanning transmission electron microscopy (STEM)

The STEM analysis shows that the FePSC sample looks totally different to the other samples (**Figure 63 a**), as the FeNPs aggregate in clusters of some hundreds of nanometers. This may be the consequence of the higher sensitivity with increased instability of the sample in matters of the sample preparation (diluting, spraying on the grid, drying under vacuum). FeCM also shows agglomeration and looks different to the other samples (**Figure 63 e**). The agglomeration in this case may be caused by the same reasons as in case of FePSC and may be promoted by charge effects since it is known that this particle shows a lower absolute ζ-potential than the other investigated formulations (**3.1.3**). FeG and FeSuc (**Figure 63 b, c**) again look different to the rest of the samples but show among themselves rather similarities. As expected LFeD1 (**Figure 63 d**) and LFeD2 (**Figure 63 i**) appear identical what is not surprising as they represent the same product with different brand names. The slight difference might be caused by the sample preparation technique. The small needles imaged at a higher resolution for HFeD (**Figure 63 g**) and HFeD_G (**Figure 63 h**) show high similarity. Monofer® (**Figure 63 f**) shows in STEM overview image most similarities with the dextran products. As TEM technique has higher resolution than STEM (**2.1.2**), it is more useful for a more detailed comparison between the different complexes (**3.2.2.1**).

Conclusion of structure analysis and elecron microscopy imaging

In Conclusion of all applied methods for the analysis of particle structures, the iron phase in LFeD1, FeCM, FeIM, LFeD2, HFeD_G and HFeD is identified as akaganéite/akaganéite-like, β-FeOOH with low levels of chloride. The iron phase in Feraheme® is identified as magnetite (Fe_3O_4) with spinel-like structure. Ferrlecit® and Venofer® were difficult to analyze; but the iron phase seems to fit a lepidocrocite/ lepidocrocite-like (*γ-FeOOH*), or a non-crystalline structure.

The combination of transmission electron and X-ray powder diffraction methods is a very helpful approach especially for low crystalline material or material with small single crystals in nano-scale. Parenteral iron containing non-biological complex drugs (Fe-NbCD) such as those investigated in this work, represent samples that are difficult to handle and to investigate by diffraction analysis. This may be caused by the small nanocrystals of the iron containing “cores” and the low levels of crystallinity that may be a consequence of interaction with the carbohydrate part of the complex. The presence of an interaction between iron in the inorganic phase and the carbohydrate chains has already been demonstrated for FeIM [95]. These formations may lead to low crystallinity and consequently to samples which are difficult to analyze by diffraction methods.

In this context, it is helpful to combine X-ray diffraction with electron diffraction. While X-ray allows higher resolution of small d-distances because of the low wavelength of about λ = 0.154 nm the combination of scanning transmission electron microscopy with diffraction analyses allows the selective investigation of crystalline areas in the sample.

For samples like FeSuc and FeG, this makes it possible to obtain information about the structure whereas each method on its own does not give sufficient information. Diffraction methods are at their limit because of the low crystallinity of the iron phase in the samples of Venofer® and Ferrlecit®.
In general, TEM investigations and X-ray results imply for all of the investigated complexes that beside a purely inorganic phase a mixed phase exists composed of carbohydrate and iron phase, respectively. In TEM pictures, a purely inorganic iron-containing phase with high electron density is imaged with very high contrast, whereas carbohydrates are not visible. Beside those areas there are also areas were a mixed phase seems to be present (lower contrast). Despite the high iron content in the products FeSuc and FeG we found X-ray powder diffraction results with low or non-iron oxide or oxy hydroxide peaks and electron diffraction (ED) results that show only ambivalent *d*-distances implying that there is a different structure with low crystallinity in these compounds.
A disadvantage of all the methods being applied in this work is that they are invasive methods with possible influence of the preparation methods on the obtained results. In every case, the samples had to dry before or during the measurements (XRPD), or they even were diluted prior to drying (TEM). Possible clustering and restructuring cannot be excluded because of this. For the FeCM sample, the effect of clustering can be seen in **Figure 63 e**.
Despite the quoted disadvantages and in respect of the missing alternatives the applied methods give an interesting insight into the molecular composition of different Fe-NbCD.
The applied physicochemical X-ray and TEM dependent analysis in combination with size and stability information makes it possible to elucidate differences between the Fe-NbCD and may additionally allow an assessment of pharmacological effects as bioavailability or toxicity.

3.3. Pharmacological safety

3.3.1. FerroZine® assay for the detection of labile iron

The coefficients of determination (R2) observed for the fitted second order polynomial in case of each complex except FeHES was always larger than 0.991 and in case of mean values for each complex always larger than 0.998. The absorption values in case of FeHES were very low. The resulting R2 observed for fitted second order polynomial was lower with a minimum of 0.961 for all samples and a minimum R2 of 0.980 in case of mean values.
Table 9 gives the mean results of the labile iron determination by FerroZine® reaction and fitting with a second-order polynomial. In **Figure 65** the graphical presentation of mean absolute values of labile iron dependent on the applied dose of 200 mg or 500 mg iron in the complex can be seen. **Figure 66** shows the mean relative labile iron dependent on the applied dose and the p-values of the Student's t-test between mean results of 200 mg and 500 mg equivalent dose. The mean values of relative labile iron content in the complexes independent from applied dose in decreasing order with p-values of the Student’s t-test for the consecutive complexes can be seen in **Figure 67**.

Table 9 - Results of labile iron determintion. Absolute values are given in µg/ml and dependent on the applied equvalent dose (D_{equ}). Relative values are normalized with the equivalent dose. Mean relative values give the mean of all measurements normalized with equivalent dose. In all cases except HFeD (P = 0.03) the relative amount (Figure 66) was significantly independent from equivalent dose (p > 0.05). In case of HFeD the difference can be related to the low number of investigated samples and the same independency can be assumed. FeS is a synonyme for FeSuc.

Complex			absolut		relative		mean relative		
	D_{equ} [mg]	*n*	**C [µg/ml]**	SD [µg/ml]	**C_{lab}/C_{total}** [%]	SD [%]	*n*	**C_{lab}/C_{total}** [%]	**SD [%]**
FeG	**200**	*15*	**3,043**	*0,363*	**4,564**	*0,545*	*22*	**4,410**	0,607
	500	*7*	**6,799**	*1,001*	**4,079**	*0,600*			
FeS	**200**	*16*	**3,293**	*0,499*	**4,939**	*0,749*	*27*	**4,756**	0,810
	500	*11*	**7,484**	*1,368*	**4,490**	*0,821*			
LFeD	**200**	*20*	**1,223**	*0,447*	**1,935**	*0,376*	*34*	**1,929**	0,391
	500	*14*	**3,202**	*0,663*	**1,921**	*0,398*			
FeIM	**200**	*13*	**0,702**	*0,091*	**1,053**	*0,137*	*10*	**1,060**	0,111
	500	*8*	**1,785**	*0,073*	**1,071**	*0,044*			
HFeD	**200**	*5*	**0,524**	*0,039*	**0,786**	*0,058*	*10*	**0,710**	0,109
	500	*5*	**1,057**	*0,156*	**0,634**	*0,094*			
HFeD_G	**200**	*5*	**0,668**	*0,078*	**1,003**	*0,118*	*21*	**0,951**	0,127
	500	*5*	**1,499**	*0,191*	**0,899**	*0,114*			
FePSC	**200**	*9*	**0,755**	*0,109*	**1,133**	*0,164*	*16*	**1,087**	0,151
	500	*8*	**1,724**	*0,190*	**1,034**	*0,114*			
FeCM	**200**	*8*	**0,482**	*0,112*	**0,723**	*0,167*	*17*	**0,773**	0,280
	500	*8*	**1,371**	*0,586*	**0,822**	*0,351*			
FeHES	**200**	*5*	**0,179**	*0,136*	**0,268**	*0,204*	*19*	**0,282**	0,155
	500	*4*	**0,497**	*0,066*	**0,298**	*0,040*			

The absolute labile iron content in the complex determined by FerroZine® assay is dependent on the applied dose (***Table 9;*** **Figure 65**) and is decreasing in the order of FeSuc ≥ FeG ($p = 0.110$) >> LFeD ($p < 0.001$)> FePSC ($p < 0.001$) ≈ FeIM ($p = 0.557$) ≥ HFeD_G ($p = 0.042$) ≥ FeCM ($p = 0.045$) ≈ HFeD ($p = 0.447$) > FeHES ($p < 0.001$) (**Figure 67**). The relative amount of labile iron (**Figure 66**) is significantly proportional to the applied dose ($p > 0.05$) except in case of HFeD with significant difference ($p = 0.03$) between 200 mg and 500 mg dose. This difference can be related to the relative low number of investigated samples and the relatively high homogeneity indicated by the low standard deviation (SD) in case of the mean results (***Table 9***).

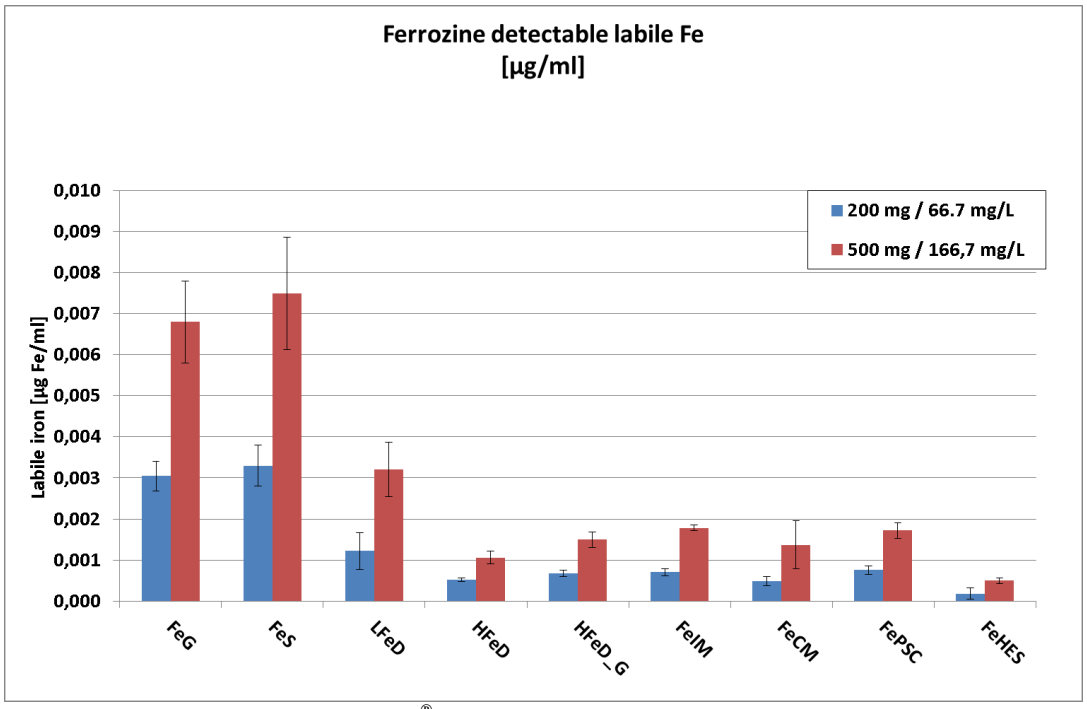

Figure 65 - Absolute values of FerroZine® detectable labile iron in the complexes (FeS = FeSuc) for equivalent doses of 200 mg (blue) and 500 mg (red) with achieved concentrations of 66.7 µg/ml and 166.7 µg/ml, respectively.

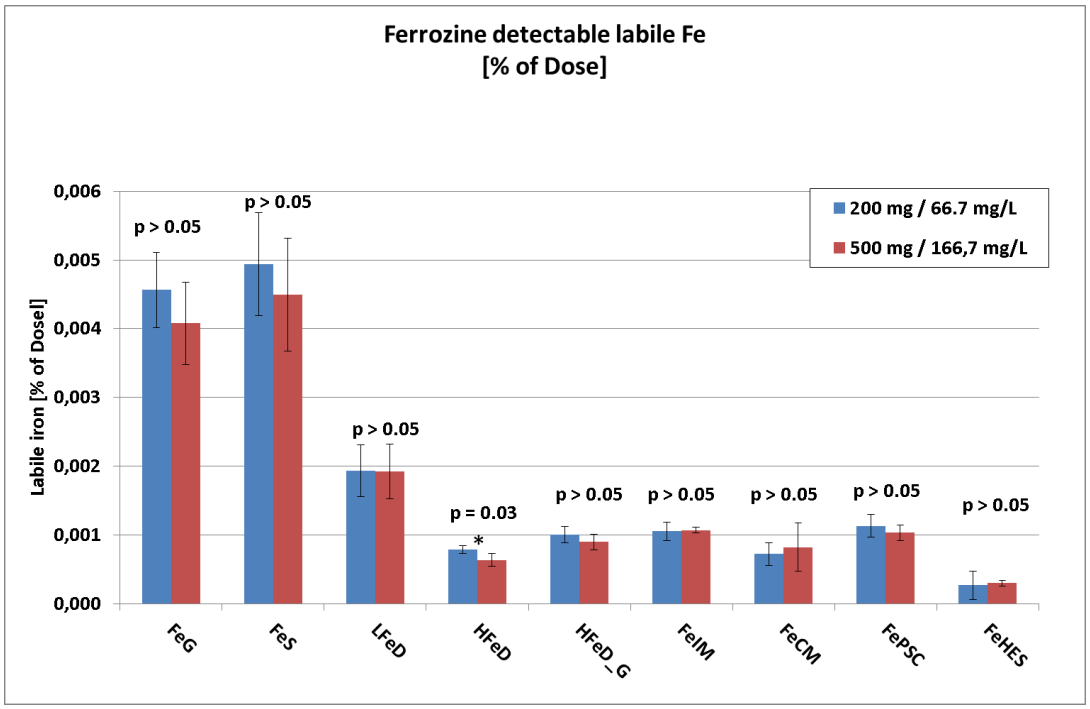

Figure 66 - Labile iron corrected with applied dose for equivalent doses of 200 mg (blue) and 500 mg (red). In all cases (p > 0.05) the detected labile iron content was independent from the applied dose except in case of HFeD (p = 0.03). FeS is a synonyme for FeSuc. The difference in this context can be related to the small number of samples with a low standard deviation for the yielded labile iron content. Thus, dose independency can be assumed for HFeD, too.

The mean results of dose independent relative labile iron content (**Figure 67*; Table 9***) of the different complexes indicate the highest fraction for FeSuc and FeG (4.4 - 4.8 % of the applied dose) with no significant difference (p = 0.110). The relative amount is ~2.5 times above the labile iron content of LFeD (app. 2 %) and even ~4.5 times (FePSC, FeIM, HFeD_G: ~1 %) or ~6 times (FeCM [~0.8 %], HFeD: [~0.7%]) higher than most of the other complexes.

The lowest content of labile iron was observed in case of FeHES (~0.3 %) which was more than 2 times lower than FeCM / HFeD, ~3 times lower than FePSC / FeIM / HFeD_G, more than 6 times lower than LFeD and even ~ 15-16 times lower than in case of FeG/FeSuc. The mean results of FePSC and FeIM showed no significant difference (p = 0.557) and were very similar to HFeD_G (p = 0.042). The p-value indicates significant difference but must be related to the measurement of HFeD_G for only one batch in one cycle and a very low SD in consequence. In general it can be seen, that in case of samples where more than one cycle with at least two batches were investigated (FeSuc, FeG, LFeD, FePSC, FeCM) the SD was notably higher than in case of measurements of only one batch and one cycle (FeHES, HFeD_G, HFeD, FeIM). FeCM and HFeD showed similar mean values (0.447) which are only marginally below the values of FePSC, FeIM and HFeD_G.

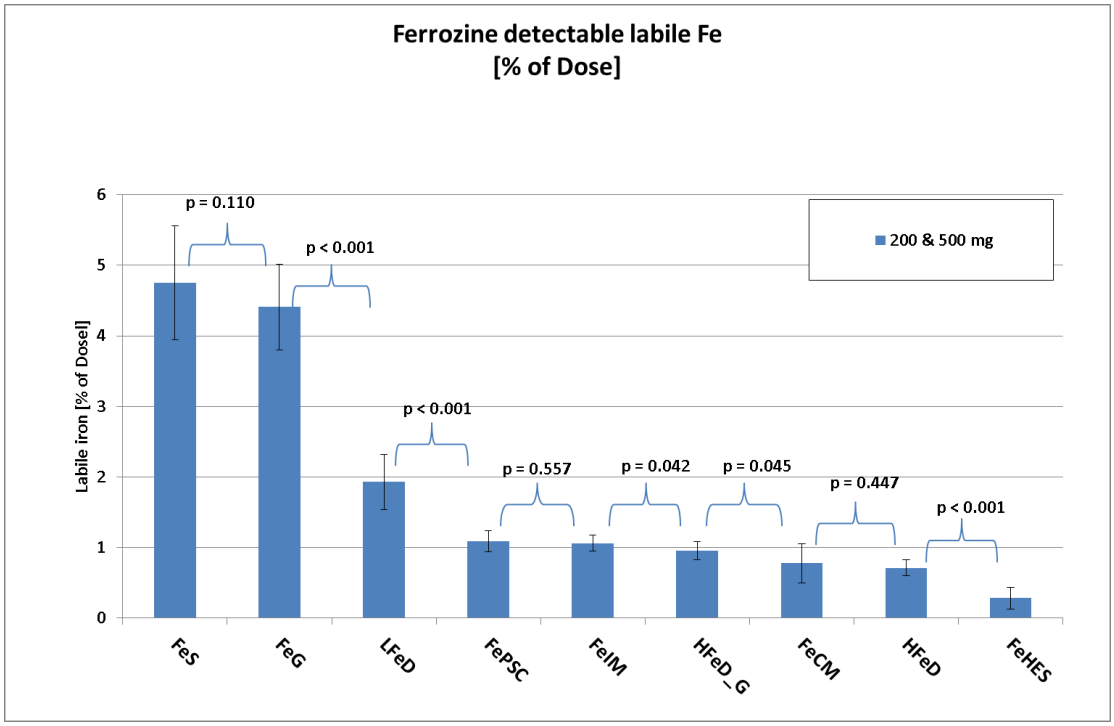

Figure 67 - Dose independent relative labile iron content in decreasing order from left to right with the results of Student's t-test in case of relative labile iron content of consecutive complexes. No significant difference was observed in case of FeSuc (=FeS) and FeG (p = 0.110), FePSC and FeIM (p = 0.557) as well as FeCM and HFeD (p = 0.447). Significant difference was observed between FeIM and HFeD_G (p = 0.042) as well as between HFeD_G and FeCM (P = 0.045). All other differences were highly significant (p < 0.001).

3.3.2. FerroZine® reaction kinetics and iron liberation

Liberation profiles were first compared to standard liberation kinetics by fitting and linear regression. Investigation of kinetic properties were performed for kinetics first- & zero-order, square root kinetics and RRSWB. RRSWB as well as first-order kinetics always showed lower R^2 mean values than zero-order and square root kinetics and can be excluded for that reason. Low R^2 values in case of FeHES can be referred to the overall low absorption values leading to higher influence of measurement errors. The R^2 values of the linear regression of the fitted liberation data can be found in ***Table 10***.

Table 10 - Mean R2 values of the fitted dose normalized VIS-spectroscopic absorption versus measurement time at 562 nm wavelength over at least 1 hr. Bold R^2-values show best accordance of the liberation profile to corresponding kinetics. FeS is a synonyme for FeSuc.

	Square root kinetics			Zero order kinetics		
	mean R^2	mean SD		mean R^2	mean SD	
FeG	**0.999**	0.001	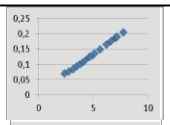	0.989	0.003	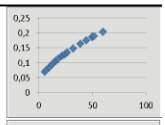
FeS	**0.999**	0.001	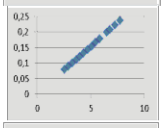	0.986	0.007	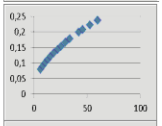
LFeD1	**0.993**	0.002	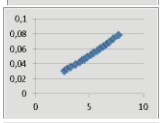	**0.994**	0.003	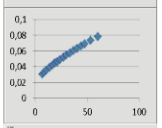
FeIM	**0.994**	0.002	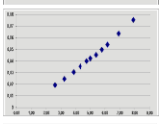	**0.995**	0.001	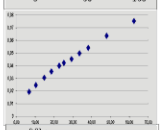
HFeD	**0.992**	0.005	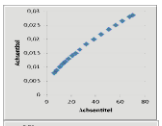	**0.992**	0.004	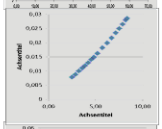
HFeD_G	**0.992**	0.003	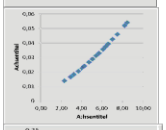	**0.994**	0.003	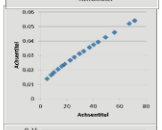
FePSC	**0.995**	0.001	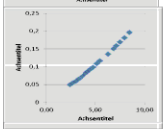	**0.992**	0.001	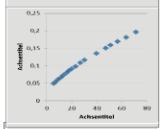
FeCM	**0.993**	0.004	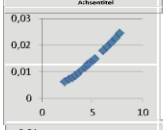	**0.992**	0.005	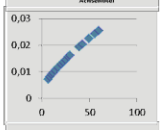
FeHES	0.969	0.016	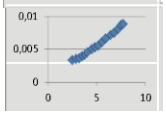	**0.986**	0.006	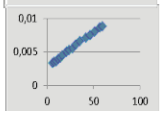

The liberation kinetics in case of the low stability complexes FeG and FeSuc can be very well related to square root kinetics with liberated amounts of app. 24 % (FeSuc)/20 % (FeG) of the complexed iron after 1 h measurement. In case of the other complexes, which show much slower degradation, the kinetics is not that clearly - perhaps as the measurement-time does not disclose the transition from lag time to equilibrium with uniform conditions. All complexes show good agreement with square root kinetics (R^2 > 0.992) except FeHES (R^2=0.969) which tends more to zero-order kinetics. However, especially in this case with detected amounts of iron below 1 % of the complete dose after 1 h measurement longer measurement time would be of advantage to clarify liberation kinetics. The liberation profiles of FeIM (R^2 =0.994; ≈ 8 % after 1 h), LFeD (R^2=0.993; ≈ 10 %) and FePSC (R^2=0.995; 8-9 %) show good accordance with square root kinetics. In case of FeCM (R^2=0.993; 3-4 %), HFeD (R^2=0.992; 3-4 %) and HFeD_G (R^2=0.992; 4-5%) the measurement time may have been too short.

Zero-order kinetics seems to fit best for FeHES (R^2= 0.986). The value is similar to FeSuc and FeG but the profile is not suitable to these two as the liberation rate obviously decreases with time (***Table 10***). The same can be seen in the profiles of LFeD, FeIM, HFeD_G, and FePSC, although the R^2 value indicates good accordance with zero-order kinetics (R^2>0.992). FeCM (R^2=0.992)and HFeD (R^2=0.994) seem to fit more to zero-order than to square root kinetics from view on the liberation profile.

Best accordance is shown in case of LFeD, HFeD, HFeD_G, FeCM, FePSC and FeIM with the fitting to $\frac{C_t}{C_{max}} = \boldsymbol{k} \cdot \sqrt[3]{\boldsymbol{t^2}}$ and R^2 values of 0.9973 (HFeD), 0.9982 (HFeD_G), 0.9985 (FeCM) 0.9989 (LFeD; FeIM) and 0.9992 (FePSC).

By fitting to square root kinetic and estimating the time until 50 % of the contained iron is released to the colored complex the increasing order of stability under the applied conditions is achieved with FeSuc ≈ FeG < FeIM ≈ FePSC < LFeD < HFeD_G < FeCM < HFeD << FeHES (***Table 11***)***.***

Half-life in case of low stability complexes may indicate higher risk of NTBI incidence as the NPs may be removed more slowly from circulation by macrophages of the MPS than they are degraded on plasma. In vivo, the half-lives listed in ***Table 11*** in case of high stable complexes are not of relevance from point of iron toxicity in serum but might indicate lower degradation rates in macrophages with consequently slower or decreased bioavailability. Nevertheless, it must be considered that in vivo enzymatical cleavage of the complex is elementary and is not considered in this *in-vitro* experiment.

Table 11 - Estimated time until 50 % of the contained iron is released from the complexes, under conditions of FerroZine® assay and assumption of square root kinetics. Fitting was performed with Formula 16 and time of 50 % release was calculated by including $\frac{Ct}{Cmax} = 0.5$. FeS is a synonyme for FeSuc.

	k [%/min$^{1/2}$]	$t_{50\% \text{ released}}$ [h]	SD [h]
FeS	3.10	4.4	0.5
FeG	2.36	7.6	1.1
FeIM	1.05	38.1	1.9
FePSC	1.01	43.5	13.1
LFeD	0.82	66.7	19.3
HFeD_G	0.57	134	25
FeCM	0.44	224	48
HFeD	0.41	267	66
FeHES	0.11	3703	1187

Square root kinetics [212] originally describes the dissolution of a soluble drug from pellets with high concentration of the drug inside an insoluble matrix, except an initial lag time and a terminal diffusion time exist [213]. The lag time is consequence of medium diffusing through the matrix and dissolving the drug. The dissolved drug has to diffuse through the matrix to be liberated into the medium. This system can be transferred to the FeNP in the investigated parenteral iron complexes. The inorganic FeOOH phase (FePSC: iron oxide) is complexed and surrounded by the carbohydrate fraction. In case of treatment with citric acid, ascorbic acid and FerroZine® (Fz) during FerroZine® assay the complexed inorganic phase is acidly dissolved, reduced from ferric to ferrous iron and complexed by Fz to form a violet colored complex. Like in the model described by Higuchi, the drug has to diffuse through a matrix before being complexed and consequently detected. A reason for the initially higher and over the time decreasing color-reaction rate may also be caused by different particle sizes and shapes. If smaller particles or/and particles with an amorphous or less crystalline structure are present, they will be dissolved more quickly and the iron is transferred more easy to the color reagent. As soon as those particle fractions are completely dissolved the dissolution of more stable (higher crystalline) and bigger particles is the rate limiting process.

In Summary, the *in-vitro* determination of labile iron, as well as the determination of the complex stability at use-oriented doses, allows the estimation of safety and might disclose one aspect, which contributes to bioavailability of the contained iron.
The estimation of complex safety is possible as dissolved iron from the complex is contributing to saturation of Tf with possible oversaturation (Tf-saturation level > ~80 %) and consequently present NTBI. Considering the relatively low buffer capacity of serum Tf (dependent on pre-saturation levels of Tf around 30 %) and the TIBC of about 12 mg in relation to iron doses of more than 100 mg and up to e.g. 1400 mg in case of a 70 kg weighing person (***Table 1***) the stability and safety aspect is essential. Especially free iron content in the formulation, loosely bound or labile iron in the complex, may cause iron toxicity in dependency on dose and complex characteristics. Loosely bound iron is dissolved by dilution in serum, or by preparation of the infusion dilution (e.g. in physiological sodium chloride solution). Labile iron is directly transferred from the particle to Tf or to low molecular weight complexing agents in serum (e.g. citrate with ~20 mmol/mL [214]).

The labile iron content as well as the degradation constant under the applied conditions is highest in case of FeG and FeSuc. LFeD shows lower, moderate labile iron content and degradation kinetics. This order of stability under different conditions is well documented in literature [48, 116, 215-227]. FeIM and FePSC show similar labile iron content and degradation kinetics. While the labile iron contents of FeIM and FePSC are lower than in case of LFeD, the degradation rate constant is minimal higher for these two complexes. Overall, they can be expected to be similary safe in respect to iron related ADEs and they might show similar bioavailability profiles if the physiological distribution profiles are comparable. The HFeD and HFeD_G as well as FeCM are degraded with similar kinetics under the applied conditions and the labile iron content is similar to FeIM and FePSC and comparable among each other. It must be generally mentioned, that batch-to-batch variations have not been investigated, but could show higher differences or more equality, than partly detected between different kinds of complexes. This could be from relevance for the relative order between FeSuc & FeG; FeIM, FePSC & LFeD; as well as FeCM, HFeD & HFeD_G in case of degradation profile. In case of labile iron content, the relative order could vary between FeSuc & FeG as well as FeIM, FePSC, HFeD_G, HFeD & FeCM when different batches are compared. LFeD in this case shows moderate lower values than the low stability FeSuc & FeG and moderate higher values than the other complexes with more tendency to FeIM or FePSC in case of batch-to-batch variations.

FeHES is outstanding in respect to complex stability as well as low labile iron content, which can be associated to the by far biggest complex size (***Table 4***). This indicates an excellent safety profile regarding iron related ADEs if the degradation in iron sensitive tissues (heart, kidney) is not remarkably increased under physiological conditions (e.g. macrophage activity during local inflammation). Nevertheless, even in such scenarios the FeHES complex is likely to be more stable than the other complexes.

3.4. Biological complex distribution in turkey embryos

3.4.1. Embryo weights

There was no significant difference between weights of control groups and intervention groups after 24 h (p = 0.120) or 120 h (p = 0.236) incubation times, respectively. (**Figure 68**) Embryo weight increases from about 25 g in mean after 24 h incubation (day 20 of egg development) to about 38 g in mean after 120 h incubation (day 24 of egg development).

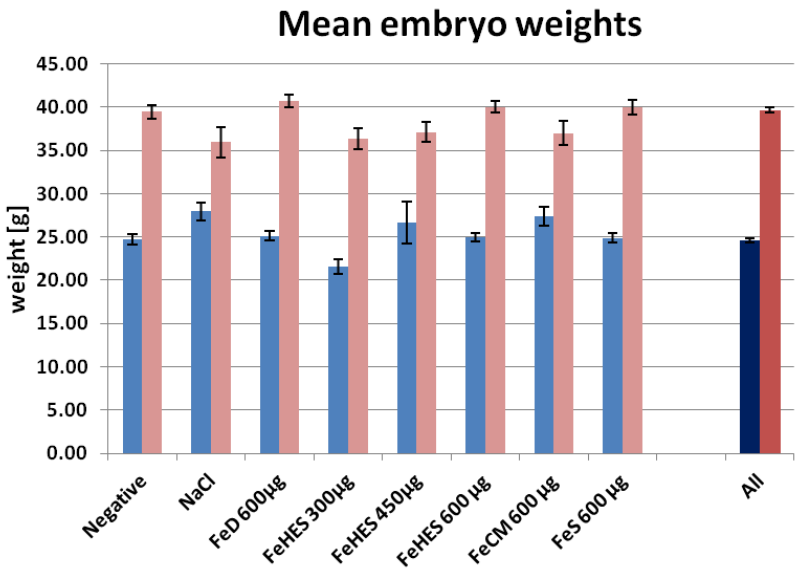

Figure 68 - Mean embryo weights after 24 h (blue) or 120 h (red) incubation, respectively. No significant difference between the groups was observed (24 h: p = 0.120; 120 h: p = 0.236). Error bars represent the standard error of the mean (SEM). FeS is a synonyme for FeSuc (iron sucrose) in the figure.

3.4.2. Identification of extreme outliers by box plot

Extreme outliers are values larger than 3 times IQR (interquartile range) in SPSS box plot evaluation. ***Table 12*** gives a list of extreme outliers. Mild outliers (values between 1.5 - 3 times IQR; circles in SPSS) are not listed. The values were not excluded from evaluation and considered like non-outliers.

Table 12 - Extreme outliers - 7 eggs negative control, 3 eggs NaCl control, 5 eggs FeD, 3 eggs FeHES, 8 eggs FeCM and 2 eggs FeSuc (FeS) yielded Fe levels in one or more tissues that were identified as extreme outliers.

Egg No.	Complex	Tissue	Egg no.	Complex	Tissue	Egg No.	Complex	Tissue
22209	Negative	Heart	22304	FeD	Heart	22235	FeCM	**
22250	Negative	Heart	22419	FeD	Heart	22462	FeCM	Heart
		Kidney	22575	FeD	Heart			Kidney
22265	Negative	Liver	22648	FeD	Kidney	22785	FeCM	Heart
22440	Negative	Liver	23117	FeD	Kidney	22823	FeCM	Heart
22503	Negative	Liver	23371	FeHES 450	Muscle	22866	FeCM	**
23004	Negative	Liver	23227	FeHES 600	Muscle	23059	FeCM	Kidney
23311	Negative	Heart	23269	FeHES 600	Heart*	23180	FeCM	Muscle
22217	NaCl	Kidney			Muscle	22624	FeS	Liver
22426	NaCl	**	22370	FeCM	Heart	22947	FeS	Heart
23093	NaCl	Heart			Kidney			Muscle

* lower outlier ** outlier for every kind of tissue

3.4.3. Embryo weights and extreme outliers: Discussion

The embryos that showed extreme outliers in one or more kind of tissues showed in some cases also physiological abnormality. For egg no. 23004 (negative control) which showed a high value for liver Fe content, the embryo weight was distinctly lower (19.6 g) than the mean weight of all embryos after 120 h (39.6 ± 4.7 g) and the liver was necrotic and colored brightly green, the same was seen for the gastro-intestinal tract. In addition, in case of egg no. 22426 (NaCl), the embryo weight was low for 120 h incubation time (29.7 g) and all tissues showed extreme outliers. The high value for muscle Fe in case of egg no. 23227 (FeHES 600) may be related to the low weight after 120 h (28.6 g). Embryo no. 22419 (FeD) had an intensive necrotic liver and the weight was quite low for 120 h incubation time (30.1 g). The weight of the embryo of egg no. 23180 (FeCM) with an outlier for muscle was also very low after 120 h incubation (24.5 g). The extreme outliers for egg no. 22866 (FeCM) in all tissues may be connected to the very low weight (17 g) after 24 h in relation to the mean value (24.6 ± 3.3 g). Egg no. 22059 (FeCM) with an outlier in case of kidney showed a green liver indicating abnormality as in case of egg no. 22947 (FeSuc) with a strange feet position, mild necrosis and yellow skin and tissues. The other extreme outliers did not show physiological abnormality.

Comparing the number of extreme outliers with the kind of treatment, FeCM and the negative control seem to produce most outliers. In case of the negative control, this could be a consequence of the way the eggs were chosen. In difference to intervention groups, eggs grouped as negative control had shown differences , as the CAM was not suitable for intravenous complex administration. This physiological difference could cause a non-coincident accumulation of abnormal embryos with extreme values. The total number of 8 outliers in case of FeCM seems to be different to the other intervention groups but in comparison to the total no. of eggs (230) no significant influence was observed ($p>0.05$). This indicates that the outliers are not reasonably determined by way or type of application.

3.4.4. Iron quantification in different tissues

An overview of the values of the Fe quantification separated for every trial and summarized for each tissue, incubation time and dose can be found in ***Table 13***.

Table 13 - Overview of the Fe quantification results:
The values are given as means of the sub-trial's results P-FeM1.13-P-FeM5.13 (FeM1.13-FeM5.13) and summarized for each incubation time and kind of tissue yielding the mean value of Fe content in the tissue of N (total number) eggs with standard error of the mean (SEM). FeS is a synonyme for FeSuc in this table.

Tissue	Iron compound	Iron dose [µg]	Iron concentration in tissue [µg/ml]														
			24h Incubation			Summary						120h Incubation			Summary				
			FeM1.13	FeM3.13	FeM5.13	Mean		N		SEM		FeM2.13	FeM4.13	FeM5.13	Mean		N		SEM	
Liver	Negative	0	52,05	39,51	37,43	44,4	45,04	47	77	5,43	4,03	48,05	77,18	30,76	53	47,5	44	70	9,94	7,91
	NaCl	0	53,03	39,06	-	46,05		30		5,99		59,19	25,13	-	38,23		26		13,10	
	FeD	600	384,83	500,29	-	449,78		32		25,98		319,61	422,51	-	380,59		27		23,59	
	FeHES	300	-	-	250,44	250,44		11		21,39		-	-	120,89	120,89		11		9,08	
	FeHES	450	-	-	355,61	355,61		11		25,30		-	-	253,24	253,15		7		40,21	
	FeHES	600	407,47	340,35	419,47	384,54		44		12,16		261,61	297,90	281,95	282,00		44		14,47	
	FeCM	600	507,87	559,86	-	536,92		34		28,75		296,51	400,83	-	361,26		29		28,23	
	FeS	600	472,48	460,18	-	465,40		33		13,38		331,35	332,93	-	332,37		28		20,24	
Heart	Negative	0	6,66	5,35	5,06	5,84	5,69	47	79	0,29	0,19	6,58	7,63	6,68	6,95	6,94	48	73	0,19	0,15
	NaCl	0	6,00	5,04	-	5,49		32		0,16		6,80	6,99	-	6,93		25		0,26	
	FeD	600	21,11	21,03	-	21,07		32		0,66		15,76	15,06	-	15,34		28		4,21	
	FeHES	300	-	-	28,70	28,7		11		1,76		-	-	16,10	16,1		11		1,73	
	FeHES	450	-	-	34,99	34,99		11		2,10		-	-	24,05	24,05		7		2,36	
	FeHES	600	43,85	45,46	44,84	44,74		45		0,96		26,48	32,71	29,44	29,84		44		6,43	
	FeCM	600	30,06	32,77	-	31,57		34		1,61		15,84	17,53	-	16,89		29		4,58	
	FeS	600	24,52	24,41	-	24,46		34		0,65		15,57	17,81	-	17,04		29		4,52	
Kidney	Negative	0	5,40	4,83	4,63	5,01	5,06	46	78	0,20	0,18	6,62	5,83	5,53	6,11	6,08	48	74	0,22	0,19
	NaCl	0	6,12	4,27	-	5,13		32		0,33		6,97	5,43	-	6,02		26		0,36	
	FeD	600	26,17	30,44	-	28,57		32		1,38		17,00	18,55	-	17,94		28		5,28	
	FeHES	300	-	-	26,21	26,21		11		1,37		-	-	16,32	16,32		11		2,72	
	FeHES	450	-	-	40,01	40,01		11		2,89		-	-	23,75	23,75		7		4,36	
	FeHES	600	42,12	47,98	52,71	47,16		44		1,72		23,44	33,26	32,17	29,84		44		8,25	
	FeCM	600	45,79	53,26	-	49,96		34		2,94		23,85	25,38	-	24,8		29		6,66	
	FeS	600	76,77	87,83	-	82,95		34		2,59		44,02	49,17	-	47,39		29		10,42	
Muscle	Negative	0	-	3,07	2,43	2,67	2,53	26	43	0,15	0,11	-	2,35	2,51	2,42	2,44	27	43	0,18	0,12
	NaCl	0	-	2,30	-	2,2996		17		0,11		-	2,46	-	2,47		16		0,13	
	FeD	600	-	25,03	-	25,03		18		3,60		-	11,02	-	11,02		19		3,09	
	FeHES	300	-	-	19,56	19,56		11		2,49		-	-	5,49	5,49		11		1,41	
	FeHES	450	-	-	19,41	19,41		11		2,50		-	-	8,61	8,61		7		1,17	
	FeHES	600	-	29,92	31,14	30,38		29		5,26		-	13,72	11,74	12,93		30		2,69	
	FeCM	600	-	29,50	-	29,50		19		3,50		-	11,24	-	11,24		19		3,68	
	FeS	600	-	11,95	-	11,95		19		5,50		-	6,97	-	6,97		19		1,76	

In case of all complexes, doses, tissues and both incubation times intervention groups showed highly significant ($p<0.001$) higher Fe concentrations than control. Additionally control groups, independently from if they were negative controls or treated with sodium chloride 0.9% solution, showed high conformity ($p > 0.375$) in cases of all tissues, except muscle after 24 h were the homogeneity was lower ($p = 0.062$).

3.4.4.1. *Liver results*

The Fe content in liver samples of each egg and the mean values corresponding to the type of complex and the incubation time for each sub-trial can be found in **Figure 69 a-c**. **Figure 69 d** gives a summary of the detected Fe contents for the complete study after 24 h and 120 h, respectively.

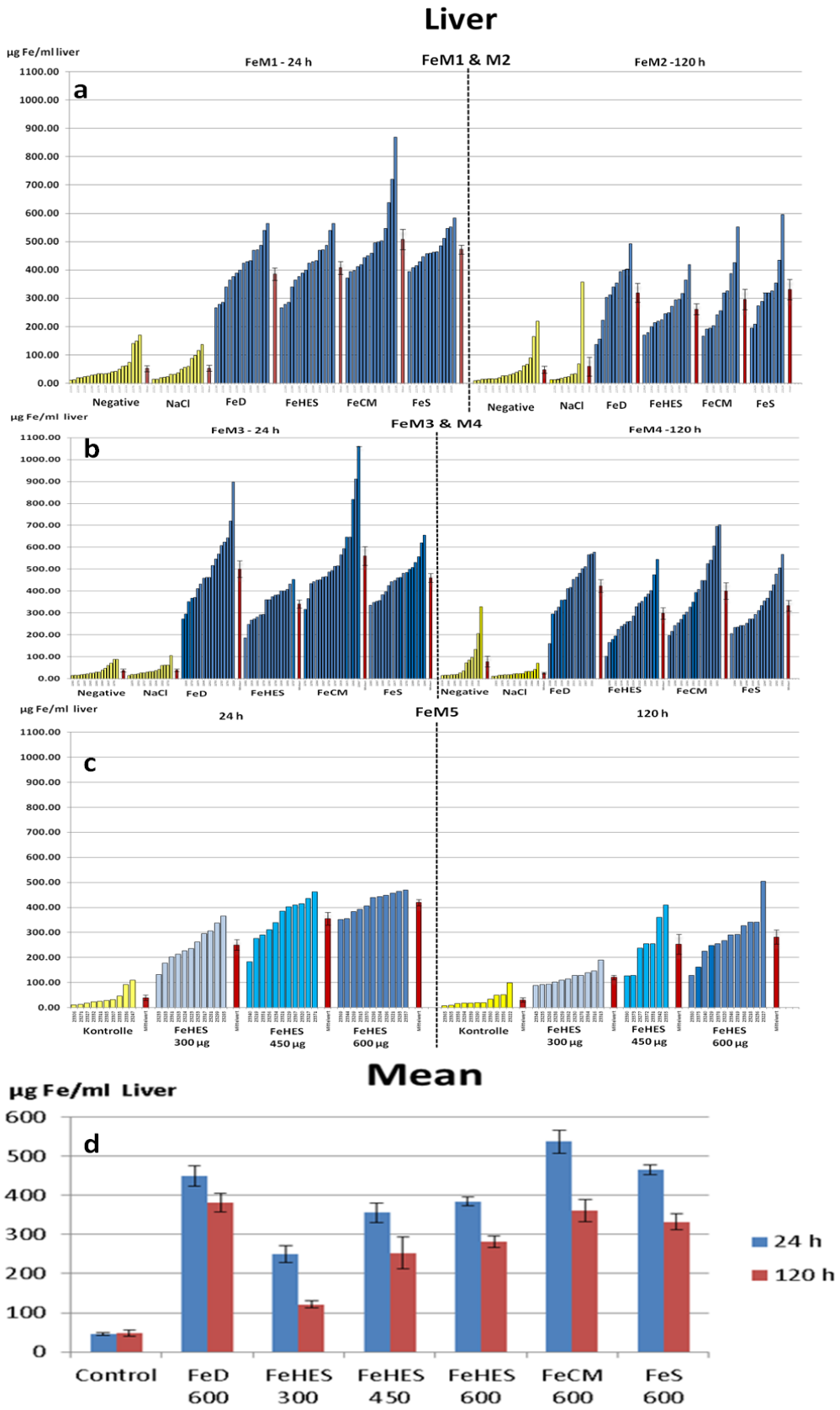

Figure 69 a-d - Fe concentration in liver for each egg and in mean after 24 and 120 h treatment, respectively. From top to bottom: trial FeM1&FeM2 (a); 3&4 (b) - all complexes (FeS = FeSuc) with a dose of 600 µg; trial FeM5 (c)- FeHES with doses of 300, 450 or 600 µg (d) the mean values for the whole study (FeM1-5) after 24 and 120 h, respectively. "Control" is the summary of "Negative" and "NaCl" control groups. Error bars are valued with ± SEM.

Control groups

Negative control and NaCl-control eggs after 24 h ($p = 0.531$) and 120 h ($p = 0.375$) showed very similar values in each sub-trial and differences between the results were considered not to be statistically significant, even when comparing 24 h values with values after 120 h ($p = 0.615$). Looking more closely at the specific values shows, that only in the case of sub-trial FeM4.13 (**Table 13**) the value for negative control showed a 3 times higher value than for NaCl-control samples. However, the difference is not significant ($p = 0.166$) as the standard error (SEM) was more than 6 times higher for negative control in comparison to NaCl control (24.5 vs. 3.7). The difference between the mean Fe levels after 24 (45.04 µg/ml) and 120 h (47.5 µg/ml) was not big but significant ($p = 0.028$).

Intervention groups

The decreasing order of Fe content in liver after 24 h incubation was in mean (**Figure 69 d**) FeCM ≥ FeSuc ($p = 0.118$) ≥ FeD ($p = 0.142$) ≥ FeHES ($p = 0.112$). P values show that there were not significant differences ($p > 0.05$). The pairwise comparison shows that FeCM liver samples contained significantly higher Fe levels than FeD ($p = 0.029$) & FeHES ($p = 0.011$) and FeSuc Fe levels were highly significantly higher ($p < 0.001$) than FeHES. Looking more closely at the results of the single sub-trials gives inconsistent information: The results of 600 µg dose of FeHES in dose dependency trial 5 (**Figure 69 c**) in comparison to trial 1 and 3 showed statistically significant different values ($p = 0.019$) which can be related to low values in trial 3, whereas results of trial 1 and 5 (**Figure 69 a, c**) were not significantly different ($p = 0.753$). By comparison of the FeHES results of trial 5 (**Figure 69 c**) with FeSuc (trial 1, 3), the difference was poorly significant ($p = 0.069$) contrary to the consideration of mean values (see above $p < 0.001$).

There was a difference between FeHES ($p = 0.019$) and FeD ($p = 0.022$) results of the first (**Figure 69 a**) and the second trial (**Figure 69 b**) resulting in FeSuc > FeD ($p = 0.005$) and FeCM > FeD ($p = 0.003$) - both very significant. No significant difference was observed between FeD and FeHES ($p = 0.520$) in **Figure 69 a**. Between FeD and FeSuc ($p = 0.294$) or FeCM ($p = 0.449$) no significant difference was observed. In case of FeD > FeHES ($p = 0.001$) a very significant difference in **Figure 69 b** was observed.

In comparison to control groups the intervention groups yielded Fe levels increased by factors in the range of 8.5 (FeHES) to 11.9 (FeCM) after an administered dose of 600 µg and 24 h incubation time.

The decreasing order of the mean liver Fe concentration after 120 h (**Figure 69 d**) is FeD ≈ FeCM ($p = 0.313$) ≈ FeSuc ($p = 0.412$) > FeHES ($p = 0.04$). Here, only FeHES liver Fe content showed significant difference to FeSuc and FeCM (both $p = 0.04$) and very significant difference to FeD ($p = 0.001$). The difference of mean values of FeD to FeSuc was not significant ($p = 0.069$). FeD results of trial 2 and 4 showed significant differences ($p = 0.026$). In trial 4 a significant difference of FeD to FeSuc ($p = 0.013$) was observed. This was not observed in case of trial 2 ($p = 0.741$).

The mean Fe level after 120 h incubation in intervention groups (600 µg dose) was between 5.9 (FeHES) and 8 (FeD) times higher than control group Fe levels.
Comparing results after 24 h and 120 h shows a reduction of Fe values by 15% (FeD, $p = 0.171$), 27% (FeHES, $p < 0.001$), 29% (FeSuc, $p < 0.001$) and 37% (FeCM, $p < 0.001$). The difference between 24 and 120 h incubation was highly significant except in case of FeD.

Dose dependency

Figure 69 c shows the results of the dose dependency test (trial 5) for FeHES. After 24 h incubation a correlation was observed with a coefficient of determination (R^2) of 0.99 (**Figure 70**). Using mean values of all sub-trials for control and 600 µg doses yields $R^2 = 0.9693$, indicating a positive correlation (**Figure 71**). Differences between the doses were: 600 µg > 450 µg ($p = 0.056$ - not significant) > 300 µg ($p = 0.007$ - very significant) and 600 µg > 300 µg ($p < 0.001$ - highly significant).
After 120 h incubation there was still a correlation with R^2 =0.94 for the trial (**Figure 70**) and R^2 =0.93 in case of the mean values for control and FeHES 600 µg values (**Figure 71**). Differences between the doses were very or highly significant for 300 µg < 450 µg ($p = 0.007$), or 300 µg < 600 µg ($p < 0.001$). The difference between 450 µg and 600 µg was not significant ($p = 0.592$).

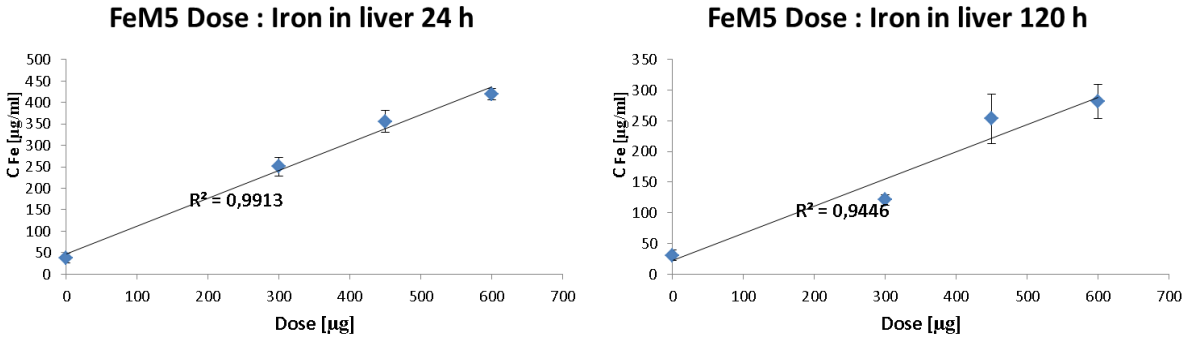

Figure 70 - Correlation between applied doses and Fe levels in liver yielded from dose dependency test FeM5 with SEM. Negative control is blank value.

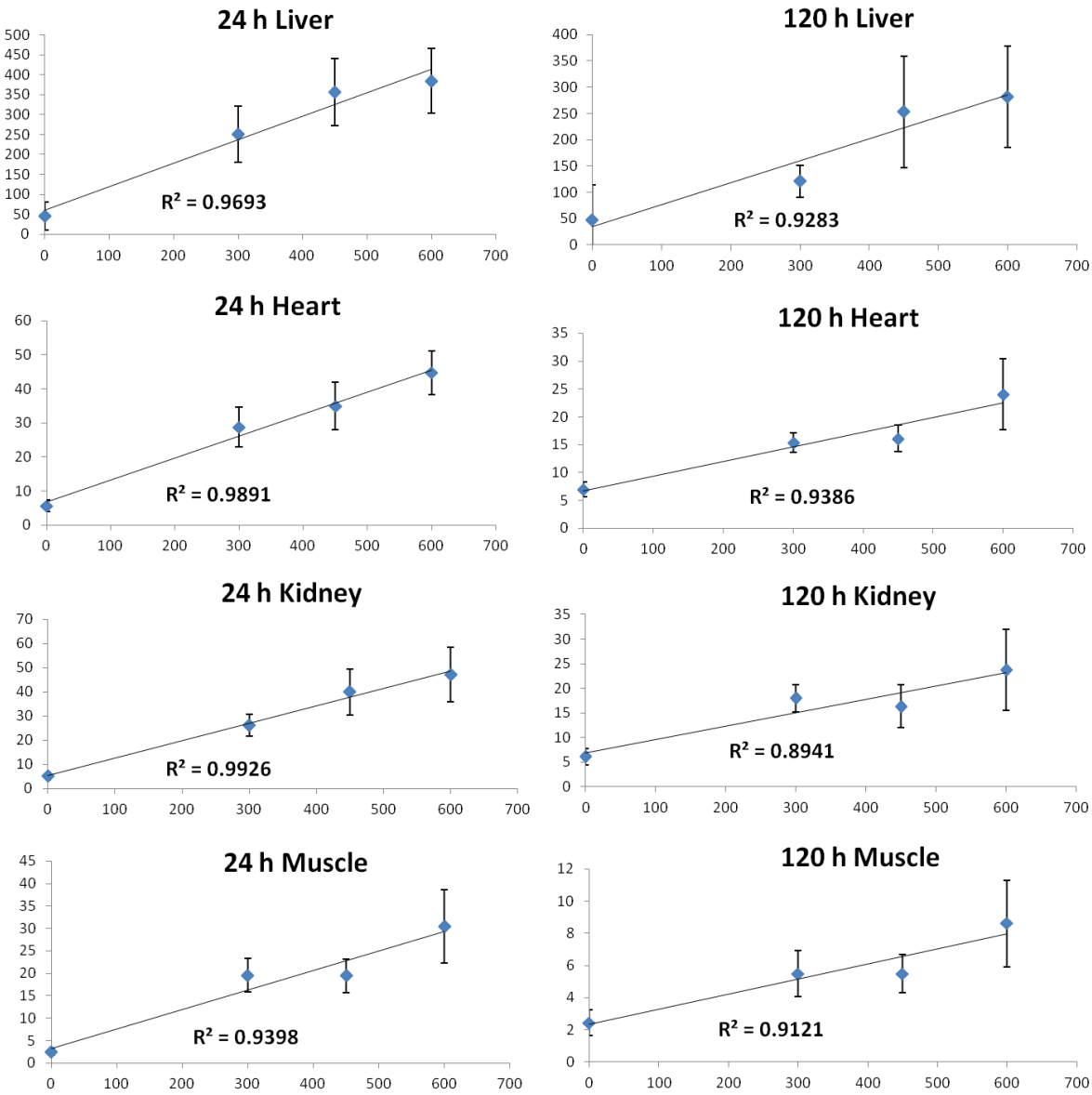

Figure 71 - Correlation of FeHES 300 µg, 450 µg tissue results of trial 5 with mean values of control groups and FeHES 600 µg of the complete study. The axis of ordinates is giving the concentration of measured iron in µg/ml of homgenized tissue and the axis of abscissa gives the administered dose of *i.v.* iron complex in µg for all diagrams. Error bars are representing the SEM. A good correlation was observed in all cases ($R^2 > 0.894$). The difference to Figure 70, Figure 73, Figure 75, and Figure 77 is the use of mean values from trial 1-5 in case of 600 µg dose.

3.4.4.2. *Heart results*

The results of Fe concentrations in heart for each sub-trial (**Figure 72 a-c**) and mean values of the complete study (**Figure 72 d**) are presented in **Table 13**.

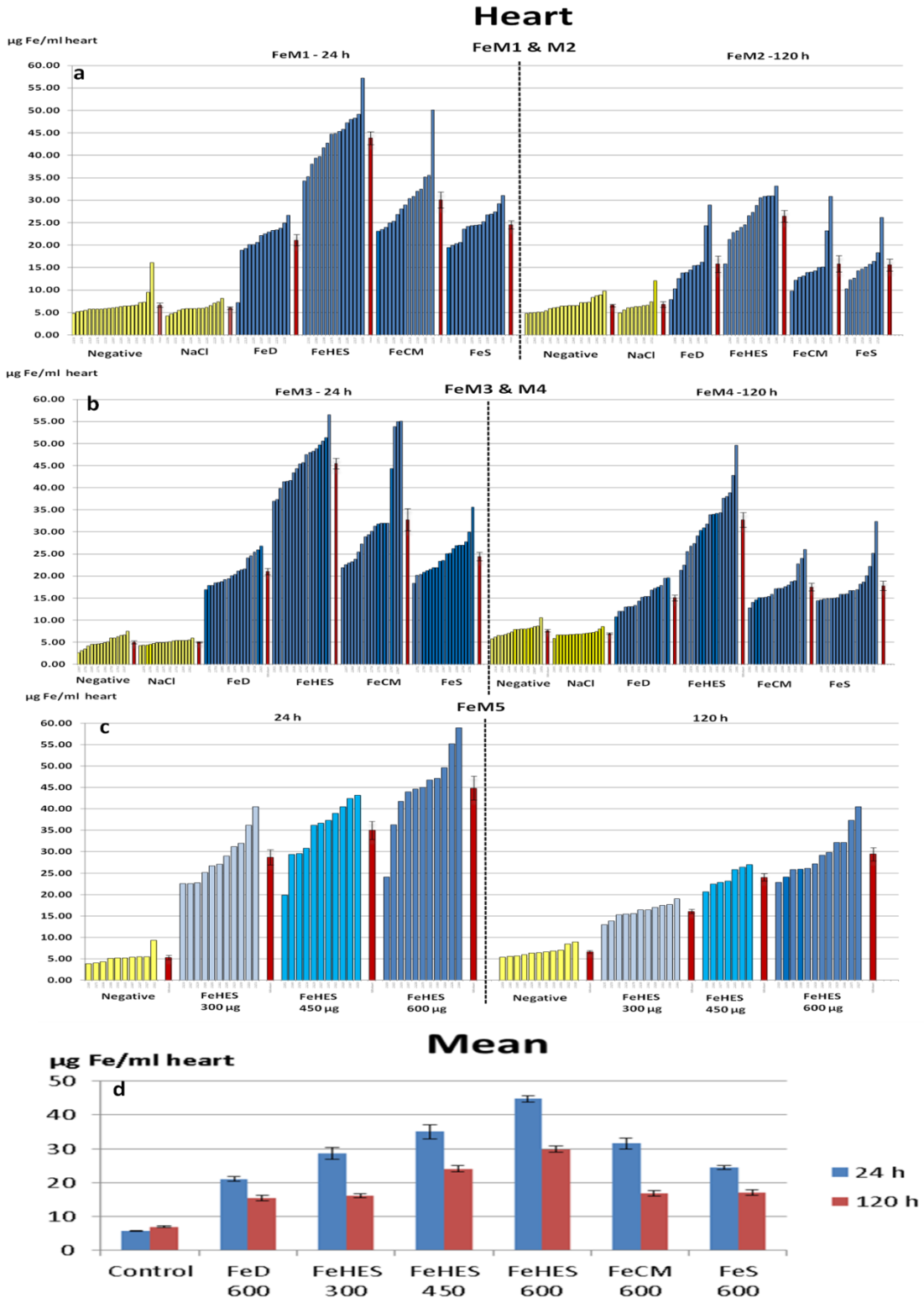

Figure 72 a-d - Fe concentration in heart for each egg and in mean after 24 and 120 h treatment, respectively. From top to bottom: trial FeM1&2 (a); FeM3&4 (b) -all complexes (FeS = FeSuc) with a dose of 600 µg; 5 (c) - FeHES with doses of 300, 450 or 600 µg; the mean values for the whole study (FeM1-5) (d), after 24 and 120 h, respectively. "Control" is the summary of "Negative" and "NaCl" control groups. Error bars are valued with ± SEM.

Control groups

As mentioned before negative and NaCl control groups after 24 h ($p = 0.401$) and 120 h ($p = 0.907$) showed high homogeneity. The difference between mean values after 24 h (5.69 µg/ml,**Table 13**) and 120 h (6.94 µg/ml) was very small but highly significant ($p < 0.001$) (**Figure 72 d**).

Intervention groups

The decreasing order of Fe concentrations in heart after 24 h incubation was in mean FeHES > FeCM ($p < 0.001$)> FeSuc ($p < 0.001$) > FeD ($p < 0.001$) (**Table 13, Figure 72 d**). FeHES had highly significant higher Fe levels ($p < 0.001$) than FeCM (+42%), FeSuc (+83%) and FeD (+112%). Even the 450 µg dose showed similar values which were not significantly higher than FeCM ($p = 0.07$) but highly significant higher than FeSuc and FeD ($p < 0.001$). The 300 µg dose showed no significant difference to FeCM ($p = 0.441$) but a significant or highly significant higher Fe concentration than FeSuc (+17%; $p = 0.026$) and FeD (+36%; $p < 0.001$). The observed results after 24 h incubation were very consistent and the results between the sub-trials for each complex (**Figure 72 a & b**) showed no significant differences for FeD ($p = 0.952$), FeHES ($p = 0.668$), FeCM ($p = 0.891$), and FeSuc ($p = 0.864$). The results of the intervention groups treated with 600 µg Fe after 24 h were between 3.7 (FeD) and 7.9 (FeHES) times above control group Fe levels.

After 120 h incubation the decreasing order of Fe concentration in heart was FeHES > FeSuc ($p < 0.001$) = FeCM ($p = 0.791$) ≈ FeD ($p = 0.188$). FeHES with 600 µg dose showed highly significant higher values than the other complexes (76-95% higher, $p < 0.001$). At a dose of 450 µg FeHES the Fe level in heart was also highly significant higher than for all the other complexes (41-57%, $p < 0.001$). At a dose of 300 µg FeHES - half dose of the other complexes - there was no significant difference to FeSuc ($p = 0.811$), FeCM ($p = 0.720$) and FeD ($p = 0.158$) in heart Fe levels (**Figure 72 d**). When looking closer at the sub-trials the results were the same as for the mean values except in case of FeD in comparison to results of FeCM. FeCM heart results of the sub-trials after 120 h were significantly not homogenous ($p = 0.019$). FeCM Fe level in trial 4 was significantly higher ($p = 0.034$) in comparison to the mean value of FeD. The Fe level after 120 h incubation among intervention groups in comparison to control groups was elevated by factors between 2.2 (FeD) and 4.3 (FeHES).

The comparison between measured Fe heart levels after 24 and 120 h showed a highly significant decrease of 14% (FeD; $p < 0.001$), 30% (FeSuc; $p < 0.001$), 33% (FeHES; $p < 0.001$) and 46% (FeCM; $p < 0.001$).

Dose dependency

Figure 72 c shows the results of the dose dependency test (FeM5) of FeHES in heart. The correlation between administered dose and measured Fe levels in heart samples can be seen in **Figure 73**. A good correlation for the single trial 5 has been observed after 24 h (R^2 = 0.988) as well as after 120 h (p = 0.989). The correlation of 300 µg and 450 µg results in trial 5 with the mean results of control and FeHES 600 µg of the complete study can be seen in **Figure 71**. A good correlation was observed after 24 h (R^2 = 0.989) and 120 h incubation (R^2 = 0.939), respectively. After 24 h, FeHES with a dose of 300 µg resulted in significantly lower Fe levels than 450 µg (p = 0.034) and 600 µg (p < 0.001 - highly significant) doses. The 450 µg dose yielded highly significant lower Fe levels than the 600 µg dose (p < 0.001). After 120 h the Fe levels in heart showed highly significant differences for 300 µg < 450 µg (p < 0.001) as well as for 300 µg < 600 µg (p < 0.001) and a very significantly lower Fe level after a 450 µg dose in comparison to a 600 µg dose (p = 0.006).

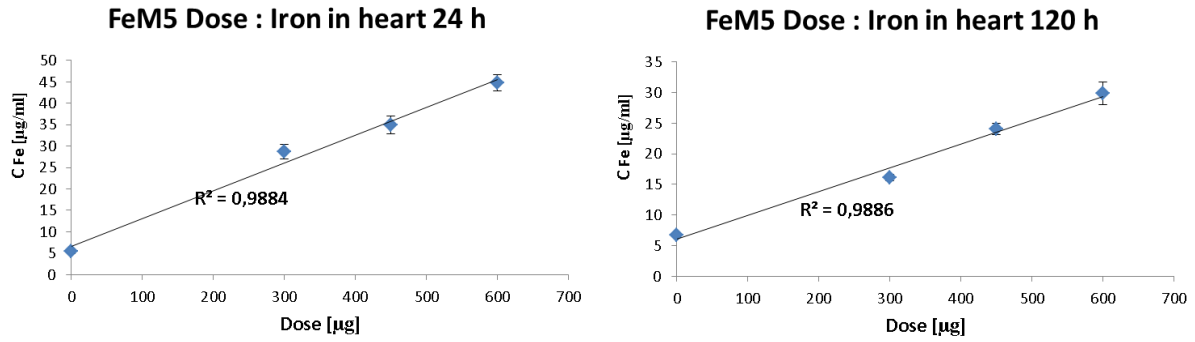

Figure 73 - Correlation between applied doses and Fe levels in heart yielded from the dose dependency test FeM5 with SEM.

3.4.4.3. *Kidney results*

The results of Fe concentrations in kidney for each sub-trial (**Figure 74 a-c**) and mean values of the complete study (**Figure 74 d**) are presented in ***Table 13***.

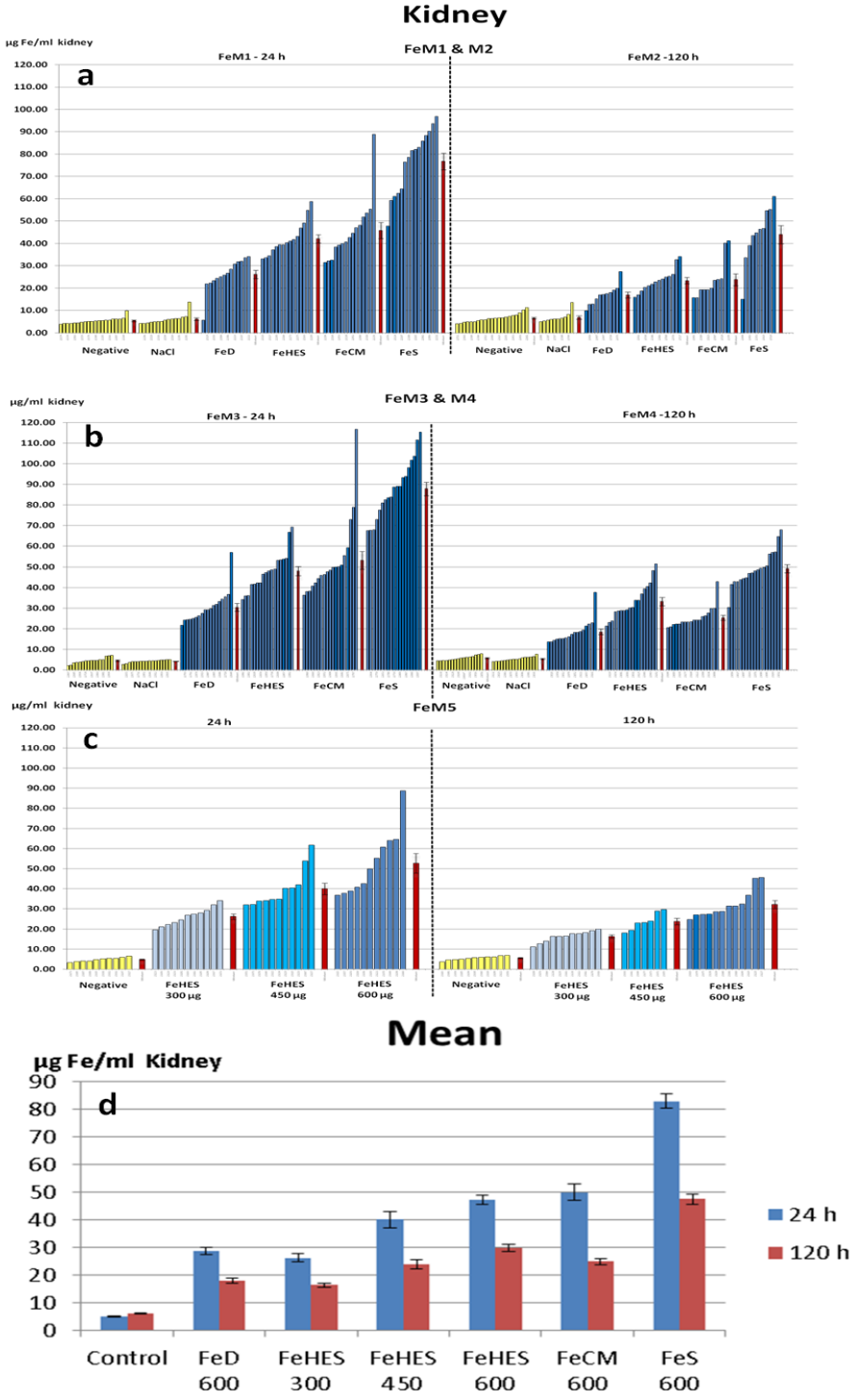

Figure 74 a-d- Fe concentration in kidney for each egg and in mean after 24 and 120 h treatment, respectively. From top to bottom: trial FeM1&2 (a); FeM3&4 (b) - all complexes (FeS = FeSuc) with a dose of 600 µg; 5 (c) - FeHES with doses of 300, 450 or 600 µg; the mean values for the whole study (FeM1-5) (d) after 24 and 120 h, respectively. "Control" is the summary of "Negative" and "NaCl" control groups. Error bars are valued with ± SEM.

Control groups

Negative and NaCl control groups of kidney samples after 24 h ($p = 0.792$) and 120 h ($p = 0.559$) showed high homogeneity. As in case of heart analysis, the difference between mean values after 24 h (5.06 µg/ml, ***Table 13***) and 120 h (6.08 µg/ml) was very small but highly significant ($p < 0.001$).

Intervention groups

The decreasing order of mean Fe levels after 24 h incubation time in kidney was FeSuc > FeCM ($p > 0.001$) ≥ FeHES ($p = 0.396$) > FeD ($p < 0.001$). FeCM and FeHES 600 µg dose results did not show significant difference whereas the differences between FeSuc and FeCM as well as FeHES and FeD were highly significant. Consequently, the difference between FeSuc and FeHES ($p < 0.001$) and between FeCM and FeD ($p < 0.001$) was highly significant as well (**Figure 74 d**). FeSuc showed very high levels of Fe in comparison to FeCM (+66%), FeHES (+76%) and FeD (+190%) - 3 times higher. The level of Fe in kidney after application of 300 µg FeHES (26.21 µg/ml) was comparable ($p = 0.241$) to the Fe level yielded after application of FeD 600 µg (28.7 µg/ml).

The Fe levels of the intervention groups were between 5.6 (FeD) and 16.4 (FeSuc) times higher than mean level of control groups.

The results of the single sub-trials were significant comparable among each other ($p > 0.09$) except in case of FeSuc ($p = 0.047$). However, as the difference of FeSuc to the other investigated complexes was very high, this had no effect on the results of significance testing as significance level was always smaller than 0.1%.

After 120 h incubation time the decreasing order of mean Fe content in kidney was FeSuc > FeHES ($p < 0.001$) ≥ FeCM ($p = 0.008$) > FeD ($p < 0.001$). The differences of the mean values were very, respectively highly significant for the mean values. In trial 2, the observed Fe level of FeHES was significantly lower than in trial 4 and 5 ($p < 0.001$). That resulted in a divergent relation in trial 2, in which no significant difference between FeHES and FeCM was observed ($p = 0.501$) contrary to trial 4 & 5 ($p < 0.001$) and the mean ($p = 0.008$) of all trials. As the differences in mean and in trial 4 & 5 were very (mean) or highly (4 & 5) significant, a difference can be assumed.

Like in case of 24 h incubation time FeSuc again showed increased Fe levels in comparison to FeHES (+59%), FeCM (+91), FeD (+164%) - more than 2.5 times higher. The application of FeHES with half the dose of FeD yielded nearly the same ($p = 0.569$) mean Fe level in kidney which was homogeneous to results of 24 h incubation.

The Fe levels in intervention groups were increased by factors between 3 (FeD) and 7.8 (FeSuc) in comparison to control groups.

The measured Fe values highly significantly ($p < 0.001$) decreased from 24 h incubation to 120 h incubation in mean by 50% (FeCM), 43% (FeSuc) or 37% (FeHES, FeD), respectively.

Dose dependency

Figure 74 c shows the results of dose dependency test FeM5 in kidney after 24 and 120 h incubation time, respectively. The correlation between administered dose and measured Fe levels in trial 5 can be seen in **Figure 75**. A very high level of correlation was observed at 24 h incubation time ($R^2 = 0.997$). The correlation at 120 h between dose and Fe concentration in kidney was very good ($R^2 = 0.987$).

If mean values of 600 µg FeHES and control groups were used for correlation (**Figure 71**), the correlation was good in case of 24 h incubation ($R^2 = 0.993$) but less good in case of 120 h ($R^2 = 0.894$), which was the consequence of the divergent results of FeHES 600 µg in sub-trial 2 in comparison to trial 4 and 5, as mentioned before. Therefore, the separate look at trial 5 was preferred in this context.

The differences between the mean Fe levels at different doses were highly significant between 300 µg and 450 µg ($p < 0.001$) and consequently between 300 µg and 600 µg ($p < 0.001$) after 24 and 120 h incubation. The difference between 450 µg and mean results of the 600 µg dose was significant at 24 h ($p = 0.02$) but not significant ($p = 0.06$) in case of 120 h. By comparing only the results of trial 5, the level of significance was reduced for 24 h ($p = 0.016$) and 120 h incubation ($p = 0.010$) yielding a significant difference. The divergent results of trial 2 of 600 µg dose, as mentioned above, determined this.

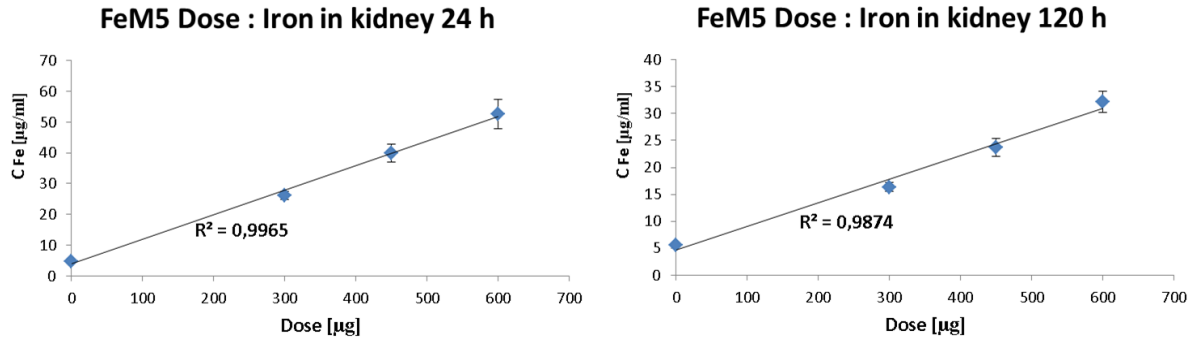

Figure 75 - Correlation between applied doses and Fe levels in kidney yielded from the dose dependency test FeM5 with SEM.

3.4.4.4. *Muscle results*

The results of Fe concentrations in muscle for each sub-trial (**Figure 76 a-b**) and mean values of the complete study (**Figure 76 c**) are presented in ***Table 13***.

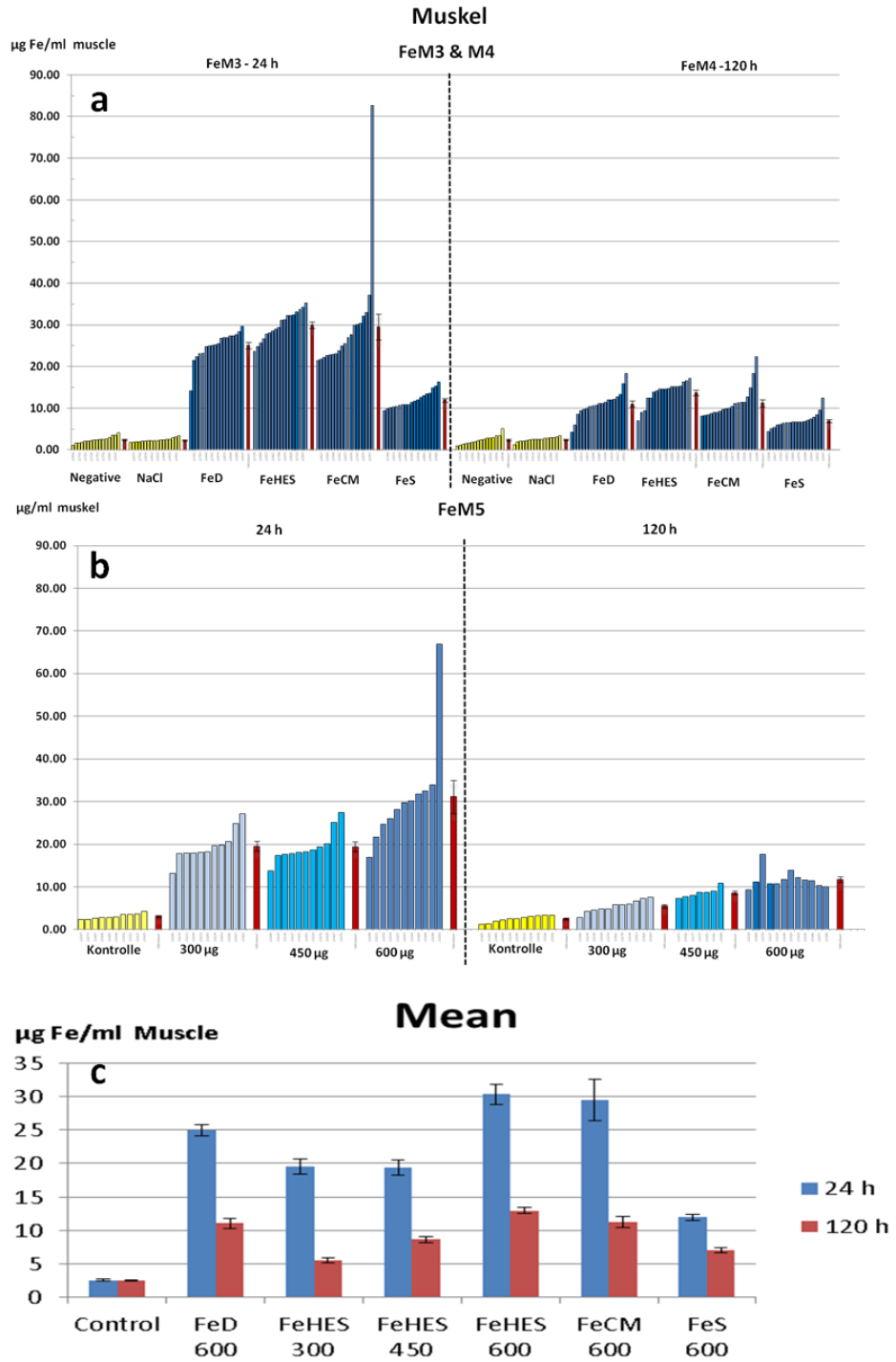

Figure 76 a-c - Fe concentration in muscle for each egg and in mean after 24 and 120 h treatment, respectively. From top to bottom: Trial FeM3&4 (a) - All complexes (FeS = FeSuc) with doses of 600 µg; Trial FeM5 (b) - FeHES with doses of 300, 450 or 600 µg; the mean values for the whole study (FeM3-5) (c) after 24 and 120 h. "Control" is the summary of "Negative" and "NaCl" control groups. Error bars are valued with ± SEM.

Control groups

Negative and NaCl control groups showed similarly very low Fe levels after 24 ($p = 0.187$) and 120 h ($p = 0.831$) incubation with highly significant differences to intervention groups ($p < 0.001$). There was also no difference ($p = 0.759$) of mean values after 24 h (2.5 µg/ml) and 120 h (2.4 µg/ml) in case of control groups.

Intervention groups

The decreasing order of mean Fe content in muscle samples after 24 h incubation was FeHES ≈ FeCM (-3%; $p = 0.062$) ≥ FeD (-15%; $p = 0.185$) > FeSuc (-52%; $p < 0.001$) (**Figure 76 c**). The mean values of FeCM and FeHES were very close to each other and no significant difference was observed although the level of significance is quite low. This was consequence of a particular value for egg no. 22866 (82.6 µg/ml, **Figure 76 a**) which was nearly 3 times higher than the mean (29.5 µg/ml, ***Table 13***) and identified as extreme outlier (***Table 12***). This also determined the obviously relative high but not significant difference between FeCM and FeD. FeHES showed highly significant ($p < 0.001$) higher Fe contents than FeD (-18%) and consequently FeSuc (-61%).

The Fe levels of the intervention groups after 24 h were increased by factors between 4.7 (FeSuc) and 12 (FeHES) in comparison with control groups.

After 120 h incubation time the decreasing order was measured with FeHES > FeCM (-13%, $p = 0.01$) ≈ FeD (-2%; $p = 0.418$) > FeSuc (-37%; $p < 0.001$). The difference between FeHES and FeCM was significant but very small (12.9 µg/ml vs. 11.2 µg/ml). While FeD mean value was marginal smaller than FeCM it was also significantly ($p = 0.028$) smaller (-15%) than FeHES. While the difference between FeHES and FeD was very significant ($p = 0.008$) in trial 4 (**Figure 76 a;** ***Table 13***) no significant difference was observed between FeD results of trial 4 and FeHES results of trial 5 ($p = 0.485$). The same was observed in case of FeHES vs. FeCM (trial 4: $p = 0.027$; trial 5: $p = 0.110$). FeSuc showed highly significant ($p < 0.001$) lower muscle Fe levels than FeHES (-46%) and FeCM (-38%).

Intervention groups were yielding Fe levels after 120 h incubation which were between 2.9 (FeSuc) and 5.3 (FeHES) times higher than Fe levels of control groups.

Dose dependency

Figure 77 shows the good correlation between administered dose and measured Fe levels of trial 5 in muscle after 24 (R^2 = 0.938) and 120 h (R^2 = 0.961), respectively. In addition, the correlation between mean values of the complete study (**Figure 71**) showed good correlating results for 24 (R^2 = 0.94) and for 120 h (R^2 = 0.912) with lower level of correlation.

There was no difference (p = 0.797) observed between mean Fe level in muscle after administration of 300 µg or 450 µg FeHES respectively after 24 h incubation (**Figure 76 b**) but a highly significant difference after 120 h incubation (p < 0.001). The difference between 450 µg and 600 µg dose was very significant (p = 0.002/ p = 0.001) after 24 and 120 h incubation time. Consequently the difference between 300 µg and 600 µg was very and highly significant (p = 0.002/ p < 0.001) after 24 and 120 h.

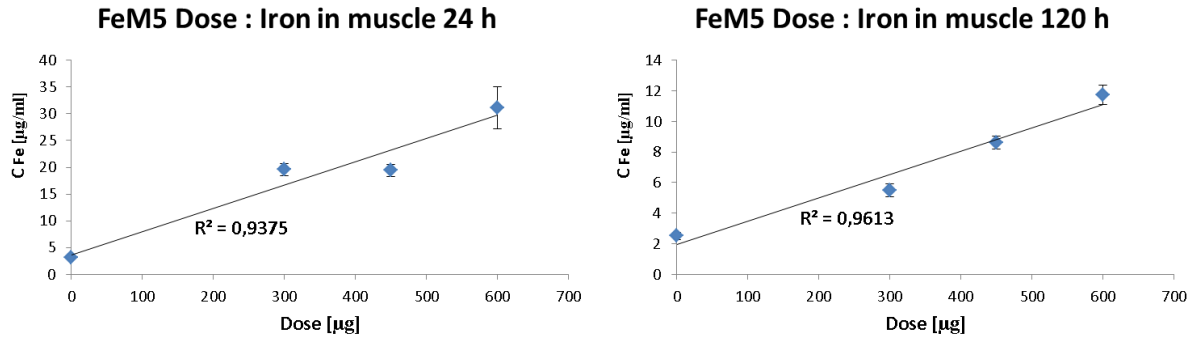

Figure 77 - Correlation between applied doses and Fe levels in muscle yielded from the dose dependency test FeM5 with SEM.

3.4.5. Recovery of iron from the complexes

The relative amount of recovered Fe is presented in **Figure 78**. The method of Fe quantification yielded Fe levels between 90.5% and 95.6% with best recovery rate for FeD and worst in case of FeCM. The increasing order of recovered Fe was FeCM ≤ FeHES (p = 0.187) ≤ FeSuc (p = 0.112) ≤ FeD (p = 0.105) with no significant difference. The ANOVA indicated highly significant differences between the groups (p < 0,001) as FeSuc yielded significantly higher recovered Fe (p = 0,019) than FeCM, and FeD showed very significant (p = 0.003/ 0.001) higher recovered Fe than FeHES and FeCM, respectively. A correlation between the applied concentration and the results of the Fe quantification can be seen in **Figure 79**. The used concentration is derived (calculated) from the concentration as given from the manufacturers. In every case a very good correlation between calculated and measured Fe concentration was observed (R^2 > 0.9991).

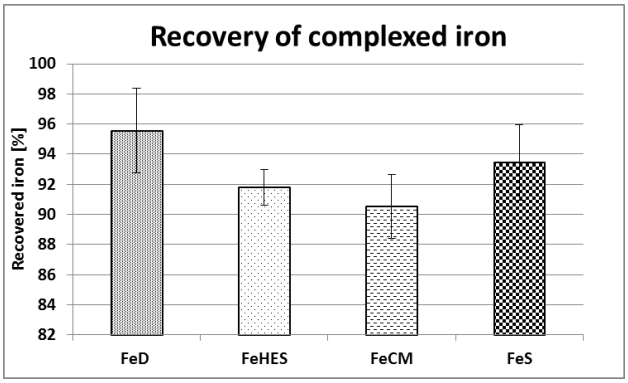

Figure 78 - Recovery of complexed iron (Fe). The graphic shows the recovered Fe [%] of the complexed Fe in the investigated compounds (FeS = FeSuc) after treating the dilutions the same way as it was done for the tissue homogenates. In all cases, the measured Fe level was lower than the theoretical amount of Fe in the complexes (< 100%). The mean values are larger than 90% for all investigated complexes in the increasing order of FeCM ≤ FeHES (p=0.187) ≤ FeSuc (p=0.112) ≤ FeD (p=0.105) indicating decreasing stability of the complexes at the applied stress conditions with acidic milieu (1 N HCl, trichloroacetic acid), heat (95°C), reducing (sodium ascorbate) & complexing (FerroZine®) agents.

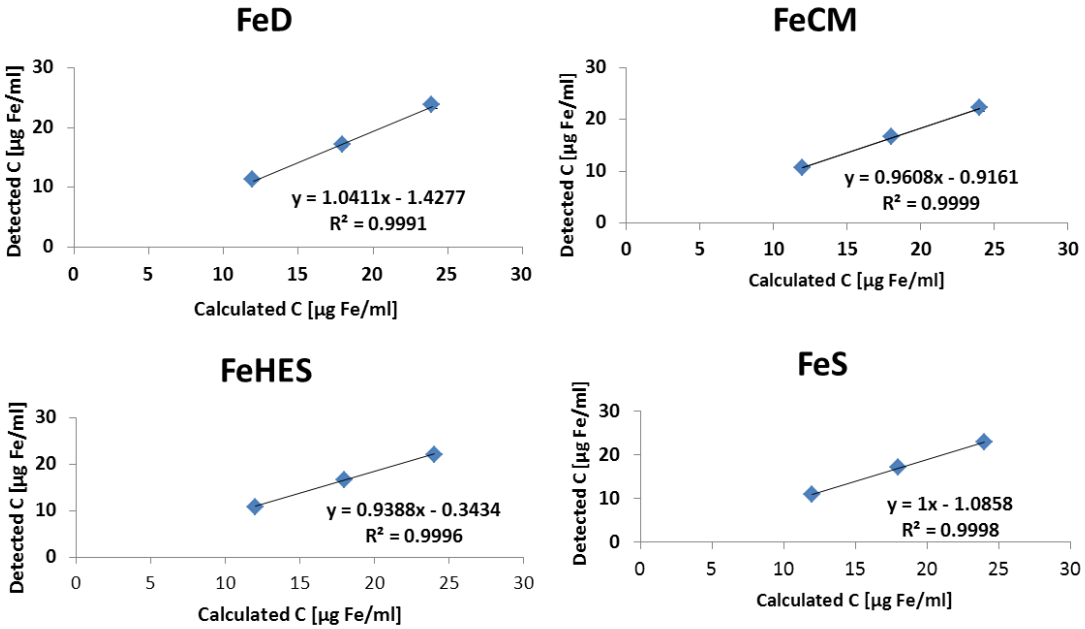

Figure 79 - Correlation of the recovered Fe concentration with the concentration theoretically present in the used complex dilution (FeS = FeSuc). A very good correlation (R^2>0.9991) was observed for all complexes indicating that the fraction of recovered Fe is independent from the applied dose or concentration from side of the quantitative method.

3.4.6. Comparison of tissue results

After 24 h (120 h) the iron (Fe) content in liver samples in comparison to heart samples was increased by the factors 8 (7) / 9 (10) for Control and iron hydroxyethyl starch (FeHES) group, respectively. The factors for the other groups were: ferric carboxymaltose (FeCM) - 17 (21), iron sucrose (FeSuc) - 19 (20) and low molecular weight iron dextran (FeD; Cosmofer®) - 21 (25). The liver Fe content in those groups was much more increased in comparison to FeHES and control groups but the reason is different.

In case of FeHES group, the heart Fe levels were significant and absolute higher than in case of the other intervention groups and on the other hand the Fe level in liver was lower than in case of the other intervention groups. For control groups, liver Fe levels were much lower than for intervention groups. This is the reason for the low factor in this case.

The kidney results were similar to results of heart in case of FeHES after 24 h ($p = 0.857$) and 120 h ($p = 0.774$). For all other groups including control groups a significant difference was observed in every case. Control groups showed very significant difference after 24 /120 h ($p = 0.01$ /$p = 0.001$). Intervention groups yielded very or highly significant different Fe values ($p \leq 0.001$). Consequently the factor of Fe decrease between liver and kidney was nearly the same for FeHES with 8 (10) but different for Control - 9 (8), FeSuc - 6 (7), FeCM - 11 (15) and FeD - 16 (21). FeSuc caused much higher Fe levels in kidney than the other complexes, which was the reason for the low factor in this case (***Table 13***). The relatively low factor for FeHES in comparison to FeD and FeCM is the consequence of the relatively low Fe levels in liver after administration of FeHES.

The Fe levels in muscle were 18 (20) times lower than for liver in case of control groups. The factors of the intervention groups were: FeHES - 13 (22), FeD - 18 (35), FeCM - 18 (32), FeSuc - 39 (48). The very high factor for FeSuc groups was the consequence of the low Fe level in muscle samples in comparison to the other intervention groups and very similar Fe levels in case of liver.

3.4.7. Tissue difference discussion

Physiological parameters

Liver and spleen are part of the mononuclear phagocyte (MPS) / reticuloendothelial system (RES) which is part of the immune system consisting of monocytes and macrophages. The reticuloendothelial (RE) macrophages of the liver are the Kupffer cells (KC) cleaning the blood from microorganisms, old red and white blood cells and foreign matters, including the applied complexes. Polymeric nanoparticles (NPs) are opsonized and removed from the bloodstream very rapidly - a matter of minutes - and usually concentrated in the liver and spleen [118, 120, 121]. KC identify the NPs after opsonin proteins have bound to the surface [117-119]. The NPs are taken up by phagocytosis forming endosomes, which fuse with lysosomes. Then, the FeNPs are cleaved enzymatical, and pH dependently. Lysosomal glycosidases degrades the carbohydrate fraction at pH levels of about 4.5 and Fe is dissolved and chelated by lactoferrin - a glycoprotein of the transferrin family. The Fe can then be

transferred to cytosol were it can be stored as ferritin and/or hemosiderin (**1.4.4**, [114, 115]).
As the discontinuous capillaries in liver are very well permeable for hydrophilic substances, those complexes penetrate easily into deeper tissue areas where they can be internalized by KC due to phagocytosis. Supplemental hepatocytes also play an important role in Fe uptake [219, 222, 228, 229]. Capillaries in kidney are fenestrated and less permeable than those in liver, but more than the continuous capillaries in heart and skeletal muscle. For that reason, NPs might predominantly distribute to tissue with a leaky endothelial wall [230-232]. A possible filter effect could play a role as previously reported in case of the distribution inside the RES where larger particles are predominantly removed by spleen and liver while smaller particles are directed to the bone marrow [233].

Clinical studies verify those finding e.g. as reported by Rostoker et al. in a study with 119 hemodialysis patients determining tissue Fe by T_1 and T_2 contrast magnetic imaging. They found a hepatic overload in 84 % of the patients being treated with 100 mg FeSuc and darbepoetin alpha - an erythropoiesis stimulating agent - and a correlation between *i.v.* Fe and hepatic Fe storage [151]. An earlier study, performed with superconducting quantum interference non-invasive magnetic measurements for the detection of non-hem hepatic Fe, gave similar results in case of patients being treated with sodium ferric gluconate [152]. FeG was not part of this study.

Another effect which is also of importance for the distribution of FeNPs is that in diseases connected with local inflammation reaction (e.g. myocardial infarction) the number of early macrophage and inflammatory cells are increased. Therefore they promote the deposition inside the related tissue (heart in case of myocardial infarction) [234].

Physiological characteristics and additionally the different regional blood flows in the tissues may play a role in generating the order of mean Fe content in the different tissues, determined by this study. In case of adult chicken as a comparable model the order of regional blood flow is published with kidney (9.96 % of cardiac output) > liver (7.05 %) > heart (5.78 %) > femora - with the upper leg muscle - (4.08 %) [235-238].

Complex distribution

Highest values in liver

In general, the applied Fe complexes were distributed to liver with higher affinity than to the other organs, resulting in measured Fe levels in liver, much higher than those in kidney, heart and muscle tissues. This tissue related difference as well as the relationship of Fe levels between control and intervention groups with an increase by factors between 8.5 - 11.9, and 5.9 - 8 after 24 h, and 120 h respectively, illustrate the major role of the liver as pharmacological target tissue beside spleen and bone marrow.

Total iron amount development in the tissues: Accumulation in liver, removal from heart, kidney & muscle

The total Fe amount in the tissues (concentration * tissue weight) of control and intervention groups increases from 24 h incubation to 120 h incubation in case of liver samples but decreases in case of heart, kidney and also muscle. Although this type of interpretation is not reasonable for muscle samples as no complete organ could be bordered in this case. The accumulation of Fe in the liver of control groups was the consequence of the liver's role in Fe homeostasis by storing it in ferritin after degradation of primative red blood cells or adult like red blood cells in early avian embryonic development or after day 5-13 of incubation, respectively [239, 240]. The degradation of the FeNPs is assumed to be determined by the same process but the way of Fe quantification does not give a hint whether the Fe is stored after degradation of the complexes or even in form of the complexes.

Percentaged tissue distribution

Calculation

The fraction of the applied dose of complex present in the different tissues was estimated by including the weight of the specific tissue after a particular incubation time. By multiplying this weight with the measured Fe concentration, the total Fe content of the tissue was calculated. By correcting this with the amount present in case of control groups, the fraction of the applied amount of Fe in the particular tissue was estimated. The total amount of Fe present in the tissue in case of liver and heart was possible to achieve, as these organs were physiologically sharply bordered and could be completely removed from the embryos. In case of kidney, the texture of the tissue was more undefined and consequently the tissue could not be completely removed in every case. Here as well as for muscle results, the calculation of total amount of Fe in the tissue was not reasonable, as only a fraction of upper leg muscle had been sampled.

Liver

After 24 h about 27 % in mean (22 % [FeHES] - 33 % [FeCM]) of the applied dose in case of 600 µg were present in the liver. After 120 h the amount rose to 32% (26% [FeHES]-38% [FeD]) as the mean weight of the liver increased from 0.391 g to 0.667 g. This observation is in good compliance with role of the liver (beside spleen) in Fe metabolism (**1.2.4**). The Total increase of Fe present in the liver between day 20 and day 24 of incubation (control groups after 24 h respectively 120 h) is in good accordance with the published [241] correlation of Fe levels in liver and embryo age. This is consequence of the utilization of the metal-containing yolk granule fraction [241].

Heart

In comparison to that, heart tissue showed only a mean fraction of 0.6% (0.4% [FeD] - 0.9% [FeHES]) of the applied dose after 24 h and 0.4% (0.3% [LFeD] - 0.7% [FeHES]) after 120 h. This effect occurred for all complexes. This is reasonable as heart is no pharmacological but more a toxicological target tissue. NPs in the tissue after 24 h were possibly reversibly de-

posited after blood perfusion. Eventually, liberated Fe from the complex was transported to liver or spleen as main storing tissues after binding to Tf.

Kidney

A similar behavior was identified in kidney, in which the mean fraction decreased from 1.02% (0.5% [LFeD] - 1.8% [FeSuc]) after 24 h to 0.79% (0.4% [LFeD] - 1.3% [FeSuc]) after 120 h incubation. This effect was not only related to the mean values but also to the results of the single complexes. Like heart, kidney is a toxicological target tissue and not consisting of specific Fe absorption systems contrary to liver and the not investigated spleen and bone marrow.

Muscle

As upper leg muscle samples, as already described, could not be removed completely the comparison between 24 and 120 h fraction of the complete dose was not reasonable and comparable to the other tissues. The fraction decreased here - as in case of heart and kidney - from 0.64 % to 0.29 % in mean.

Theoretical tissue concentrations

Calculation

As 27% (after 24 h) and 32% (after 120 h) of the applied Fe dose had been stored in the liver the theoretical tissue concentration ([dose-amount in liver]/[$m_{mean\ of\ embryo}$-$m_{mean\ of\ liver}$]) would be 17.34 µg/ml after 24h and 9.73 µg/ml after 120 h, respectively. This concentration is of theoretical nature as Fe levels are theoretically different (especially in spleen and bone marrow) and it is likely that the complexes enter more easily in some tissues than into others.

Muscle

The comparison between theoretical Fe concentrations and mean tissue concentrations showed, that overall muscle Fe levels in case of 600 µg doses after 24 h (24.94 µg/ml) (***Table 13***Table) and 120 h (10.84 µg/ml) were in the range of the theoretical Fe concentration. This implies that there was no specific or passive Fe or FeNP accumulation present. Especially FeSuc after 24h (11.96 µg/ml) and 120 h (6.97 µg/ml) yielded very low muscle Fe levels below the theoretical concentration. As the spleen is part of the RES, and should contain an increased amount of the applied dose, the real theoretical tissue concentration may have even be lower than the above calculated values.

This and the fact that all other investigated tissues yielded much higher Fe levels may determine this low Fe level for FeSuc. Muscle Fe levels in case of FeD, FeHES and FeCM after 24 h were a little higher than the theoretical Fe tissue concentration and indicate a marginally higher affinity than FeSuc. After 120 h, the Fe concentration was slightly above the theoretical tissue concentration for all these three complexes.Heart

FeD (21.1 µg/ml) like FeSuc (24.5 µg/ml) showed mean heart Fe levels in the range of theoretical tissue concentration after 24 h. Heart Fe levels especially in case of FeHES but also

FeCM were elevated in comparison to that. Contrary to the result after 24h, FeCM after 120 h incubation showed comparable heart Fe levels with FeD and FeSuc. They all were above the theoretical Fe concentration.

Summary

In general the overall distribution of the iron nanoparticles (FeNPs) contained in the administered complexes is in good compliance with results being obtained in case of in vivo or post mortem investigations of patients being treated with *i.v.* Fe [234]. In case of hemodialysis Ali et al. [153] reported massive deposits of Fe in liver and spleen, abundant deposits in adrenal glands, lymph nodes, and lungs and sparse deposits in heart, kidneys, and pancreas after administration of *i.v.* Fe. As in case of the embryos in this study, tissue Fe overload is probable in hemodialysis patients but the clinical consequences are not clear. Fishbane et al. stated that it is unlikely that *i.v.* Fe results in organ damage due to excessive Fe accumulation, as iron levels need to be high over many years in people who suffer from genetic hemochromatosis to cause injuries. In comparison to that HD patients suffer from lower Fe exposure [46]. A reported case of a 70 year old woman who had received Fe infusions over several years and who probably died of Fe overload cardiomyopathy is notable in this context. Iron overload was reasoned from Fe deposits in organs, including the heart, liver, kidneys, thyroid gland, adrenal glands, gastrointestinal tract, and skin [242]. The question is, whether this is only an individual or extreme case.

In summary, after *i.v.* iron treatment most iron is accumulated in the MPS/RES, like the KC in the liver - as a tissue investigated in this study - or macrophages in the spleen and bone marrow. There it is stored as Ftn or haemosiderin and/or exported and bound to Tf in plasma and stored predominantly inside hepatocytes after Tf-Fe_2 uptake. Thus, the liver is the most important and proportionately biggest place of iron storage and utilization. The results of this study with most iron increase in liver in comparison to heart, kidney and skeletal muscle reflect the liver's major role in iron metabolism.

3.4.8. Iron complex comparison in the tissues

3.4.8.1. *Fe complexes in liver*

Liver results after 24 h and 120 h showed that the absolute values of iron (Fe) in the tissues between the different complexes were very similar. The homogeneity of ferric carboxymaltose (FeCM), low molecular weight iron dextran (FeD) and iron sucrose (FeSuc) especially in case of 120 h with the lowest values in case of FeHES demonstrated that the uptake of this complex was decreased by KC. This might have been determined by lower immunogenicity than in case of other complexes with less detection by avian immune cells including KC. If this possible explanation is correct, the consequence could be that particles with low immunogenicity and consequently low detection rate by monocytes like KC remain longer in the circulation. This could probably enhance iron related side effects in toxicologically sensitive tissues if the stability of the complex is not sufficiently high. The immunogenicity may therefore be of disadvantage in case of inducing anaphylactic reactions. However,

the immunogenicity could play a role in the time-related uptake of the particles into the target tissue circumventing iron related toxicological side effects by prolonged circulation and deposits in non-target tissues.

The size of the FeHES particle with a Z-average of about 63 nm (**3.1.1.2, *Table 1***) determined by dynamic light scattering (DLS), in comparison to particle sizes of FeSuc (11-12 nm), FeD (14-16 nm), and FeCM (27-29 nm) could play a role here. Smaller particles can more easily pass the discontinuous capillary wall and penetrate deeper into the tissue. Cellular uptake of particles also seems to underlie size influence and surface charge [201-203]. Compared to phagocytic cells, non-phagocytic cells may favor the uptake of smaller particles [243].

Neutral particles undergo a much lower opsonization rate than charged particles indicating an enhanced uptake of charged in comparison to neutral particles by cells of the RES system [118, 244]. In this context, the ζ-potential (**3.1.3**, **Table 7**) could be from interest. At physiological pH values, FeCM is uncharged, which is contrary to the hypothesis in this context. The charge may have an influence but other factors are more important at least in case of FeCM. Thus, the low value of FeHES in liver may be determined by the low charge of the complex.

Interestingly *in-vitro* investigations in cell lines of HepG2 cells as a model for human hepatocytes yielded higher absorption of FeHES preparations than for FeD. The uptake in THP-1 cells as model for macrophages showed no difference [229]. This is not in good agreement with results of this study as FeD yielded higher Fe levels in liver after 24 h and 120 h. This difference could have been generated by the difference between *in-ovo* avian model and *in-vitro* human model. Alternatively, it is more realistic that the *in-vitro* cell model does not reflect the possible *in vivo* interaction between macrophages and hepatocytes as HepG2 cell line and the THP-1 cell line were investigated separately. This is especially relevant as the authors stated that the Fe, that was taken up by the THP-1 cells, was almost completely released. *In vivo* this released Fe could readily be bound to Tf in plasma followed by uptake into hepatocytes and storage as ferritin or hemosiderin. Additionally hepcidin regulation inhibiting the release of iron from macrophages in case of higher Tf-saturation is absent *in-vitro* (**1.2.4**). The different incubation times of 3 h vs. 24 /120 h should be noted as important impact factors.
Another study using HepG2 cells as a model observed no considerable uptake of Fe into HepG2 cells in case of FeD whereas FeSuc and Fe gluconate yielded highly significant ($p < 0.001$) elevated Fe levels [178]. This observation could substantiate the effect of preferred uptake of smaller particles into hepatocytes as HepG2 cells are a model for that and FeD is smaller than (FeSuc-8.3 nm, Fe gluconate - 8.6 nm, FeD - 12.2 nm) [95].

3.4.8.2. *Fe complexes in heart*

Intranvenous iron and cardiovascular risk

The redox activity is from essential meaning in the iron's role as cofactor for the supply of oxygen as well as for the production of energy (ATP) in the electron transport chain (NADH dehydrogenase, succinate dehydrogenase, cytochromes) for and in living cells. The properties determining the Fe's role in this context are directly connected to its negative influence on the production of reactive oxygen species (ROS) resulting in oxidative stress (**1.2.7**). The hydroxyl radical generated by Fenton reaction is toxic through reaction with DNA, proteins and lipids [48, 245, 246]. There is a negative effect of reactive oxygen species on a diversity of diseases like cardiovascular, metabolic and neurological diseases [56].

Cardiovascular disease (CVD) is a leading cause of death in hemodialysis (HD) patients. Investigations on endothelial tissue culture showed a stimulation of cellular apoptosis, inhibition of proliferation and monocyte adhesion under *i.v.* iron treatment with concentrations at pharmacological range. Fe also inhibited vascular relaxation in an isolated ring model [247]. Rooyakers et al. found a similar effect in volunteers being treated with 100 mg of FeSuc leading to inhibition of vascular relaxation [248]. In mice it was shown, that atherosclerotic lesions contain significant amounts of Fe and a low Fe diet reduces the Fe content and size of plaques with the consequence of increased plaque stability. In human a strong positive correlation between Fe content and protein oxidation products in atherosclerotic plaques has been observed [249, 250]. Other investigations also showed effects of Fe on arterial remodeling and atherosclerosis in rabbit [251]. Fe and lipoprotein interaction was demonstated to induce plaque instability which is related to acute cardiovascular events [252]. Oxidation of the vasculature with a proportional prevalence of atherosclerosis and increase of carotid artery thickness in relation to annual dose of *i.v.* Fe has also been shown [253]. Omiya S et al. showed that Fe-induced oxidative damage results in cell death in cardiomyocytes [254]. In HD patients with increased hepcidin levels an association with fatal and nonfatal cardiovascular events was observed explained by trapping of iron in atherosclerotic macrophages [255] with enhanced oxidative stress and atherogenicity [256]. A direct or indirect connection between *i.v.* Fe and Fe overload in endothelial dysfunction and atherosclerosis is indicated by all these observations [46].

Beside those negative findings of Fe overload and the negative consequences for the heart, Fe supplementation in patients with chronic heart failure (HF) shows beneficial effects in ADEs of properly selected groups of patients, as IDA seems to be a contributor to HF worsening. Some studies show that even if IDA is not present in HF patients that there is a short-term clinical improvement [257-260].

It was already shown in human long-term hemodialysis (HD) patients that the treatment with FeSuc in combination with erythropoietin showed in some patients a correlation with Fe overload in liver and spleen, but not in the heart. As an indicator for oxidative stress, 19 out of 115 patients showed increased MDH levels - a product of DNA and lipid peroxidation - as consequence of Fe toxicity. It was also shown that the tissue Fe was utilized, when *i.v.* Fe therapy was stopped under continuing EPO treatment for 18 month, having no negative ef-

fect on Hb levels but normalizing Tf saturation and serum ferritin levels [261]. (Supplemental information in section **1.4.5**)

Biodistribution into heart

As shortly discussed under **3.4.6** iron levels of iron hydroxyethyl starch (FeHES) were elevated after 24 h and 120 h incubation in comparison to the other investigated complexes (low molecular weight iron dextran [FeD]; ferric carboxymaltose [FeCM]; iron sucrose [FeSuc = FeS in the tables and figures]). FeHES showed heart Fe levels elevated by a factor off approximately 2 in comparison to the other three complexes after 120 h incubation. A dose of 300 µg FeHES yielded Fe levels in heart in the range of the other particles independently from incubation time (See **3.4.4.2**; **Figure 72**).

On the first view this seems to be a negative aspect of FeHES as elevated Fe levels after Fe infusions - or in consequence of hemochromatosis - are associated with an Fe overload cardiomyopathy [242, 262]. It is conspicuous that independent from incubation time heart and kidney Fe levels were very similar (24 h: $p = 0.87$; 120 h: $p = 0.661$) by looking closer at the absolute results of FeHES in kidney and heart

This indicates that there was obviously no specific affinity to heart tissue, which may cause regional side effects. Ferric carboxymaltose (FeCM) and especially iron sucrose (FeSuc) show higher affinity to kidney than to heart leading to the possible misinterpretation of increased Fe levels in heart in case of FeHES. Nevertheless, the elevated Fe values in heart in case of FeHES have to be investigated more closely. It has to be clarified, whether this phenomenon is only relevant at the embryonic development stage, if this is species dependent, and if that - in case of relevance for human - is a potential risk. On the other hand, it may also be possible that the iron nanoparticles (FeNPs) are degraded, ferric iron is bound to transferrin, and transported via the circulation into hepatocytes. In case of complexes with increased stability, this would circumvents possibly toxic effects by the generation of free radicals by triggering generation of non-transferrin bound iron (NTBI), catalytic active or labile iron.

In this context the increased stability of FeHES in comparison to all other Fe containing complex drugs [229] (FerroZine® assay: **3.3.1**, Ferrozin reaction kinetic: **3.3.2**) could be of positive consequence. This study also demonstrated that the complexes are partly reversibly deposited in heart and kidney, possibly without complete degradation if phagocytic cells are not mainly responsible for the uptake or deposition there. FeHES is about 4 times more stable *in-vitro* than the highly stable complexes FeCM, HFeD (high molecular weight iron dextran; not part of the biodistribution study) & HFeD_G (generic high molecular weight iron dextran; not part of biodistribution study) (**3.4**) in comparison to heart complex concentrations elevated by ~33% in comparison to FeCM.

3.4.8.3. *Fe complexes in kidney*

Agarwal et al. [263] showed in patients with chronic kidney disease being treated with either iron sucrose (FeSuc) or sodium ferric gluconate (FeG) - which was not part of biodistribution study - that FeSuc treatment resulted in proteinuria - with higher incidence and dose-dependently. This outcome could indicate renal toxic effects of FeSuc that could be related to "free" Fe or oxidative injury. These results are interesting when compared to those of a previously published turkey egg study performed with FeSuc, FeD (low molecular weight iron dextran) and Fe gluconate [178]. FeG showed even higher kidney Fe content there. But it is remarkable that the results in kidney as well as in liver concerning FeD and FeSuc are not in good accordance with the results obtained in the present study as no differences were observed by Roth et al. [178]. This difference is probably caused by the unreliable way of administration (egg white injection, CAM application). The results of the present study with statistically highly significant highest iron (Fe) values in kidney in case of FeSuc after 24 h and 120 h incubation ($p < 0.001$) in comparison to ferric carboxymaltose (FeCM), iron hydroxyethyl starch (FeHES) and FeD also indicate a high affinity of FeSuc to kidney tissue. FeD showed the lowest affinity to kidney with only marginally higher values than recognized in heart. FeCM and FeHES values were comparable - after 24 h ($p = 0.396$) more than after 120 h ($p = 0.008$). However, FeHES showed similar values in heart and kidney whereas FeCM is slightly preferred distributed to kidney. This could be a consequence of tissue composition, blood perfusion and vascular structure as described under **3.4.4.**

3.4.8.4. *Fe complexes in muscles*

Iron (Fe) plays an important role in upholding the muscle activity in its function as cofactor in myoglobin. Myoglobin is a globular protein with a molecular weight of 17 kDa and hem as active center. Contrary to hemoglobin, myoglobin is able to bind oxygen independently from surrounding oxygen concentration and is for this reason the oxygen supplier for ATP generation inside the muscle cells by transporting oxygen intracellularly from the membrane to the mitochondria. Myoglobin is predominantly present in skeletal and heart muscle cells and causes the typical red color to the muscle.

The general Fe concentration is for that reason relatively high in muscles. But as the most Fe in muscle is bound inside the myoglobin to hem (hem-Fe) it is not of relevance for the yielded Fe concentration in this study - like hemoglobin from blood in case of e.g. heart - because FerroZine® as quantification tool is not able to bind hem-Fe.

The present study shows that Fe containing nanoparticles (NPs) distribute to upper leg muscles and probably also to other kinds of skeletal muscles with lower prevalence than in case of kidney, heart and the outstanding liver in this set-up. As muscle tissue is not part of the reticuloendothelial / mononuclear phagocyte system (RES/MPS), phagocytotic cells do not play a quantitatively important role as long as no inflammation is locally present. Therefore, the uptake of the complexes could be passively and perhaps reversibly performed by blood perfusion like in heart muscle. The uptake of nanoparticular complexes into non-phagocytotic cells may then be size and also charge dependent as already discussed [243].

Additionally the stability of the complex could play a role here too, as less stable iron complexes like iron sucrose (FeSuc) could liberate more iron than more stable iron complexes like low molecular weight iron dextran (FeD) ferric carboxymaltose (FeCM), or iron hydroxyethyl starch (FeHES) and therefore directly contribute to the iron store (ferritin) inside cells. In case of high dose or long-term application, this could cause iron overload with possible toxic effects like discussed for the other tissues. The decrease of iron levels between 24 h and 120 h indicates a reversible deposition. In comparison to the other tissues the decrease was higher in case of FeD (-56 %), FeHES (-57.4 %) and FeCM (-61.9 %). FeSuc, which is small and has a lower stability than the other complexes being applied, decreased (-41.7 %) in a comparable rate like in case of kidney (-52.9 %) but more than in case of liver and heart (***Table 13***).

3.4.9. Summary of biological complex distribution study

Tissue iron overload is related to oxidative stress and thus relevant for tissue damage and severe side effects in case of low stable complexes under lysosomal conditions. By quick liberation of the contained iron from the complex, the cellular labile iron pool (LIP) is rapidly enhanced. Cellular reactive oxygen species (ROS) generation is consequently increased and export of iron to plasma via ferroportin (Fpn) takes place. Possible consequences are protein, lipid, or DNA damage by ROS activity, and the presence of non-transferrin bound iron (NTBI) in case of Tf oversaturation, causing acute iron related adverse reactions like flushing, hypotension, vomiting, diarrhea and nausea.

Liver iron fraction increased between 24 and 120 h from 27 % in mean (22% [FeHES - iron hydroxyethyl starch] - 33% [FeCM - ferric carboxymaltose]) to 32% (26% [FeHES]-38% [FeD - low molecular weight iron dextran]). The absolute values decreased in case of concentrations, but the mean liver weight increased from 0.391 g to 0.667 g. Iron concentrations in intervention groups were elevated by factors between 8.5-11.9 and 5.9-8 after 24 h, and 120 h respectively in comparison to control groups.

Heart iron levels were investigated as cardiovascular (CV) risks in connection to *i.v.* iron treatment are a controversial discussed issue and highly relevant because of severe consequences in case of negative impact. FeHES showed moderate but highly significant higher iron levels than the other complexes after 24 and 120 h in heart. With total fractions of 0.6% (0.4% [FeD] - 0.9% [FeHES]) of the applied dose after 24 h and 0.4% (0.3% [FeD] - 0.7% [FeHES]) after 120 h the complexes distributed to the heart with much lower incidence than to liver.

Kidney iron overload is related to tissue damage in case of long-term and high dose *i.v.* iron treatment with low stable iron complexes. The kidney iron fractions - like in heart - decreased from 1.02% (0.5% [LFeD] - 1.8% [FeSuc]) after 24 h to 0.79% (0.4% [LFeD] - 1.3% [FeSuc]) after 120 h incubation. Iron levels in kidney were elevated in case of FeCM and es-

pecially for FeSuc in comparison to heart iron levels. In case of FeHES iron levels were very similar between heart and kidney (24 h: $p = 0.87$; 120 h: $p = 0.661$) indicating no specific affinity to heart or kidney. LFeD showed the lowest fraction of tissue iron in heart and liver.

The study shows that Fe containing nanoparticles (NPs) distribute to **upper leg muscle** and probably also to other skeletal muscles with lower prevalence than in case of kidney, heart and the outstanding liver in this set-up.

As the used iron quantification method cannot discriminate between iron present in the administered complexed shape or iron released from the complex and present "free" (e.g. in cellular LIP) or stored in ferritin or hemosiderin, the results of this study should always be seen in connection to stability data. Alternatively or additionally, they should be supplemented with data about (1) physiological response in Tf saturation (bioavailability) or better efficacy (Hb increase) and (2) markers of oxidative stress in tissue.

The establishment of a method in the future, distinguishing between iron present in the administered complexed shape and released iron from the complex giving valid information about the iron status inside the tissues is very much appreciated.

4. General discussion

4.1. Background

The most common consequence of iron deficiency worldwide with at least 2 billion people suffering from it is anemia [11, 264]. Nanoparticular iron complex drugs for parenteral administration beside erythropoietin stimulating agents have an outstanding status in the treatment of iron deficiency anemia in patients who are affected by chronic Kidney diseases (CKD) and require frequent hemodialysis treatment [265].

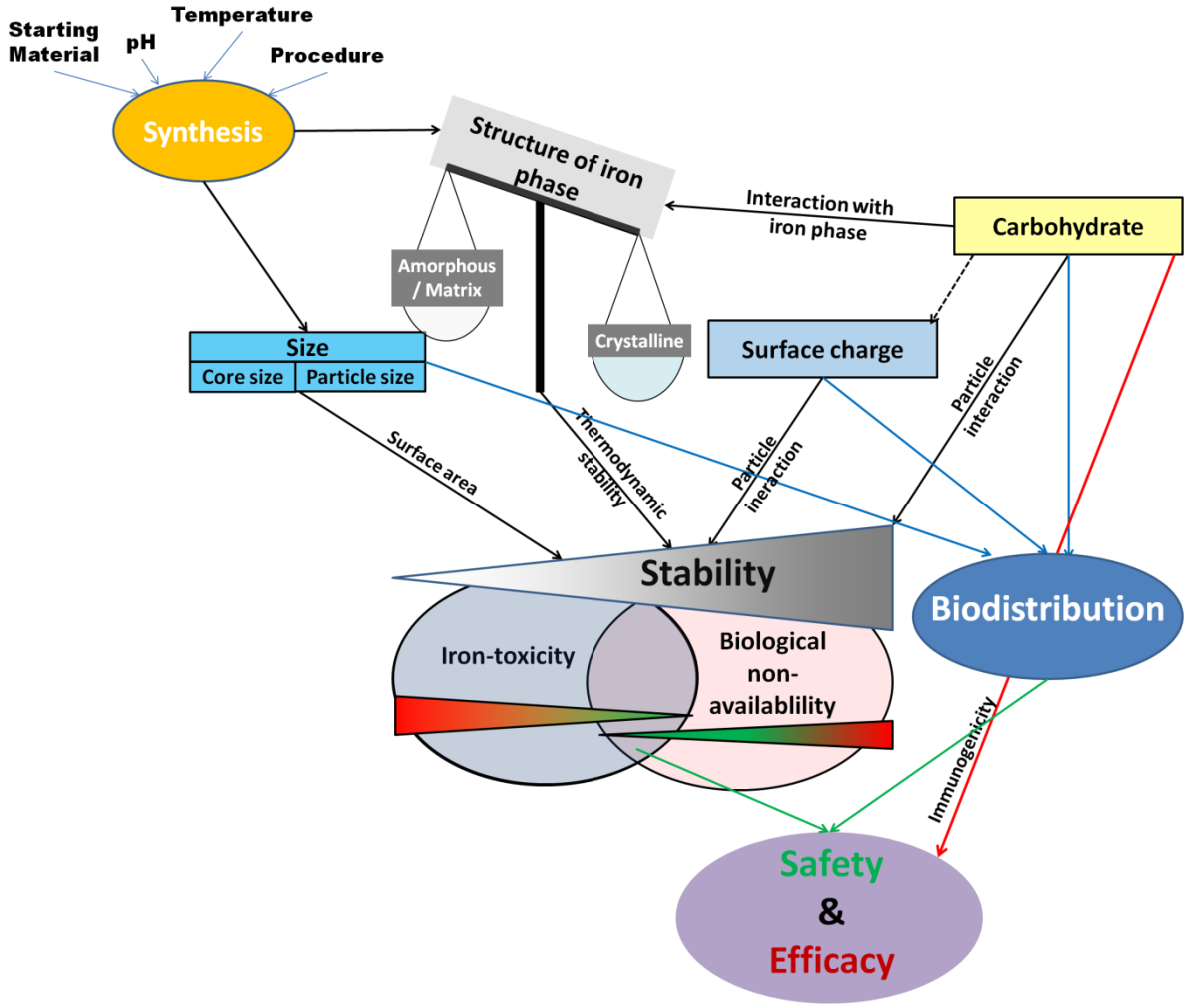

Figure 80 - Mind map summarizing the aspects of *i.v.* iron preparations influencing safety and efficacy in clinical use.

Considering their clinical use, it is important to estimate the risk of side effects of iron containing non-biological complex drug products (Fe-NbCD) (**Figure 80**). Released iron from pharmaceutical complexes is available for many reactions such as induction of oxidative stress [48, 245, 246], promotion of bacterial growth [1] and depression of neutrophil function [266] and is considered toxic for the body [227]. In addition to loosely bound iron present in the formulation or dissolved from the particle by dilution, there is a labile iron pool defined as the fraction of the total iron content that is not dissolved by dilution but can be willingly transferred to transferrin in blood [116] or *in-vitro* by iron complexing agents, e.g. EDTA [267] or FerroZine®[95]. This labile iron fraction is the consequence of weakly bound

iron in or on the surface of the complex (**Figure 83**) and is available for redox-reactions as well [48, 268]. When ferrous iron is bound to transferrin, after oxidation to ferric iron by circulating ceruloplasmin or membrane associated hephaestin, it is maintained in a redox-inert state circumventing the formation of toxic free radicals [269]. Especially in the case of high dose administration of complexes with low stability, there is a risk of potential intoxication with iron due to oversaturation of the transferrin pool with ferric iron (Fe^{3+}) [227].

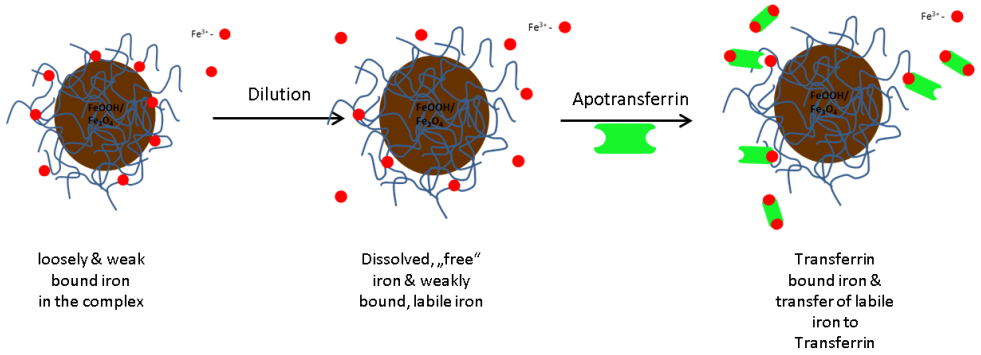

Figure 81 - Visualization of loosely and weak bound, "free", labile iron and Transferrin bound iron in plasma.

The knowledge of the structure, size/surface area, charge and type of carbohydrate in the complex, with their influence on the biodistribution, bioavailability, immunological tolerance and toxicity, may in the future lead to the synthesis of complexes with improved characteristics for clinical use. For this reason physicochemical data characterizing structure, size or chemical behavior are important to elucidate differences between Fe-NbCD and they provide evidence for the necessity to perform comparative clinical studies when new or generic products are introduced to the market [172, 173, 176].

In the present work, physicochemical characterization methods were combined with *in-vitro* stability and toxicity investigations as well as an *in-ovo* biodistribution model on turkey eggs with different iron complexes. The aim was to elucidate differences between the complexes with the possible impact on their clinical safety and efficacy profile. The aims can be summarized as follow:

- Finding physicochemical differences between different iron complexes regarding size (size of the inorganic phase by transmission electron microscopy [TEM], hydrodynamic diameter by dynamic light scattering [DLS]), charge (dispersion media dependent surface charge by ζ-potential), structure of the inorganic iron oxy hydroxide phase (electron & X-ray-powder diffraction)
- Comparing the stability (acidic hydrolysis in presence of a complexing agent) and the fraction of labile or loosely bound iron in human serum (FerroZine® assay) of the different complexes as indicators for the biological safety profile
- Assessment of the distribution of different complexes into pharmacological and toxicological target tissues
- Combination of the applied methods to estimate clinical safety and efficacy

4.2. Results of this work

Table 14 summarizes the results obtained in this work. Biological distribution results are not presented in the overview as they are much too extensive, complex and hence difficult to condense. X-ray powder diffraction (**XRPD**) ***size*** results (**3.1.1.1**, **Table 3**)were estimated values as the determination method was uncertain (**0**). Nevertheless, the values were similar to size values obtained from transmission electron microscopy (**TEM**) images in case of "core" size except in case of sodium ferric gluconate (FeG), iron sucrose (FeSuc = FeS) and iron isomaltoside 1000 (FeIM) where no sufficient amounts of pure cores were possible to observe in TEM images. The values for these complexes were comparable with particle diameters obtained from TEM images. Iron hydroxyethyl starch (FeHES) results in case of TEM size and XRPD structure were based on information directly received from the manufacturer. The images respectively diffractograms of this sample are not part of this work as it was provided by the manufacturer.

The **ζ-Potential** at non-adjusted pH value in double-distilled water indicated negative charges for ferumoxytol (FePSC), FeG, FeSuc (=FeS), FeIM, high molecular weight iron dextran (HFeD), generic high molecular weight iron dextran (HFeD_G) and low molecular weight iron dextran (LFeD). In case of FeCM as well as FeHES positive surface charge was indicated by ζ-Potential and might determine the incidence of hypophosphatemia reported in case of FeCM [111, 138]. The surface charge is reported to have influence on the clearance of the nanoparticle (NP) in vivo [201-203] and might also play a role in biological distribution.

The determination of the **iron oxide / oxy hydroxide modification** yielded a akaganéite like structure in case of FeIM, LFeD, HFeD, HFeD_G & FeCM, magnetite structure in case of FePSC and for FeSuc & FeG a more amorphous kind of structure with low level of accordance with lepidocrocite but high similarity among each other. High order arrangement of the inorganic phase with good accordance to the reference standard iron oxy hydroxide (FeOOH) (FePSC: iron oxide) was hardly possible. This is consequence of the small mean nanocrystal sizes of 5-10 nm for all complexes. The distances between the lattice planes in the crystal are at small diffraction angles up to 1 nm hence a single crystal is only some lattice planes in thickness. The influence of the inorganic phase's structure on the stability and safety of the NP is further discussed in **4.3**.

The **Particle morphology** was extracted and interpreted from TEM images (**3.2.2.1**, **3.2.2.3, Figure 64**).

Table 14 - Overview of all applied methods and corresponding results. Particle morphology is obtained from TEM images and refers to the models (a-e) presented in Figure 64: (a) pure core with carbohydrate shell, (b) polynuclear NP with quasi-cores, (c) matrix structure; (d) homogenous /more amorphous NP, (e) mixture between (b) and (d).

IV Iron Complex	Lable	Brand Name	Size [nm]				Zeta-Potential* [mV]	pH	Structure of the Core	Particle Morphology (TEM)***	Chemical Degradation			Biological Distribution Study
			XRD	TEM Core	TEM Particle	DLS: Z-average					Labile Iron Content [%]	k [%/min^1/2]	halflife [h]	
Sodium ferric gluconate	FeG	Ferrlecit[5]	4.7	-	4.1	13.6	-43	8.4	Lepidocrocite / amorphous	b, d, [e]	4.41	2.4	4.4	-
Iron sucrose	FeS	Venofer[5]	4.9	-	5	11.7	-39	10.8	Lepidocrocite / amorphous	b, d, [e]	4.76	3.1	7.6	x
LMWID	LFeD	CosmoFer[5]	6.2	5	12.6**	14.8	-25	6.4	Akaganéite	a, b, d, [e]	1.93	0.8	66.7	x
		InFed[5]	6.4	4.8	14.9**	15.3	-28	6						
HMWID	HFeD	Dexferrum[5]	8.8	8.7	17.1	31	-31	6.7	Akaganéite	a, b, d, [e]	0.71	0.4	267	-
Generic iron dextran	HFeD_G	Ironate[5]	7.2	7.5	17.5	23.9	-13	5.8	Akaganéite	a, b, d, [e]	0.95	0.6	134	-
Iron isomaltosid 1000	FeIM	Monofer[5]	5.7	-	6.3	13.3	-33	6.3	Akaganéite	b, c, d	1.06	1.1	38.1	-
Ferumoxytol	FePSC	FeraHeme[5] / Rinso[5]	7.5	6.6	16.7	29.9	-59	7	Magnetite	a, b, c, d, [e]	1.09	1.0	43.5	-
Ferric carboxymaltose	FeCM	Ferinject[5] / Injectafer[5]	7.7	5.9	18.6	27.5	5	5.4	Akaganéite	b, d, [e]	0.77	0.4	224	x
Iron hydroxyethyle starch	FeHES	Feramyl[5]	-	-	28.2****	63.3	18	4.9	Akaganéite****	-	0.28	0.1	3703	x

* pH Influence

** SD must be considered; particle size of Cosmofer[5] and Infed[5] can be considered equivalent

*** Particle morphology types corresponding to Figure 60

**** Information from manufacturer/ source-data not presented

The **Labile iron content** determined by FerroZine® assay (**3.3.1**) indicates the safety profile of the complexes as it is source of iron related ADEs in case of Tf oversaturation. FeSuc and FeG showed the highest fractions of labile iron content followed by LFeD and the other complexes. FeHES showed the by far the lowest labile iron fraction. This and the very high **stability** (**3.3.2**) under the applied conditions (with the acidifying, iron chelating citric acid under reductive condition by ascorbate) indicated a very good safety profile for FeHES in plasma.
Bioavailability investigations, clarifying whether the contained iron is readily released from the complexes in the RES or is showing the same stability with consequently low bioavailability, are of high interest in this connection. The low stability of FeSuc and FeG were in well accordance with literature data. FeIM and FePSC showed a similar stability, which was much higher than that of FeSuc and FeG. LFeD < HFeD_G < FeCM = HFeD showed high stability under the applied conditions only outreached by FeHES.

The **biodistribution study** was performed in a turkey egg model with tissue sampling of the whole liver, heart and kidney as well as a fraction of upper leg muscle after 24 and 120 h, respectively in case of FeSuc, LFeD, FeCM and FeHES. It shows comparative distribution profiles of the different complexes in the liver as part of the mononuclear phagocyte system (MPS) / reticoloendothelial system (RES) as well as in toxicological target tissues (kidney & heart).
Concentration in muscle was measured to investigate the distribution into a peripheral tissue.

4.3. Structure, size & stability

A relationship between size and stability has already been published for some of these compounds [95]. Labile iron content can be adjusted with the surface to volume ratio. This correction factor considers the inverse dependency of the dissolution rate from the diameter of a disperse phase. In case of the iron containing non-biological complex drugs (Fe-NbCD) this is related to the dissolution of iron from the complex in human serum e.g. by reductive agents (ascorbic acid).

Low stability complexes with high labile iron content (low binding affinity of the carbohydrate / serum-enzyme degradable carbohydrates / low crystallinity of the contained iron fraction (lower solubility **2.2.3**)) and small single nanoparticles (NPs) (increased dissolution rate & solubility pp. **52-52**) may be rapidly degraded not only in the mononuclear phagocyte system (MPS) / reticoloendothelial system (RES) but even in plasma which overloads transferrin (Tf) binding capacity causing iron related adverse drug events (ADEs).

Complexes with high stability and low labile iron content (high binding affinity of the carbohydrate and/or serum stable carbohydrate (non-α-1-4-gylycoside; e.g. dextran) and/or high crystalline fraction (higher solubility) and/or larger NPs (decreased dissolution rate & solubility) may show lower incidences of iron toxicity but might be slowly degraded and show therefore low or retarded bioavailability (**Figure 9**).

The correction of the labile iron content to surface to volume ratio (**3.3.1**), as well as the correction of liberation of iron from the complex to surface to volume ratio (**3.3.2**) was performed, using the size information yielded from dynamic light scattering (DLS; Z-average) in case of the complete complex, and X-ray powder diffraction (XRPD) in case of inorganic iron oxy hydroxide (FeOOH) fraction (mean nanocrystal size). The transmission electron microscopy (TEM) core diameters have not been recognized in case of every kind of complex. As described in section **2.2.1** the nanoparticle (NP) size influences the dissolution rate (Noyes-Whitney equation: *Formula 10*) as well as the solubility (Ostwald-Freundlich equation: Formula 12). The surface of the complete particle represents the boundary surface of interaction between high molecular weight complexing agents or molecules (e.g. Tf) and the particle. Small particles (core plus shell) will show increased interaction with Tf in comparison to larger particles and thus show higher levels of labile iron. This is even more relevant in case of loosely bound iron on the surface of the complex. The surface of the core represents the possible interaction between the medium in which the complex is dispersed and physicochemical characteristics of the medium (acidity, reducing agents). Thus, small cores will dissolve faster than larger particles.

Accordingly, big particles show increased stability. However, size of parenteral applied particles is limited, as the size distribution might drift during storage of the formulations and increased paticle size in this context might have severe consequences after application: The circulating particles are surrounded by plasma proteins (a so called protein corona) giving them an increased hydrodynamic diameter with the potential risk of embolism if those particles show *in-vivo* diameters in the scale of thin capillaries (~5 µm). In case of the iron complexes used for the treatment of iron definiency anemia, all the investigated nanoparticles

show diameters below this scale with sized below 100 nm, circumventing the risk of fatal embolisms.

A thick carbohydrate shell surrounding the core(s) protects the inorganic core or inorganic fraction (in case of homogenous particles) from being rapidly dissolved. The NP will thus show increased stability against any kind of physical and chemical impact as long as the carbohydrate fraction remains intact (absence of enzymatic degradation in case of non-dissociating carbohydrates).

In respect of these influences the labile iron fraction (F_{LFe}) in the complex as well as the liberating constant (k) of assumed square root kinetics are corrected with the volume (V) to surface (A) ratio of the core (**Figure 83**, **Figure 85**) and of the whole particle (**Figure 82**, **Figure 84**), respectively :

$$F_{LFe_{corr}} = F_{LFe} \cdot V/A$$

$$k_{corr} = k \cdot \frac{V}{A}$$

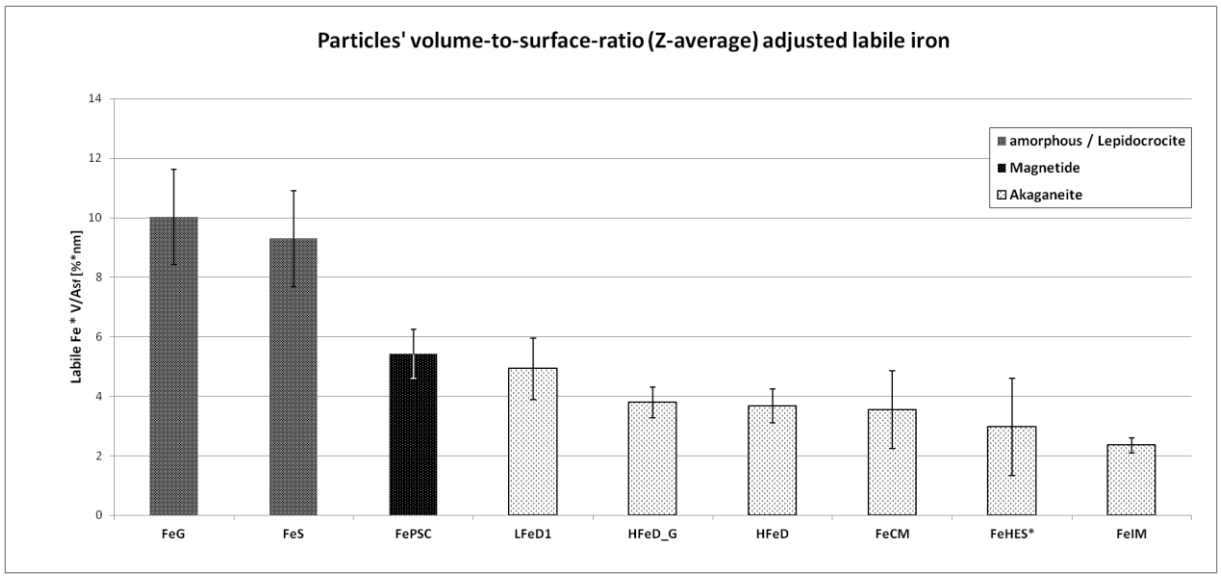

Figure 82 - Labile iron corrected with volume to surface ratio of the complete particle determined by DLS.

Corrected labile iron by volume to surface ratio of the complete particle (**Figure 82**) demonstrates that sodium ferric gluconate (FeG) as well as iron sucrose (FeSuc = FeS) show highest labile iron contents, even after correction. The labile iron content of ferumoxytol (FePSC) is at the same range as in case of low molecular weight iron dextran (LFeD) and relatively increased in comparison to uncorrected labile iron content. This indicates lower stability of the complex, which may be related to the iron modification of the "iron core" or the interaction between the iron fraction and the carbohydrate. There is a good homogeneity among the complexes containing akaganéite like FeOOH fractions in **Figure 82**. The lowest corrected labile iron content in case of FeIM might indicate that the structural specialness (**3.2.2.1**) with FeOOH fractions bedded in a kind of matrix has a stabilizing influence on the complex.

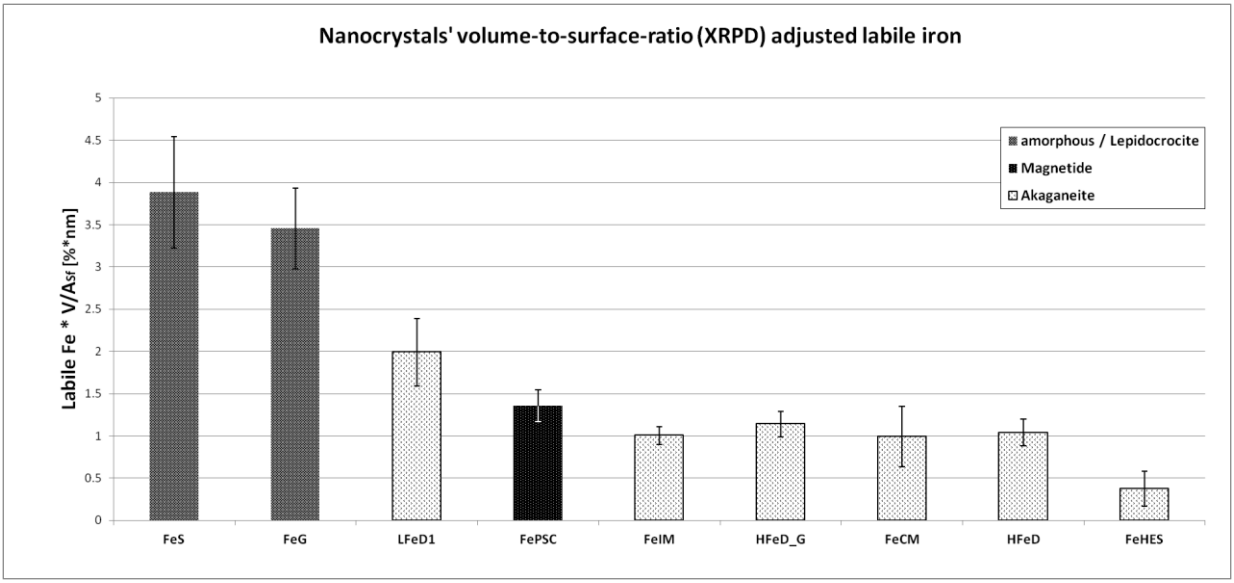

Figure 83 - Labile iron corrected with volume to surface ratio of the mean single nanocrystal determined by XRPD.

The corrected labile iron by volume to surface of the nanocrystals (**Figure 83**) with relatively low fraction in case of ferumoxytol (FePSC) is an evidence that the higher fraction in **Figure 82** might be determined by the interaction between carbohydrate and the inorganic fraction.

The relatively low content of corrected labile iron in case of iron hydroxyethyl starch (FeHES) in **Figure 83** and the similar value in relation to other akaganéite like samples in **Figure 82** indicate that the increased size of the particle is the main reason for the low labile iron content in this case. The altering corrected values in **Figure 83** and the higher similarity among complexes with similar modifications of the iron fraction in case of **Figure 82** indicate that the labile iron content does not well correlate with the size of the mean single nanocrystal but more with the size of the complete particle. This is well comprehensible as labile iron is measured in serum and transferrin (Tf) is able to bind iron directly from the surface of the particle and less probably from the core as it is protected by the carbohydrate fraction.

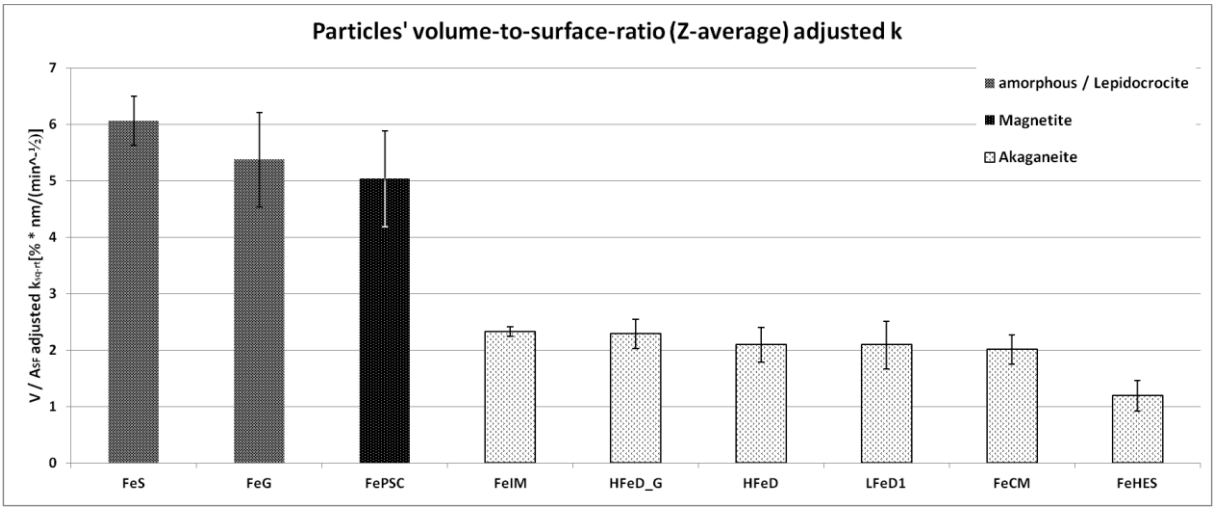

Figure 84 - Liberation constant (k) corrected with the volume to surface ratio of the complete particle determined by DLS.

The corrected liberation constant indicates highest stability of FeHES independent from size of the core (**Figure 85**) and size of the complete particle (**Figure 84**).

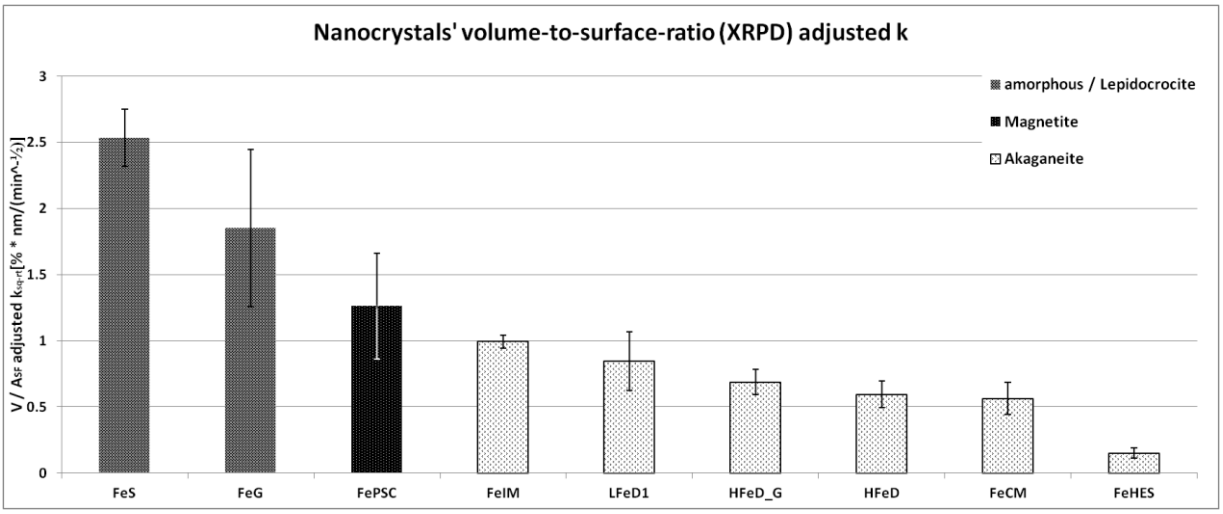

Figure 85 - Liberation constant (k) corrected with the volume to surface ratio of a single nanocrystal determined by XRPD.

This indicates a high stabilizing influence of the carbohydrate on the inorganic iron fraction. In case of lysosomal degradation, the presence of glycosidases may abolish this stabilizing effect and enhance degradability with positive influence on bioavailability.
However, some kind of carbohydrates (e.g. dextrans; carboxymaltose) show immunogenic behavior which is increasing with rising particle sizes, triggering opzonisation and subsequent uptake into phagocytic cells were the complex is degraded inside lysosomes.
Corrected values for FeSuc (=FeS) and FeG show highest instabilities of the complexes (**Figure 84**) as well as for the purely inorganic crystalline fraction (**Figure 85**).

The high value of the corrected liberation constant of FePSC in **Figure 84** indicated that the size of the complete particle has a positive influence on the degradation of the complex under the applied conditions. The relatively high corrected liberation constant of FePSC and the order among the complexes in **Figure 84** and **Figure 85** can be related to the dissolution rates of reference iron oxide/oxy hydroxide modifications. The different solubility factors of the different types of iron oxide/oxy hydroxide phases forming the particle could cause this order among the different complexes. There is good accordance to the dissolution rates in 0.5 M HCl: Lepidocrocite ($6.43 \cdot 10^4$ g*Fe*m^{-2}*h^{-1}) > magnetite ($3.48\ 10^4$ g*Fe*m^{-2}*h^{-1}) > akaganéite ($1.4\ 10^4$ g*Fe*m^{-2}*h^{-1}) [270].

The stability under the applied conditions thus is referred to the kind of iron oxide / iron oxy hydroxide in the nanoparticles. Iron sucrose and sodium ferric gluconate contain lepidocrocite or an amorphous kind of structure. Ferumoxytol contains magnetite, while akaganéite is recognized in low molecular weight iron dextran, generic high molecular weight iron dextran, iron isomatoside 1000, high molecular weight iron dextran, ferric carboxymaltose, and iron hydroxyethyl starch.

4.4. Biological distribution and complex characteristics

The biodistribution study (**3.4**) gives an interesting insight into the biodistribution of four different iron containing nanoparticular formulations for the intravenous administration in a turkey egg model. In general, the complexes behaved quite comparable - with small but significant differences between the different complexes. All complexes showed as expected by far highest values in the liver as main pharmacological target tissue and part of the reticuloendothelial system (RES) beside spleen and bone marrow. There they were taken up, degraded by lysosomes and the contained iron was stored in ferritin and was consequently bioavailable.
As the liver is a major pharmacological target tissue for intravenous iron treatment, the results of the present study give an important comparative overview on the uptake of different iron complexes into the liver. As the liver is the main storage of iron in form of ferritin inside the hepatocytes [228] it might therefore indicate bioavailability of the iron in the different complexes. At the other hand, iron overload leading to increased labile iron levels will increase oxidative stress in tissues like the heart and kidney, and can induce severe negative effects. As the quantification method applied in this study does not differ between (I) iron present free or catalytic active or (II) iron present complexed in the applied form, the measured values cannot directly be connected with the presence of free or catalytically active iron and consequently toxic effects. The stability of each complex is strongly determined by the physicochemical properties like size, kind of carbohydrate in the complex, structure of the inorganic iron phase, and level of interaction between carbohydrate and the complexed iron (matrix structure / core shell structure). High stability complexes (like iron hydroxyethyl starch [FeHES] or ferric carboxymaltose [FeCM]) might be degraded slowly insight the lysosomes in comparison to lower stability complexes (iron sucrose [FeSuc]) influencing the rate of response in hemoglobin level enhancement but not necessarily the absolute bioavailable amount of iron. On the other hand, the iron related toxicity profile of high stability complexes might be lower, caused by the same principle. Thereby, highly stabile complexes are supposed to be administered in higher doses per clinical session and patients might therefore be spared from more frequent infusions. The reduction of occurance and extent of side effects by free and therefore toxic iron overload could be an additional benefit of high stable complexes like FeCM and FeHES.
The complex stability plays a major role in this context. A complex with higher physical and chemical stability (demonstrated *in-vitro* by FerroZine® detectable labile iron assay (**3.3**), or acid soluble iron determination [95]) is expected to lead not to unbound iron - if not degraded actively by lysosomal cells (like Kupffer cells in the liver). Thus, it will not contribute to toxic effects caused by reactive oxygen species (ROSs) at equivalent doses, in comparison to complexes with lower stability.

Significant differences between the applied and physicochemical different complexes were observed by the biodistribution study in this work. Physicochemical properties like size, surface charge, and kind of carbohydrate influence the biodistribution of nanoparticular com-

plexes as reported [119] and as shown by physicochemical characterization within this work. Linking the physicochemical properties (size, structure of the iron phase, kind of carbohydrate) and stability data (FerroZine® detectable labile iron assay or liberation kinetics) with the biodistribution observed in the present study could be a very helpful tool in forecasting benefit to risk profiles of iron complexes. To validate and proof the quality of those predictions it would be helpful to perform additional investigations determining effects of local oxidative stress by ROSs and the response in hemoglobin enhancement by the complexes. Additional information gained from other species is also helpful to transfer those data to human and establish a confident model for the estimation of the benefit to risk profile for every iron complex drug for parenteral administration.

From high interest is the establishment of a method distinguishing between iron present in the native (complexed) shape and released iron from the complex, giving valid information about the iron status inside the tissues. In future, this could probably be implemented by microscopy using radioactive labeled complexes manufactured by the same process as the reference complex. An alternative could be the visualization of the complexes probably with fluorescent lectins specifically conjugating the iron complexing carbohydrate of the nanoparticle (NP) and making the lectin coupled complex visible under the microscope.

5. Conclusion

Within the last couple of years some new kind of commercial complexes as well as generic preparations entered the market. There is a high demand for methods clarifying benefit to risk profiles of old and new kind of complexes. It is also necessary to disclose interchangeability between originator and intended copies to avoid severe anaphylactic and anaphylactoid side reaction

The investigations presented in this work include physicochemical characterization of nine different parenteral iron containing non-biological complex drugs (Fe-NbCD). These are drugs, partly only marketed in some countries. Namely, iron sucrose (IS; brand name Venofer®), sodium ferric gluconate sucrose (FeG; Ferrlecit®), low molecular weight iron dextran (LMWID: LFeD1; CosmoFer® and/or LFeD2; InFed®), high molecular weight iron dextran (HMWID: HFeD; Dexferrum®), a generic iron dextran identified as generic HMWID (HFeD_G; Ironate®), iron isomaltoside 1000 (FeIM; Monofer®), ferric carboxymaltose (FeCM; Ferinject®), and ferumoxytol (FePSC; Feraheme®). Iron hydroxyethyl starch (FeHES, Feramyl®) as a new kind of complex at the stage of market authorization completes the group of investigated nanoparticular *i.v.* iron products.
The ζ-potential measurements were performed to characterize the different Fe-NbCD in respect to medium dependent surface charge (**3.1.3**). The investigations of the hydrodynamic size of the particles by dynamic light scattering (DLS, **3.1.1.2**), the size of the iron containing phase by transmission electron microscopy (TEM) and the mean diameter of single nanocrystals of iron oxide respectively oxy hydroxide (FeOOH) crystals (**3.1.1.1**) allowed the assessment of fundamental differences of the particles with influence on dissolution rate and solubility. The Dissolution rate and solubility directly influence safety and efficacy of *i.v.* iron complexes as the contained iron exhibits toxicity in case of enhanced liberation to plasma with severe adverse drug events (ADEs, **1.2.7**), or it lacks bioavailability in case of slow degradation of the complexes in macrophages (**1.4.4**).
We developed an *in-vitro* assay, which allows the quantification of labile iron (**Figure 81**) in the different complexes after complex dilution to relevant concentrations in human serum. This FerroZine® assay (**3.3.1**) was used to compare the different complexes in respect to labile iron content and it additionally allowed the estimation of complex stability by evaluation of degradation kinetics (**3.3.2**) at the applied conditions. This in combination with morphologic evaluation from TEM images (**3.2.2**) and structure determination by diffraction methods via electrons (ED) and X-rays (XRPD) (**3.2.1**) allowed the correlation of size, stability and structure (**4.3**).
Additionally, an *in-ovo* study was performed at the BfArM (Federal Institute for Drugs and Medical Devices in Germany) to compare different complexes in respect to biological distribution (**3.4**). The *i.v.* application of four different complexes (LFeD1, FeSuc, FeCM and FeHES) into turkey eggs and the iron quantification in liver, heart, kidney, and upper leg muscle after two incubation times, yielded information about differences between the complexes in respect to biodistribution. This in combination with complex stability information allowed the

risk estimation of potential local acute and chronic reactions to iron overload in e.g. heart (cardiovascular risk) and kidney (**3.4.8.3**) but should always be combined with studies in other species (e.g. rodents) to estimate relevance for humans.
The combination of complex stability and biodistribution as well as the combination of structure, size and stability represent helpful tools for the physicochemical characterization of iron containing non-biological complex drugs and for the estimation of pharmacological safety. The example of Ironate®, as generic iron dextran, for which the results show relevant differences to low molecular weight iron dextran (LMWID), shows that these methods can be applied to compare an intended copy to the reference product before using bioequivalence studies. This is especially relevant in case of the iron dextrans as LMWID shows significant lower rates of anaphylaxis than HMWID (**1.4.5**).

The methodology applied within this work can be used to clarify differences between different iron containing non-biological complex drugs (Fe-NbCD) in respect to current opinions of regulatory authorities (**1.4.7**) especially the following specifications:
Quality characterization:

- "Size (and size distribution) and specific surface area of the iron core"
  → XRPD - Scherrer, TEM (**3.1.1.1**)
- "the fraction of labile iron released from the product when administered"
  → FerroZine® detectable labile iron (**3.3.1**)
- "polymorphic form of the inorganic iron compound comprising the core"
  → XRPD (**3.2.1**)
- "Morphology e.g. microscopic evaluation of the iron distribution in the iron complex (e.g. iron surrounded by a carbohydrate coat, iron distributed through a carbohydrate matrix)"
  →TEM (**3.2.2**)
- "Particle size, size distribution"
  → DLS (**3.1.1.2**)
- "Charge, of the iron-carbohydrate complexes"
  → ζ-Potential (**3.1.3**)
- "*in-vitro* iron release rate from the iron-carbohydrate complex in physiologically/clinically relevant media. Reliable and discriminating validated in vitro release methods should be developed using models that represent the extracellular (plasma/serum) release of labile iron and acid degradation kinetics"
  → FerroZine® reaction kinetics & liberation (**3.3.2**)
- "validated analytical methods for the quantification of analytes in blood/plasma and tissue"
  → iron quantification in tissue by a modified version of the method corresponding to Rebouche et al. (**2.4.3,** [200])
- "Biodistribution studies in a relevant animal model with focus on RES, plasma and pharmaceutical as well as toxicological target tissues (liver, heart, kidney, lung)"

→ Biological distribution study in turkey eggs with sampling of liver, heart, kidney & muscle (**3.4**)

This work thus represents an up to date summary of some relevant methods for the characterization of *i.v.* iron complex drugs in respect to pharmaceutical quality, pharmacological safety and aspects of efficacy.

By these methods similarities and differences between the different kinds of iron containing non-biological complex drugs (Fe-NbCD) can be demonstrated. We were able to demonstrate physicochemical differences between the complexes in respect to the size of the inorganic fraction, size and size distribution of the complete particles, structure of the inorganic iron fraction, morphology of the complexes and charge of the complexes. These characteristics were completed with the establishment of an *in-vitro* experiment in human serum allowing the determination of comparative labile iron contents in the different complexes. This FerroZine®-assay is thus a useful tool to estimate the pharmacological safety in respect of iron related adverse drug events and it additionally allows the identification of the complex stability. The *in-ovo* turkey model rounding up his work gave significant information on the biological behavior of different complexes. It is thus very helpful to verify differences and similarities between iron containing non-biological complex drugs.

The information obtained by the combination of the methods within this work are helpful for authorities and physicians to estimate the safety and efficacy profile of different iron containing non-biological complex drugs with decreased requirement of complex and expensive clinical studies. Moreover, this work allows companies and scientists to estimate benefit to risk profiles of new kind of complexes at early stage of development.

The physicochemical characterization, the estimation of pharmacological safety from labile iron content and in-vitro stability as well as the biological distribution of the complexes in different tissues give useful information in this context. In future, there is still demand of quantitative methods distinguishing between iron liberated from *i.v.* pharmaceutical formulations and iron present in the native (complexed) shape to disclose bioavailability of the complexes.

Iron deficiency is the most common deficiency disease worldwide with many patients who require *i.v.* iron. Forward-looking, it is worthwhile that the methods within this work will contribute to the development and/or characterization of iron containing nanoparticular formulations with beneficial efficacy and safety profiles.

6. References

[1] A. Barton Pai, M.P. Pai, J. Depczynski, C.R. McQuade, R.C. Mercier, in, Karger Publishers, 2006, pp. 304-309.
[2] P. Williams, E. Griffiths, in, Springer, 1992, pp. 301-322.
[3] N.C. Andrews, Nat Rev Genet, 1 (2000) 208-217.
[4] R.R. Crichton, J.R. Boelaert, Inorganic biochemistry of iron metabolism: from molecular mechanisms to clinical consequences, 2 ed., Wiley, 2001.
[5] J. Wang, K. Pantopoulos, in, 2011, pp. 365-381.
[6] M.W. Hentze, M.U. Muckenthaler, B. Galy, C. Camaschella, in, Elsevier, 2010, pp. 24-38.
[7] J.D. Cook, W.E. Barry, C. Hershko, G. Fillet, C.A. Finch, in, American Society for Investigative Pathology, 1973, pp. 337.
[8] T. Ganz, E. Nemeth, Biochimica et Biophysica Acta (BBA) - Molecular Cell Research, 1823 (2012) 1434-1443.
[9] K. Pantopoulos, S.K. Porwal, A. Tartakoff, L. Devireddy, Biochemistry, 51 (2012) 5705-5724.
[10] A.R. West, P.S. Oates, World J Gastroenterol, 14 (2008) 4101-4110.
[11] E.C. Theil, in, Am Soc Nutrition, 2011, pp. 724-728.
[12] A. McKie, in, 2008, pp. 1239-1241.
[13] H. Gunshin, B. Mackenzie, U.V. Berger, Y. Gunshin, M.F. Romero, W.F. Boron, S. Nussberger, J.L. Gollan, M.A. Hediger, Nature, 388 (1997) 482-488.
[14] M. Shayeghi, G.O. Latunde-Dada, J.S. Oakhill, A.H. Laftah, K. Takeuchi, N. Halliday, Y. Khan, A. Warley, F.E. McCann, R.C. Hider, Cell, 122 (2005) 789-801.
[15] A. Qiu, M. Jansen, A. Sakaris, S.H. Min, S. Chattopadhyay, E. Tsai, C. Sandoval, R. Zhao, M.H. Akabas, I.D. Goldman, Cell, 127 (2006) 917-928.
[16] T.A. Rouault, in, Elsevier, 2005, pp. 649-651.
[17] R. Gräsbeck, I. Kouvonen, M. Lundberg, R. Tenhunen, Scandinavian journal of haematology, 23 (1979) 5.
[18] L.L. Dunn, Y.S. Rahmanto, D.R. Richardson, in, Elsevier, 2007, pp. 93-100.
[19] I. Yanatori, M. Tabuchi, Y. Kawai, Y. Yasui, R. Akagi, F. Kishi, in, BioMed Central Ltd, 2010, pp. 39.
[20] K.M. O'Callaghan, V. Ayllon, J. O'Keeffe, Y. Wang, O.T. Cox, G. Loughran, M. Forgac, R. O'Connor, in, ASBMB, 2010, pp. 381-391.
[21] A.A. Khan, J.G. Quigley, Molecular Aspects of Medicine, 34 (2013) 669-682.
[22] A. Uc, J.B. Stokes, B.E. Britigan, Am J Physiol Gastrointest Liver Physiol, 287 (2004) G1150-1157.
[23] J.G. Quigley, Z. Yang, M.T. Worthington, J.D. Phillips, K.M. Sabo, D.E. Sabath, C.L. Berg, S. Sassa, B.L. Wood, J.L. Abkowitz, in, Elsevier, 2004, pp. 757-766.
[24] B.C. Lee, in, Wiley Online Library, 1995, pp. 383-390.
[25] M. Paoli, B.F. Anderson, H.M. Baker, W.T. Morgan, A. Smith, E.N. Baker, in, Nature Publishing Group, 1999, pp. 926-931.
[26] A. Donovan, C.A. Lima, J.L. Pinkus, G.S. Pinkus, L.I. Zon, S. Robine, N.C. Andrews, in, Elsevier, 2005, pp. 191-200.
[27] S. Soe-Lin, S.S. Apte, B. Andriopoulos, M.C. Andrews, M. Schranzhofer, T. Kahawita, D. Garcia-Santos, P. Ponka, in, National Acad Sciences, 2009, pp. 5960-5965.
[28] E. Nemeth, M.S. Tuttle, J. Powelson, M.B. Vaughn, A. Donovan, D.M. Ward, T. Ganz, J. Kaplan, in, American Association for the Advancement of Science, 2004, pp. 2090-2093.

[29] D.M. Frazer, S.J. Wilkins, E.M. Becker, C.D. Vulpe, A.T. McKie, D. Trinder, G.J. Anderson, Gastroenterology, 123 (2002) 835-844.
[30] N.P. Mena, A.s. Esparza, V. Tapia, P. ValdÃ©s, M.T. NÃºÃ±ez, in, Am Physiological Soc, 2008, pp. G192-G198.
[31] C. Brasse-Lagnel, Z. Karim, P. Letteron, S. Bekri, A. Bado, C. Beaumont, in, Elsevier, 2011, pp. 1261-1271. e1261.
[32] T.S. Koskenkorva-Frank, G. Weiss, W.H. Koppenol, S. Burckhardt, in, Elsevier, 2013, pp. 1174-1194.
[33] P. Piccinelli, T. Samuelsson, in, Cold Spring Harbor Lab, 2007, pp. 952-966.
[34] T.A. Rouault, in, Nature Publishing Group, 2006, pp. 406-414.
[35] B. Galy, D. Ferring-Appel, S. Kaden, H.-J. Grone, M.W. Hentze, in, Elsevier, 2008, pp. 79-85.
[36] G. Cairo, A. Pietrangelo, in, 2000, pp. 241-250.
[37] N. Andrews, in, 2005.
[38] M.W. Hentze, M.U. Muckenthaler, N.C. Andrews, in, Elsevier, 2004, pp. 285-297.
[39] D.R. Richardson, E. Baker, in, Wiley Online Library, 1994, pp. 160-168.
[40] W. Breuer, A. Ronson, I.N. Slotki, A. Abramov, C. Hershko, Z.I. Cabantchik, Blood, 95 (2000) 2975-2982.
[41] P. Aisen, in, Elsevier, 2004, pp. 2137-2143.
[42] C. Hershko, G. Graham, G.W. Bates, E.A. Rachmilewitz, Br J Haematol, 40 (1978) 255-263.
[43] A. Silva, R.C. Hider, in, Elsevier, 2009, pp. 1449-1458.
[44] R.C. Hider, A.M.N. Silva, M. Podinovskaia, Y. Ma, in, Wiley Online Library, 2010, pp. 94-99.
[45] B.P. Esposito, W. Breuer, P. Sirankapracha, P. Pootrakul, C. Hershko, Z.I. Cabantchik, Blood, 102 (2003) 2670-2677.
[46] S. Fishbane, A. Mathew, N.D. Vaziri, Nephrology Dialysis Transplantation, (2013) gft269.
[47] J. Parkkinen, L. von Bonsdorff, S. Peltonen, C. Gronhagen-Riska, K. Rosenlof, Nephrology Dialysis Transplantation, 15 (2000) 1827-1834.
[48] B.P. Esposito, W. Breuer, I. Slotki, Z.I. Cabantchik, Eur J Clin Invest, 32 Suppl 1 (2002) 42-49.
[49] J.F. Collins, C.A. Franck, K.V. Kowdley, F.K. Ghishan, in, Am Physiological Soc, 2005, pp. G964-G971.
[50] M. Shindo, Y. Torimoto, H. Saito, W. Motomura, K. Ikuta, K. Sato, Y. Fujimoto, Y. Kohgo, in, Elsevier, 2006, pp. 152-162.
[51] P. Brissot, M. Ropert, C. Le Lan, O. Loreal, in, Elsevier, 2012, pp. 403-410.
[52] K. Jomova, D. Vondrakova, M. Lawson, M. Valko, in, Springer, 2010, pp. 91-104.
[53] C. LeeYoung, in, National Science Council, 2000, pp. 151-155.
[54] L.D. Horwitz, E.A. Rosenthal, in, SAGE Publications, 1999, pp. 93-99.
[55] D.G. Meyers, in, Wiley Online Library, 1996, pp. 925-929.
[56] D.B. Kell, BMC medical genomics, 2 (2009) 2.
[57] M. Patel, D. Ramavataram, in, Springer, 2012, pp. 322-332.
[58] N.D. Chasteen, P.M. Harrison, in, Elsevier, 1999, pp. 182-194.
[59] G.W. Richter, in, American Society for Investigative Pathology, 1978, pp. 362.
[60] T.C. Iancu, H.B. Neustein, British Journal of Haematology, 37 (1977) 527-535.
[61] World Health Organization, The World Health Report 2002: Reducing Risks, Promoting Healthy Life, 1 ed., WHO, 2002.

[62] World Health Organization, Preventing and Controlling Iron Deficiency Anaemia Through Primary Health Care: A Guide for Health Administrators and Programme Managers, 1 ed., WHO, 1989.
[63] A.F. Goddard, M.W. James, A.S. McIntyre, B.B. Scott, in, BMJ Publishing Group Ltd and British Society of Gastroenterology, 2011, pp. 1309-1316.
[64] N.C. Andrews, N Engl J Med, 341 (1999) 1986-1995.
[65] J.W. Eschbach, Best Pract Res Clin Haematol, 18 (2005) 347-361.
[66] L. Thomas, C. Thomas, H. Heimpel, in, 2005, pp. 580-586.
[67] K. Liu, A.J. Kaffes, in, LWW, 2012, pp. 109-116.
[68] T. Büchner, Anämien, in: Therapie innerer Krankheiten, Springer, 2005, pp. 1063-1077.
[69] B. Dresow, D. Petersen, R. Fischer, P. Nielsen, in, Springer, 2008, pp. 273-276.
[70] C. Hutchinson, W. Al-Ashgar, D.Y. Liu, R.C. Hider, J.J. Powell, C.A. Geissler, in, Wiley Online Library, 2004, pp. 782-784.
[71] K. Schümann, S. Kroll, M.E. Romero-Abal, N.A. Georgiou, J.J.M. Marx, G. Weiss, N.W. Solomons, in, Karger Publishers, 2012, pp. 98-107.
[72] K. Schümann, N.W. Solomons, M.-E. Romero-Abal, M. Orozco, G. Weiss, J. Marx, in, Nevin Scrimshaw International Nutrition Foundation, 2012, pp. 128-136.
[73] P. Geisser, Arzneimittel-Forschung, 57 (2007) 439-452.
[74] R. Ortiz, J.E. Toblli, J.D. Romero, B. Monterrosa, C. Frer, E. Macagno, C. Breymann, in, Informa Healthcare London, 2011, pp. 1347-1352.
[75] J.E. Toblli, R. Brignoli, Arzneimittelforschung, 57 (2007) 431-438.
[76] I.C. Macdougall, Kidney Int Suppl, 69 (1999) S61-66.
[77] S. Fishbane, Am J Kidney Dis, 34 (1999) S47-52.
[78] K. Mengel, Antianaemika, in: Arzneiverordnungs-Report 2012, Springer Berlin Heidelberg, 2012, pp. 299-309.
[79] NICE-guideline, National Institute for Health and Clinical Excellence, (2008).
[80] J.W. Eschbach, J.D. Cook, B.H. Scribner, C.A. Finch, in, Am Coll Physicians, 1977, pp. 710-713.
[81] W.H. Hörl, I.C. Macdougall, J. Rossert, R.M. Schaefer, in, ERA-EDTA, 2007, pp. iii2-iii6.
[82] C. Hutchinson, C.A. Geissler, J.J. Powell, A. Bomford, in, BMJ Publishing Group Ltd and British Society of Gastroenterology, 2007, pp. 1291-1295.
[83] R.C. Kopelman, L. Smith, L. Peoples, R. Biesecker, A.R. Rizkala, in, Wiley Online Library, 2007, pp. 238-246.
[84] S. Fishbane, G.L. Frei, J. Maesaka, Am J Kidney Dis, 26 (1995) 41-46.
[85] V. Allegra, G. Mengozzi, A. Vasile, in, Karger Publishers, 1991, pp. 175-182.
[86] H. Li, S.-x. Wang, in, Karger Publishers, 2008, pp. 151-156.
[87] I.C. Macdougall, B. Tucker, J. Thompson, C.R. Tomson, L.R. Baker, A.E. Raine, Kidney Int, 50 (1996) 1694-1699.
[88] M. Munoz, S. Gomez-Ramirez, J.A. Garcia-Erce, World J Gastroenterol, 15 (2009) 4666-4674.
[89] M. Muñoz, C. Breymann, J.A. García□Erce, S. Gómez□Ramírez, J. Comin, E. Bisbe, in, Wiley Online Library, 2008, pp. 172-183.
[90] S.D. Anker, C. Colet, New England Journal of Medicine, (2009).
[91] M. Auerbach, H. Ballard, Journal of the National Comprehensive Cancer Network (JNCCN), 6 (2008) 585-592.
[92] M. Muñoz, R. Leal-Noval, J.A. García-Erce, in, Elsevier, 2006, pp. S39-S42.
[93] S.S. Gordon, P.E. Hadley, D.B. Van Wyck, Obstet Gynecol, 109 (2007) 1S-127S.

[94] C. Breymann, C. Richter, C. Huttner, R. Huch, A. Huch, European journal of clinical investigation, 30 (2000) 154-161.
[95] M.R. Jahn, H.B. Andreasen, S. Fütterer, T. Nawroth, V. Schünemann, U. Kolb, W. Hofmeister, M. Munoz, K. Bock, M. Meldal, P. Langguth, European Journal of Pharmaceutics and Biopharmaceutics, 78 (2011) 480-491.
[96] S. Slomkowski, J.V. Alemán, R.G. Gilbert, M. Hess, K. Horie, R.G. Jones, P. Kubisa, I. Meisel, W. Mormann, S.a. Penczek, in, International Union of Pure and Applied Chemistry, 2011, pp. 2229-2259.
[97] J.S.G. Cox, G.R. Kennedy, J. King, P.R. Marshall, D. Rutherford, in, Wiley Online Library, 1972, pp. 513-517.
[98] D.S. Kudasheva, J. Lai, A. Ulman, M.K. Cowman, J Inorg Biochem, 98 (2004) 1757-1769.
[99] G.M. London, Journal of Pharmaceutical Sciences, 93 (2004) 1838-1846.
[100] A.K. Gupta, M. Gupta, Biomaterials, 26 (2005) 3995-4021.
[101] J. Xiao, J. Deng, J. Feng, B. Xiao, in, Google Patents, 2008.
[102] G. Nadamuni, C.S. Venkatesan, S. Sridevi, S. Sathiyanarayanan, R.K. Sreekant, S.A. Prem, in, IN, 2010.
[103] T.K. Jain, M.A. Morales, S.K. Sahoo, D.L. Leslie-Pelecky, V. Labhasetwar, Molecular Pharmaceutics, 2 (2005) 194-205.
[104] D. Maity, D.C. Agrawal, in, Elsevier, 2007, pp. 46-55.
[105] D.L. Huber, in, Wiley Online Library, 2005, pp. 482-501.
[106] W. Zimmermann, J. Lukowczyk, in, Google Patents, 2011.
[107] J.E. Toblli, G. Cao, L. Olivieri, M. Angerosa, in, ERA-EDTA, 2010, pp. 3631-3640.
[108] S. Neiser, M. Wilhelm, K. Schwarz, F. Funk, P. Geisser, S. Burckhardt, in, 2011, pp. 219-224.
[109] P. Reimer, T. Balzer, European Radiology, 13 (2003) 1266-1276.
[110] P. Geisser, E. Philipp, W. Richle, in, Google Patents, 2006.
[111] M. Muñoz, S. Gómez-Ramírez, E. Martín-Montañez, J. Pavía, J. Cuenca, J.A. García-Erce, in, SciELO Espana, 2012, pp. 1817-1836.
[112] B.G. Danielson, in, Am Soc Nephrol, 2004, pp. S93-S98.
[113] R.S. Ohgami, D.R. Campagna, E.L. Greer, B. Antiochos, A. McDonald, J. Chen, J.J. Sharp, Y. Fujiwara, J.E. Barker, M.D. Fleming, Nat Genet, 37 (2005) 1264-1269.
[114] A.S. Arbab, L.B. Wilson, P. Ashari, E.K. Jordan, B.K. Lewis, J.A. Frank, NMR in Biomedicine, 18 (2005) 383-389.
[115] L. Adlerova, A. Bartoskova, M. Faldyna, Veterinarni Medicina, 53 (2008) 457-468.
[116] D. Van Wyck, J. Anderson, K. Johnson, Nephrol Dial Transplant, 19 (2004) 561-565.
[117] M.M. Frank, L.F. Fries, Immunology Today, 12 (1991) 322-326.
[118] D.E. Owens III, N.A. Peppas, International Journal of Pharmaceutics, 307 (2006) 93-102.
[119] F. Alexis, E. Pridgen, L.K. Molnar, O.C. Farokhzad, Molecular Pharmaceutics, 5 (2008) 505-515.
[120] L. Illum, L. Jacobsen, R. Müller, E. Mak, S. Davis, Biomaterials, 8 (1987) 113-117.
[121] Z. Panagi, A. Beletsi, G. Evangelatos, E. Livaniou, D. Ithakissios, K. Avgoustakis, International Journal of Pharmaceutics, 221 (2001) 143-152.
[122] Y.-S. Sohn, H. Ghoti, W. Breuer, E. Rachmilewitz, S. Attar, G. Weiss, Z.I. Cabantchik, in, Ferrata Storti Foundation, 2012, pp. 670-678.
[123] Y. Chao, P.P. Karmali, D. Simberg, Role of carbohydrate receptors in the macrophage uptake of dextran-coated iron oxide nanoparticles, in: Nano-Biotechnology for Biomedical and Diagnostic Research, Springer, 2012, pp. 115-123.

[124] M. Nairz, A. Schroll, T. Sonnweber, G. Weiss, in, Wiley Online Library, 2010, pp. 1691-1702.
[125] S. Soe-Lin, S.S. Apte, M.R. Mikhael, L.K. Kayembe, G. Nie, P. Ponka, in, Elsevier, 2010, pp. 609-617.
[126] M. Kruszewski, Mutat Res, 531 (2003) 81-92.
[127] W. Breuer, M. Shvartsman, Z.I. Cabantchik, in, Elsevier, 2008, pp. 350-354.
[128] M.R. Jahn, T. Nawroth, S. Fütterer, U. Wolfrum, U. Kolb, P. Langguth, Molecular Pharmaceutics, 9 (2012) 1628–1637.
[129] I.C. Macdougall, Journal of Renal Care, 35 (2009) 8-13.
[130] G.R. Aronoff, J Am Soc Nephrol, 15 Suppl 2 (2004) S99-106.
[131] D.W. Coyne, M. Auerbach, in, Wiley Online Library, 2010, pp. 311-312.
[132] G.M. Rodgers, M. Auerbach, D. Cella, G.M. Chertow, D.W. Coyne, J.A. Glaspy, D.H. Henry, in, Am Soc Nephrol, 2008, pp. 833-834.
[133] G.M. Chertow, P.D. Mason, O. Vaage-Nilsen, J. Ahlme?n, Nephrology Dialysis Transplantation, 21 (2006) 378-382.
[134] Acute-Kidney-Injury-Work-Group, in: Kidney Disease: Improving Global Outcomes (KDIGO) International Society of Nephrology, 2012, pp. 6-61-138.
[135] G.R. Bailie, in, ASHP, 2012, pp. 310-320.
[136] S. Santosh, P. Podaralla, B. Miller, in, Oxford University Press, 2010, pp. 341-342.
[137] J. Ring, R. Valenta, in, 2011, pp. 219-224.
[138] in: FDA Advisory Committee Briefing Document, 2008, pp. 1-63.
[139] W. Richter, Int Arch Allergy Appl Immunol, 41 (1971) 826-844.
[140] K.-G. Ljungström, Journal of Vascular Surgery, 43 (2006) 1070-1072.
[141] EMA-CHMP, in, CHMP, http://www.ema.europa.eu/docs/en_GB/document_library/Press_release/2013/06/WC500144874.pdf, 2013.
[142] M.M. Okam, E. Mandell, N. Hevelone, R. Wentz, A. Ross, G.A. Abel, American Journal of Hematology, 87 (2012) E123-E124.
[143] S. Fishbane, E.A. Kowalski, Semin Dial, 13 (2000) 381-384.
[144] D.B. Van Wyck, Nephrology Dialysis Transplantation, 15 (2000) 36-39.
[145] J.A. García-Erce, J. Cuenca, S. Gómez-Ramírez, I. Villar, A. Herrera, M. Muñoz, in, 2009, pp. 17-27.
[146] R. Agarwal, N. Vasavada, N.G. Sachs, S. Chase, Kidney Int, 65 (2004) 2279-2289.
[147] T.A. Conner, C. McQuade, J. Olp, A.B. Pai, in, Springer, 2012, pp. 961-969.
[148] P.-S. Lim, Y.-H. Wei, Y.L. Yu, B. Kho, in, ERA-EDTA, 1999, pp. 2680-2687.
[149] A. Ganguli, H.S. Kohli, M. Khullar, K. Lal Gupta, V. Jha, V. Sakhuja, in, Informa UK Ltd UK, 2009, pp. 106-110.
[150] B.V. Stefánsson, B. Haraldsson, U. Nilsson, Nephron Clinical Practice, 118 (2011) c249-c256.
[151] G. Rostoker, M. Griuncelli, C. Loridon, R. Couprie, A. Benmaadi, C. Bounhiol, M. Roy, G. Machado, P. Janklewicz, G. Drahi, The American Journal of Medicine, 125 (2012) 991-999. e991.
[152] C. Canavese, D. Bergamo, G. Ciccone, F. Longo, F. Fop, A. Thea, G. Martina, A. Piga, Kidney International, 65 (2004) 1091-1098.
[153] M. Ali, A.O. Fayemi, R. Rigolosi, J. Frascino, T. Marsden, D. Malcolm, JAMA: the journal of the American Medical Association, 244 (1980) 343-345.
[154] F. Locatelli, B. Canaud, K.U. Eckardt, P. Stenvinkel, C. Wanner, C. Zoccali, Nephrol Dial Transplant, 18 (2003) 1272-1280.

[155] J.L. Sullivan, Lancet, 1 (1981) 1293-1294.
[156] J.T. Salonen, K. Nyyssonen, H. Korpela, J. Tuomilehto, R. Seppanen, R. Salonen, Circulation, 86 (1992) 803-811.
[157] S.J. Duffy, E.S. Biegelsen, M. Holbrook, J.D. Russell, N. Gokce, J.F. Keaney, Jr., J.A. Vita, Circulation, 103 (2001) 2799-2804.
[158] S. Kiechl, J. Willeit, G. Egger, W. Poewe, F. Oberhollenzer, Circulation, 96 (1997) 3300-3307.
[159] K. Klipstein-Grobusch, J.F. Koster, D.E. Grobbee, J. Lindemans, H. Boeing, A. Hofman, J.C. Witteman, Am J Clin Nutr, 69 (1999) 1231-1236.
[160] R.G. DePalma, V.W. Hayes, B.K. Chow, G. Shamayeva, P.E. May, L.R. Zacharski, in, Elsevier, 2010, pp. 1498-1503.
[161] T. Drueke, V. Witko-Sarsat, Z. Massy, B. Descamps-Latscha, A.P. Guerin, S.J. Marchais, V. Gausson, G.M. London, Circulation, 106 (2002) 2212-2217.
[162] D.M. Baer, I.S. Tekawa, L.B. Hurley, Circulation, 89 (1994) 2915-2918.
[163] J. Danesh, P. Appleby, Circulation, 99 (1999) 852-854.
[164] R.F. Franco, M.A. Zago, M.D. Trip, H. ten Cate, A. van den Ende, M.H. Prins, J.J. Kastelein, P.H. Reitsma, Br J Haematol, 102 (1998) 1172-1175.
[165] J.L. Sullivan, in, Elsevier, 2009, pp. 718-723.
[166] E. Lapice, M. Masulli, O. Vaccaro, in, Springer, 2013, pp. 1-14.
[167] G.R. Bailie, J.A. Clark, C.E. Lane, P.L. Lane, Nephrol Dial Transplant, 20 (2005) 1443-1449.
[168] P. Paffetti, S. Perrone, M. Longini, A. Ferrari, D. Tanganelli, B. Marzocchi, G. Buonocore, Biological Trace Element Research, 112 (2006) 221-232.
[169] U.A. Nilsson, M. Bassen, K. SÃ¤vman, I. Kjellmer, in, Informa UK Ltd UK, 2002, pp. 677-684.
[170] B.P. Esposito, S. Epsztejn, W. Breuer, Z.I. Cabantchik, Anal Biochem, 304 (2002) 1-18.
[171] L. von Bonsdorff, E. Lindeberg, L. Sahlstedt, J. Lehto, J. Parkkinen, Clinical Chemistry, 48 (2002) 307-314.
[172] G. Borchard, B. Flühmann, S. Mühlebach, Regulatory Toxicology and Pharmacology, (2012).
[173] J.E. Toblli, G. Cao, L. Oliveri, M. Angerosa, Inflamm Allergy Drug Targets, 11 (2012) 66.
[174] J.E. Toblli, G. Cao, L. Oliveri, M. Angerosa, in, Editio Cantor Verlag, 2009, pp. 176-190.
[175] A. Martin-Malo, A. Merino, J. Carracedo, M.A. Alvarez-Lara, R. Ojeda, S. Soriano, R. Crespo, R. Ramirez, P. Aljama, in, ERA-EDTA, 2012, pp. 2465-2471.
[176] J. Stein, A. Dignass, K.U. Chow, Curr Med Res Opin, 28 (2012) 241-243.
[177] H. Schellekens, E. Klinger, S. Mühlebach, J.-F. Brin, G. Storm, D.J.A. Crommelin, in, Elsevier, 2011, pp. 176-183.
[178] S. Roth, P. Langguth, K. Spicher, H. Enzmann, Translational Research, 151 (2008) 36-44.
[179] CHMP, in, EMA, 2013, pp. 1-10.
[180] W. Borchardt-Ott, Kristallographie, Springer, 2009.
[181] L. Reimer, H. Kohl, Transmission electron microscopy: physics of image formation, Springer, 2008.
[182] B. Fultz, J.M. Howe, Transmission electron microscopy and diffractometry of materials, Springer, 2012.
[183] J.M. Cowley, J.C.H. Spence, in, North-Holland, 1978, pp. 433-438.
[184] J.M. Zuo, M. Gao, J. Tao, B.Q. Li, R. Twesten, I. Petrov, in, Wiley Online Library, 2004, pp. 347-355.
[185] M.R. Jahn, in, 2009, pp. 1-223.

[186] U. Schwertmann, R.M. Cornell, Iron oxides in the laboratory, 1 ed., Wiley-VCH, 1991.
[187] M. Instruments, in, 2011.
[188] R.F.T. Stepto, in, International Union of Pure and Applied Chemistry, 2009, pp. 351-353.
[189] M. Instruments, in, 2009, pp. 1-12.
[190] W. Brown, Dynamic light scattering: the method and some applications, Oxford University Press, USA, 1993.
[191] C.R. Gibbs, Analytical Chemistry, 48 (1976) 1197-1201.
[192] Roche/Hitachi, in, 2010.
[193] J. Siedel, A.W. Wahlefeld, J. Ziegenhorn, in, 1984, pp. 975.
[194] J.S.G. Cox, G.R. Kennedy, J. King, P.R. Marshall, D. Rutherford, Journal of Pharmacy and Pharmacology, 24 (1972) 513-517.
[195] C. Giacovazzo, H.L. Monaco, D. Viterbo, F. Scordari, G. Gilli, G. Zanotti, M. Catti, Crystallographic computing, in: Fundamentals of crystallography, Oxford University Press, New York, 1992, pp. 61-140.
[196] V.S. Balakrishnan, M. Rao, A.T. Kausz, L. Brenner, B.J.G. Pereira, T.B. Frigo, J.M. Lewis, European Journal of Clinical Investigation, 39 (2009) 489.
[197] U. Schwertmann, Plant and Soil, 130 (1991) 1-25.
[198] H.P. Koch, in, 1984, pp. 130-139.
[199] EMA, in, Eurpean Medicines Agency (EMA) - Committee for Medicinal Products for Human Use (CHMP), 2011.
[200] C.J. Rebouche, C.L. Wilcox, J.A. Widness, J Biochem Biophys Methods, 58 (2004) 239-251.
[201] S. Patil, A. Sandberg, E. Heckert, W. Self, S. Seal, Biomaterials, 28 (2007) 4600-4607.
[202] O. Harush-Frenkel, N. Debotton, S. Benita, Y. Altschuler, Biochemical and Biophysical Research Communications, 353 (2007) 26-32.
[203] C. Chouly, D. Pouliquen, I. Lucet, J. Jeune, P. Jallet, Journal of Microencapsulation, 13 (1996) 245-255.
[204] ATSDR, in, U.S. Department of Health and Human Services http://www.atsdr.cdc.gov/toxguides/toxguide-15.pdf, 2005.
[205] J.D. Webster, T.F. Parker, A.C. Alfrey, W.R. Smythe, H. Kubo, G. Neal, A.R. Hull, Ann Intern Med, 92 (1980) 631-633.
[206] R.M. Cornell, U. Schwertmann, The iron oxides: structure, properties, reactions, occurrences and uses, Wiley-vch, 2003.
[207] K. Thorstensen, I. Romslo, Biochemical Journal, 271 (1990) 1-10.
[208] B. Halliwell, J.M. Gutteridge, Methods Enzymol, 186 (1990) 1-85.
[209] F. Funk, G.J. Long, D. Hautot, R. Büchi, I. Christl, P.G. Weidler, Hyperfine Interactions, 136 (2001) 73-95.
[210] L. Gutiérrez, M. del Puerto Morales, F. José Lázaro, Journal of Magnetism and Magnetic Materials, 293 (2005) 69-74.
[211] F. Locatelli, J. Bommer, G.M. London, A. Martin-Malo, C. Wanner, M. Yaqoob, C. Zoccali, Nephrol Dial Transplant, 16 (2001) 459-468.
[212] T. Higuchi, in, Wiley Online Library, 1963, pp. 1145-1149.
[213] H. Fesssi, J.P. Marty, F. Puisieux, J.T. Carstensen, in, Elsevier, 1978, pp. 265-274.
[214] M. Walser, in, American Society for Clinical Investigation, 1961, pp. 723.
[215] R. Agarwal, in, Nature Publishing Group, 2004, pp. 1139-1144.
[216] P. Geisser, M. Baer, E. Schaub, Arzneimittel-Forschung, 42 (1992) 1439-1452.

[217] R. Legssyer, P. Geisser, H. McArdle, R.R. Crichton, R.J. Ward, Biometals, 16 (2003) 425-433.
[218] J.M. Lewis, J. Am. Soc. Nephrol., 14:771A (2003).
[219] B. Scheiber-Mojdehkar, B. Sturm, L. Plank, I. Kryzer, H. Goldenberg, Biochem Pharmacol, 65 (2003) 1973-1978.
[220] P.A. Seligman, R.B. Schleicher, Clin Chem, 45 (1999) 898-901.
[221] G. Sengoelge, J. Kletzmayr, I. Ferrara, A. Perschl, W.H. Horl, G. Sunder-Plassmann, J Am Soc Nephrol, 14 (2003) 2639-2644.
[222] B. Sturm, H. Goldenberg, B. Scheiber-Mojdehkar, Eur J Biochem, 270 (2003) 3731-3738.
[223] B. Sturm, H. Laggner, N. Ternes, H. Goldenberg, B. Scheiber-Mojdehkar, Kidney Int, 67 (2005) 1161-1170.
[224] R.A. Zager, Kidney International, 68 (2005) 1533-1542.
[225] R.A. Zager, A.C.M. Johnson, S.Y. Hanson, S. Lund, American Journal of Physiology - Renal Physiology, 288 (2005) F290-F297.
[226] R.A. Zager, A.C. Johnson, S.Y. Hanson, H. Wasse, Am J Kidney Dis, 40 (2002) 90-103.
[227] R.A. Zager, A.C. Johnson, S.Y. Hanson, Kidney Int, 66 (2004) 144-156.
[228] R.E. Fleming, P. Ponka, New England Journal of Medicine, 366 (2012) 348-359.
[229] N. Ternes, B. Scheiber-Mojdehkar, G. Landgraf, H. Goldenberg, B. Sturm, Nephrol. Dial. Transplant., (2007) gfm315.
[230] S.-D. Li, L. Huang, Molecular Pharmaceutics, 5 (2008) 496-504.
[231] W. Forth, D. Henschler, W. Rummel, K. Starke, Mannheim/Leipzig/Wien/Zürich: Wissenschaftsverlag, (1996).
[232] Y. Baratli, A.-L. Charles, V.r. Wolff, L. Ben Tahar, L. Smiri, J. Bouitbir, J. Zoll, F.o. Piquard, O. Tebourbi, M. Sakly, in, Elsevier, 2013, pp. 2142-2148.
[233] S. Moghimi, H. Hedeman, I. Muir, L. Illum, S. Davis, Biochimica et Biophysica Acta (BBA)-General Subjects, 1157 (1993) 233-240.
[234] S.R. Alam, A.S. Shah, J. Richards, N.N. Lang, G. Barnes, N. Joshi, T. MacGillivray, G. McKillop, S. Mirsadraee, J. Payne, Circulation: Cardiovascular Imaging, 5 (2012) 559-565.
[235] P.D. Sturkie, Avian physiology, New York, 1976.
[236] P.D. Sturkie, J.A. Vogel, American Journal of Physiology--Legacy Content, 197 (1959) 1165-1166.
[237] J.N. Boelkins, W.J. Mueller, K.L. Hall, Comparative Biochemistry and Physiology Part A: Physiology, 46 (1973) 735-743.
[238] L.A. Sapirstein, F.A. Hartman, American Journal of Physiology--Legacy Content, 196 (1959) 751-752.
[239] E.C. Theil, G.M. Tosky, Developmental Biology, 69 (1979) 666-672.
[240] E.C. Theil, British Journal of Haematology, 45 (1980) 357-360.
[241] M.P. Richards, B.T. Weinland, Biological Trace Element Research, 7 (1985) 269-284.
[242] T. Kobayashi, H. Tadokoro, K. Matsumoto, Internal medicine (Tokyo, Japan), 52 (2012) 1369-1373.
[243] C. He, Y. Hu, L. Yin, C. Tang, C. Yin, Biomaterials, 31 (2010) 3657-3666.
[244] M. Roser, D. Fischer, T. Kissel, in, Elsevier, 1998, pp. 255-263.
[245] R.A. Zager, Clin J Am Soc Nephrol, 1 (2006) S24-31.
[246] R. Michelis, R. Gery, S. Sela, R. Shurtz-Swirski, N. Grinberg, T. Snitkovski, S.M. Shasha, B. Kristal, Nephrol Dial Transplant, 18 (2003) 924-930.
[247] R.G. Carlini, E. Alonzo, E. Bellorin-Font, J.R. Weisinger, Nephrology Dialysis Transplantation, 21 (2006) 3055-3061.

[248] T.M. Rooyakkers, E.S. Stroes, M.P. Kooistra, E.E. van Faassen, R.C. Hider, T.J. Rabelink, J.J. Marx, Eur J Clin Invest, 32 Suppl 1 (2002) 9-16.
[249] N. Stanley, N. Stadler, A.A. Woods, P.G. Bannon, M.J. Davies, Free Radical Biology and Medicine, 40 (2006) 1636-1643.
[250] S.V. Shah, M.G. Alam, Am J Kidney Dis, 41 (2003) S80-83.
[251] E. Porreca, S. Ucchino, C. Di Febbo, N. Di Bartolomeo, D. Angelucci, A.M. Napolitano, A. Mezzetti, F. Cuccurullo, Arteriosclerosis, Thrombosis, and Vascular Biology, 14 (1994) 299-304.
[252] M. Nairz, I. Theurl, S. Ludwiczek, M. Theurl, S.M. Mair, G. Fritsche, G. Weiss, Cellular Microbiology, 9 (2007) 2126-2140.
[253] T. Drüeke, V. Witko-Sarsat, Z. Massy, B. Descamps-Latscha, A.P. Guerin, S.J. Marchais, V. Gausson, G.M. London, Circulation, 106 (2002) 2212-2217.
[254] S. Omiya, S. Hikoso, Y. Imanishi, A. Saito, O. Yamaguchi, T. Takeda, I. Mizote, T. Oka, M. Taneike, Y. Nakano, Journal of Molecular and Cellular Cardiology, 46 (2009) 59-66.
[255] J.L. Sullivan, in, Maywood, NJ: The Society, c2001-, 2007, pp. 1014-1020.
[256] N.C. Van der Weerd, M.P. Grooteman, M.L. Bots, M.A. Van den Dorpel, C.H. den Hoedt, A.H. Mazairac, M.J. Nubé, E.L. Penne, J.F. Wetzels, E.T. Wiegerinck, Nephrology Dialysis Transplantation, (2012).
[257] G.W. Dec, in, 2009, pp. 2475-2477.
[258] G.W. Dec, in, Am Coll Cardio Found, 2006, pp. 2490-2492.
[259] Y.-D. Tang, S.D. Katz, in, Am Heart Assoc, 2006, pp. 2454-2461.
[260] P. Leszek, B. Sochanowicz, M. Szperl, P. Kolsut, K. Brzóska, W. Piotrowski, T.M. Rywik, B. Danko, H. Polkowska-Motrenko, J.M. Różański, International Journal of Cardiology, 159 (2012) 47-52.
[261] H. Ghoti, E.A. Rachmilewitz, R. Simon-Lopez, R. Gaber, Z. Katzir, E. Konen, T. Kushnir, D. Girelli, N. Campostrini, E. Fibach, European Journal of Haematology, 89 (2012) 87-93.
[262] S.-J. Park, C.-W. Han, Journal of Korean Medical Science, 23 (2008) 320-323.
[263] R. Agarwal, D.J. Leehey, S.M. Olsen, N.V. Dahl, Clinical Journal of the American Society of Nephrology, 6 (2011) 114-121.
[264] N. Milman, in, Springer, 2011, pp. 369-377.
[265] Acute-Kidney-Injury-Work-Group, in: KDIGO Clinical Practice Guideline for Acute Kidney Injury. , 2012, pp. 1-138.
[266] R. Deicher, F. Ziai, G. Cohen, M. Mullner, W.H. Horl, Kidney International, 64 (2003) 728-736.
[267] M.R. Jahn, Y. Mrestani, P. Langguth, R.H.H. Neubert, Electrophoresis, 28 (2007) 2424 - 2429.
[268] O. Kakhlon, Z.I. Cabantchik, Free Radic Biol Med, 33 (2002) 1037-1046.
[269] K. Gkouvatsos, G. Papanikolaou, K. Pantopoulos, Biochim Biophys Acta, 1820 (2012) 188-202.
[270] P.S. Sidhu, Clays & Clay Minerals, 29 (1981) 269-276.

List of figures & tables

Figures

Tables

List of published work

Articles

Fütterer, S., Andrusenko, I., Kolb, U., Hofmeister, W., & Langguth, P. (2013). Struktural characterization of iron oxide / hydroxide nanoparticles in nine different parenteral drugs for the treatment of iron deficiency anaemia by electron diffraction (ED) and X-ray powder diffraction (XRPD). *Journal of pharmaceutical and biomedical analysis*, *86*, 151-160.

Jahn, M. R., Andreasen, H. B., Fütterer, S., Nawroth, T., Schünemann, V., Kolb, U., Hofmeister, W.; Munoz, M.; Bock, K.; Meldal, M.; Langguth, P.; (2011). A comparative study of the physicochemical properties of iron isomaltoside 1000 (Monofer®), a new intravenous iron preparation and its clinical implications. European Journal of Pharmaceutics *and Biopharmaceutics*, *78*(3), 480-491.

Jahn, M. R., Nawroth, T., Fütterer, S., Wolfrum, U., Kolb, U., & Langguth, P. (2012). Iron oxide /hydroxide nanoparticles with negatively charged shells show increased uptake in Caco-2 cells. *Molecular Pharmaceutics*, *9*(6), 1628-1637.

Poster presentations

Fütterer, S.; Andreasen, H.;Jahn, M.; Nawroth, T.; Jørgensen, S.L.; Kolb, U.; Hofmeister, W.; Langguth, P. Comparison of nanoparticular iron formulations for parenteral use - Are they similar and readily exchangeable? *Poster presentation at the DPhG annual conference 2010: "Personalisierte Therapeutika - Traum oder Wirklichkeit?", Braunschweig*